


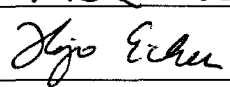
INVESTIGATING THE RETENTION OF BRIGHT AND DARK EJECTA FROM
SMALL RAYED CRATERS ON MARS


By

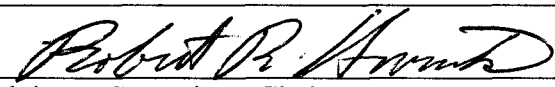
Fred J. Calef III

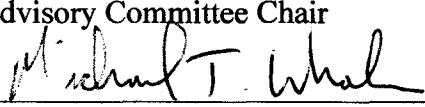
RECOMMENDED:



Ken Dean


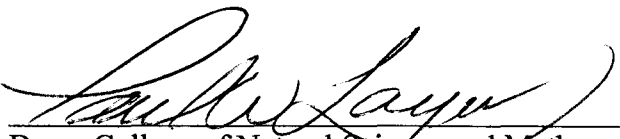
Hajo Eicher


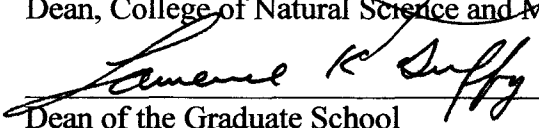
V. Romanouk


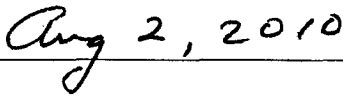
Robert P. Armitage
Advisory Committee Chair


Michael T. Whalen
Chair, Department of Geology and Geophysics

APPROVED:



Paul W. Layer
Dean, College of Natural Science and Mathematics


Lorraine K. Suffy
Dean of the Graduate School


Date

INVESTIGATING THE RETENTION OF BRIGHT AND DARK EJECTA FROM
SMALL RAYED CRATERS ON MARS

A
THESIS

Presented to the Faculty
of the University of Alaska Fairbanks
in Partial Fulfillment of the Requirements
for the Degree of

DOCTOR OF PHILOSOPHY

By

Fred J. Calef III

Fairbanks, Alaska

August 2010

UMI Number: 3436654

All rights reserved

INFORMATION TO ALL USERS

The quality of this reproduction is dependent upon the quality of the copy submitted.

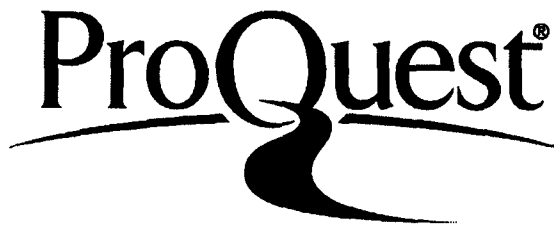
In the unlikely event that the author did not send a complete manuscript and there are missing pages, these will be noted. Also, if material had to be removed, a note will indicate the deletion.



UMI 3436654

Copyright 2010 by ProQuest LLC.

All rights reserved. This edition of the work is protected against unauthorized copying under Title 17, United States Code.



ProQuest LLC
789 East Eisenhower Parkway
P.O. Box 1346
Ann Arbor, MI 48106-1346

Abstract

Impact cratering is one of the principal geologic processes operating throughout the solar system. On Mars, small rayed impact craters (SRC) form continuously and randomly on the surface. Ejecta retention, the timespan and ability of excavated ejecta to remain in place around a crater rim, records a lineage of recent surface processes. However, the timescales under which small rayed craters are produced and their origin, whether terrestrial or cosmic, plays an important role in further investigating surface processes and possible recent climate variations. By examining thousands of randomly chosen panchromatic images from the Mars Orbiter Camera Narrow Angle (MOCNA) camera, a population of 630 SRC was catalogued across three equatorial and two polar regions on Mars. The survey of MOCNA images also revealed intriguing Enigmatic Linear Features (ELFs) in the northern hemisphere of Mars, which a short side study revealed to be a unique form of dust-devil track. From statistically examining several physical parameters, dust deposition and periglacial erosion were found to be the major factors affecting ejecta retention for the SRC. SRC morphology revealed ejecta retention sequences that followed four stages of ejecta retention from the initial impact to eventual erasure from the surface. By reconstructing the current cratering rate from estimates of atmospheric filtering, it was possible to calculate the ejecta retention age across Mars. In general, SRC ejecta are retained on the surface for <100 ka. Based on ejecta morphology and retention age estimates, a possible shift from depositional to erosional processes just south of the Martian equator is suspected to have occurred within this timeframe.

Table of Contents

	Page
Signature Page	i
Title Page	ii
Abstract	iii
Table of Contents	iv
List of Figures	ix
List of Tables	xiv
Acknowledgements	xvi
GENERAL INTRODUCTION.....	1
REFERENCES	7
CHAPTER 1: Enigmatic Linear Features in the Northern Hemisphere of Mars: Their Formation Process.....	9
ABSTRACT.....	9
1.1 INTRODUCTION	10
1.2 STUDY AREA	11
1.3 METHODOLOGY	12
1.4 RESULTS	13
1.4.1 General Observations.....	13
1.4.2 Population Statistics.....	15
1.4.3 Orientation Analysis	16
1.5 DISCUSSION	16

1.6 CONCLUSION.....	18
REFERENCES	19
TABLES	21
FIGURES.....	24
CHAPTER 2: Geomorphic Analysis of Small Rayed Craters on Mars: Examining Primary versus Secondary Impacts.....	30
ABSTRACT.....	30
2.1 INTRODUCTION	32
2.1.1 SRC Primary and Secondary Populations.....	35
2.1.2 Geologic Setting.....	36
2.2 METHODOLOGY	38
2.3 OBSERVATIONS.....	43
2.3.1 Primary SRC	43
2.3.2 Secondary SRC	46
2.4 RESULTS	48
2.4.1 Crater Measurements	49
2.4.2 Ejecta Measurements	50
2.4.3 Directional Analysis.....	52
2.5 DISCUSSION.....	53
2.5.1 Differences between Primary and Secondary Ejecta Retention	53
2.5.2 Similarity of Primary and Secondary Crater Rims	61
2.5.3 Identification of New Primary Cratering Events	62

2.5.4 Crossover between Primary and Secondary Cratering Events	63
2.6 Conclusions.....	68
REFERENCES	69
TABLES	79
FIGURES.....	80
CHAPTER 3: Global Distribution of Small Rayed Craters on Mars: Sequences of Ejecta Retention.....	109
ABSTRACT.....	109
3.1 INTRODUCTION	112
3.1.1 Small Impact Craters as Tools for Understanding Current Surficial Processes.....	112
3.1.2 The Effects of Secondaries	114
3.1.3 Research Goals.....	117
3.2 METHODOLOGY	118
3.2.1 Image Sampling	118
3.2.2 Hypothesized Ejecta Retention Models.....	120
3.2.3 Surface Property Statistics	122
3.2.4 Correcting for Secondary Impacts: a case study of the large primary crater Zunil.....	124
3.2.5 Study Regions.....	126
3.3 OBSERVATIONS AND RESULTS.....	127
3.3.1 SRC Global Distribution.....	127

3.3.2 SRC Ejecta and Crater Morphology	131
3.3.3 Formation Properties and SRC Spatial Distribution.....	133
3.3.4 Statistical Correlations of SRC Occurrence and Formation Properties	134
3.3.5 Identification of Erosional and Depositional Sequences	136
3.3.6 Zunil and non-Zunil SRC.....	140
3.4. DISCUSSION.....	140
3.4.1 Spatial Variability of Ejecta Retention on Mars	140
3.4.2 Estimated Primary to Secondary Ratio around Zunil	148
3.5 Conclusions.....	149
REFERENCES	151
TABLES	158
FIGURES.....	163
CHAPTER 4: Small Rayed Crater Ejecta Retention Age Calculated from Current Crater Production Rates on Mars.....	182
ABSTRACT.....	182
4.1 INTRODUCTION	184
4.1.1 Understanding Small Rayed Crater Ejecta Retention.....	184
4.1.2 Dating small <i>D</i> craters on Mars	187
4.1.3 Estimating the Current Cratering Rate for Small Rayed Craters on Mars.....	190
4.2 METHODOLOGY	192
4.2.1 Estimating Ejecta Retention Age.....	192
4.2.2 Correcting for Atmospheric Filtering	193

4.2.3 Rayed Crater Counting	196
4.3 RESULTS AND DISCUSSION	198
4.3.1 Hartmann Production Function Ejecta Retention Ages across Mars.....	198
4.3.2 Current Production Function Ejecta Retention Ages across Mars.....	200
4.3.3 Ejecta Retention Ages for Mars.....	201
4.4 CONCLUSION.....	203
REFERENCES	205
TABLES	209
FIGURES.....	216
GENERAL CONCLUSIONS.....	222
APPENDIX.....	224

List of Figures

	Page
Figure 1.1: A section of MOC-NA images M1003516 containing dust devil tracks (A) and M0001362 containing ELF's (B).	24
Figure 1.2: Subsection of study area in the northern hemisphere of Mars	25
Figure 1.3: Example of the orientation analysis selection process.	26
Figure 1.4: Section of MOC-NA image M0307347 with preferential placement of ELF's.	27
Figure 1.5: Occurrence of ELF's in the study area and dust devils in Amazonis Planitia and the Hellas Basin (southern hemisphere) as a function of L_s	28
Figure 1.6: Orientation analysis of 10 ELF images and dust devil track image M1003516.	29
Figure 2.1: Example of primary small rayed crater on Mars	80
Figure 2.2: Example of several Zunil secondary small rayed craters on Mars.....	81
Figure 2.3: Example of ejecta planform from the atmospheric breakup of the primary meteorite before impact	82
Figure 2.4: Location of twenty primary [Malin et al., 2006] and thirty-eight secondary SRC derived from MOCNA images	83
Figure 2.5: Secondary SRC found in MOCNA and HiRISE RED images from this study.	84
Figure 2.6: Geologic formations encountered within the study area	85

Figure 2.7: Measurements of ejecta planform based on distal extent of continuous ejecta deposit.....	86
Figure 2.8: Measurements of crater planform based on highest discernable edge of rim.	87
Figure 2.9: Air-blast region surrounding primary impact crater.....	88
Figure 2.10: Continuous and discontinuous rays from primary impact craters.....	89
Figure 2.11: Craters from suspected fragmented meteorites.	90
Figure 2.12: ‘No ejecta’ primaries in MOCNA ROTO and HiRISE imagery.....	91
Figure 2.13: Primary crater with nested depression and boulder strewn ejecta.....	92
Figure 2.14: Crater field created by a primary impact.....	93
Figure 2.15: Examples of secondary SRC ejecta, crater rims and floors	94
Figure 2.16: Wind modified secondary craters.....	95
Figure 2.17: Total crater counts binned by crater diameter.....	96
Figure 2.18: (A) Circularity (C_R) and (B) Form Ratio (F_R) results for primary and secondary crater rims	97
Figure 2.19: Fractal Dimension Index (FD_I) results for primary and secondary crater rims.	98
Figure 2.20: Circularity (C_R) and Form Ratio (F_R) results for primary and secondary ejecta planforms.	99
Figure 2.21: Fractal Dimension Index (FD_I) results for primary and secondary ejecta planforms	100
Figure 2.22: Distal ejecta range for primaries and secondaries, normalized by crater radii (R).....	101

Figure 2.23A: Rose diagrams for crater rim long-axis orientation and ejecta uprange azimuth for secondary craters	102
Figure 2.23B: Rose diagrams for crater rim long-axis orientation and ejecta uprange azimuth for secondary craters	103
Figure 2.24: Linear orientation of secondary craters near Zunil	104
Figure 2.25: SRC of different ages in Elysium Planitia.....	105
Figure 2.26: Transition from bright-rayed to dark-rayed craters in Athabasca Valles...	106
Figure 2.27: Dark and bright SRCs indicating two vertically distinct stratigraphic units	107
Figure 2.28: Two candidate primaries in the Elysium Planitia region, Mars	108
Figure 3.1: Twelve examples of small (subkilometer diameter) rayed craters (SRC) on Mars	163
Figure 3.2: Comparison of spatial distribution and resolution for a 5% sample and complete MOCNA image database.	164
Figure 3.3: Percent surface area covered by elevations in 1km bins for Mars and our sample of MOCNA images.....	165
Figure 3.4: Percent surface area covered by age units for Mars and our sample of MOCNA images.	166
Figure 3.5: Size-diameter relationship for maximum secondary size distal to Zunil	167
Figure 3.6: SRC within the secondary field of Zunil.....	168
Figure 3.7: Five generalized physiographic regions for our study	169
Figure 3.8: Small rayed crater indices for Mars	170

Figure 3.9: Latitude and longitude dependance of the global SRC population	171
Figure 3.10: Large rayed craters on Mars.....	172
Figure 3.11: SRC continuous ejecta morphology across Mars.....	173
Figure 3.12: Geologic age unit distribution, thermophysical units and SRC occurrence on Mars	174
Figure 3.13: Night-time thermal inertia values, albedo and dust cover with SRC occurrence on Mars.....	175
Figure 3.14: SRC occurrences versus MOLA elevation and water equivalent hydrogen	176
Figure 3.15: Box plots of SRC occurrence and non-occurrence from our study images.	177
Figure 3.16: Observed SRC ejecta retention sequence on Mars.....	178
Figure 3.17: Ejecta retention sequence statistics for SRC	179
Figure 3.18: SRC from different events.....	180
Figure 3.19: SRC images classified by the erosion or deposition ejecta retention sequence on Mars	181
Figure 4.1: Small rayed craters on Mars.....	216
Figure 4.2: Mars location map for study areas from Calef et al. [2010].....	217
Figure 4.3: Example of an isochron dating plot using data from Calef et al. [2010]	218
Figure 4.4: Corrections to the Malin et al. [2006] correct crater production function on Mars	219

Figure 4.5: Hartmann production function (HPF) ejecta retention ages for SRC on Mars

..... 220

Figure 4.6: Current production function (CPF) ejecta retention ages for SRC on Mars 221

List of Tables

	Page
Table 1.1: Geologic Units Underlying ELF Images	21
Table 1.2: ELF and Dust Devil Population Statistics for 10 Images	23
Table 2.1: Criteria for recognizing Primary versus Secondary Craters on Mars.....	79
Table 3.1: Diameter-distance relationship for Zunil SRC	158
Table 3.2: Crater diameter statistics for SRC by region on Mars.....	159
Table 3.3: Statistics for 5% MOCNA image sample and presence/absence of SRC for five formation parameters	160
Table 3.4: F-Test and T-Test Statistics for MOCNA Images with and without SRC	161
Table 3.5: Zunil SRC and non-Zunil SRC Counts	162
Table 4.1: Crater counts by study region.....	209
Table 4.2: Atmospheric correction factors for the crater production function	210
Table 4.3: Martian isochrons extrapolated from the CPF.....	211
Table 4.4: Craters per km ² by study region	212
Table 4.5: 1- σ crater count error as $\pm N^{(1/2)}$ /area of study region	213
Table 4.6: HPF Ejecta Retention (E_{ret}) estimates for five regions on Mars.....	214
Table 4.7: CPF Ejecta Retention (E_{ret}) estimates for five regions on Mars	215
Table A-1: Primary crater diameter(s) and rim measurements from MOCNA and HIRISE imagery	224
Table A-2: Primary rayed crater ejecta measurements from MOCNA and HIRISE imagery	227

Table A-3: Secondary crater diameter(s) and rim measurements from MOCNA and HIRISE imagery.....	228
Table A-4: Secondary rayed crater ejecta measurements from MOCNA and HIRISE imagery	235
Table A-5: Small rayed crater (SRC) database.....	240

Acknowledgements

It has been a long and sometimes enigmatic odyssey from 2001 to this moment. Though I can say, at the very least, I made it!

I would like to start by thanking my committee for being patient while I worked methodically through the thesis process both at the University of Alaska Fairbanks (UAF) and 3000+ miles away. Thanks go to Buck Sharpton for bringing me to UAF to start my Ph.D. and to Robbie Herrick for taking over as committee chair and bringing me to the finish line. For their overwhelming patience, the rest of my committee, Hajo Eicken, Ken Dean, and Vladimir Romanovsky, deserve much heartfelt praise. To the group of new geologists who started with me or during my time at UAF: Emily, Leslie, Lily, Mike, Rich, Rob, Sean at Natural Sciences and Andrea, Candace, Christina, Courtney, at the GI; I finally caught up to you! Thanks also to the Planetary Lab crew: Cindy, John, Roman, Rosanna, and Sharon; could not have survived the journey without your friendship, humor, and perspective.

Thanks to Mom and Dad who deserve credit for supporting me in my pursuit of higher education these many long years, even if they didn't understand why it was important to go this far academically. Auntie Lee and Uncle Robert, thanks for showing interest in my 'Mars Trek' and always surprising me with some scintillating rocks. Thanks to my siblings, Craig, Cameron, Chase and my 'lost' brother Nick; you guys are the best. Not to forget, Jan, for bridging the gap from the past to the future in our family. To my wife, Monika, your dedication, encouragement, and help through the 'dark years'

that has been this nine year voyage is well appreciated, even if I didn't show it as much as I could and should have. Orion and Hudson, my beautiful and intelligent sons, you make the world spin just a little faster on its axis. I look forward to watching you grow and hope you get to explore the planets and stars that you are named for.

To Doug Bregoli and Ned Morse, the two most bizarre, funny, artistic and weird friends a person could ever wish for. Thanks for bringing the entertainment that is your friendship in ways that only you two could. I will bring home the Martian germ hordes and compress the atmosphere, so there! In New York, thanks goes to Maggie, Sara, Zack, Tom and Sensei Tracy for throwing me around. OSU!

This dissertation is dedicated to my grandfather, Fred J. Calef Sr., who introduced me to Nature and showed me that every rock has a story to tell.

GENERAL INTRODUCTION

Impact cratering occurs on all of the terrestrial planets and satellites, though the current state of activity is low compared to the initial heavy bombardment period when the solar system was formed [Wagner, 1991]. Researchers have used crater morphology (such as the depth to diameter ratio or shape and size of the ejecta blanket), lithology (e.g. maximum block size, horizontal distribution of excavated material, optical and geochemical properties) to gather information about the history and material properties of the solar system bodies on which craters occur [e.g. Melosh, 1989; French, 1998 and references therein]. Crater ejecta contain information about the target surface and subsurface, as well as the impactor itself. In general, a rayed ejecta crater is considered younger than a similar diameter crater without ejecta. Small rayed craters (SRC) with visually bright or dark ejecta rays that extend up to hundreds of crater radii have been observed on Mercury [Hapke et al., 1975], the Moon [Blewett et al., 1993], outer solar system satellites like Ganymede [Schenk and McKinnon, 1985], and recently on Mars [Grier and Hartmann, 2000]. Given that not all Martian craters have optically visible ejecta, understanding the length of time that ejecta are retained on the surface tells us about the deposition (e.g. dust) and erosion (e.g. wind) occurring on the planet as well as about the current crater production rate on Mars. In addition, unlike other geologic processes which are spatially limited to distinct latitudes and morphologic locations (e.g. Martian gullies are predominately limited to crater rims), craters are emplaced randomly and monotonically across Mars' surface. These unique and ubiquitous geologic features

can serve as a proxy to understand climatic and subsurface process active in Mars' recent past. This can be accomplished if one can identify ejecta retention processes and the time period over which they operate.

Hartmann [1999] created isochrons (lines of equivalent crater production age) that are based on lunar sample dates tied to impact surfaces on the Moon and estimates of the cratering rate (R_{bolide}) over the last 4 billion years. Plotted as power-laws on crater size/frequency distribution graphs, estimates of the absolute age of a bedrock surface can be determined without the need for physical samples. Such samples have only been gathered for a few locales on the Moon and from a much smaller set of meteorites blasted from the surface of Mars lacking any geologic context. With the initial decrease of pixel size (<10m/pixel) brought about by visible wavelength “push broom” cameras such as the Mars Orbiter Camera Narrow Angle instrument (MOCNA) and more recently the High Resolution Imaging Science Experiment (HiRISE), this dating technique has been augmented to work with smaller craters (tens to hundreds of meters in diameter) yielding increasingly younger dates. For example, the age of the interior of the Olympus Mons caldera is estimated to be only 1 Ma [e.g. Hartmann et al., 2001; Neukum et al., 2004] and suspected fluvial gullies on crater rims as young as 100 ka [Dickson and Head, 2009]. Recent works by several authors [Block and Barlow, 2005; McEwen et al., 2005; Plescia, 2005; Tornabene et al., 2005] have argued that dating surfaces using these small craters may be in error. Even Hartmann [2005] admits that dating using the small cratering record could be improved by a better understanding of the primary versus secondary crater flux. McEwen et al. [2005] calculate the number of sub-kilometer

secondaries created by a 10 km primary impact named Zunil that was found using night-time thermal images. Estimates of 10^{10} secondaries were calculated from this one impact alone [McEwen et al., 2005]. These researchers assert that secondary cratering dominates the sub-kilometer population over primaries resulting in erroneous dates using this technique. If SRC represent the youngest crater population on Mars, the ejecta retention rate is constant, and this crater population can be separated into primary versus secondary craters, a better understanding of the primary versus secondary production rate on Mars can be obtained. This in turn can add to the debate of using sub-kilometer diameter craters for absolute dating.

Small rayed craters are important because they are a record of the recent cratering rate in terms of size and frequency, provide information on the material properties of the subsurface, and represent a continuous record of active surface processes in the recent past. With this in mind, my dissertation seeks to answer the following questions regarding SRC ejecta retention:

- Where are ejecta retained across Mars?
- What geologic process(es) control ejecta retention?
- How are ejecta retained (i.e. morphology over time)?
- Does origin (i.e. primary versus secondary impacts) differentiate SRC?
- How long are ejecta retained?

This thesis is composed of four related chapters seeking to answer these questions:

1. *Enigmatic Linear Features in the Northern Hemisphere of Mars: Their Formation Process* – This initial chapter leads to an understanding of wind as a geologic process and the timescales that dust and dust-related features exist on Mars. I investigated the relationship of enigmatic linear features (ELFs) in the northern plains of Mars, while bearing a resemblance to thermal expansion cracks (i.e. ice-wedge polygons), they were genetically related to dust devils and their tracks. In terms of ejecta retention, directional analysis and experience in identifying wind-related features assisted in later classifying SRC and assessing ejecta blanket morphology.
2. *Geomorphic Analysis of Small Rayed Craters on Mars: Examining Primary versus Secondary Impacts* – The main goal of this chapter was to explore the ejecta planar morphology of known primary and secondary craters on Mars with the attempt to discern quantifiable differences between the two populations of SRC. Three area-to-perimeter ratios were calculated for the crater rim and ejecta planform as well as directional analysis of the ejecta blanket to trace secondaries back to their originating primaries. Interestingly, each metric provided some, though not complete, separation of SRC primaries from secondaries, unlike similar measurements from lunar craters. Uprange impact angle did point back to an originating primary for most cases and crater rim planforms were often orthogonal to impact azimuth, possibly indicating a very low angle impact. Current impacts were found to have significant numbers of breakup before

impacting; creating a strewn field that may share many characteristics with clustered secondaries once the ejecta is removed.

3. *Global Distribution of Small Rayed Craters on Mars: Sequences of Ejecta Retention* – Having gained an understanding of the differences (or lack thereof) between SRC primaries and secondaries, an exploration of the global SRC population was conducted. By examining thousands of randomly chosen MOCNA images, a population of 630 SRC was catalogued across three equatorial and two polar regions on Mars. This SRC distribution was statistically compared to various surface properties (such as albedo). I found that dust distribution and deposition plays a major role in ejecta retention. SRC morphology revealed ejecta retention sequences follow four stages of ejecta retention from the initial impact to eventual erasure from the surface. Using the unique diameter-distance (i.e. fragment size-velocity) property of secondary cratering spatial distributions, I extracted potential SRC primaries to compare to all SRC within 2000 km radial to the large primary Zunil that is predominately saturated with secondaries. The primary to secondary ratio was very high and consistent with a dominance of small craters with diameter, D , at $D < 125$ m.

4. *Small Rayed Crater Ejecta Retention Age Calculated from Current Cratering Production Rates on Mars* – Building on the work from the previous chapter, I estimated SRC ejecta retention ages for each of five regions across Mars. In

addition, I adjusted a current crater production function for atmospheric filtering to generate new Martian isochrons to estimate the ejecta retention age (E_{ret}) for regolith-based SRC. In comparison to Hartmann production function (HPF) isochrons, I found SRC retention to be over an order of magnitude younger at tens of ka for most sub-kilometer diameter craters. In general, SRC are found to be less than ~100 ka in age making them some of the most recent features on Mars and records of the recent climatic past.

It is the intention of this research to provide a suite of studies to qualitatively and quantitatively illustrate the importance of small rayed craters on Mars; both in terms of what they tell us now about active surface processes and what criteria allows us to differentiate between primary and secondary impacts.

REFERENCES

- Blewett D. T., B. R. Hawke, and P. G. Lucey (1993), Spectral and multispectral imaging studies of lunar mantled mare deposits, Proc. Lunar and Planet. Sci. Conf. XXIV, 133-134.
- Block K. M. and N. G. Barlow (2005), Secondary Cratering Rates on the Basaltic Plains of Mars and the Moon, Lunar Planet. Sci. [CDROM], XXXVI, Abstract 1816.
- Dickson, J. L. and J. W. Head (2009), The formation and evolution of youthful gullies on Mars: Gullies as the late-stage phase of Mars' most recent ice age, *Icarus*, 204, 1, 63-86, doi:10.1016/j.icarus.2009.06.018.
- French B. M. (1998), *Traces of Catastrophe: A handbook of shock-metamorphic effects in terrestrial meteorite impact structures*, Lunar and Planetary Institute, Houston, TX.
- Grier, J. A. and W. K. Hartmann (2000), Rayed craters as probes of the upper surface of Ma'adim Vallis and Elysium Planitia: Images from Mars Global Surveyor. Lunar Planet. Sci. XXXI. Abstract 1478.
- Hapke B., G. E. Jr. Danielson, K. Klaasen, and L. Wilson (1975), Photometric observations of Mercury from Mariner 10, *Journal of Geophysical Research*, 80, 17, 2431-2443.
- Hartmann, W. K. (1999), Martian cratering VI: Crater count isochrons and evidence for recent volcanism from Mars Global Surveyor, *Meteorit. Planet Sci.*, 34, 167-177.
- Hartmann, W. K., J. M. Anguita de la Casa, D. Berman, and E.V. Ryan (2001), Martian cratering. 7. The role of impact gardening, *Icarus*, 149, 37-53.
- Hartmann, W. K. (2005), Adventures (Arrrggghh!) in Crater Counting: Small Crater Controversies, Lunar Planet. Sci. [CDROM], XXXVI, Abstract 1427.

McEwen, A. S., B. S. Preblich, E. P. Turtle, N. A. Artemieva, M. P. Golombek, M. Hurst, R. L. Kirk, D. M. Burr and P. R. Christensen (2005), The rayed crater Zunil and interpretations of small impact craters on Mars, *Icarus*, 176, 351–381, DOI:10.1016/j.icarus.2005.02.009.

Melosh, H. J. (1989), *Impact Cratering: A Geologic Process*. Oxford University Press, New York, New York, USA.

Neukum, G., Jaumann R., H. Hoffmann, E. Hauber, J. W. Head, A. T. Basilevsky, B. A. Ivanov, S. C. Werner, S. van Gasselt, J. B. Murray, T. McCord & The HRSC Co-Investigator Team (2004), Recent and episodic volcanic and glacial activity on Mars revealed by the High Resolution Stereo Camera, *Nature*, 432, 23/30, 971-979.

Plescia, J. B. (2005), Small-Diameter Martian Craters: Applicability for Chronology – or not, *Lunar Planet. Sci. [CDROM]*, XXXVI, Abstract 2171.

Schenk, P.M., and McKinnon, W.B. (1985), Dark halo craters and the thickness of grooved terrain on Ganymede, in *Lunar and Planetary Science Conference 15th*, Houston, 1984, Proceedings, part 2: *Journal of Geophysical Research*, v. 90, p. C775–C783.

Tornabene, L. L., H. Y. McSween Jr., J. E. Moersch, J. L. Piatek, K. A. Milam and P. R. Christensen (2005), Recognition of rayed craters on Mars in THEMIS thermal infrared imagery: Implications for Martian Meteorite source regions, *Lunar Planet. Sci. [CDROM]*, XXXIV, Abstract 1700.

Wagner, J. K. (1991), *Impact Cratering*, In book: *Introduction to the Solar System*, Saunders College Publishing, Holt, Rinehart and Winston, Inc., Orlando, FL.

CHAPTER 1:

Enigmatic Linear Features in the Northern Hemisphere of Mars: Their Formation
Process¹

ABSTRACT

A variety of explanations have been proposed for intersecting networks of dark linear features on Mars. To better understand the origin and significance of these enigmatic linear features (ELFs), we have characterized ELFs located between 20°W and 80°W in the northern hemisphere of Mars. Our results show that while ELFs have several unusual characteristics, they are nevertheless dust devil tracks. Both features occur during equivalent Mars seasonal climatic conditions and trend in similar directions. While our data support the dust devil hypothesis, ELFs have atypical patterns that have implications for understanding the local and regional climate on Mars.

¹Published as Calef, F. J., III, and V. L. Sharpton (2005), Enigmatic linear features in the Northern Hemisphere of Mars: Their formation process, *Geophys. Res. Lett.*, 32, L24202, doi:10.1029/2005GL023868.

1.1 INTRODUCTION

The Martian climate is partially dictated by dust cycling on the planet [Christensen, 1988; Kahn et al., 1992]. It has long been recognized that atmospheric conditions on Mars are conducive to dust devil formation [Ryan, 1964] and that dust devils are a significant driver of the Martian dust cycle [Greeley and Iversen 1985]. Thomas and Gierasch [1985] and Metzger [1999] recognized that dust devil activity has the ability to uplift and transport hundreds of kilograms of dust per occurrence. Numerous curvilinear to linear features captured on Viking imagery were postulated to be ground tracks created by passing vortices that were either tornadoes or dust devils [Grant and Schultz, 1987]. Recently, the Mars Global Surveyor (MGS) Mars Orbiter Camera Narrow Angle camera (MOC-NA) [Malin and Edgett, 2001] has directly imaged the active creation of dark tracks by vortices with vertical and horizontal structure equivalent to terrestrial dust devils [Malin and Edgett, 2001]. Martian dust devils appear to vertically entrain a thin, optically bright dust layer revealing a darker substrate that becomes its track [Malin and Edgett, 2001].

Terrestrial dust devils have several distinct morphological traits. Field observations have recorded them exhibiting meandering horizontal motion and being steered by regional winds [Ives, 1947; Sinclair, 1966]. They are also transient and vary in width, height and intensity according to the boundary layer temperature regime [Carroll and Ryan, 1970]. Martian dust devil tracks follow this model (Figure 1.1A).

Several workers (Ormö et al. [2001] and Ormö and Komatsu [2002]) have noted networks of dark highly linear surface features that are unlike classic dust devil trails and have proposed a variety of mechanisms for their formation (e.g. Figure 1.1B). From visual Earth-analog comparisons, Komatsu et al. [2000] suggested a sub-glacial stream bed, ice scouring or plowmarks from icebergs as plausible explanations, especially the latter with ‘depressions’ linked to some features possibly indicating iceberg grounding in a shallow sea. Ormö et al. [2001] claimed that a fractured layer of ground ice could form these features based on their ability to cross surface topography without deviation or interruption and their high linearity. These workers noted that dust devils were a viable hypothesis for the ELF’s [Ormö et al., 2002], but offered no quantitative assessment to support this premise.

Our goal is to understand the formational mechanism of ELF’s and to develop their potential significance for understanding the atmospheric and geological activity on Mars. To accomplish this, we compare morphological statistics of ELF and dust devil tracks and quantified the possible relationship between these two features. We also catalog feature attributes such as the spatial range, morphology, and orientation.

1.2 STUDY AREA

Our study area encompassed the region between 20°W-80°W longitude and 0°-90°N latitude (partially shown in Figure 1.2). This area includes roughly equal areas across the crustal dichotomy, a geographic divide separating the southern uplands and northern lowlands on Mars, and the complete range of northern latitudes. Elevations

range from a maximum of ~8000m to a minimum of -5100m relative to Mars datum. The area contains several geologic provinces whose ages are predominately Amazonian to Hesperian [Scott and Tanaka, 1986]. One image near the Hellas Basin with indisputable dust devil tracks is selected as a 'type' image for our comparisons.

1.3 METHODOLOGY

We searched for ELF images in all MOC-NA images for the first Mars year (up to January 31st, 2005, mapping sub-phase M23) within the study area. Using the centroid of each candidate ELF image, underlying geologic units from the geologic map of Mars [Scott and Tanaka, 1986] were recorded, as well as the elevation from the Mars Orbiter Laser Altimeter (MOLA) 1/64° gridded dataset. Following ELF image identification, we selected a subset of ELF images for further analysis. For this subset, we recorded solar longitude (L_s), to deduce the Martian season, digitized center profiles for each ELF to compile length, width, density, and orientation statistics, and reviewed topographic profiles from original (non-gridded) MOLA point data to assess general slope and relief. One image with irrefutable dust devil tracks (Figure 1.1A) was analyzed with the same methodology for comparison.

Eleven images (ten MOC-NA ELF images and one image with unambiguous dust devil tracks) were selected for orientation analysis. Associated MOC-WA context images were reviewed for regional wind patterns denoted by aeolian features like wind streaks and crater 'tails'.

Each ELF or dust devil track was digitized along the middle of its width for its total length. Orientation was then calculated using start and end point coordinates for each ELF or dust devil track and values were assigned in degrees clock-wise from north. To circumvent the bias introduced by the large aspect ratio of MOC-NA images, we assessed ELF orientation from within circular subsections of images (Figure 1.3) using a semi-automated approach. Each subsection had a diameter slightly less than the image width, centered along the image centerline, beginning at the north end of the image. This was repeated until all features were selected by moving the center of the subsection one radius below the previous search area. All features crossing the subsections had their orientations compiled in 10° bins.

1.4 RESULTS

1.4.1 General Observations

After reviewing 2407 MOC-NA images we found 69 images containing ELFs (Figure 1.2). The L_S of these images ranged from 33° to 206° ; the majority captured during the Martian northern summer. ELFs were found in 48 images on Hesperian (~ 1.8 to 3.5 billion years ago) units in the Vastitas Borealis Formation (Table 1.1). Twenty-one of the images were in adjacent units primarily of Amazonian age (0 to ~ 1.8 billion years ago). ELF images cover a latitudinal band between 48° and 70°N and elevations at the image centroid ranged from -2570 m to -5165 m. The images reveal mostly young plains with very few, if any, craters larger than a few hundred meters. The majority of craters that do appear are either $>1\text{km}$ in diameter and have subdued or buried rims, or are

relatively pristine with diameters <500 meters and sharp rims. Surface morphology is predominately gentle undulating plains with low slopes and rare prominences. Near-surface ice-generated patterned ground ('basketball' texture of Head et al., 2003), common at this latitude, coincide with, but do not disrupt the ELF's.

Image M1003516 intersects a 22 km diameter Noachian (>3.5 billion years ago) [Scott and Tanaka, 1986] crater covering the southern half of the image and a smooth inter-crater plain in the northern half with abundant dust devil tracks (Figure 1.1A). The plain area is craterless and devoid of other prominences or depressions greater than ~10 meters in relief. Its L_S is 273° , which corresponds to the early Martian southern summer. The image center latitude is 58° south with an average elevation around 400m and is also covered with patterned ground. Tracks in the image tend to have three morphologies: highly sinuous and looping, sinuous (changing within 90° along its length), and nearly linear (staying within 30° along its length). The higher albedo tracks exhibit fewer convolutions along their length.

Image M0307347 shows ELF's constrained by a change in terrain (Figure 1.4). A crater rim and ejecta pedestal does not deflect the ELF orientation, yet they nearly disappear beyond this boundary. The pedestal is texturally smooth in comparison with the surrounding terrain and appears stratigraphically and topographically higher as determined by the shading at the base of the pedestal ejecta. This pedestal crater is part of a larger dissected layer occurring in other sections of the image with an underlying rougher plain covered with patterned ground. In this case, the smooth terrain preserves the ELF's, while they disappear when they cross onto the rough terrain.

Superposition relationships are unclear for ELF s or dust devil tracks; no one feature appears to obscure another that it crosses. No discernable albedo patterns were recorded among either feature type, although areas dense with ELF intersections do appear darker (Figure 1.1B).

1.4.2 Population Statistics

ELF and dust devil tracks range from 5m to >100m in width (Table 1.2). While most ELF s maintain their width along their length (within 5m to 15m), dust devil tracks vary by tens of meters along their length in M1003516. ELF lengths up to 10 km and ~4.5 km for dust devil tracks are recorded, though image dimensions limit the maximum values. Additionally, 65% of the dust devil tracks were wholly contained by M1003516 compared to only ~33% of ELF s in the subset images. Densities for ELF s range from 2 to 12.9 features/km², with an average of 5.8 features/km² compared to 29 features/km² for dust devil tracks in the northern half of M1003516.

L_S for the subset of 10 ELF images ranged from 91° to 203°, while six of them occurred between 160° and 170°, during the Martian northern summer (Table 1.2). The plot of L_S as a function of ELF density (Figure 1.5) reveals a rough Gaussian distribution, albeit with some discontinuity most likely reflecting the small dataset. In Figure 1.5, we also show how ELF densities compare with those of dust devils in Amazonis Planitia [Fisher et al., 2005] and dust devil tracks in the Hellas region [Balme et al., 2003]. All three show peak densities during the summer season for their respective hemispheres.

1.4.3 Orientation Analysis

Both ELF and dust devil tracks display pronounced trends in their orientations. Nine out of the ten images containing ELFs display a primary and secondary trend (Figure 1.6). We found the majority of 1800 ELFs were oriented between 40° and 145° , while ~ 800 dust devil tracks were aligned predominantly between 110° to 160° . Six out of the ten ELF primary trends fell within the predominant range of dust devil track orientations. A distinguishing feature about ELFs, however, is that the variance in the trend direction is lower (10° to 20°), compared to dust devil tracks (50°). Secondary trends in the ELF populations deviated from 30° to orthogonal from the primary trend with no obvious secondary trend in the dust devil track graph. Wind directions deduced from crater wind streaks and/or aeolian sculpted terrain in four MOC-WA context images showed an orientation centered around 111° [ESE]. This is consistent with the preferred orientation of ELFs within 6 out of the 10 images as well as with the dust devil tracks.

1.5 DISCUSSION

The visual difference between ELFs and dust devil tracks is striking with dust devil trails varying in width and orientation more randomly. However, our analysis shows a number of important similarities. Both features have similar widths and occur over a range of lengths, although ELFs are considerably longer on average than dust devil trails. Since two-thirds of ELFs in our study area extend beyond their image boundaries, it is likely that ELFs are predominantly longer on average. The rose diagrams indicate that the majority of ELF and dust devil tracks are not randomly oriented with most ELF trends in

the same quadrant as the dust devil tracks. Wind patterns derived from wind streak orientations in context images reinforced the connection between ELF's and aeolian activity. Given that ELF's and dust devil tracks are captured mostly in images recorded during the Martian summer, climatic conditions are comparable during the times that they appear. This also suggests that dust devil trails are highly ephemeral, with the majority lasting less than half a Martian year. Geographically, both features are also coincident in relative latitude and over smooth surface topography. Image M0307347 indicates that some terrains, perhaps dust covered or with fine texture, are more conducive than others to the formation or presentation of dust devil tracks.

Terrestrial dust devil tracks with similar morphologic characteristics to ELF's have been observed in Advanced Spaceborne Thermal Emission Spectrometer (ASTER) images in the Ténéré Desert, Niger [Rossi and Marinangeli, 2004]. These mostly linear tracks have average lengths of 3km (8.5 km maximum), widths in the tens of meters and densities up to four tracks per km² with a primary trend in a NW-SE direction. This is orthogonal to the regional wind direction determined from wind streaks by Rossi and Marinangeli [2004] who determined that these tracks lasted several weeks or months before being obliterated. Thus, these terrestrial tracks are less dense and slightly shorter, but are morphologically closer to ELF's than Martian dust devil tracks.

Atmospheric boundary layer conditions must be very specific to produce an ELF rather than a conventional dust devil track. Stability or uniformity of the wind field would be required to move ELF's in such homogeneity across a Martian plain. ELF's as dust devils suggest a transition of dust devil from a loopy sinuous stage to a more regimented

condition as wind speeds increase. Some validity can be lent to this idea by closely examining images like M1003516 (Figure 1.1A) that reveal similar groups of dust devil shapes, not all necessarily formed at the same time or under the same atmospheric constraints.

1.6 CONCLUSION

While visual comparison of classic dust devil tracks and ELF tracks lead to the assumption of a separate process for these two unique features, orientations and comparison with predominant wind direction indicates that ELFs are an aeolian feature. Besides lifting dust in the local vicinity, ELFs do not cause major disruptions of surface features as evident by the lack of disturbance of small-scale features like the 'basketball' terrain prevalent in many ELF images we studied. In addition, our study suggests that the dust devils that produce ELFs are driven by regional wind patterns, contrary to the assertions of Rossi and Marinangeli [2004]. Considering our current understanding of vortex movement on Mars, ELFs as dust devils with such consistently oriented tracks requires a stability of the wind field in the atmospheric boundary layer that is likely the result of a very particular combination of wind regime, temperature, and latitude for their formation. As ELFs appear to be seasonally transient, conditions must occur annually, possibly associated with seasonal regime changes. Such an atmospheric state would constrain dust lifting rates and/or inputs to climate models on the regional and global scale.

REFERENCES

Balme M. R., P. L. Whelley, and R. Greeley (2003), Mars: Dust devil track survey in Argyre Planitia and Hellas Basin, *J. Geophys. Res.*, 108, E8, 5086, doi:10.1029/2003JE002096, 2003.

Christensen, P.R., (1988), Global albedo variations on Mars: implications for active aeolian transport, deposition, and erosion, *J. Geophys. Res.*, 93, 7611-7624.

Carroll J. J. and J. A. Ryan (1970), Atmospheric Vorticity and dust devil rotation, *J. Geophys. Res.*, 75, 5179-5184.

Fisher J. A., M. I. Richardson, C. E. Newman, M. A. Szwast, C. Graf, S. Basu, S. P. Ewald, A. D. Toigo, R. J. Wilson (2005), A survey of Martian dust devil activity using Mars Global Surveyor Mars Orbiter Camera images, *J. Geophys. Res.*, 110, E03004, doi:10.1029/2003JE002165, 2005

Grant J. A. and P. H. Schultz (1987), Possible tornado-like tracks on Mars, *Science*, 237, 883-885.

Greeley R. and J. D. Iversen (1985), *Wind as a Geological Process on Earth, Mars, Venus, and Titan*. Cambridge Univ. Press, Cambridge.

Head J. W., J. F. Mustard, M. A. Kreslavsky, R. E. Milliken and D. R. Marchant (2003), Recent ice ages on Mars, *Nature*, 426, 797-802.

Ives R. L. (1947), Behavior of dust devils, *Bull. Amr. Meteorl. Soc.*, 18, 168-174.

Kahn R. A., T. Z. Martin and R. W. Zurek (1992), The Martian Dust Cycle, in *Mars*, edited by H. H. Kieffer et al., pp. 1017-1053, Univ. of Ariz. Press, Tuscon, AZ.

Komatsu G., A. P. Rossi, J. Ormo, and J. S. Kargel (2000), Glacier landforms in the northeastern Hellas basin, *Lunar Planet. Sci. [CDROM]*, XXXI, Abstract 1451.

Malin M. C. and K. S. Edgett (2001), Mars Global Surveyor Mars Orbiter Camera: Interplanetary cruise through primary mission, *J. Geophys. Res.*, 106, 23429-23570.

Metzger S. M. (1999), Feeding The Mars Dust Cycle; Surface Dust Storage And Dust Devil Entrainment, *Lunar Planet. Sci. [CDROM]*, XXX, Abstract 6196.

Ormö J., G. Komatsu, A. P. Rossi, and S. Di Simone (2001), Thin linear features on Mars visible in MOC images: the occurrences in the Hellas basin, *Lunar Planet. Sci. [CDROM]*, XXXII, Abstract 1517.

Ormö J. and G. Komatsu (2002), Mars Orbiter Camera observation of linear and curvilinear features in the Hellas basin: Indications for multiple processes of formation, *J. Geophys. Res.*, 108(E6), 5059, doi:10.1029/2002JE001980, 2003.

Ryan J. A. (1964), Notes on the Martian Yellow Clouds, *J. Geophys. Res.*, 69, 3759-3770.

Rossi A. P. and L. Marinangeli (2004), The first terrestrial analogue to Martian dust devil tracks found in Ténéré Desert, Niger, *Geophys. Res. Lett.*, 31, L06702, doi:10.1029/2004GL019428, 2004.

Scott D. H. and K. L. Tanaka (1986), Geologic map of the western equatorial region of Mars, Map I-1802-A, U. S. Geological Survey, Reston, Virginia.

Sinclair, P. C. (1966), A quantitative analysis of the dust devil, Ph.D. dissertation, University of Arizona, Tucson.

Thomas P. C. and P. J. Gierasch (1985), Dust devils on Mars, *Science*, 230, 175-177.

TABLES

Table 1.1: Geologic Units Underlying ELF Images

MOC-NA IMAGE	Elevation (km)	Geologic Unit	Unit Name	FORMATION
FHA01342	-3949	Hvk	Knobby member	VASTITAS BOREALIS
M0001120	-4163	Hvk	Knobby member	VASTITAS BOREALIS
M0001362	-5083	Hvr	Ridged member	VASTITAS BOREALIS
M0001378	-3314	AA1	Member 1, volcanic	N. PLAINS ASSEMB. ARCADIA
M0001522	-3899	Hchp	Older flood-plain material	CHANNEL-SYSTEM MATERIALS
M0001860	-5135	Hvm	Mottled member	VASTITAS BOREALIS
M0002151	-5045	Hvr	Ridged member	VASTITAS BOREALIS
M0200490	-4766	Hvm	Mottled member	VASTITAS BOREALIS
M0200516	-3672	AA1	Member 1, volcanic	N. PLAINS ASSEMB. ARCADIA
M0200518	-3860	Hvk	Knobby member	VASTITAS BOREALIS
M0201131	-3440	Hvk	Knobby member	VASTITAS BOREALIS
M0201135	-4040	Hvr	Ridged member	VASTITAS BOREALIS
M0201689	-4313	Hvm	Mottled member	VASTITAS BOREALIS
M0202734	-3617	cs	Superposed	IMPACT CRATER MATERIAL
M0202736	-3868	Hvk	Knobby member	VASTITAS BOREALIS
M0203112	-3832	Hvk	Knobby member	VASTITAS BOREALIS
M0203388	-4820	cs	Superposed	IMPACT CRATER MATERIAL
M0203957	-3380	AA1	Member 1, volcanic	N. PLAINS ASSEMB. ARCADIA
M0204255	-4902	Hvk	Knobby member	VASTITAS BOREALIS
M0204284	-3948	Hvk	Knobby member	VASTITAS BOREALIS
M0300621	-4350	Hvm	Mottled member	VASTITAS BOREALIS
M0301220	-4010	Hvk	Knobby member	VASTITAS BOREALIS
M0301677	-4537	Hvm	Mottled member	VASTITAS BOREALIS
M0301717	-3515	cs	Superposed	IMPACT CRATER MATERIAL
M0301719	-4162	Hvk	Knobby member	VASTITAS BOREALIS
M0301853	-4261	Hvm	Mottled member	VASTITAS BOREALIS
M0302298	-3950	Hchp	Older flood-plain material	CHANNEL-SYSTEM MATERIALS
M0302486	-4021	Hvk	Knobby member	VASTITAS BOREALIS
M0305910	-3619	AA1	Member 1, volcanic	N. PLAINS ASSEMB. ARCADIA
M0306887	-3483	AA1	Member 1, volcanic	N. PLAINS ASSEMB. ARCADIA
M0307028	-3955	Npl1	Cratered unit	PLATEAU SEQUENCE
M0307347	-3702	AA1	Member 1, volcanic	N. PLAINS ASSEMB. ARCADIA
M0400333	-3727	Npl1	Cratered unit	PLATEAU SEQUENCE
M0400619	-4305	Hvm	Mottled member	VASTITAS BOREALIS
M0401742	-4100	Hchp	Older flood-plain material	CHANNEL-SYSTEM MATERIALS
M0700767	-2963	Hal	Lower member	ALBA PATERA
M0701699	-3949	Npl1	Cratered unit	PLATEAU SEQUENCE
M0702630	-3939	Ach	Younger channel material	CHANNEL-SYSTEM MATERIALS
M1800467	-3355	AA1	Member 1, volcanic	N. PLAINS ASSEMB. ARCADIA
M1900630	-4336	Hvk	Knobby member	VASTITAS BOREALIS

Table 1.1 cont.: Geologic Units Underlying ELF Images

MOC-NA IMAGE	Elevation (km)	Geologic Unit	Unit Name	FORMATION
M2100609	-5094	Hvk	Knobby member	VASTITAS BOREALIS
M2101666	-4052	Hvk	Knobby member	VASTITAS BOREALIS
M2201022	-4176	Hvm	Mottled member	VASTITAS BOREALIS
M2201023	-4783	Hvr	Ridged member	VASTITAS BOREALIS
M2201024	-5165	Hvr	Ridged member	VASTITAS BOREALIS
M2201164	-5006	Hvr	Ridged member	VASTITAS BOREALIS
M2201214	-4028	Hvm	Mottled member	VASTITAS BOREALIS
M2201410	-4646	Hvm	Mottled member	VASTITAS BOREALIS
M2201423	-3436	Hvk	Knobby member	VASTITAS BOREALIS
M2300112	-2898	Hal	Lower member	ALBA PATERA
M2301705	-2570	AA1	Member 1, volcanic	N. PLAINS ASSEMB. ARCADIA

Table 1.2: ELF and Dust Devil Population Statistics for 10 Images^a

MOC-NA IMAGE	Pixel Size	Mars °Ls	Feature Type	Image Area	Feature/ km	Length			Width		
						(mean)	(min)	(max)	σ	(min)	(max)
M0002151	3.8	124	ELF	59.4	2.6	2.150	0.387	5.539	1.049	0.011	0.100
M0200490	9.1	151	ELF	29.7	19.6	1.205	0.018	6.758	1.052	0.018	0.122
M0204255	1.9	161	ELF	12.0	7.0	1.776	0.415	7.964	1.080	0.005	0.105
M0204284	4.5	161	ELF	14.4	4.2	2.927	0.709	5.729	1.083	0.005	0.120
M0300621	3.0	165	ELF	3.6	11.9	2.103	0.548	6.950	1.040	0.008	0.060
M0301220	6.0	166	ELF	24.8	4.6	3.476	0.803	7.642	1.014	0.014	0.085
M0301677	3.0	168	ELF	10.8	7.1	1.697	0.369	3.537	0.603	0.009	0.115
M0301853	4.5	168	ELF	124.8	2.2	2.865	0.060	7.977	1.368	0.013	0.170
M0701699	7.5	203	ELF	62.4	2.0	3.199	0.510	9.921	1.294	0.021	0.080
M2201423	5.1	91	ELF	28.8	3.2	2.290	0.237	3.796	1.098	0.014	0.045
AVERAGE					7.1	2.277	0.377	6.585	1.068	0.013	0.096
MINIMUM					2.0	1.205	0.018	3.537	0.603	0.005	0.045
MAXIMUM					19.6	3.476	0.803	9.921	1.368	0.021	0.170
M1003516	3.6	273	DUST DEVIL	28	29.4	0.628	0.041	4.314	0.567	0.010	0.100

^aAll values in kilometers unless otherwise noted.

FIGURES

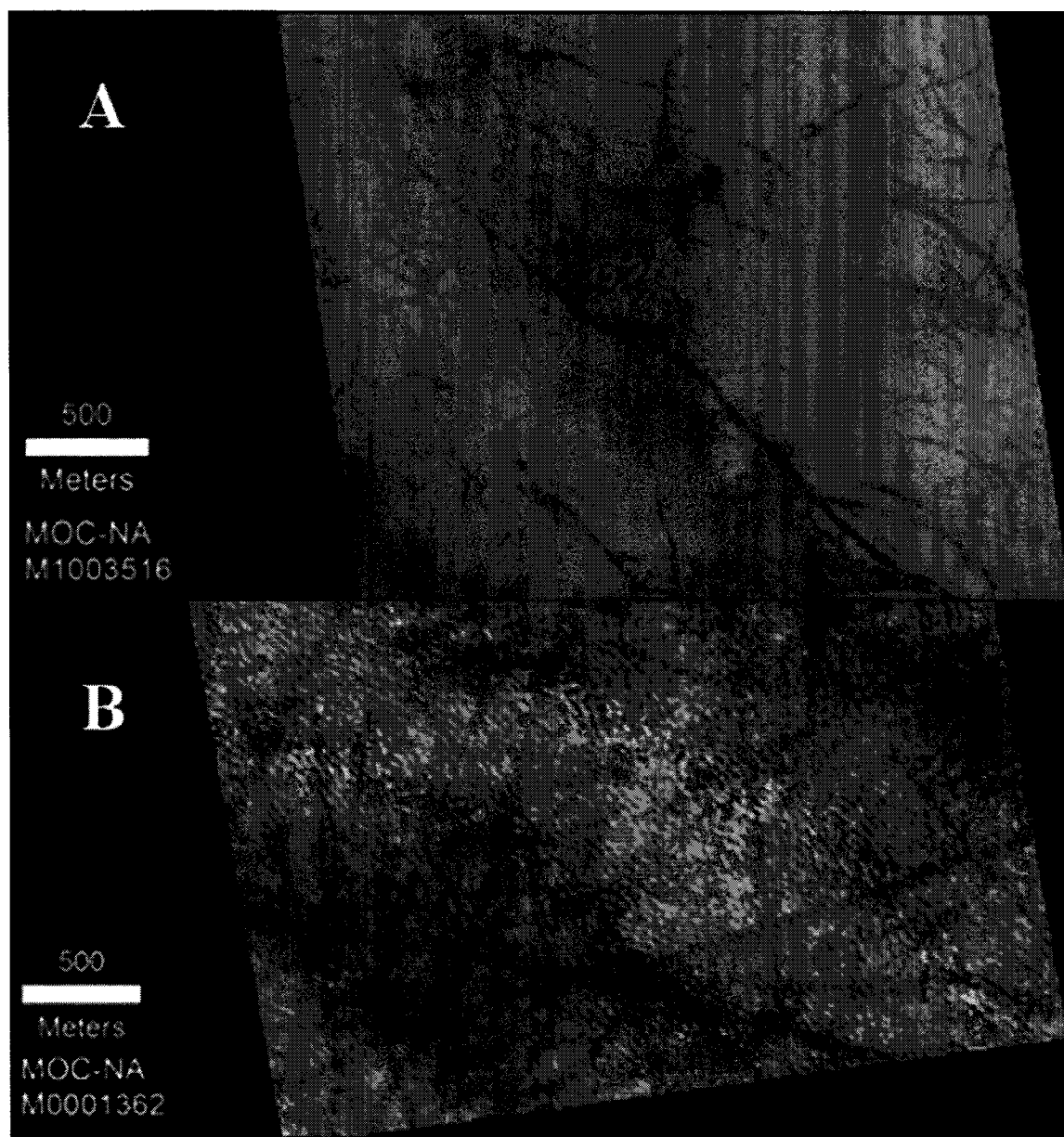


Figure 1.1: A section of MOC-NA images M1003516 containing dust devil tracks (A) and M0001362 containing ELFs (B).

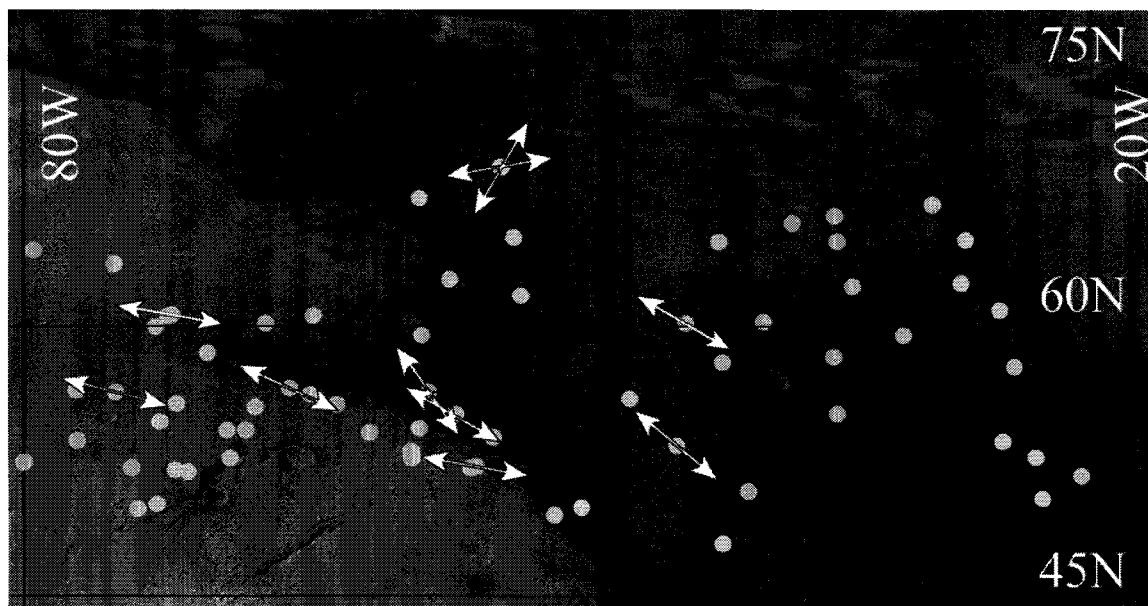


Figure 1.2: Subsection of study area in the northern hemisphere of Mars. Grey dots represent centroids for images containing ELFs. White arrows are predicted wind direction based on ELF primary trends (from Figure 6).



Figure 1.3: Example of the orientation analysis selection process. Here all ELFs (white lines) found in the bottom circle are selected (grey).

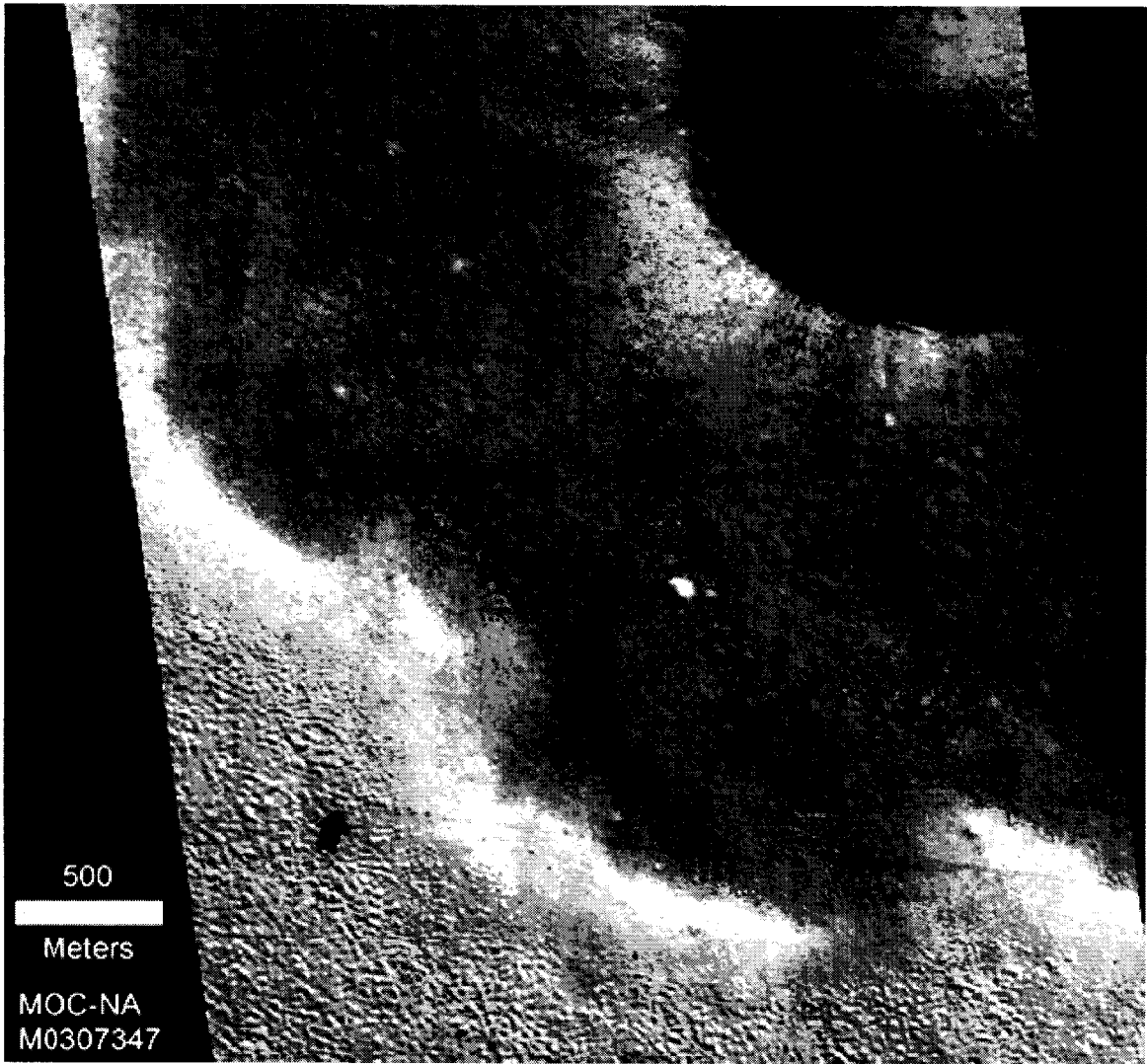


Figure 1.4: Section of MOC-NA image M0307347 with preferential placement of ELF's. Notice how ELF's disappear off the crater pedestal in the southwest corner of the image (at black arrow).

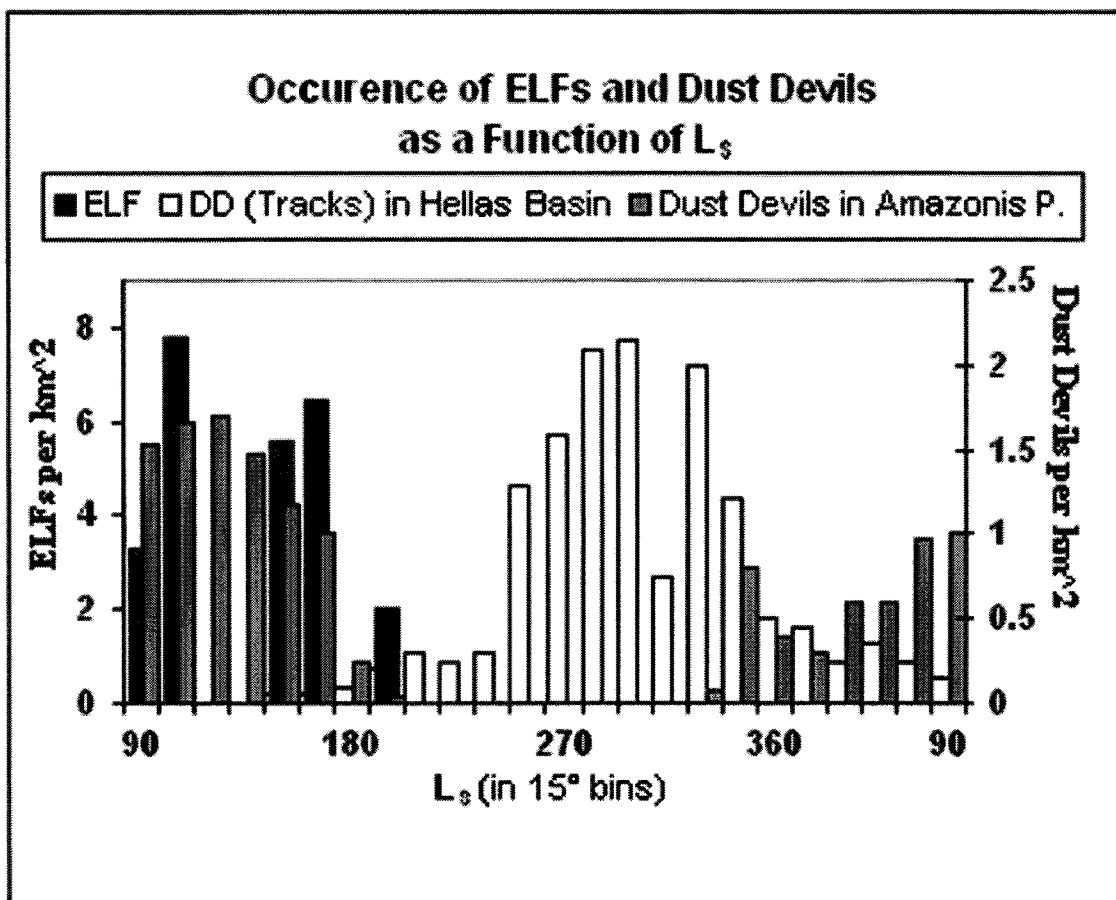


Figure 1.5: Occurrence of ELFs in the study area and dust devils in Amazonis Planitia and the Hellas Basin (southern hemisphere) as a function of L_s . Dust devil data from Fisher et al. 2005 (Amazonis Planitia) and Balme et al. 2003 (Hellas Basin).

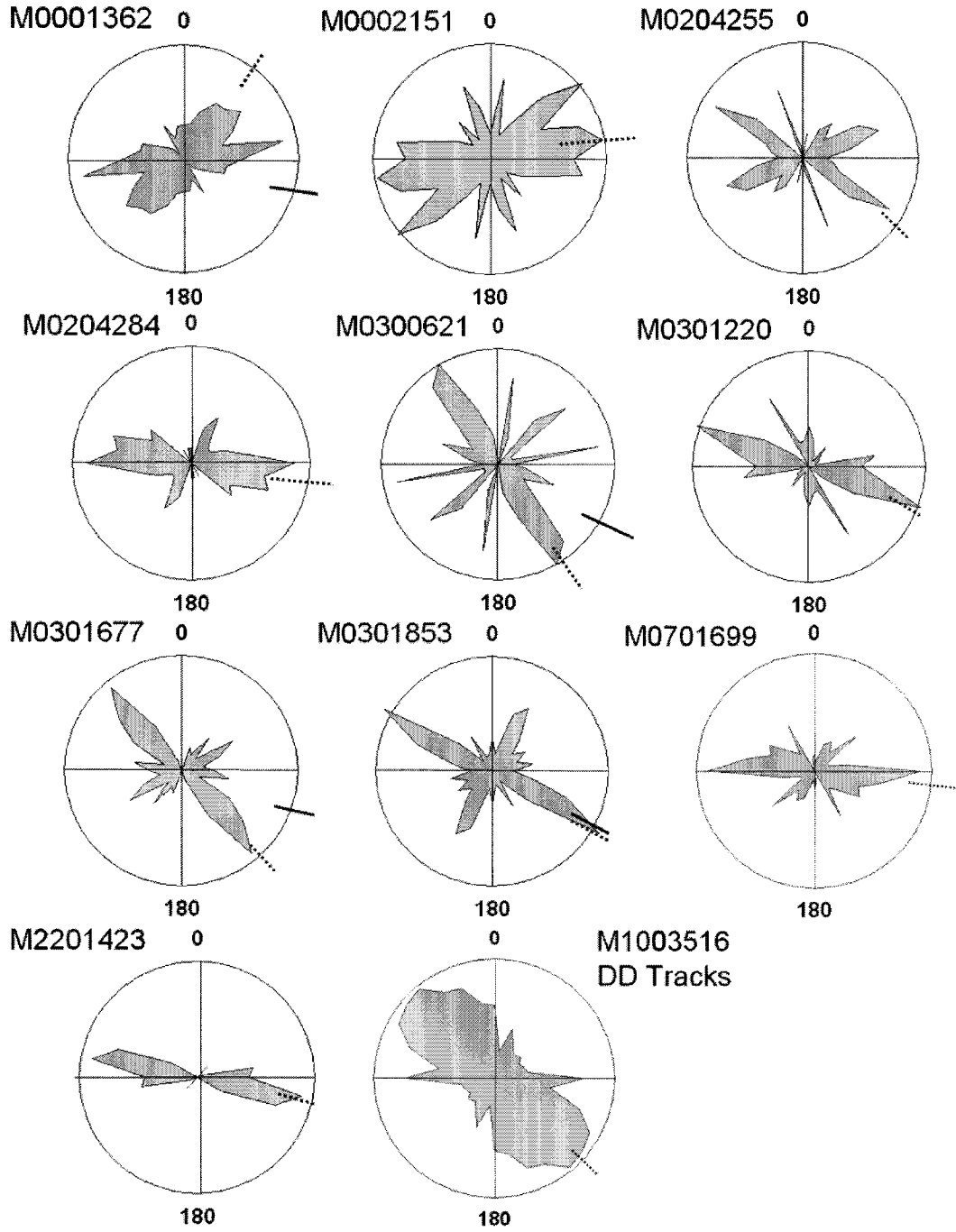


Figure 1.6: Orientation analysis of 10 ELF images and dust devil track image M1003516. Dotted line represents hypothesized primary wind direction. Dark line denotes actual wind direction.

CHAPTER 2:

Geomorphic Analysis of Small Rayed Craters on Mars: Examining Primary versus
Secondary Impacts¹

ABSTRACT

Twenty confirmed impacts over a 7-year time period on Mars were qualitatively and statistically compared to 287 secondary craters believed to originate from Zunil, an ~500 ka, 10-km diameter, primary crater. Our goal was to establish criteria to distinguish secondaries from primaries in the general crater population on the basis of their horizontal planforms. Recent primary impacts have extensive “air blast” zones, distal ray systems (>100 crater radii, R), and ephemeral ejecta. Recent primaries formed clusters of craters from atmospheric fragmentation of the meteoroid body. Secondary craters have ejecta blankets with shorter rays that are consistent with emplacement by low-impact velocities (near 1 km/s). The mean extent of the continuous ejecta blankets was less distal for secondaries ($5.38 \pm 1.57R$) versus primaries ($18.07 \pm 7.01R$), though primary ejecta were less fractal (Fractal Dimension Index (FDI) < 1.30) and more circular on average (Circularity Ratio (CR) = 0.55 ± 0.25 versus 0.27 ± 0.13 for secondaries). Crater rims were remarkably circular (primaries CR = 0.97 ± 0.02 , secondaries at 0.94 ± 0.05), though secondaries have the lowest values (CR < 0.9). Secondary crater rims were

¹Published as Calef, F. J., III, R. R. Herrick, and V. L. Sharpton (2009), Geomorphic analysis of small rayed craters on Mars: Examining primary versus secondary impacts, *J. Geophys. Res.*, 114, E10007, doi:10.1029/2008JE003283.

elongated toward or orthogonal to their primary of origin. Uprange source directions for most secondaries, determined by ejecta planform and crater rim ellipticity, point toward Zunil, although contamination from other primaries is considered in some areas. Ejecta blanket discrepancies between recent primaries and Zunil secondaries are attributable to differences in impact velocity and retention age. After removal of the ejecta blanket, crater rims are generally not diagnostic for determining crater origin. Fragmentation of primaries may play some role in steepening the size-frequency distribution of crater diameters (D) in the $5 \text{ m} < D < 30 \text{ m}$ range.

2.1 INTRODUCTION

Understanding the geologic evolution of individual terrestrial planets in our solar system is limited by the absence of absolute chronological ages from their surfaces. This is due to a lack of samples returned from them, with the exception of the Earth and a spatially limited collection from the Moon. One widely used dating methodology is the measurement of the size-frequency distribution of impact craters. A planetary surface age is derived by comparing the crater distribution to an extrapolation of the impactor flux over time for that planet [e.g. Hartmann, 1999]. Our solar system meteoroid flux has decreased in object size and frequency over geologic time [Hartmann and Neukum, 2001; Bottke et al., 2005], though a continuous bombardment streams onto planetary surfaces daily. Over time, this geologic process builds up a record of impact history that can be used to date geologic surfaces in the solar system [Shoemaker et al., 1963; McGill, 1977]. Crater-counting measurements have established a production function and time-dependant cratering rate [Hartmann, 2002] on the Moon that combined with the absolute chronology of impact events from lunar samples [e.g. Turner, 1970; Schaeffer et al., 1970] can extrapolate absolute dating to derive surface ages on other planets [Neukum et al., 2001; Ivanov, 2001], including Mars [Hartmann and Neukum, 2001]. However, utilizing this dating technique with $D < 1$ km craters has come under intense scrutiny on Mars [Bierhaus et al., 2005; McEwen et al., 2005], as well as Europa [Bierhaus et al., 2005; McEwen and Bierhaus, 2006]. The argument against using small ($D < 1$ km) craters for dating is that large ($D =$ several kilometers) primary impacts may produce $\sim 10^9$ distant small secondary craters of $D \geq 10$ m [McEwen et al., 2005] that, over time, can be

indistinguishable from primary impacts in the same size range, as was recognized during the first intensive studies of impacts on the Moon [Shoemaker, 1965]. Thus, the “steep branch” of the production function, where more craters are expected for smaller crater diameters [Hartmann, 2005], has been said to occur because of the numerous secondaries that increase the size-frequency distribution in this size range [McEwen et al., 2005; McEwen and Bierhaus, 2006]. The crossover diameter, when the number of primaries greater than diameter D exceeds the number of secondary craters, indicates most craters with $D \geq 12$ m should be primaries, yet observations near the $D = 10.1$ km Martian primary Zunil show most craters in this size range to be obvious secondaries [McEwen et al., 2005]. Direct measurements of the impactor flux for small craters on Mars have been measured [Malin et al., 2006] that are approximately in agreement with crater-dating isochrons. However, the amount of dating error introduced by secondary impacts on crater-based dating continues to be debated [Bierhaus et al., 2005; McEwen and Bierhaus, 2006; Quantin et al., 2007; Hartmann, 2007; Hartmann et al., 2008; Werner et al., 2009]. It is clear that being able to distinguish secondary craters from primary craters in the small crater record would be useful in either affirming or adjusting dating on many planetary bodies that have not had samples returned for absolute dating. Furthermore, a better understanding of the primary to secondary ratio in the $D < 1$ km population can yield better insight into the current small crater impactor flux, the crossover diameter for secondary cratering dominance in the geologic record, and the validity of crater chronologies calculated from subkilometer diameter craters.

The latest impacts are recognizable by their prominent rayed ejecta extending several crater radii beyond their continuous ejecta blankets (Figure 2.1). Malin et al. [2006] identified 20 rayed craters believed to be recent impacts, on the basis of their appearance after 1999 and before 2006 in the dusty regions of Amazonis, Tharsis and Arabia. These small rayed craters (SRC) exhibit sharp crater rims and bright-rayed or dark-rayed ejecta extending tens of crater radii distal to the impact site. Many have an “air blast” region, assumed to be the result of local dust removed by a pressure wave during impact [Malin et al., 2006]. Other SRC, initially identified by Grier and Hartmann [2000], show similar crater rim and ejecta morphology, except the rays tend to be shorter (Figure 2.2). These, frequently bright-rayed SRC have been identified as secondaries from a larger primary crater, Zunil [McEwen et al., 2005]. Many fall in clusters within its large ray system, as observed in the thermal infrared [McEwen et al., 2005; Preblich et al., 2007]. Because of the quantity and asymmetric spatial distribution of these secondary SRC, it has been proposed that most SRC, and most craters less than 200 m in diameter, are secondaries that may skew dating based on crater counts in this size range [Bierhaus et al., 2005; McEwen and Bierhaus, 2006]. This “pollution” of the primary impact record is reinforced by nine other large-diameter ($2 < D < 15$ km) rayed primaries on the Martian surface [Tornabene et al., 2006; Tornabene and McEwen, 2008; A. S. McEwen, *personal communication*, 2009] that each may have contributed upwards of 10^6 to 10^8 or greater secondaries to the background crater production rate. On Mars, the crossover diameter for SRC on young surfaces (<10 Ma) is ~ 60 m [McEwen et al., 2005].

This research attempts to separate primary from secondary impacts in the SRC population on Mars on the basis of qualitative and quantitative observations of crater rim and ejecta planform. This is accomplished by creating a database of known primary and secondary SRC populations, digitizing their crater rim and continuous ejecta perimeters, and applying morphometric formulas to ascertain any process differences in simple crater formation and morphology.

2.1.1 SRC Primary and Secondary Populations

Malin et al. [2006] discovered the first confirmed recent (≤ 6 Earth years) impacts onto Mars by comparing Mars Orbiter Camera (MOC) Wide-Angle (MOCWA) images at ~ 230 m/pixel from mission start (1999) to new MOCWA imagery in 2006. By looking exclusively in the dusty regions of Amazonis Planitia, Tharsis Montes, and Arabia Terra, a “difference map” was created to identify dark or bright spots indicative of new impacts. Subsequent Roll-Only Targeted Observation (ROTO) and compensated Pitch and Roll Targeted Observations (cPROTO) MOC Narrow-Angle (MOCNA) images with 0.5 m/pixel along-track and 1.5 m/pixel cross-track confirmed initial assessments of 20 new SRC with crater diameters from 2 m to 148 m (Figure 2.3). Except for one 148 m diameter crater, the largest crater diameter observed for each primary impact was between 10 to 37 m, averaging ~ 20 m. All new primary SRC, except one, exhibit extensive air blast regions surrounding their main crater (Figure 2.1). Several primaries also contain multiple craters in a clustered pattern indicating breakup during atmospheric entry before impact (Figure 2.4).

Ten known large ($2 \text{ km} < D < 10 \text{ km}$) primaries have been documented on Mars using night-time infrared imagery to reveal distinct rayed ejecta (Figure 2.5) [Tornabene et al., 2006; Tornabene and McEwen, 2008; A. S. McEwen, *personal communication*, 2009]. One large primary at $D = 10.1 \text{ km}$, Zunil [McEwen et al., 2005], produced thousands of secondaries that were first recognized by their bright-rayed ejecta [Grier and Hartmann, 2000], but not clearly identified [McEwen et al., 2005] or quantified [Preblich et al., 2007] until recently. These secondaries are readily distinguished by their clustering within or near Zunil rays, many with shallow floors and irregular rims (Figure 2.2). Zunil secondaries have been observed over 1600 km from their source, and some candidates may be 3000 km distant [Tornabene et al., 2006; Preblich et al., 2007]. At a distance of 1600 km, projectile velocity was in the range of 3 km s^{-1} [Preblich et al., 2007], though still below Mars' escape velocity of 5 km s^{-1} . As has been previously stated [Melosh, 1989; McEwen and Bierhaus, 2006], distant or far-field [after Werner et al., 2009] secondary impacts approaching at several km s^{-1} may share many or all the characteristics of a primary impact. Many more near-field secondaries [after Werner et al., 2009] occur several hundred kilometers from Zunil.

2.1.2 Geologic Setting

Zunil secondaries in the Elysium Planitia region occur over a circular area of approximately 1700 km in radius from Zunil [Preblich et al., 2007, Figure 10]. The most distant Zunil rays (and secondaries) lie west of Zunil due to its moderately shallow 30° - 60° ENE impact angle [McEwen et al., 2005]. Bedrock in this area is composed primarily

of two Amazonian aged formations; volcanic assemblages of the Elysium Formation composed of lava flows of varying superposition and ridged plain units [Tanaka et al., 2005] and bounded to the south by the Medusae Fossae Formation (MFF), considered a young highly erodible [Preblich et al., 2007] pyroclastic deposit [Tanaka et al., 2005]. Though evidence strongly supports a pyroclastic origin for the MFF, the exact formation mechanism is still debated [Watters et al., 2007]. SRC in this study are concentrated in the young Amazonian lava plains west and north of Zunil, centered on Cerberus Fossae and Athabasca Valles (Figure 2.6). Athabasca Valles contains streamlined features indicative of catastrophic aqueous flooding [Burr et al., 2002], subsequently overlain by recent volcanic flood lavas from Cerberus Fossae [Berman and Hartman, 2002; Jaeger et al., 2007] and other vents in the vicinity [Plescia, 1990], generating rootless volcanic cones indicative of lava and ground ice interaction [Mouginis-Mark, 1985; Lanagan et al., 2001; Fagents and Thordarsun, 2007; Jaeger et al., 2007].

The small primaries from Malin et al., [2006] fall into two geologic regions: Arabia Terra (AR), a highly cratered and dissected Noachian plain and Amazonis Planitia/Tharsis Montes (AT), dominated by the smooth plains of Amazonis that are composed of the MFF and the numerous lava flows and wrinkle ridges from the Tharsis volcanoes to the east (Figure 2.3). The AT region appears to be most similar in geologic terms and potentially in physical properties to the target material impacted by secondaries in Elysium Planitia. Together, the AT and Elysium regions form a “corridor” [Dohm et al., 2008] hypothesized to be an area of recent volcanic and hydrologic activity anywhere from <1 Ga [Plescia, 2003] to ~10 Ma (lava flows dated by Hartmann and Berman,

[2000] and Hartmann and Neukum, [2001] with fluvial episodes dated by Burr et al. [2002] and Berman and Hartmann [2002]).

2.2 METHODOLOGY

Databases were constructed from MOCNA ~6 m/pixel and Mars Reconnaissance Orbiter (MRO) High-Resolution Imaging Science Experiment (HiRISE) [McEwen et al., 2007] ~0.25 m/pixel images for examining the primary and secondary populations. SRC images were selected along an approximate downrange transect extending west and at several azimuths relative to Zunil to assess any change in crater morphology with increasing distance or orientation from the launch origin. For each SRC, the crater rim and ejecta blanket planform were manually vectorized into a geographic information system (GIS). For SRC in MOCNA images, the crater rim was digitized based on a hypothetical circular rim using the crater centroid and one point on the rim that defined an approximate average crater diameter. Using this two-point method is not expected to deviate significantly from a more accurate three-point method [Hopp, 1994]. In HiRISE images, the actual crater rim was digitized at a constant scale of 1:500. The perimeter around the primary ejecta blanket planform was also digitized at its distal extent, at a constant scale of 1:5000 for MOCNA and 1:2000 for HiRISE images.

All primary SRC identified in Malin et al. [2006] were examined as a “type” population for primary SRC on Mars. MOCNA ROTO images for each crater were radiometrically and geometrically processed in ISIS (version 3) to a Mercator projection with a latitude of origin equal to the image centroid latitude. Reference numbers, herein

assigned as identification numbers (ID) as designated by Malin et al. [2006] (e.g. “Impact Site 8”) in their supplementary catalogue is maintained for continuity. Primaries with multiple craters are labeled with the original ID number followed by a dashed reference number (e.g. 8-1, 8-2, etc.). HiRISE images were also examined for sixteen of the primaries. Calibrated and projected HiRISE images were downloaded directly from the HiRISE instrument website (<http://HiRISE.lpl.arizona.edu>).

Building on work from Preblich et al. [2007], 49 SRC were examined from MOCNA images identified as crossing Zunil rays, including 237 SRC from HiRISE images we identified as near or crossing the same ray system, giving a high probability that these SRC are indeed Zunil secondary cratering events. Since most MOCNA images have 2 to 5 times the pixel size of ROTO images, secondary craters with diameters larger by a factor of 2 to 3 (tens of meters) were chosen to best resolve interior and exterior crater features, while remaining well within an order of magnitude diameter size range (< 200 m) compared to the primary population. SRC identified in HiRISE images were resolution-limited only to craters of $D < \sim 2\text{-}5$ m, though a lower limit of $\sim D = 10$ m was used for delineating ejecta. Sufficient image resolution allowed discrimination of the primary ejecta blanket distal edge, as well as crater rim and floor morphology for the secondary population. A secondary SRC was only included in our study when the crater rim and ejecta planform were readily resolved; therefore, our counts do not represent the total number of secondaries per image. SRC were also excluded when crater rims or ejecta planform were modified by subsequent or simultaneous impacts, again lowering

the total number of SRC catalogued per image. Each secondary was assigned a unique number for its crater and corresponding ejecta, independent of the primary ID numbers.

Ejecta planforms were evaluated by measuring their radial extent relative to the crater center, planform morphology via three area-perimeter formulae, and downrange orientation (Figure 2.7). Minimum, maximum and mean ejecta ranges, normalized by individual average crater radii, were calculated from the digitized planform perimeter and crater rim centroid. Ejecta blanket symmetry for each of the impacts was evaluated with three equations:

$$C_R = 4\pi A/P^2 \quad (2.1)$$

$$F_R = 4A/\pi L^2 \quad (2.2)$$

$$FD_I = 2\ln(P)/\ln(A) \quad (2.3)$$

the Circularity Ratio (C_R) [Selkirk, 1982], Form Ratio (F_R) [Selkirk, 1982], and Fractal Dimension Index (FD_I) [McGarigal and Marks, 1994], respectively. In the formulas, A is the ejecta area (including the area inside the crater rim), P is the ejecta perimeter, and L is the maximum distance between any two points along the ejecta blanket perimeter. Both ratios attempt to measure “compactness”, an approximation of the efficiency of a feature’s areal distribution [Selkirk, 1982]. Long sinuous areas will have values closer to 0 while more circular “compact” features will approach 1. C_R is also reciprocal to ejecta lobateness, Γ :

$$\Gamma = (1/CR)^{1/2} \quad (2.4)$$

used to measure the sinuosity of single, double and multiple lobe Martian rampart ejecta deposits [Kargel, 1986; Barlow, 1994]. FD_I measures the spatial complexity of a natural planar object [McGarigal and Marks, 1994] and will also be used as a proxy for asymmetries in the ejecta blanket; a symmetric ejecta blanket will have $FD_I = \sim 1$ (e.g. circular), while more chaotic, fractal ejecta would have $FD_I > 1$. Since oblique impacts generate more ejecta downrange from the impact azimuth and uprange “forbidden zones” [Gault and Wedekind, 1978], and secondaries from Zunil were theoretically impacting at oblique angles based on experimental data [Cintala et al., 1999; Anderson et al., 2003], one would expect secondaries to have similar ejecta planforms to other oblique impacts. We estimated the SRC uprange azimuth in degrees clockwise from north on the basis of the criteria of downrange ejecta and uprange “forbidden zones” to create rose diagrams that in theory point toward the primary crater that the secondaries originated from. Effects of planetary rotation (i.e. Coriolis force) were ignored since modeling has shown that only ejecta with launch velocities of 3-5 km/s, at high latitude, and ballistic distances beyond a quarter hemisphere were greatly affected [Dobrovolskis, 1981; Wrobel and Schultz, 2004]; none of these criteria are met by this secondary population (to be discussed in section 2.5.1). Initial launch velocities calculated via distances from Zunil would represent overestimates due to the counterclockwise (relative to the north pole) rotation of Mars. Atmospheric effects were also disregarded as minor or beyond the scope of this study. We estimate that the uprange azimuth is accurate to within $\pm 15^\circ$.

Crater rims were also investigated for circularity (similar to measurements of lunar crater rims by Murray and Guest [1970]) using the same formulae as for the ejecta planform. Long-axis crater orientation (i.e. crater rim ellipticity) was estimated by calculating the standard deviation ellipse (SDE) from the rim planform. A standard deviation ellipse calculates the standard deviation of the x-y coordinates from the mean center of a set of points to define the two major axes of an ellipse oriented along a spatial trend [Environmental Systems Research Institute, 2006]. The vertices of the digitized crater rim were used as a point set to calculate the SDE to 1 standard deviation (covering ~68% of the points), hence the long-axis orientation of the crater (Figure 2.8). We estimate that the orientation derived from this method is good to within $\pm 10^\circ$ of the true crater long-axis azimuth. Similar to the ejecta, we plotted the long-axis orientation, from $0^\circ \leq \theta \leq 180^\circ$, in a rose diagram to evaluate secondary crater ellipticity in relation to the suspected source primary. Two MOCNA images, E1101849 and M401791, were visually estimated for secondary crater long-axis orientation to compare with the SDE results. To remove any directional bias, crater long-axis values were divide by 2 and placed in opposing bins (i.e. if three craters fell into the East ($90^\circ \pm 22.5^\circ$) bin, the data were split evenly into both the due East and West ($270^\circ \pm 22.5^\circ$) bins). Erring on the conservative side, each ejecta or rim azimuth was plotted into 45° bins to eliminate systematic error or bias in either the SDE or uprange/downrange estimate. Azimuths to six large primaries from Tornabene et al., [2006] and Tornabene and McEwen [2008] (Corinto, Dilly, Naryn, Tomini, Thila, and Zunil) were estimated from polar map projections centered on each

individual crater and placed on the rose diagrams for evaluation of the likely primary of origin.

The geologic target is a significant factor during the excavation stage [Wünneman et al., 2006; Collins and Wünneman, 2007] and its role is examined against the above measurements to make comparisons between the primary and secondary impacts. Several primary SRC were removed from our analysis because of ephemeral ejecta blankets that did not allow delineation from the larger air blast region. Some subjectivity is introduced by manual ejecta blanket digitization, so any results should be considered first order measurements, especially in regard to the highly diffuse primary crater ejecta. The secondary SRC, with their sharp contrast between bright ejecta and darker background, allow more concise and reliable measurements.

2.3 OBSERVATIONS

2.3.1 Primary SRC

The most distinguishing features of the primary SRC population are the air blast region, long distal rays and evidence of impactor fragmentation. Each primary, except for primary 17 display the results of a suspected downward/lateral atmospheric pressure shockwave, i.e. air blast [Malin et al., 2006], that disturbed dust-sized surface particles beyond the continuous ejecta blanket at distances >100 crater radii (e.g. Figure 2.9). The affected region ranges from somewhat circular about the main crater, as in Figure 2.9, to a distal buffered area around the continuous ejecta, as in Figure 2.1. In most cases, the boundary between air blast and ejecta is diffuse and not readily separated. Half of the

primaries have continuous and discontinuous rays extending tens to >100 crater radii past the continuous ejecta blanket (Figure 2.10). These rayed primaries appear to have downrange ejecta and uprange forbidden zones, even in the air blast planform (e.g. Figure 2.10B), indicating non-vertical impact angles. Given that half of incoming meteoroids enter the atmosphere at less than 45° from horizontal [Shoemaker, 1962], this is expected. Based on MOCNA ROTO imagery, resultant craters average $D = \sim 28$ m or even lower to ~ 17 m if we exclude primary 17 at $D = 148$ m, the only $D > 30$ m crater in this population. In HiRISE images, eight primaries (40% of this population) show evidence of fragmentation with multiple sharp-rimmed, though not rocky, craters in the central area of continuous ejecta (Figure 2.11). Primaries 3, 7, 8, 13, 15 and 19, all located in Arabia Terra, have little to no discernable ejecta or rays (except 13) at the image scale (Figure 2.12). A boulder-strewn crater rim is visible only in primary 17, the largest among them (Figure 2.13). This nested crater has perhaps 10^4 2-5 m boulders within 3 to 4 crater radii. Given that these primaries excavated only a few meters below the surface, this depth may be insufficient to reach bedrock in many areas on Mars. However, at least ten of the primaries have bright ejecta over the darker “blast” scoured surface indicating interception of a brighter subsurface layer (e.g. Figure 2.10B). Six primaries (3, 6, 7, 8, 13, and 19) appear to be almost vertical impacts based on their circular air blast regions, though many of these have little to no ejecta to confirm this (Figure 2.11). All “no ejecta” primaries cluster in the upper member of the Arcadia Formation, a relatively young Amazonian deposit interpreted as pyroclastic and flow material from the Tharsis region [Tanaka et al., 2005] with most craters well below 50

km in diameter based on gridded measurements from Mars Orbiter Laser Altimeter (MOLA) elevation data [Smith et al., 1999]. Primary 13 could also be considered part of this “no-ejecta” group, but a faint ejecta layer is discernable (Figure 2.12). Primaries 1, 6 and 9 (e.g. Figure 2.9) do have ejecta in the same Arcadia formation, but at a lower elevation to the north (see Figure 2.3), categorized as a volcanic unit [Tanaka et al., 2005]. Hypothetically, this unit may be an older emplaced lava flow that is more indurated than the upper units or perhaps the regolith is thinner here causing more spall from a “hard” target [Head et al., 2002].

Of particular note is the “crater field” created by primary 20 (Figure 2.4 and Figure 2.14). The two largest craters in the field are $D = 16$ m and $D = 13$ m (2.14A). If we look closely at the crater floor of the $D = 13$ m crater, rather than the larger crater because of insufficient lighting, the floor appears somewhat flat and irregular with several blocks or slumps of material, though less than five or so $D < 1$ m blocks reside within 1 crater radii outside the rim (Figure 2.14B). Given that this is a flat-floored crater, we use a simple equation to calculate the crater depth, d :

$$d = L/\tan\theta \quad (2.5)$$

where L equals the horizontal shadow length and θ equals the solar incidence angle for the image [Chappelow and Sharpton, 2002]. With $L = \sim 3.75$ m and $\theta = 58$, the depth (d) is ~ 2.3 m with a depth/diameter (d/D) ratio equal to ~ 0.18 , slightly lower than the expected value of ~ 0.20 for small primaries on Mars [Pike, 1980; Pike and Davis, 1984].

Tens of craters in the $D = 5\text{-}10$ m range and perhaps hundreds more with $D < 5$ m can also be seen within the continuous ejecta blanket (Figure 2.14A). Within 200 m of the main ejecta body are tens of $1\text{ m} < D < 5$ m dark-rayed craters. Dark rays from these meter-sized craters form a 'V' in their planform, assumed to point uprange towards their entry azimuth (Figure 2.14B and 2.14C). The V-shaped ejecta all point approximately north, regardless of whether they are north or south of the main crater field. This indicates to us that these are not secondaries, but actually primaries from the same body, albeit more dispersed. Based on this observation, the original impactor appears to have fragmented and/or dispersed over a minimum of 1 km crossrange and 1.3 km downrange. One cluster of three dark V-shaped rayed craters with $1\text{ m} < D < 3$ m occurs ~ 1.7 km north and ~ 1.1 km west of the main crater field (Figure 2.14D) indicating that the crater field may extend over 1.5 km crossrange and 2.5 km downrange.

2.3.2 Secondary SRC

Secondaries in this population appear nearly uniform in their planform morphology. The predominate type consists of an optically bright, continuous primary ejecta blanket with several rays of varying length and width (Figure 2.15A). A dark annulus of ejecta is frequently found within one crater radii (Figure 2.15B), suggesting excavation of a two-layer target. Crater rims range from irregular (western crater, Figure 2.7) to nearly circular (eastern crater, Figure 2.7). Meter-sized boulders are visible near the rim, as might be expected for a secondary cratering event [Bart & Melosh, 2007], but their frequency varies from crater to crater (e.g., Figure 2.8). Crater floors are typically

dark, though bright fill in the form of aeolian emplaced dunes is not unusual, often superimposed above the dark floor material that appears to represent the in situ regolith at depth (Figure 2.15C). Aeolian reworking of bright or dark crater floor material is universal. The continuous ejecta blanket is composed of several lobes or rays that in many cases appear to point downrange with an uprange forbidden zone in relation to their impact azimuth (e.g. Figure 2.7 and Figure 2.15D). However, the ejecta do not appear as axial symmetric downrange and often displays a chaotic border, “ramparting” as evident from cast shadows, and a sharp ejecta perimeter (e.g. Figure 2.15A and 2.15D). Signs of filamentary ray or ejecta structure beyond the primary ejecta blanket are nonexistent, though some discontinuous ejecta members do occur (white arrow, Figure 2.15D), but at a limited extent (one or two crater radii) past the continuous ejecta. Unlike the primaries, no atmospheric air blast region can be discerned down to the submeter level. Underlying topographic structures are still visible beneath the ejecta, signifying a thin ejecta layer, at least to the edge of submeter image resolution (Figure 2.15E). At meter scale, many secondaries look pristine, though submeter pixel sizes reveal wind scalloping and faceting of thicker ejecta material (Figure 2.15D, inset). This ventifact-like erosion gives the impression that the ejecta are indurated (e.g. Figure 2.15A and 2.15D). Further wind modification can be seen in some cases, but appears to be more depositional versus erosional (Figure 2.16).

Another secondary type consists of a nearly “sans-ejecta” crater rim with only a hint of the past excavated material (usually the dark annulus), but sharing crater rim and floor morphology (Figure 2.15E). Since these two types are almost always mutually

exclusive within one image, it would suggest differences in target material at the separate impact sites. Using the same methodology as in section 2.3.1, we measured the depth/diameter ratio of one secondary crater (ID 279) having a $D = 106$ m, $L = \sim 41.5$ m and $\theta = 57^\circ$, yielding a depth (d) of ~ 27 m with a d/D ratio equal to ~ 0.25 , well above the values for secondaries obtained by McEwen et al. [2005]. We are fairly certain these SRC are secondaries as they fall along a linear trend pointing back towards Zunil in image PSP_002806_1870_RED.

2.4 RESULTS

We measured crater rims produced by 16 primary and 286 secondary impacts (Figure 2.17). To reiterate, these counts do not represent every secondary (or number of craters per primary) in every image, but a select population that allowed crater rim and ejecta planform to be measured; so no size/frequency distribution is implied. Actual secondary densities for some MOCNA images used in this study can be found in Preblich et al., [2007]. From these populations, 16 primary and 197 secondary continuous ejecta blankets were delineated for analysis. Some secondary craters had diffuse or little ejecta; thus the total number of secondary craters does not match the count of ejecta blankets. In cases where primaries have multiple impacts, the ejecta planform data was not used in comparison with the secondaries to normalize the data to one crater per ejecta planform. Measurements were rounded to whole meters to be conservative in our results; therefore all numbers in the tables are ± 1 m. Crater diameter, calculated as twice the mean rim radius, may appear 1 m larger or smaller than expected because of the measurement

rounding. Primary craters with overlapping or shared rims (e.g., ID 7; Figure 2.12B) were excluded from analysis.

2.4.1 Crater Measurements

The Circularity and Form Ratios calculated for crater rims were plotted versus crater diameter for the primary and secondary populations (Figure 2.18). Primary and secondary crater rims averaged $C_R = 0.97 \pm 0.02$ (one standard deviation) and 0.94 ± 0.05 , respectively. From these values alone, one could only say that a crater rim with a $C_R \leq \sim 0.90$, hence more elliptical, is a candidate secondary, though 87% of secondary crater rims fell above this value. The Form Ratio yielded even less differentiation among the crater rims with primaries averaging $F_R = 0.83 \pm 0.10$ and secondaries 0.84 ± 0.07 . No obvious trend was noted in either ratio. The Fractal Dimension Index measured a distinct exponential trend from the primary to secondary population. While the FDI for primary rims was 1.70 ± 0.24 and 1.38 ± 0.06 for secondaries, an FDI versus crater diameter plot showed evidence of a power law relationship (Figure 2.19A). If the data are plotted in log-log space (Figure 2.19B), a trend line interpolated from the data gives us three relationships:

$$FD_I = 2.4936D^{-0.1826}, R^2 = 0.83 \quad \text{for primaries (2.6)}$$

$$FD_I = 1.8420D^{-0.0801}, R^2 = 0.94 \quad \text{for secondaries (2.7)}$$

$$FD_I = 2.1726D^{-0.1247}, R^2 = 0.88 \quad \text{for all SRC (2.8)}$$

where D equals crater diameter in meters and r^2 is the correlation coefficient. The strong correlation of the index from small to large craters is somewhat verified by the one $D = 160$ m crater (ID 17) that has a diameter larger than any secondary measured in our study (Figure 2.19). It is possible that the FD_I values are only showing a scale effect with less “detail” of rim features being captured for smaller craters, yet in the $10 \text{ m} < D < 25 \text{ m}$ range there is strong agreement where the two populations overlap. Since these craters are well within the strength regime for Martian craters, it is reasonable that smaller diameter craters (i.e., less energy at impact) are more irregular (i.e., “fractal”) than larger diameter craters that required more energy to form and thus able to overcome the inherent strength of the target. Target type did not appear to significantly affect the data trend as the primaries occurred over a heterogeneous range of possible targets compared to the more homogenous Elysium Planitia region of the secondaries. The seeming uniformity of target strength may indicate that all of these craters are regolith-based and never penetrated deep enough to reach the basement rock in these areas. The one exception may be the largest primary (ID 17) with its nested depression in the crater floor (Figure 2.13) though it too plotted on the secondary FD_I trend.

2.4.2 Ejecta Measurements

The Circularity and Form Ratios calculated for ejecta planforms were plotted versus crater diameter for the primary and secondary populations (Figure 2.20). Primary

and secondary ejecta averaged $C_R = 0.55 \pm 0.25$ (1 standard deviation) and 0.27 ± 0.13 , respectively. The considerable range for the primary ejecta C_R values reflects the difficulty in separating the continuous ejecta versus air blast areas. If one counted the air blast region as part of the ejecta, the primaries would potentially have higher C_R values, though even the air blast can be chaotic (e.g., Figure 2.1). One might conclude that SRC with $C_R > \sim 0.60$ were candidate primaries; however, there is too much variation in this data set to draw any firm conclusions. The Form Ratio was even more muddled with primaries averaging $F_R = 0.51 \pm 0.14$ and secondaries 0.39 ± 0.11 . Again, qualifying the ejecta planform has reduced the usefulness of this statistic with the primary population. A clearer differentiation can again be found with the FD_I (Figure 2.21). The FD_I for primary ejecta was 1.29 ± 0.05 and 1.40 ± 0.06 for secondaries. Each population clusters above and below the 1.30 line for most size ranges. Secondary ejecta appear to have a weakly correlated negative sloping trend with no $D < \sim 40$ m craters below 1.30, while primary ejecta clusters below this point for most of the craters. Ignoring scaling effects and some arbitrariness to selecting ejecta boundaries, $FD_I < \sim 1.30$ may represent candidate primaries to the first order (Figure 2.22). Even accounting for different geologic terrains, the six Amazonis/Tharsis (AT) primaries with mean $FD_I = 1.29 \pm 0.04$ were nearly identical to the four in Arabia Planitia (AR) with a mean $FD_I = 1.29 \pm 0.06$. From these results, one may deduce that the secondary population has more “fractal”, irregular ejecta planforms than primaries in the same size range. In the case of a low angle ($< 15^\circ$) primary impact, ejecta asymmetries may be indistinguishable when compared to

secondaries, as appears to be the case for some primaries in this study (e.g., primary ID 20 in Figure 2.22).

A significant difference was found between minimum, mean, and maximum continuous ejecta planform range from the crater center (Figure 2.22). Normalized by crater radius (R), secondary SRC were a factor of three to four times lower in ejecta range. Secondary ejecta were nearly uniform in its distribution from crater to crater with a mean value of $5.4 \pm 1.6R$ (1 standard deviation). The primary ejecta distributed more broadly with a mean value of $18.0 \pm 7.0R$. The greater variance among the primary ejecta range data can be partially explained by the ambiguous continuous ejecta perimeter; however, the continuous ejecta range for the primaries was several factors more distal than the extent of any secondary (Figure 2.10) suggesting the average values are not off by a large factor. Impact theory does not offer a reasonable explanation for this disparity unless the target properties (e.g., granite versus pumice targets in the work of Gault and Wedekind [1978]) or impact velocities [Hartmann, 1985] are dissimilar.

2.4.3 Directional Analysis

We plotted both crater rim long-axis orientation and ejecta uprange azimuth to determine whether secondary crater or ejecta planform could be used as a proxy to “find” the primary they originated from and hence identify them as secondaries (Figure 2.23A and 2.23B). Our results indicate that the majority of ejecta blankets that we measured do point back towards Zunil, regardless of the distance or azimuth from this primary. We did have one image, HiRISE PSP_002820_1860_RED, where all secondary ejecta pointed

uprange towards the primary Corinto (Figure 2.23A). Other images (e.g. 6801_1935 or 6788_1955 in Figure 2.23B) also appear to have non-Zunil secondaries “buried” in their secondary populations. Preblich et al. [2007] noted that contamination of the Zunil secondary field with non-Zunil secondaries was possible; our research confirms this assertion.

Crater long-axis data generally orient both toward (e.g., HiRISE PSP_006801_1935_RED) and orthogonal (e.g., secondaries in HiRISE PSP_006788_1935_RED) to Zunil (Figure 2.23B). In two images with “no ejecta” craters, PSP_002806_1870_RED and PSP_003874_1815_RED, the directional analysis was either ambiguous (3874_1815) or contradictory when originating primaries occur parallel to the crater long-axis at opposite azimuths (2806_1870) (Figure 2.23A). On the basis of the north-south linear emplacement of all secondaries in image 3874_1815, it still remains unclear whether they originate from Zunil (29° clockwise from north) or Dilly (-23° clockwise), unlike other SRC that fall along a line directly to Zunil (Figure 2.24). In the absence of ejecta, the uprange azimuth based on crater planform alone may not be sufficient to determine origin.

2.5 DISCUSSION

2.5.1 Differences between Primary and Secondary Ejecta Retention

Ejecta preservation can be described in terms of formation, the unique properties of the target that form the ejecta, and retention, the depositional and erosive environment; the resulting preservation being a combination of both factors. Similar to the concept of

optical maturity used on lunar crater rays [Lucey et al., 2000], some ejecta maintain a visible bright or dark tone because it has a different tone than the surface they overlay and retain their visible properties over time despite erosional processes (i.e., formation). Other ejecta are truly “young” because they have been recently emplaced and not weathered to the background tone (i.e., retention) [Hawke et al., 2004]. Unlike comminution and agglutinate formation from impact gardening on the lunar surface [Heiken et al., 1991], the current foremost mechanism of erosion on Mars is aeolian [Greeley et al., 2004], perhaps followed by periglacial activity (i.e., patterned ground, thermokarst, etc.) operating at latitudes poleward of $\pm 50^\circ$ [Mangold et al., 2004], where abundant stable water ice exists near the surface in diffusive equilibrium with water vapor in the atmosphere [Mellon et al., 2004]. Given that the primaries in this study are equatorward of $\pm 30^\circ$ latitude and the secondaries fall between 5°N and 15°N , the dominant retention process should be wind-related. However, during times of high obliquity, modeling has shown that ground ice would be stable near the equator [Mellon and Jakosky, 1995]. Evidence of polygonal ground [Page, 2007] and sorted stone circles [Balme et al., 2009] in the Elysium Planitia region offers the possibility that some additional erosion is derived from freeze-thaw action during the aforementioned periods. In regards to formation, the primaries impacted into a dusty desiccated regolith with nine impacts in the Amazonis Planitia region dominated by volcanic features; an area geologically similar and near Elysium Planitia where the secondaries impacted. One would expect, given the low latitude and shallow depth of excavation for both primaries and secondaries, the formation properties should be roughly equivalent. This should leave

only retention properties (i.e., erosion/deposition rates) to explain any differences in ejecta planform between the two populations. Experimental results have shown that a mere 1.5×10^{-4} g/cm² deposition of ≤ 5 μ m diameter dust is sufficient to reduce some visible wavelength reflectance by 70% [Wells et al., 1984]. Martian dust deposition, based on dust streak formation rates, has been estimated at $\sim 4 \times 10^{-5}$ g/cm²/a [Aharonson et al., 2003], though this may be a maximum as the streaks fall in predominately low thermal inertia/high dust index areas. A dust layer 3 μ m to 10 μ m thick on both Mars Exploration Rovers (MER) caused a 37% to 42% reduction in reflectance on their dark solar panels over a mere 150 Mars sols [Kinch et al., 2007]. In contrast, aeolian erosion has been estimated as low as ~ 0.03 nm/a on the Gusev plains (the closest site to the secondaries) to a high of 10 nm/a at Meridiani [Golombek et al., 2006]. Annual deflation rates (dust lifted by wind) are low in Elysium Planitia [Haberle et al., 2003], though dust deposition is also currently low [Ruff and Christensen, 2002] and perhaps stable for long time spans [Haberle et al., 2003]. Using the high end of the MER landing sites dust deposition and bedrock erosion estimates, a rough linear extrapolation equates to ~ 10 m/Ma dust deposition to 0.01 m/Ma erosion. Given the temporal difference between the primaries and secondaries, one would expect dust deposition to exceed erosion in modifying ejecta on timescales < 1 Ga. While we do not see visible evidence of meter-scale dust deposition, there are no signs that the ratio of deposition to erosion is < 1 , meaning net deposition in this section of Elysium dominates, even if only slightly.

Our systematic and statistical examination has revealed several unique attributes that differentiate the ejecta planform of primary and secondary populations in our study.

The majority of primaries observed have air blast regions surrounding their continuous ejecta blanket (Figure 2.9), are somewhat more circular (Figure 2.20A), with regular/less “fractal” ejecta planforms (Figure 2.21), have substantially longer ray systems (Figure 2.10) and more distal continuous ejecta relative to crater diameter (Figure 2.22). Primary continuous ejecta appears thin and in some cases ephemeral (Figure 2.12). To the contrary, secondary ejecta planforms have significantly shorter ray lengths (e.g., Figure 2.7 and Figure 2.22) and more irregular/“fractal” planforms (Figure 2.21). Many secondary continuous ejecta appear to have thicker bright ejecta with ramparts at a sharp distal boundary (e.g., Figure 2.15A) and some display discontinuous ejecta “islands” (Figure 2.15). A subset of secondaries have little to no ejecta with only a 1-2 crater radii annulus of dark, perhaps blockier, ejecta, but thinner or nonexistent bright ejecta. The pitted and sometimes ventifact-like surface of some secondary ejecta retains the evidence of wind erosion (Figure 2.15D, inset), though it also appears indurated and able to resist current aeolian activity to some degree (Figure 2.16). While these qualitative and quantitative differences are potentially revealing as to the origin for these two populations, the time variable between the primaries and secondaries is significant. We know the primaries are currently < 10 years old [Malin et al., 2006] and the Zunil secondaries are $\sim 5 \times 10^5$ years on the basis of age estimates of Zunil [Kreslavsky, 2008]. The primaries also occur in regions of high dust cover [see Ruff and Christensen, 2002, Figure 14], indicating that the more ephemeral ejecta features are probably unique to impacts in dust-prone areas; further supported by ~ 50 new impacts identified in similar dust-laden regions [Daubar and McEwen, 2009]. The original reflectance of ephemeral

features such as the air blast and distal rays could be completely obscured by dust perhaps within a few centuries or readily in a few millennia, when they exist. Regardless, the presence of an air blast and/or distal rays (tens of crater radii) for craters with diameter $5 \text{ m} < D < 200 \text{ m}$ is evidence of an $\sim 10^2$ year old primary, since there are no known secondaries in this diameter range produced within the last few centuries on Mars. Differences in the distal extent of continuous ejecta are diagnostic between the two populations; whether this is solely attributable to their age differences remains to be determined. The other indisputable difference is the notable thickness of some secondary ejecta that should, all things being equal except time, be thinner (i.e., more eroded) than ejecta from a primary of similar size. Hartmann [1985] experimentally investigated the effects of impact velocity on several factors including ejecta extent and thickness. His results indicate that at impact velocities below 1100 m/s, less than $\sim 1\%$ of impact energy goes into excavating ejecta material [Hartmann, 1985]. This has the concomitant result of reducing ejecta range (i.e., lower ejection velocities), thereby increasing ejecta thickness toward the crater rim. As impact velocities increase past 1100 m/s, energy input into excavation increases with more ejecta being launched distally (i.e., at higher velocities) resulting in a thinner, dispersed ejecta blanket overall. The majority of secondaries we measured landed between 300 km to 600 km away from Zunil, which can be achieved with an initial launch velocity of between $\sim 1050 \text{ m/s}$ to $\sim 1450 \text{ m/s}$ respectively, as calculated from a planetary ballistic range formula from Melosh [1989] and ignoring atmospheric drag. Secondary crater range, and thus the launch velocity, toward the west of Zunil (where the majority of secondaries exist) are overestimated because of planetary

rotation and perhaps impact-generated winds which would increase these values. Therefore, impact velocities are lower in the Athabasca Valles/Cerberus Fossae region than our estimates. Examining the radial distance of the continuous ejecta blanket, we find primaries with thin distal ejecta and secondaries with thick ejecta proximal to the crater rim (Figure 2.22) that appears to reflect the factor of ~ 10 difference in impact velocities.

Three images illustrate the effects of formation versus retention with SRC. The first shows a number of bright-rayed secondaries with one SRC with darker toned ejecta. We can quickly rule out formation as a factor, because the bright SRC are in close proximity around the darker SRC, they have roughly similar crater diameters, and all overlay the same terrain; a homogenous volcanic lava flow (Figure 2.25A). Since the target is horizontally uniform (and for all intents and purposes, vertically uniform as well) as far as can be observed, the difference in tonal quality of the ejecta must be due to retention. Looking more closely at one of the lava flow layers, we can see bright material deposited by erosion (mass wasting?) at their distal edge (Figure 2.25B). The deposits have a visually identical tone to the bright SRC, though would be younger if their deposition is ongoing. Upon closer examination, the dark SRC appears to be a thinner and less bright (though not truly “dark”) example of the bright secondaries with similar ejecta planform (though subdued) and irregular crater rim whose rim appears to be structurally controlled by the linearity of adjacent target features (Figure 2.25C). The crater interior contains several wind-derived ripples of somewhat darker toned material than the background deposits interstitial to the knobby background (Figure 2.25C), while

the bright secondary crater interiors hold bright material in equal tone to the ejecta. At the very least, we can conclude that the one “dark” SRC is either older or younger, but not contemporaneous, with the bright secondaries; otherwise we would expect a similar level of ejecta retention shared by the bright secondaries proximal to it. Given that the lava cliff face appears to yield bright material and the “dark” SRC has thinner ejecta as well as dark material within its crater rim, we posit this SRC must be older and likely a secondary based on its morphological similarity to the other secondaries.

A second image, M0200581, gives a clear case of formation overriding retention properties. In this image (Figure 2.26), a lava front divides the image with older terrain (more craters) in the north half of the image and younger terrain (the lava flow with less craters) to the south. The terrain north of the young lava flow has several “no-ejecta” secondary craters with only a brief dark annulus (Figure 2.26A). At the transition from the older basement to the younger embaying lava flow, one “no-ejecta” crater can be seen on the stratigraphically lower unit (Figure 2.26B). However, secondaries on the young flow all have bright ejecta typical of many Zunil secondaries (Figure 2.26C). No observable bright secondaries appear in the northern half of this image. This leads us to conclude that the young lava flow unit is responsible for the bright ejecta, hence a product of formation. This leads us to consider that all SRC in this image are contemporaneous and likely a secondary cluster, though we cannot definitively rule out that the SRC in Figure 2.26A are from a different event.

The final image, PSP_002661_1895_RED, displays several bright-rayed and dark-rayed craters (Figure 2.27). The dark SRC have a diffuse “star”-shaped ejecta

planform with dark crater floors, while the bright-rayed craters have the “typical” sharp boundaries of Zunil secondaries with bright crater floors. Relative ray lengths for the bright and dark SRC are well within the maximums found for the secondary population (Figure 2.22). Another difference between them is the crater sizes; the dark SRC diameters range from $\sim 38 \text{ m} < D < \sim 60 \text{ m}$, while the bright SRC have $D < \sim 23 \text{ m}$. One exception occurs with SRC F that has a dark floor, but predominately bright continuous ejecta with $D = \sim 34 \text{ m}$. The disparity of ejecta brightness with crater diameter indicates a target with two distinct stratigraphic units. Since SRC F has bright ejecta, but a dark floor indicating it penetrated a lower dark layer yet it did not contribute the majority of the continuous ejecta, it must be near the boundary for the two units. Based on the standard depth-to-diameter (d/D) ratio of 0.2 for parabolic simple craters [Pike, 1980], the bright unit must transition between $\sim 4.6 \text{ m}$ to $\sim 6.8 \text{ m}$ below the surface to the dark unit. The bright ejecta from SRC E and F have a clear uprange forbidden zone while all the dark SRC ejecta have no such impact direction indicators; one would expect them to share a similar ejecta pattern if they represented a simultaneous impacting event. Some $< 10 \text{ m}$ diameter bright SRC are coincident with some of the dark ejecta and it appears that dark blocks override some of the bright ejecta (especially just north of SRC C). However, the image resolution does not entirely reveal if the blocks sit on top of the bright ejecta or are simply too big to be buried by it. In either case, the dark and bright SRC appear to be from separate events given their dissimilar ejecta planforms. We cannot determine whether the dark SRC are primaries or secondaries based on their planforms alone.

2.5.2 Similarity of Primary and Secondary Crater Rims

Our results show that, in terms of the crater rim, secondaries are remarkably similar in planform to primaries within 1 standard deviation (Figure 2.18 and 2.19). The majority of the secondary population displayed remarkably circular and “orderly” rims, making most of them indistinguishable from the primary population in this regard. This is in contrast to similar work done on the Moon where secondaries were significantly less circular (circularity = 0.54 versus 0.82 for primaries, [Pike and Wilhelms, 1978]). There is a definitive break at $C_R = 0.9$; only secondaries had crater rims lower than this value. However, many secondary crater rims have similar long-axis orientations either parallel or orthogonal to the uprange azimuth of possible originating primaries (Figure 2.23A and 2.23B). In experimental data using single projectiles, crater rim circularity only becomes more elliptical downrange when the impact angle is $\leq 30^\circ$ for “hard” targets and $\leq 10^\circ$ in non-cohesive sandy targets [Gault and Wedekind, 1978]. For cohesive “dusty” targets, experiments with single projectiles at impact angles between 10° - 35° are elliptical in the cross-track dimension, oblique to the impact azimuth [Gault and Wedekind, 1978]. However, Schultz and Gault [1985], using clustered projectiles, experimentally produced downrange elongated craters at angles as high as 60° . Experiments by Anderson et al., [2003], showed a 30° angled primary impact produced secondary “blocks” ejected at (and assumed to land at) angles $\leq 40^\circ$ during the first moments of high-velocity crater excavation flow. It remains unclear whether any inference to impact angles can be deduced from these crater planforms as we cannot ascertain whether each secondary crater formed from one impacting projectile or a dispersed cluster.

2.5.3 Identification of New Primary Cratering Events

Based on our results, we have identified two rayed craters we believe were primary cratering events. The first is a dark-rayed crater in image MOCNA R0600296, located at approximately 150°E, 8.27°N (Figure 2.28A). It has a diameter $D < \sim 40$ m, a dark ejecta signature close to the crater rim and several long, ephemeral dark rays with one extending ~ 2.9 km or ~ 72.5 crater radii, which fits well with our ejecta observations (Figure 2.10) and measurements (Figure 2.22) for primaries. There may be a faint air blast signature with a slight brighter intensity behind the rays and a darker signature just around the western edge of the feature that gives the appearance of a forbidden zone south/southwest of the crater, though it appears mostly faded at this time. Two bright-rayed secondaries may be overlain by rays ~ 400 m and ~ 620 m to the north/northwest of this crater, but the resolution of this image limits verification. This dark candidate primary has also been imaged in Thermal Emission Imaging System (THEMIS) visible (VIS) image V14186017 and V1603005, though no earlier image records this area other than this MOCNA image in 2003.

A second candidate primary comes from image PSP_006801_1935 that has all of the diagnostic characteristics typical for definitive primaries in our study (Figure 2.28B). Four craters make up this cluster; the main crater at $D = \sim 6$ m and three “child” craters at $D = \sim 3$ m, making this the smallest primary yet reported for Mars. Since the meteoroid that formed these craters did fragment, it was likely a stony meteorite though the small crater diameters could also suggest an iron [Popova et al., 2003; Chappelow and

Sharpton, 2005]. The cluster spreads over ~280 m west-east and 120 m north-south. Bright air blast regions surround each crater with a darker inner annulus of assumed ejecta material. Discernable ejecta appears ephemeral, unable to bury meter-sized to submeter-sized blocks, and looks well formed. The crater rim looks almost hexagonal with a possible floor modification (nested crater?) (Figure 2.29B, inset). Image resolution limits further quantification (e.g., measuring the FD_I of the ejecta), despite the 0.25 m pixel size. No discernable forbidden zone is noted, indicating a probable impact angle $\geq 60^\circ$. The most distal ray from the $D = \sim 6$ m crater is ~ 150 m or 25 crater radii which puts it on the low end for a primary, but the high end for secondaries (Figure 2.22), although a nearby secondary (ID 164) has a maximum ray length < 7 crater radii. Compared to nearby secondaries, it is clear that this cluster is morphologically unique.

2.5.4 Crossover between Primary and Secondary Cratering Events

The problems inherent with using $D < 1$ km craters for crater dating can be either ignored because both primaries and distant, non-clustered secondaries are counted together for generating isochron-based dates [Hartmann, 2007; Hartman et al., 2008; Werner et al., 2009] or these problems must be identified because secondaries dominate the crater counts in some regions causing orders of magnitude error in surface age estimates [McEwen et al., 2005; Bierhaus et al., 2005]. When rayed ejecta are still retained around a crater, we have qualitatively and quantitatively shown that recent primaries have unique attributes that distinguish them from older secondaries. Over time (10^7 to 10^9 years), classification to an individual crater as a secondary or primary using

only the crater rim and floor, as are the majority of cases on Mars once ejecta has been eroded or buried, becomes increasingly difficult. Except for some outliers, secondary crater rims are as round as primaries. Even some craters that fell in obvious linear trends were not readily associated with their primary (Figure 2.24), although modeling efforts of Popova et al. [2003] show that only secondaries would fall in this manner, while primaries cluster within a few hundred meters of each other because of low lateral velocities during breakup. We did not examine depth/diameter (d/D) akin to Pike and Wilhelms [1978] as our goal was to evaluate the horizontal planform, and most areas lack stereo coverage with sufficient image resolution (<1 m/pixel) to resolve 2 m or 3 m vertical relief. However, for illustrative purposes, we did measure the d/D of one “flat-floored” primary (Figure 2.14B) and one secondary (Figure 2.15F) whose shadow extended to the approximate center of the crater floor. Simple shadow measurements showed the primary with $d/D = \sim 0.18$ and the secondary at $d/D = \sim 0.25$; both values near the expected martian d/D for primaries at ~ 0.20 [McEwen et al., 2005]. While a statistic of one is not definitive, and we agree that many secondaries we examined were qualitatively “flat-floored”, it does show that “bowl-shaped” craters are not strictly primary forms. It is also unclear what role aeolian deposition/erosion or crater relaxation from thermokarst processes (at higher latitudes) have on SRC d/D considering they excavate predominately in the upper few meters of the surface where such activity dominates. Since the primary population we examined appeared to excavate only into regolith (except the floor of the one $D > 100$ m crater), over time their crater floors may

also become shallow, though some argue that d/D is not affected by infilling in craters of this size range [McEwen et al., 2005].

Not only can secondaries “masquerade” as primaries, but the reverse can also be true. As is the case for primary ID 20 (Figure 2.14), this one primary produced hundreds of craters $D < 10$ m, indicative of breakup of a weak stony meteorite according to Popova et al. [2003], as are likely the other fragmented primaries we have measured [Hartmann, 2007]. Unique to this primary field are the hundred of “microprimaries” ($1 \text{ m} < D < 5 \text{ m}$, perhaps even more $D < 1 \text{ m}$) that extend crossrange ~ 1.5 km by 2.5 km downrange. Popova et. al., [2003, 2007] predicted crater clustering to remain within a few hundred meters, yet here the ranges are an order of magnitude farther. To reiterate, what happens once the ejecta disappears? If this primary field is buried and exhumed, could you tell that these craters were all primaries? In the target surface are numerous craters in the same diameter range ($D < 10$ m) that, on the basis of the overlying dust layer, existed before the impact. Could you distinguish the new primary population from this one impact event versus the background craters after a few millennia? We would argue that even in the case of primaries, the total number of craters (without ejecta) with diameter $D < \sim 200$ m on a surface is skewed positive because to breakup. During high obliquity cycles, which occur every $\sim 10^6$ years on Mars starting at 3×10^6 years or earlier [Bills, 1990; Mellon and Jakosky, 1995], atmospheric temperature would increase [Bills, 1990; Mellon and Jakosky, 1995; Laskar et al., 2004] and pressure ranges anywhere from 30 mb [James et al., 1992] to approaching 80 mb or more at $>30^\circ$ obliquity in “thick” atmospheric models [Manning et al., 2006]. Fragmentation would increase with such

atmospheric pressures causing even larger meteorites to fragment yielding larger crater diameters [Popova et al., 2003; Chappelow and Sharpton, 2005]. Thus, secondaries, as well as primaries, may “inflate” crater counts over a diameter range. This result complicates estimating the crossover diameter as both secondaries and primaries produce crater fields that are currently indistinguishable in many characteristics compared to a background population, especially once ejecta has been removed. As a thought experiment, let us consider the total number of confirmed primary craters produced during the past ~10 years (an underestimate if more impacts occurred during the past 3 years) when nineteen primaries impacted ~15% of the surface area of Mars (excluding the anomalous $D > 100$ m primary). These nineteen primaries produced 81 craters $5 \text{ m} < D < 30 \text{ m}$ over that time period. Multiplying these values by 6.9 to estimate the global cratering rate, yields ~127 primaries and ~543 craters/10 years within the aforementioned diameter range and timespan. During the period it would take to produce a Zunil (~500 ka) [Kreslavsky, 2008] with $\sim 10^8$ secondaries $D \geq 10 \text{ m}$, $\sim 6.36 \times 10^6$ primaries could impact creating 2.72×10^7 craters $D < 30 \text{ m}$. This ignores two possible “peaks” in the atmospheric pressure over the past 0.5 Ma [James et al., 1992; Manning et al., 2006] that should cause more fragmentation of larger meteorite bodies [Chappelow and Sharpton, 2005] increasing the primary count. Admittedly, there are also “troughs” where the atmosphere “collapses” into CO_2 ice caps at both poles [Kreslavsky and Head, 2005], decreasing the fragmentation rate, while also reducing the current atmospheric filtering of smaller meteorites. It remains unclear whether the fragmentation-to-filtering ratio

increases or decreases the net count of primaries permitted to the Martian surface during changes in Mars' atmospheric pressure.

With these albeit simplistic calculations, if the number of primary craters produced was constant over 2 Ma, and no other >1 km diameter primaries occurred, the primary-to-secondary ratio of craters in the $5 \text{ m} < D < 30 \text{ m}$ diameter range across Mars could be closer to parity. This would make sense as the secondary cratering size-frequency fits a Weibull distribution [Werner et al., 2009], resulting in a flattening of counts in this diameter range. Malin et al. [2006] found the primaries to fall within an order of magnitude of their correct age on Hartmann [2005] isochrons extrapolated to single digit years. Hartmann [2007] also finds only an order of magnitude difference in isochron age when theoretical counts of primaries and secondaries over 10 and 100 million years ago are added together. While it does appear that the “steep branch” of the isochron graphs may well result from secondary contamination of crater counts, they do not appear to “crossover” beyond a small factor of the primary production rate [Hartmann et al., 2008; Werner et al., 2009], perhaps also because of primary fragmentation, even in the current thin (~ 6 mb) Martian atmosphere. Not only are small secondaries “statistically clustered” in time [McEwen et al., 2005; Bierhaus et al., 2005; Hartmann, 2006], to some degree so are primaries. From these results, we estimate the primary to secondary ratio could approach parity (i.e., 1:1) for craters $5 \text{ m} < D < 30 \text{ m}$.

2.6 Conclusions

Understanding the ratio of primary-to-secondary crater formation on Mars, and all planetary bodies, is deemed critical for dating geologic surfaces and events, as well as defining the current primary crater production rate. Secondaries share many morphologic features with primary impacts, though some differences in the ejecta blanket planform and crater rim shape are quantifiable. We offer a matrix for resolving the similarities and differences between the primaries and secondaries in this study (Table 2.1). While these criteria are not absolute and better for a population-based estimate, they do provide some quantitative measure to evaluate SRC as to their origin; planetary or cosmic. Some caution must be taken as it is clear that target material and ejecta retention rates do play a factor in these results. It is also apparent that primary production rates based on crater counts alone are multifaceted not only by far-field secondaries [after Werner et al., 2009], but also by meteorite fragmentation.

REFERENCES

Aharonson, O., N. Schorghofer and M. F. Gerstell (2003), Slope streak formation and dust deposition rates on Mars, *J. Geophys. Res.*, 108, E12, 5138, doi:10.1029/2003JE002123.

Anderson, J. L. B., P. H. Schultz, and J. T. Heineck (2003), Asymmetry of ejecta flow during oblique impacts using three dimensional particle image velocimetry, *J. Geophys. Res.*, 108, E8, 5094, doi:10.1029/2003JE002075.

Balme, M. R., C. J. Gallagher, D. P. Page, J. B. Murray and J. P. Muller (2009), Sorted stone circles in Elysium Planitia, Mars: Implications for recent martian climate, *Icarus*, 200, 30-38, doi:10.1016/j.icarus.2008.11.010.

Barlow, N. G. (1994), Sinuosity of Martian rampart ejecta deposits, *J. Geophys. Res.*, 99, E5, 10927-10935.

Bart, G. D., and H. J. Melosh (2007), Using lunar boulders to distinguish primary from distant secondary impact craters, *Geophys. Res. Lett.*, 34, L07203, doi:10.1029/2007GL029306.

Berman, D. C., and W. K. Hartmann (2002), Recent fluvial, volcanic, and tectonic activity on the Cerberus plains of Mars, *Icarus*, 159, 1-17.

Bierhaus, E. B., C. R. Chapman, and W. J. Merline (2005), Secondary craters on Europa and implications for cratered surfaces, *Nature*, 437, 1125-1127, doi:10.1038/nature04069.

Bills, B. G. (1990), The rigid body obliquity history of Mars, *J. Geophys. Res.*, 95, 14137-14153.

Bottke, W. F., D. Durda, D. Nesvorny, R. Jedicke, A. Morbidelli, D. Vokrouhlicky, and H.F. Levison (2005), The fossilized size distribution of the main asteroid belt, *Icarus*, 175, 111-140.

Burr, D. M., J. A. Grier, L. P. Keszthelyi, and A. S. McEwen (2002), Repeated aqueous flooding from the Cerberus Fossae: Evidence for very recently extant, deep groundwater on Mars, *Icarus*, 159, 53–73.

Chappelow J. E., and Sharpton V. L. (2002), An improved shadow measurement technique for constraining the morphometry of simple impact craters, *Meteorit. Planet. Sci.*, 37, 479-486.

Chappelow J. E., and Sharpton V. L. (2005), Influences of atmospheric variations on Mars' record of small craters, *Icarus*, 178, 40–55.

Christensen, P. R., B. M. Jakosky, H. H. Kieffer, M. C. Malin, H. Y. McSween, Jr., K. Neelson, G. L. Mehall, S. H. Silverman, S. Ferry, M. Caplinger, and M. Ravine (2004), The Thermal Emission Imaging System (THEMIS) for the Mars 2001 Odyssey Mission, *Space Science Reviews*, 110, 85-130.

Cintala, M. J., L. Berthoud, and F. Hörz (1999), Ejection-velocity distributions from impacts into coarse-grained sand, *Meteorit. Planet. Sci.*, 34, 605–623.

Collins, G. S., and K. Wünnemann (2007), Modeling crater growth in porous targets: The effect of porosity and friction on ejection velocity and angle, *Icarus*, in press.

Daubar, I. J., and A. S. McEwen (2009), Depth to Diameter Ratios of Recent Primary Impact Craters on Mars, *Lunar Planet. Sci. Conf. XL*, Abstract #2419.

Dobrovolskis, A. (1981), Ejecta Patterns Diagnostic of Planetary Rotations, *Icarus*, 47, 203-219.

Dohm, J. M., R. C. Anderson, N. G. Barlow, H. Miyamoto, A. G. Davies, G. J. Taylor, V. R. Baker, W. V. Boynton, J. Keller, K. Kerry, D. Janes, A. G. Fairén, D. Schulze-Makuchi, M. Glamoclija, L. Marinangeli, G. G. Orij, R. G. Strom, J. Williams, J. C. Ferris, J. A. P. Rodríguez, M. A. de Pablo, and S. Karunatillake (2008), Recent geological and hydrological activity on Mars: The Tharsis/Elysium corridor, *Planetary and Space Science*, 56, 985–1013.

Environmental Systems Research Institute (2006), ArcGIS Desktop Help, 380 New York Street, Redlands, CA 92373.

Fagents, S. A. and T. Thordarson (2007), Rootless volcanic cones in Iceland and on Mars, in *The Geology of Mars: Evidence from Earth-based Analogs*, edited by Mary Chapman, pp. 151-177, Cambridge University Press, New York.

Gault, D.E. and J. Wedekind (1978), Experimental studies of oblique impact, *Lunar Planet. Sci. Conf.* 9th, 3843-3875.

Golombek, M. P., et al. (2006), Erosion rates at the Mars Exploration Rover landing sites and long-term climate change on Mars, *J. Geophys. Res.*, 111, E12S10, doi:10.1029/2006JE002754.

Greeley, R., S. D. Thompson, P. L. Whelley, S. Squyres, G. Neukum, R. Arvidson, M. Malin, R. Kuzmin, P. Christensen, S. Rafkin, T. Michaels, P. Pinet, B. Joliff, N. Cabrol, L. Richter, E. Hauber, H. Hoffmann, R. Jaumann, and the Athena, HRSC, THEMIS, and MOC science teams. (2004), Coordinated observations of aeolian features from the Mars Exploration Rovers (MER) and the Mars Express High Resolution Stereo Camera and other orbiters, *Lunar Planet. Sci. Conf.* XXXV, Abstract #2162.

Grier, J. A., and W. K. Hartmann, (2000), Rayed craters as probes of the upper surface of Ma'adim Vallis and Elysium Planitia: Images from Mars Global Surveyor, *Lunar Planet. Sci. Conf.* XXXI, Abstract #1478.

Haberle, R. M., J. R. Murphy, and James Schaeffer (2003), Orbital change experiments with a Mars general circulation model, *Icarus*, 161, 66–89.

Hartmann, W. K. (1985), Impact Experiments 1. Ejecta velocity distributions and related results from regolith targets, *Icarus*, 63, 69–98.

Hartmann, W. K. (1999), Martian cratering. VI. Crater count isochrons and evidence for recent volcanism from Mars Global Surveyor, *Meteorit. Planet. Sci.*, 34, 167–177.

Hartmann, W. K. (2002), Interplanetary Correlation Of Geologic Time Using Cratering Data, Lunar Planet. Sci. Conf. XXXIII, Abstract #1876.

Hartmann, W. K. (2005), Martian cratering. 8. Isochron refinement and the chronology of Mars, *Icarus*, 174, 294–320.

Hartmann, W. K. (2006), Utilizing Martian Craters To Derive Chronologic Information, Workshop on Surface Ages and Histories: Issues in Planetary Chronology, Lunar and Planetary Institute, Houston, Texas, Abstract #6011.

Hartmann, W. K. (2007), Martian cratering 9: Toward resolution of the controversy about small craters, *Icarus*, 189, 274–278, doi:10.1016/j.icarus.2007.02.011.

Hartmann, W. K., and D. C. Berman (2000), Elysium Planitia lava flows: Crater count chronology and geological implications, *J. Geophys. Res.*, 105, 15,011–15,026.

Hartmann, W. K., and G. Neukum (2001), Cratering Chronology and the Evolution of Mars, *Space Science Reviews*, 96, 1-4, 165-194, doi:10.1023/A:1011945222010.

Hartmann, W. K., G. Neukum, and S. Werner (2008), Confirmation and utilization of the “production function” size-frequency distributions of Martian impact craters, *Geophys. Res. Lett.*, 35, L02205, doi:10.1029/2007GL031557.

Hawke, B. R., D. T. Blewett, P. G. Lucey, G. A. Smith, J. F. Bell III, B. A. Campbell, and M. S. Robinson (2004), The origin of lunar crater rays, *Icarus*, 170, 1–16, doi:10.1016/j.icarus.2004.02.013.

Head, J. N., H. J. Melosh, and B. A. Ivanov (2002), Martian meteorite launch: High-speed ejecta from small craters, *Science*, 298, 1752–1756.

Heiken, G., D. Vaniman and B. M. French (1991), *Lunar Sourcebook: A User's Guide to the Moon*, pp. 307-311, Cambridge University Press.

Hopp, T. (1994), The Sensitivity of Three-Point Circle Fitting, NISTIR 5501, National Institute of Standards and Technology, Gaithersburg, MD.

Ivanov, B. A. (2001), Mars/Moon cratering ratio estimates, *Space Sci. Rev.*, 96, 87–104.

Jaeger, W. L., L. P. Keszthelyi, A. S. McEwen, C. M. Dundas, and P. S. Russell (2007), Athabasca Valles, Mars: A Lava-Draped Channel System, *Science*, 317, 1709-1711, doi:10.1126/science.1143315.

James, P.B., H. H. Kieffer, and D. A. Paige (1992), The seasonal cycle of carbon dioxide on Mars. In: (Eds.), *Mars*, edited by H. H. Kieffer, B. M. Jakosky, C. W. Snyder, M. S. Matthews, pp. 934–968, Univ. of Arizona Press, Tucson, Arizona.

Kargel, J. S. (1986), Morphologic variations of Martian rampart crater ejecta and their dependencies and implications, *Lunar and Planet. Sci. Conf. XVII*, 410–411.

Kinch, K. M., J. Sohl-Dickstein, J. F. Bell III, J. R. Johnson, W. Goetz, and G. A. Landis (2007), Dust deposition on the Mars Exploration Rover Panoramic Camera (Pancam) calibration targets, *J. Geophys. Res.*, 112, E06S03, doi:10.1029/2006JE002807.

Kreslavsky, M. (2008), Young populations of small craters on Mars: A case study, *European Planetary Science Congress, Vol. 3*, EPSC2008-A-00237.

Kreslavsky, M. A., and J. W. Head (2005), Mars at very low obliquity: Atmospheric collapse and the fate of volatiles, *Geophys. Res. Lett.*, 32, L12202, doi:10.1029/2005GL022645.

Lanagan, P. D., A. S. McEwen, L. P. Keszthelyi, and T. Thordarson (2001), Rootless cones on Mars indicating the presence of shallow equatorial ground ice in recent times, *Geophys. Res. Lett.*, 28, 12, 2365-2367.

Laskar, J., A.C.M. Correia, M. Gastineau, F. Joutel, B. Levrarda, P. Robutel (2004), Long term evolution and chaotic diffusion of the insolation quantities of Mars, *Icarus*, 170, 343–364, doi:10.1016/j.icarus.2004.04.005.

Lucey, P. G., D. T. Blewett, G. J. Taylor, and B. R. Hawke (2000), Imaging of lunar surface maturity, *J. Geophys. Res.*, 105, E08, 20377-20386.

Malin, M. C., K. S. Edgett, L. V. Posiolova, S. M. McColley, and E. Z. Noe Dobrea (2006), Present-Day Impact Cratering Rate and Contemporary Gully Activity on Mars, *Science*, 314, 5805, 1573 – 1577, doi:10.1126/science.1135156.

Mangold, N., S. Maurice, W. C. Feldman, F. Costard, F. Forget (2004), Spatial relationships between patterned ground and ground ice detected by the Neutron Spectrometer on Mars, *J. Geophys. Res.*, 109, E08, doi:10.1029/2004JE002235.

Manning, C. V., C. P. McKay, K. J. Zahnle (2006), Thick and thin models of the evolution of carbon dioxide on Mars, *Icarus*, 180, 38–59, doi:10.1016/j.icarus.2005.08.014.

McEwen A. S., B. S. Preblich, E. P. Turtle, N. A. Artemieva, M. P. Golombek, M. Hurst, R. L. Kirk, D. M. Burr and P. R. Christensen (2005), The rayed crater Zunil and interpretations of small impact craters on Mars, *Icarus*, 176, 351–381, doi:10.1016/j.icarus.2005.02.009.

McEwen, A. S., and E. B. Bierhaus (2006), The Importance of Secondary Cratering to Age Constraints on Planetary Surfaces, *Annual Review of Earth and Planetary Sciences*, 34, 535-567, doi:10.1146/annurev.earth.34.031405.125018.

McEwen A. S., E. M. Eliason, J. W. Bergstrom, N. T. Bridges, C. J. Hansen, W. A. Delamere, J. A. Grant, V. C. Gulick, K. E. Herkenhoff, L. Keszthelyi, R. L. Kirk, M. T. Mellon, S. W. Squyres, N. Thomas, and C. M. Weitz (2007), Mars Reconnaissance Orbiter's High Resolution Imaging Science Experiment (HiRISE), *J. Geophys. Res.*, 112, E05S02, doi:10.1029/2005JE002605.

McGarigal, K., and B. J. Marks (1994), FRAGSTATS: spatial pattern analysis program for quantifying landscape structure, 134 pp., USDA For. Serv. Gen. Tech. Rep. PNW-351, Oregon State University, Corvallis.

McGill, G. E. (1977), Craters as “fossils”: The remote dating of planetary surface materials, *Geological Society of America Bulletin*, 88(8), 1102–1110, doi:10.1130/0016-7606(1977)88.

Mellon, M. T. and B. M. Jakosky (1995), The distribution and behavior of Martian ground ice during past and present epochs, *J. Geophys. Res.*, 100, E6, PAGES 11,781-11,799.

Mellon, M. T., W. C. Feldman and T. H. Prettyman (2004), The presence and stability of ground ice in the southern hemisphere of Mars, *Icarus*, 169, 324–340.

Melosh, H. J. (1989), *Impact Cratering: A Geologic Process*, Oxford University Press, New York, New York.

Mouginis-Mark, P. J. (1985), Volcano/ground ice interactions in Elysium Planitia, Mars, *Icarus*, 64, 265-284.

Murray, J. B. and J. E. Guest (1970), Circularities of craters and related structures on Earth and Moon, *Modern Geology*, 1, 149-159.

Neukum, G., B. A. Ivanov, and W. K. Hartmann (2001), Cratering Records in the Inner Solar System in Relation to the Lunar Reference System, *Chronology and Evolution of Mars*, 96, 1-4, doi:10.1023/A:1011989004263.

Page, D. P. (2007), Recent low-latitude freeze–thaw on Mars, *Icarus*, 189, 83–117, doi:10.1016/j.icarus.2007.01.005.

Pike, R. J. (1980), Control of crater morphology by gravity and target type: Mars, Earth, Moon, *Lunar and Planet. Sci. Conf.* 11th, 2159–2189.

Pike, R. J., and P. A. Davis (1984), Toward a Topographic Model of Martian Craters from Photoclinometry, *Lunar and Planet. Sci. Conf.* XV, 645–646.

Pike, R. J., and D. E. Wilhelms (1978), Secondary-impact craters on the Moon: topographic form and geologic process, *Lunar and Planet. Sci. Conf.* 9th, 907–909.

Plescia, J. B. (1990), Recent flood lavas in the Elysium region of Mars, *Icarus*, 88, 465.

Plescia, J. B. (2003), Cerberus Fossae, Elysium, Mars: A source for lava and water, *Icarus*, 164, 79–95.

Popova, O. P., I. Nemtchinov, and W. K. Hartmann (2003), Bolides in the present and past martian atmosphere and effects on cratering processes, *Meteorit. Planet. Sci.*, 38, 905–925.

Popova O. P., W. K. Hartmann, I. V. Nemtchinov, D. C. Richardson , and D. C. Berman (2007), Crater clusters on Mars: Shedding light on martian ejecta launch conditions, *Icarus*, 190(1), 50-73, doi:10.1016/j.icarus.2007.02.022.

Preblich, B. S., A. S. McEwen, and D. M. Studer (2007), Mapping rays and secondary craters from the Martian crater Zunil, *J. Geophys. Res.*, 112, E05006, doi:10.1029/2006JE002817.

Quantin, C., N. Mangold, W. K. Hartmann, and P. Allemand, (2007), Possible longterm decline in impact rates 1. Martian geological data, *Icarus*, 186, 1–10.

Ruff, S. W., and P. R. Christensen (2002), Bright and dark regions on Mars: Particle size and mineralogical characteristics based on Thermal Emission Spectrometer data, *J. Geophys. Res.*, 107, E12, doi:10.1029/2001JE001580.

Schaeffer, O. A., J. G. Funkhouser, D. D. Bogard, and J. Zahringer (1970), Potassium-Argon Ages of Lunar Rocks from Mare Tranquillitatis and Oceanus Procellarum, *Science*, 170, 161-162, doi:10.1126/science.170.3954.161.

Schultz, P. H., and D. E. Gault (1985), Clustered impacts: Experiments and Implications, *J. Geophys. Res.*, 90, B5, 3701-3732.

Selkirk, K. E. (1982), *Pattern and Place: An Introduction to the Mathematics of Geography*, Cambridge University Press, Cambridge, New York.

Shoemaker E. M. (1962), Interpretation of lunar craters, in *Physics and Astronomy of the Moon*, edited by Z. Kopal, pp. 283-359, Academic Press, New York and London.

Shoemaker, E. M. (1965), Preliminary analysis of the fine structure of the lunar surface in Mare Cognitum, JPL Tech. Report No. 32-700, in *The Nature of the Lunar Surface*, edited by W. N. Hess, D. H. Menzel, and J.A. O'Keefe, pp. 23-77, Johns Hopkins Press, Baltimore.

Shoemaker, E. M., R. J. Hackman, and R. E. Eggleton (1963), Interplanetary correlation of geologic time, *Adv. Astronaut. Sci.*, 8, 70 – 89.

Smith, D. E., M. T. Zuber, S. C. Solomon, R. J. Phillips, J. W. Head, J. B. Garvin, W. B. Banerdt, D. O. Muhleman, G. H. Pettengill, G. A. Neumann, F. G. Lemoine, J. B. Abshire, O. Aharonson, C. D. Brown, S. A. Hauck, A. B. Ivanov, P. J. McGovern, H. J. Zwally, and T. C. Duxbury (1999), The Global Topography of Mars and Implications for Surface Evolution, *Science*, 284, 1495-1503.

Tanaka, K. L., J. A. Skinner, Jr., and T. M. Hare (2005), *Geologic Map of the Northern Plains of Mars*, Map SIM-2888, 1:15M, U. S. Geological Survey, Reston, Virginia.

Tornabene, L. L., and A. S. McEwen (2008), Recent channel systems emanating from Hale crater ejecta: implications for the Noachian landscape evolution of Mars, *Lunar and Planet. Sci. Conf. XXXIX*, Abstract #2108.

Tornabene, L. L., J. E. Moersch, H. Y. McSween Jr., A. S. McEwen, J. L. Piatek, K. A. Milam, and P. R. Christensen (2006), Identification of large (2–10 km) rayed craters on Mars in THEMIS thermal infrared images: Implications for possible Martian meteorite source regions, *J. Geophys. Res.*, 111, E10006, doi:10.1029/2005JE002600.

Turner, G. (1970), Argon-40/ Argon-39 Dating of Lunar Rock Samples, *Science*, 167, 3918, 466 – 468, doi:10.1126/science.167.3918.466.

Watters, W. A., B. A. Campbell, L. M. Carter, C. J. Leuschen, J. J. Plaut, G. Picardi, A. Safaeinili, S. M. Clifford, W. M. Farrell, A. B. Ivanov, R. J. Phillips, E. R. Stofan and the MARSIS Science Team, (2007), MARSIS subsurface radar sounding of the Medusae Fossae Formation, Mars, Lunar Plant. Sci. Conf. XXXVIII, Abstract #1661.

Wells, E. N., J. Veverka and P. Thomas (1984), Mars: Experimental study of albedo changes caused by dust fallout, *Icarus*, 58, 3, 331-338, doi:10.1016/0019-1035(84)90079-4.

Werner, S. C., B. A. Ivanov, G. Neukum (2009), Theoretical analysis of secondary cratering on Mars and an image-based study on the Cerberus Plains, *Icarus*, 200, 406-417, doi:10.1016/j.icarus.2008.10.011.

Wrobel, K. E., and P. H. Schultz (2004), Effect of planetary rotation on distal tektite deposition on Mars, *J. Geophys. Res.*, 109, E05005, doi:10.1029/2004JE002250.

Wünnemann, K., G. S. Collins, H. J. Melosh (2006), A strain-based porosity model for use in hydrocode simulations of impacts and implications for transient crater growth in porous targets, *Icarus*, 180, 514-527.

TABLES

Table 2.1: Criteria for recognizing Primary versus Secondary Craters on Mars.

Properties		Crater Type	
		Primary ^a	Secondary ^b
General	'Air-blast' Zone	Yes	No
	Rayed Ejecta Radius	tens to hundreds of crater radii	a few to low tens of crater radii
	Mean Continuous Ejecta Blanket Radius ^c	18.1±7.0	5.4±1.6
	Ejecta Morphology	thin, ephemeral, diffuse boundaries	thick, ramparted, 'clotty', sharp boundaries
Crater Rim	Circularity Ratio (C _R)	0.97±0.02 (none below 0.90)	0.94±0.05 (some less than 0.90)
	Form Ratio (F _R)	0.83±0.10	0.84±0.07
	Fractal Dimension Index (FD _I)	2.4936D ^{-0.1826} R ² = 0.83	1.842D ^{-0.0801} R ² = 0.94
		2.1726D ^{-0.1247} , R ² = 0.88 (For all SRC)	
Ejecta Planform	Circularity Ratio (C _R)	0.55±0.25	0.27±0.13
	Form Ratio (F _R)	0.51±0.14	0.39±0.11
	Fractal Dimension Index (FD _I)	1.29±0.05 (majority below 1.30)	1.40±0.06 (majority above 1.30)

^aPrimaries found over ~7a as published in Malin et al., 2006.

^bSecondaries predominately produced by Zunil (McEwen et al., 2005)

^cRadius normalized to crater radius.

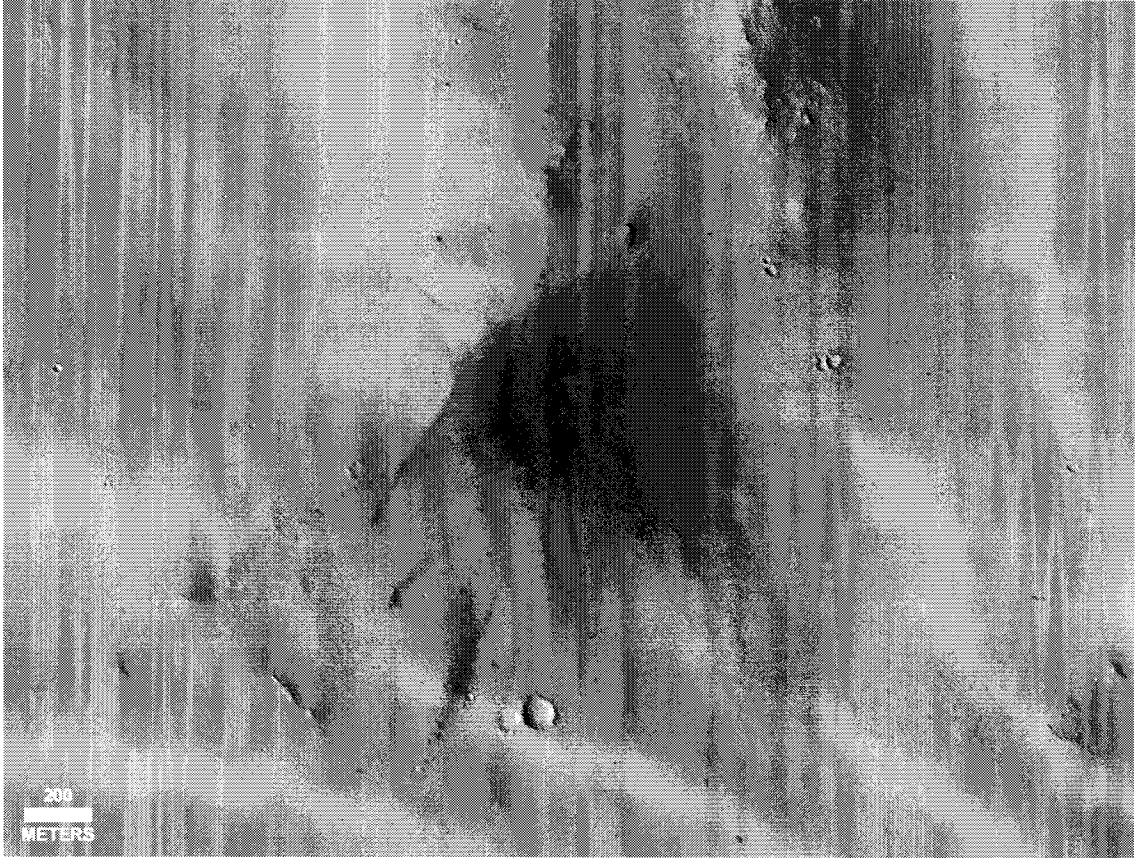
FIGURES

Figure 2.1: Example of primary small rayed crater on Mars. Note both continuous and discontinuous rays extending beyond the primary ejecta blanket, as well as extensive “air blast” region surrounding the continuous ejecta blanket. Image cropped from PSP_003101_2065_RED, courtesy NASA/Jet Propulsion Laboratory (JPL, Pasadena, California)/University of Arizona.

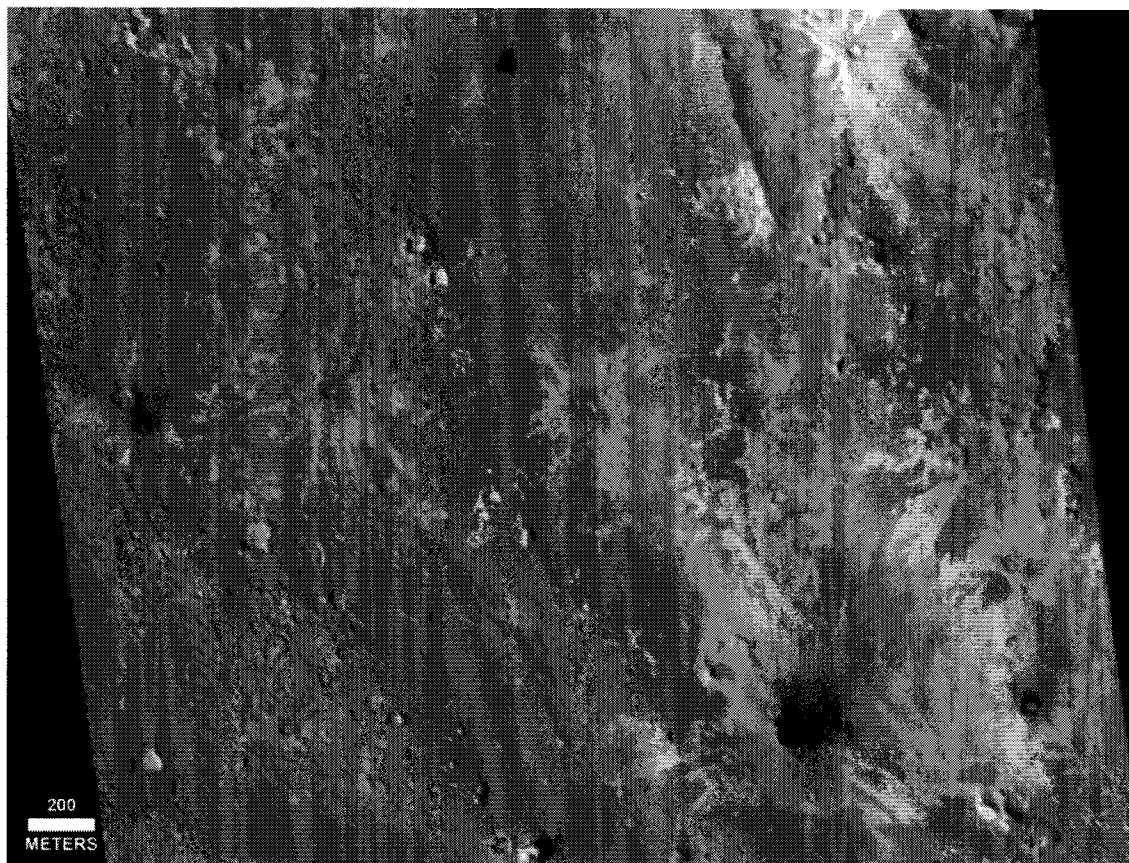


Figure 2.2: Example of several Zunil secondary small rayed craters on Mars. Note sharp ejecta boundaries and relatively short rays relative to crater radius, compared to Figure 2.1 at same scale. Image cropped from MOCNA M0401791, courtesy NASA/JPL/Malin Space Science Systems (MSSS).

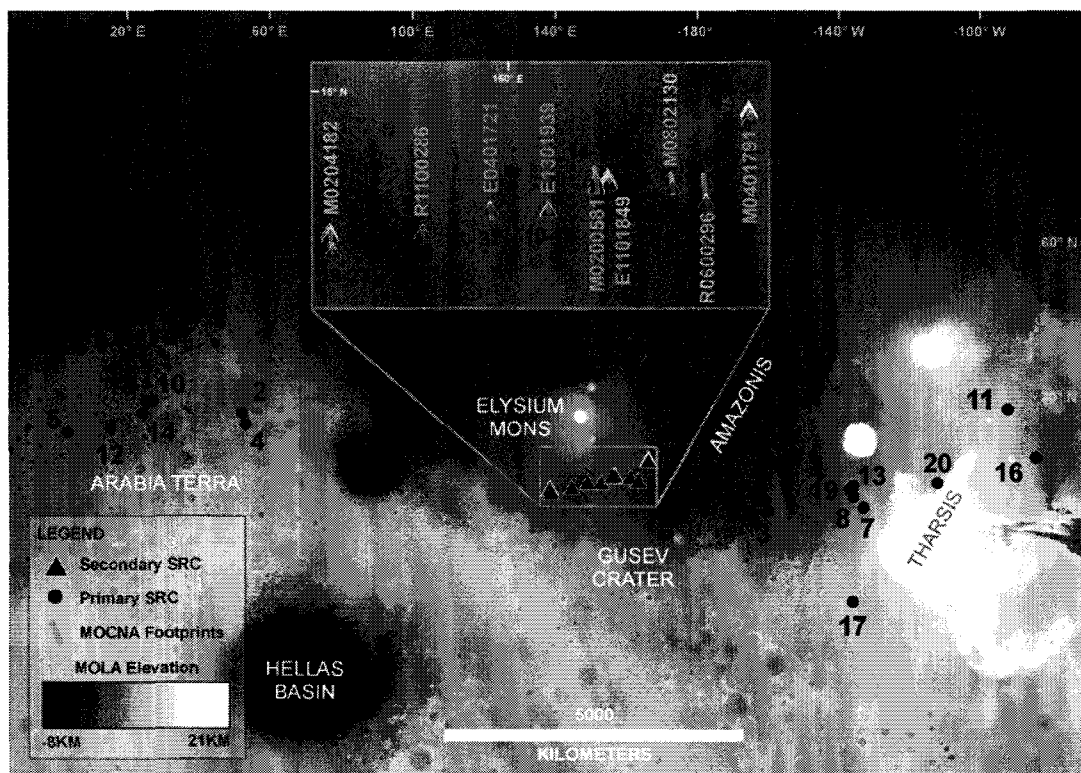


Figure 2.3: Location of twenty primary [Malin et al., 2006] and thirty-eight secondary SRC derived from MOCNA images. Clustering of primary impacts is artificial due to the limited study area of Malin et al. [2006]. Primaries in the Amazonis region are more similar in spatial and possibly target properties compared to Zunil secondary SRC. Identification numbers refer to SRC in this study. North is up in this Mercator projection centered at 150°E longitude. Background Mars Orbiter Laser Altimeter (MOLA) data are courtesy of the MOLA Science Team.

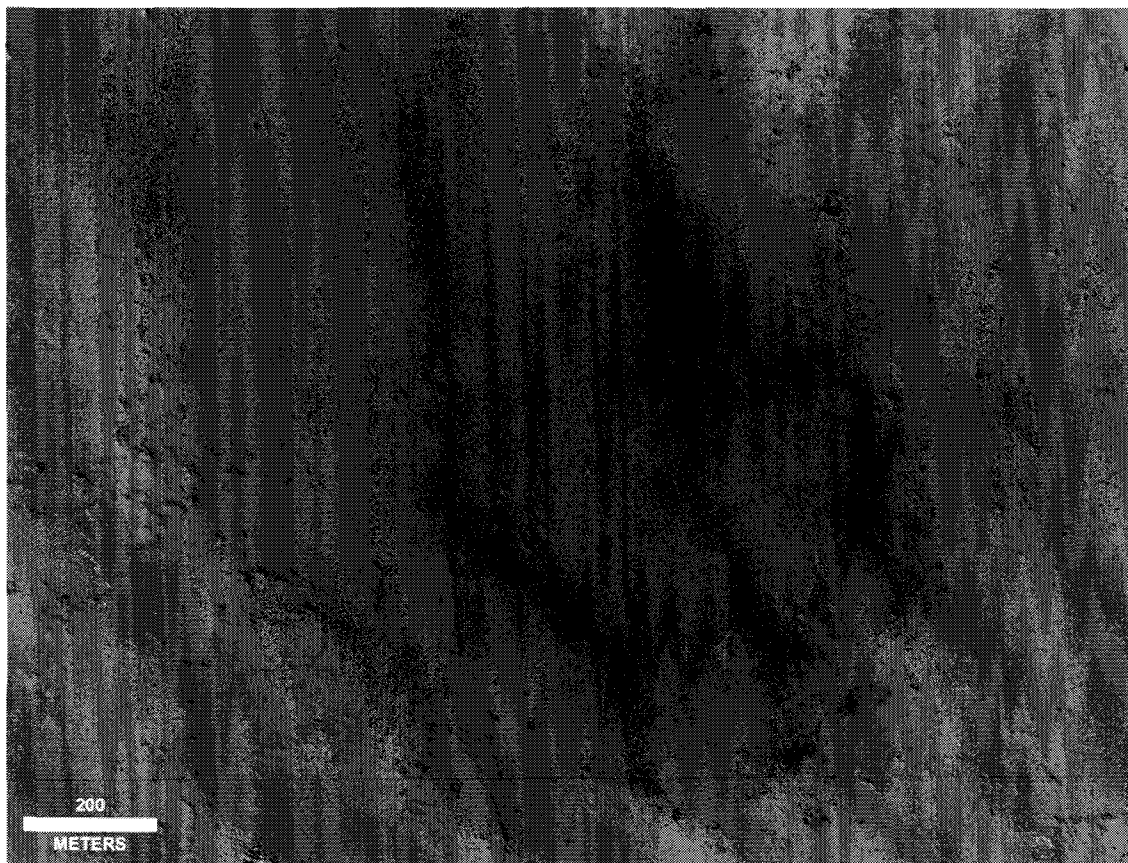


Figure 2.4: Example of ejecta planform from the atmospheric breakup of the primary meteorite before impact. Note multiple craters in the central bright ejecta deposit surrounded by a dark air blast region. Dark ephemeral streaks extending to the upper left are likely post-impact wind modification. North is up. Image cropped from PSP_003172_1870_RED, courtesy NASA/JPL/University of Arizona.

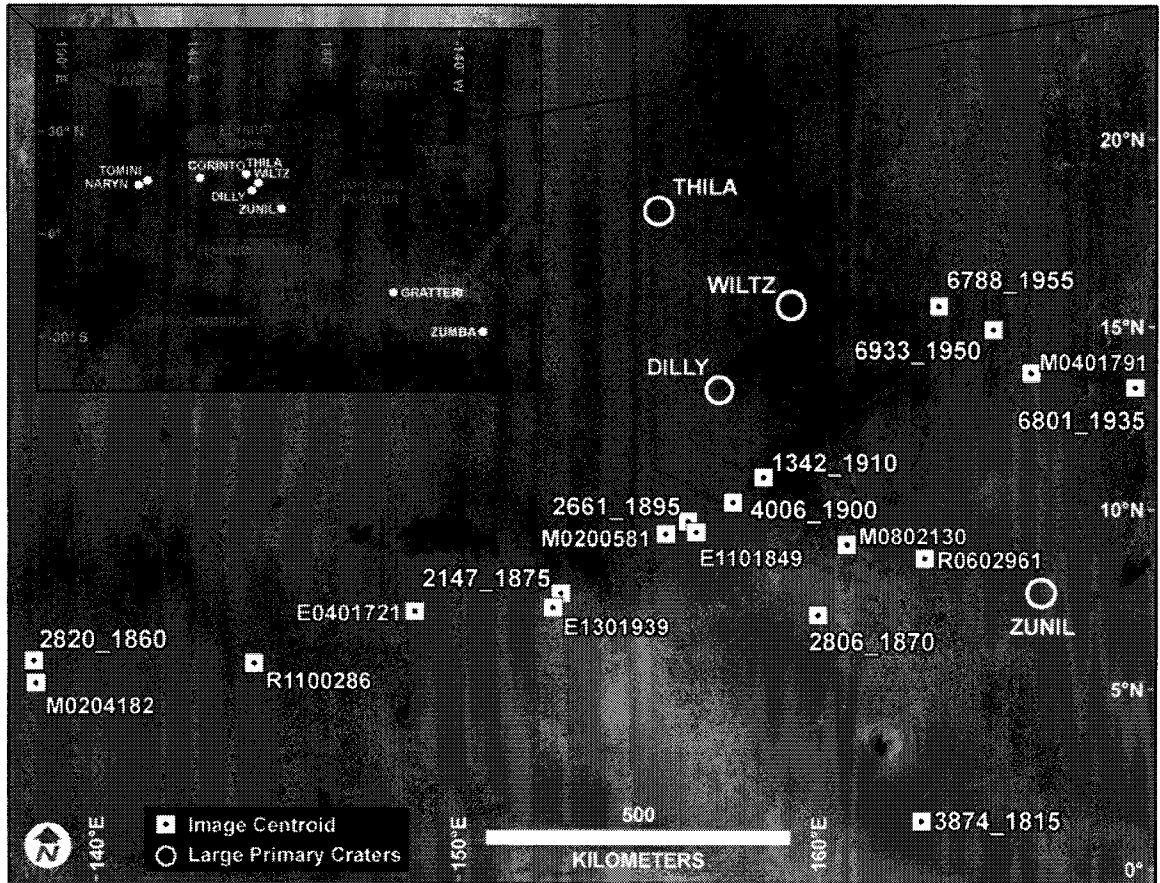


Figure 2.5: Images containing secondary SRC found in MOCNA and High-Resolution Imaging Science Experiment (HiRISE) RED images from this study. Inset map shows location of nine large primaries [Tornabene et al., 2006; Tornabene and McEwen, 2008] in relation to secondary SRC study area. Background night-time infrared image derived from the Thermal Emission Imaging System Infrared (THEMIS-IR) instrument [Christensen et. al., 2004]. Mars Orbiter Camera Wide-Angle Atlas in inset background created by Malin Space Science Systems (<http://www.msss.com/>).

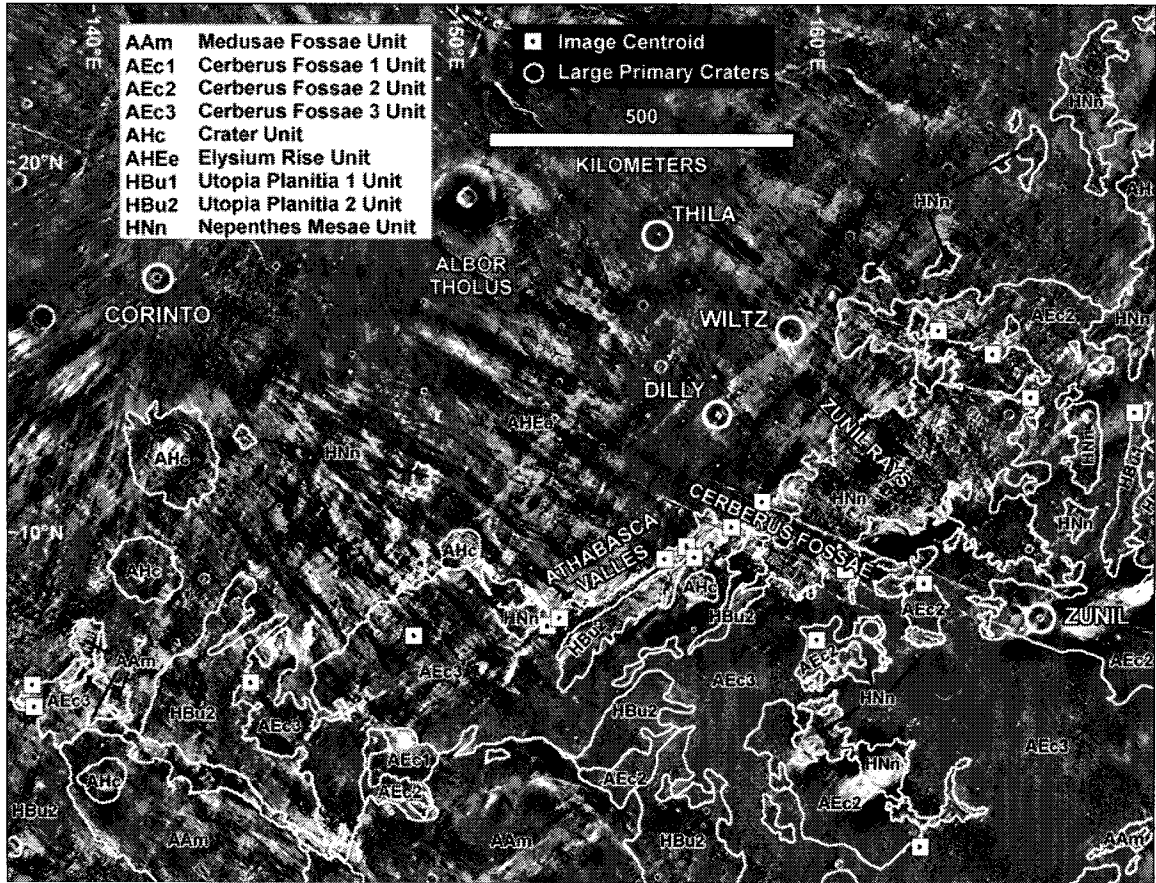


Figure 2.6: Geologic formations encountered within the study area. SRC located in MOCNA and HiRISE images fall mainly in Amazonian volcanic deposits north and west of Zunil. Several images fall in the Athabasca Valles/Cerberus Fossae region. Martian geologic units as codified by Tanaka et al., [2005]. Background night-time infrared image derived from the THEMIS-IR instrument [Christensen et. al., 2004]. Image names removed for clarity; see Figure 2.5.

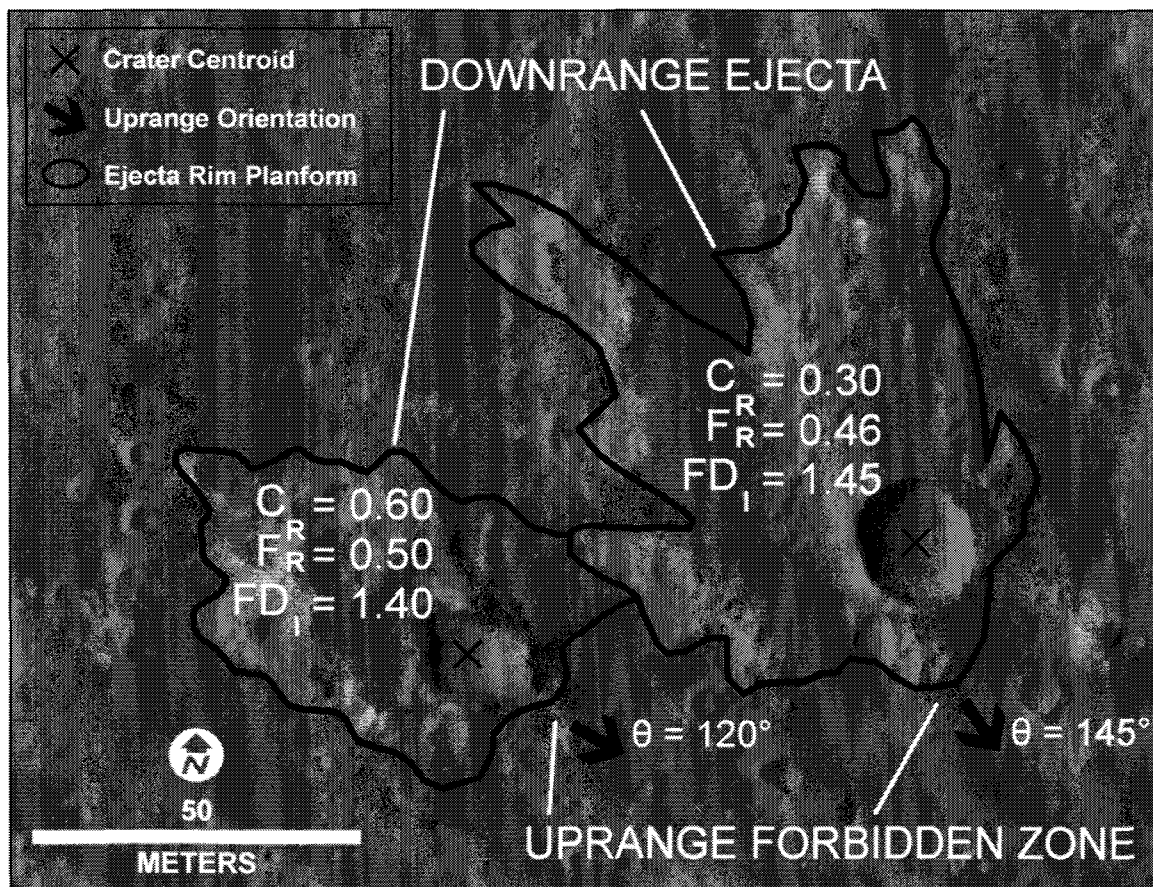


Figure 2.7: Measurements of ejecta planform based on distal extent of a continuous ejecta deposit. Uprange azimuth toward primary estimated from placement of downrange ejecta and uprange forbidden zone. Note the higher circularity (Circularity ratio (C_R)) and Form (F_R) ratio for the western crater with little to no rays and increased Fractal Dimension Index (FD_I) for the eastern crater with more distal rays. Background image PSP_001342_1910_RED courtesy NASA/JPL/University of Arizona.

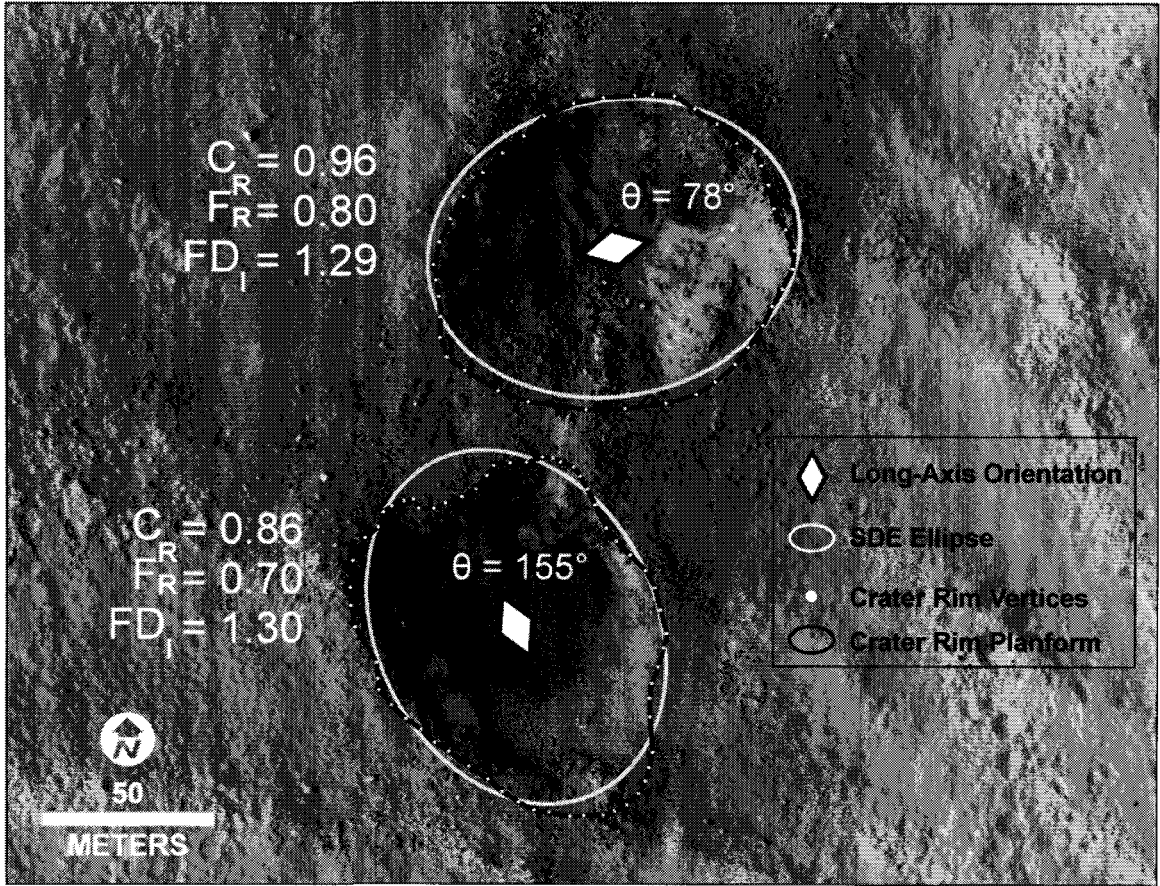


Figure 2.8: Measurements of crater planform based on highest discernable edge of rim. Crater long axis was estimated by calculating the standard deviation ellipse (SDE) (white line), from the rim vertices (white dots). Axis orientation is based on 180° clockwise from north. Note the higher circularity (C_R) and Form (F_R) ratio for the northern crater, but nearly equal Fractal Dimension Index (FD_I) for both craters. Background image PSP_002806_1870_RED courtesy NASA/JPL/University of Arizona.

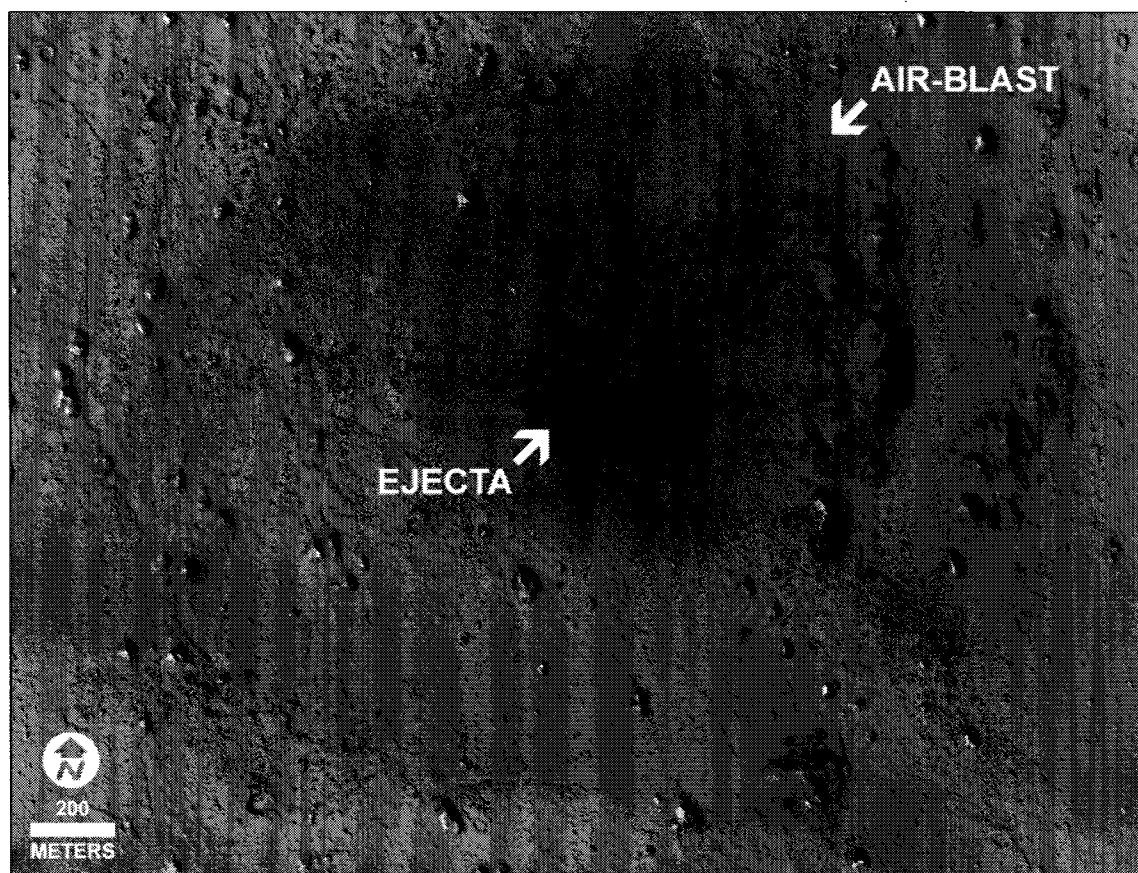


Figure 2.9: Air blast region surrounding primary impact crater. Dark continuous ejecta blanket and “gray” air blast labeled with white arrows. Air blast extends to over 1 km radially from the distal edge of the ejecta. Note the flattened southeastern edge of the air blast region that appears to coincide with the uprange direction based on the ejecta planform $D = \sim 10$ m as measured from HiRISE imagery (ID 9). Background image PSP_004123_1915_RED courtesy NASA/JPL/University of Arizona.

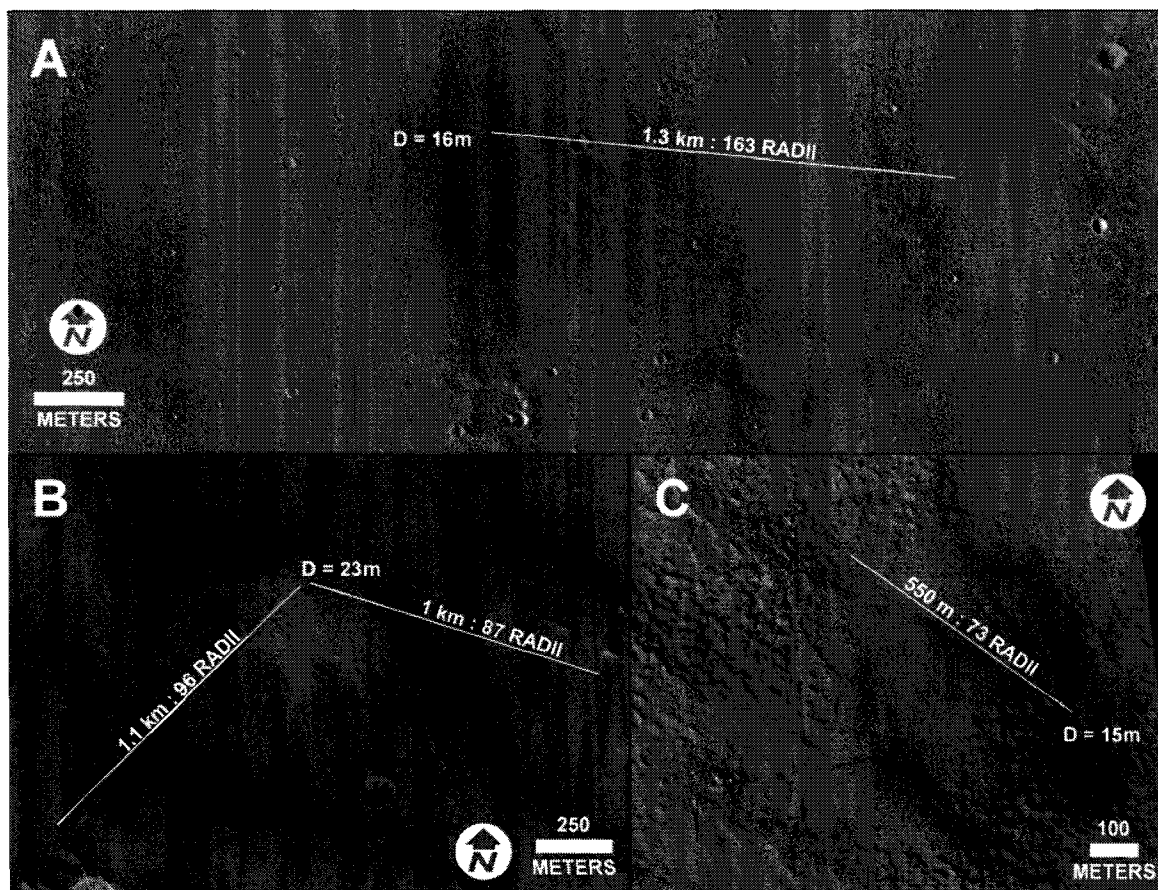


Figure 2.10: Continuous and discontinuous rays from primary impact craters. These ray patterns can extend upwards of 100 crater radii and a factor of 2 to 3 past the distal edge of the continuous ejecta blanket. Background images from (a) ID 11 PSP_002736_2075_RED, (b) ID 5 PSP_004038_2005_RED and (c) ID 10 PSP_003958_2025_RED courtesy NASA/JPL/University of Arizona.

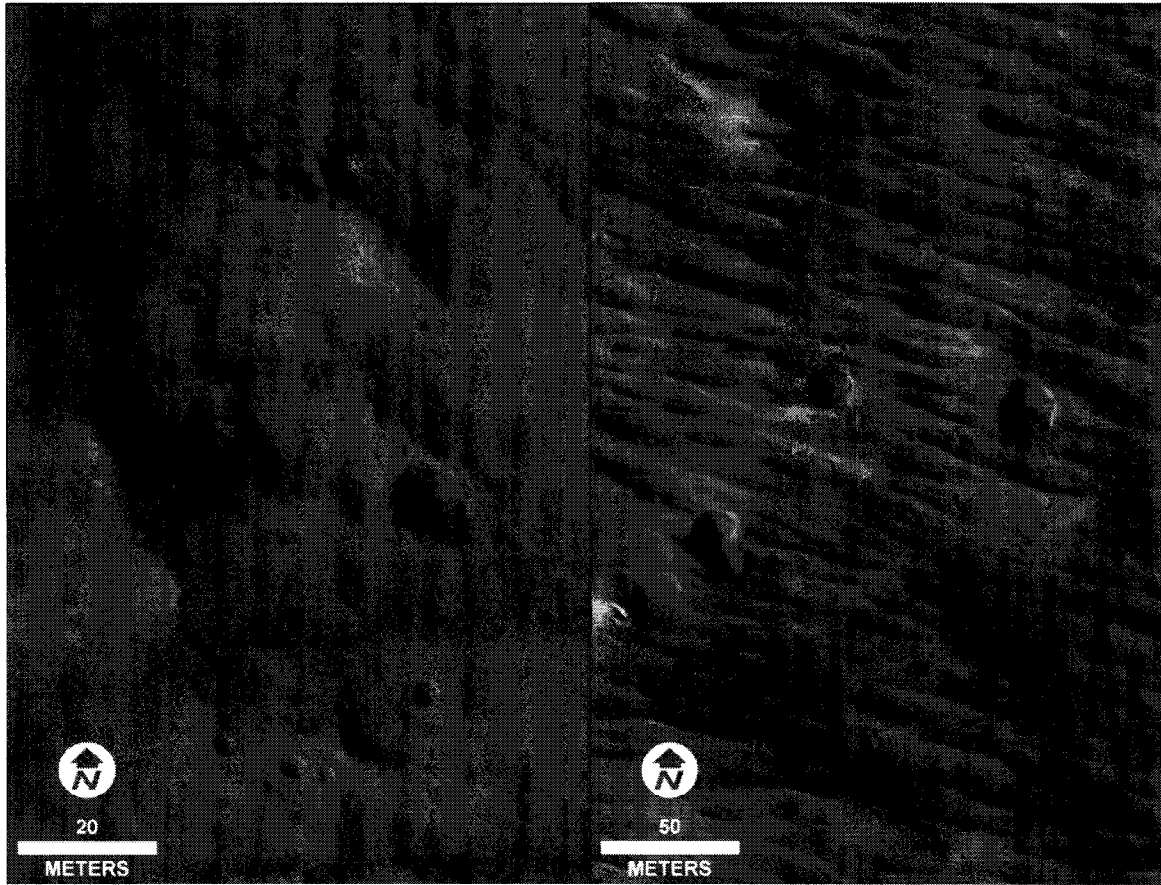


Figure 2.11: Craters from suspected fragmented meteorites. (left) Image (ID 16) contains two craters $D = \sim 14$ m (center left) and ~ 13 m (center right) with many other $D < 5$ m craters that may be additional impacts from the original meteor body. (right) Image (ID 8) contains three craters $D = \sim 24$ m, ~ 18 m and ~ 17 m with many other $D \leq 10$ m craters. Background images PSP_003527_1940_RED (Figure 2.11, left) and PSP_005942_1825_RED (Figure 2.11, right) courtesy NASA/JPL/University of Arizona.

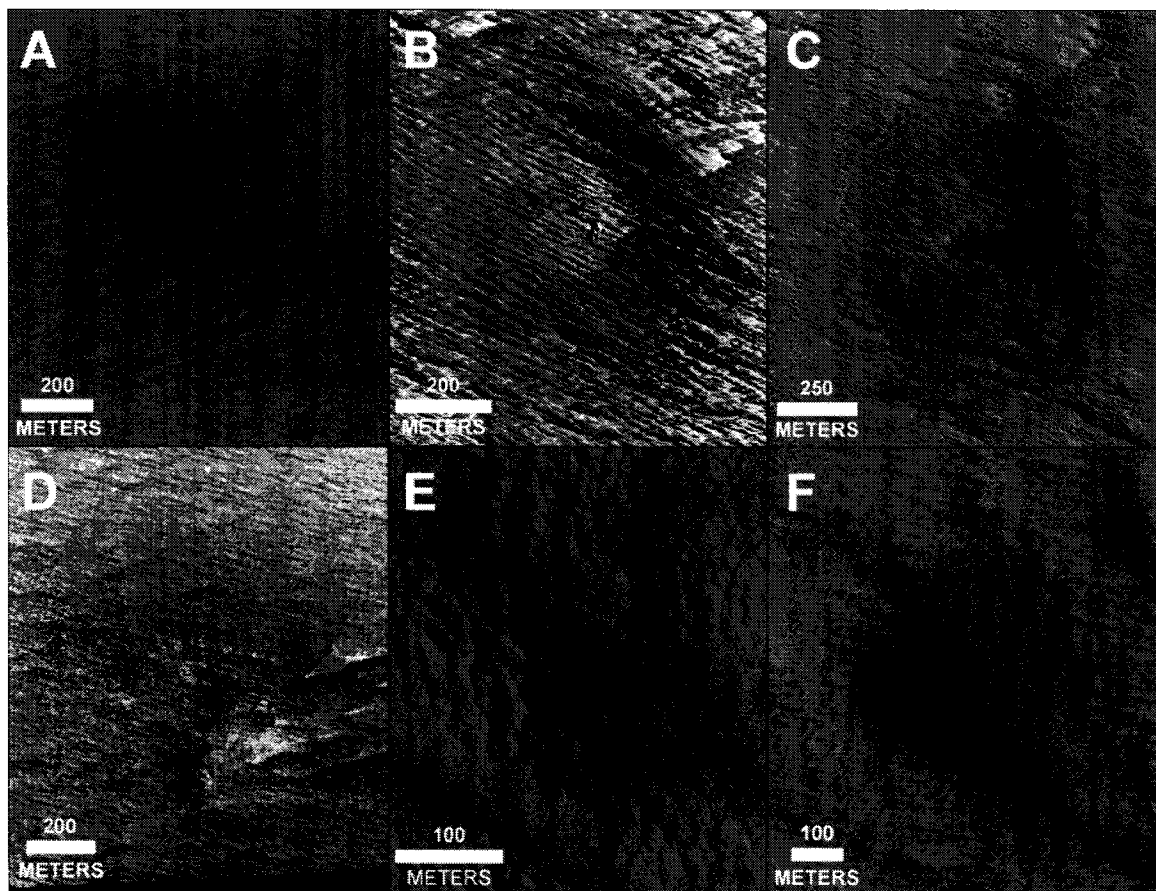


Figure 2.12: “No ejecta” primaries in MOCNA ROTO and HiRISE imagery. These primaries show little to no ejecta about their crater rim. The background surface texture is undisturbed other than a change in reflectivity. Primaries in Figures 2.12B and 2.12C show some bright ejecta, and 2.12D has some discernable rays (image stretched), but ejecta thickness appears substantially thinner than the meter-to-sub-meter-scale topography which it overlies. Background images for (A) ID 3, S1502488, (D) ID 13, S1601331, and (F) ID 19, S1701972 courtesy NASA/JPL/MSSS. Background images for (B) ID 7, PSP_002764_1800_RED, (C) ID 8, PSP_005942_1825_RED, and (E) ID 15, PSP_003754_1815_RED courtesy NASA/JPL/University of Arizona.

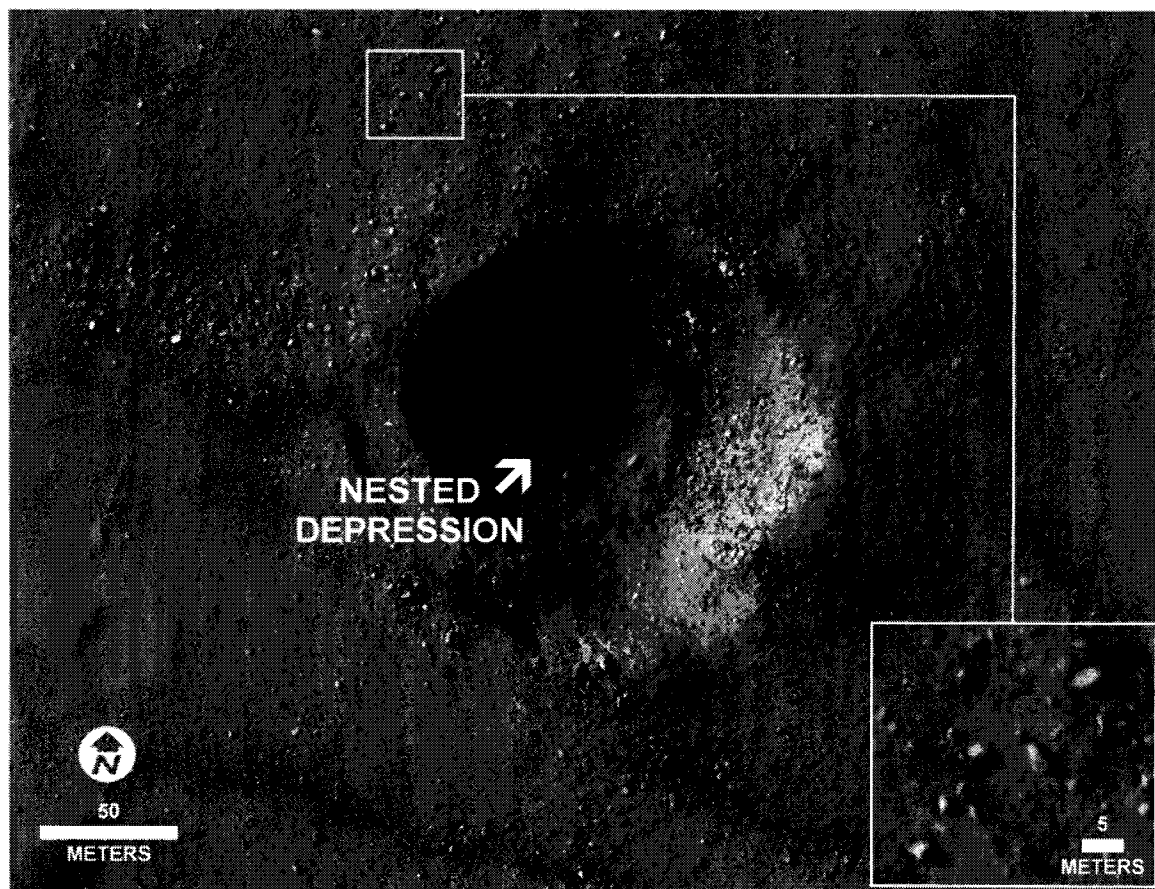


Figure 2.13: Primary crater with nested depression and boulder strewn ejecta. Inset shows close-up of ≤ 5 m boulders that extend distally beyond the image to 2-4 crater radii. Background image (ID 17, PSP_002039_1545_RED) courtesy NASA/JPL/University of Arizona.

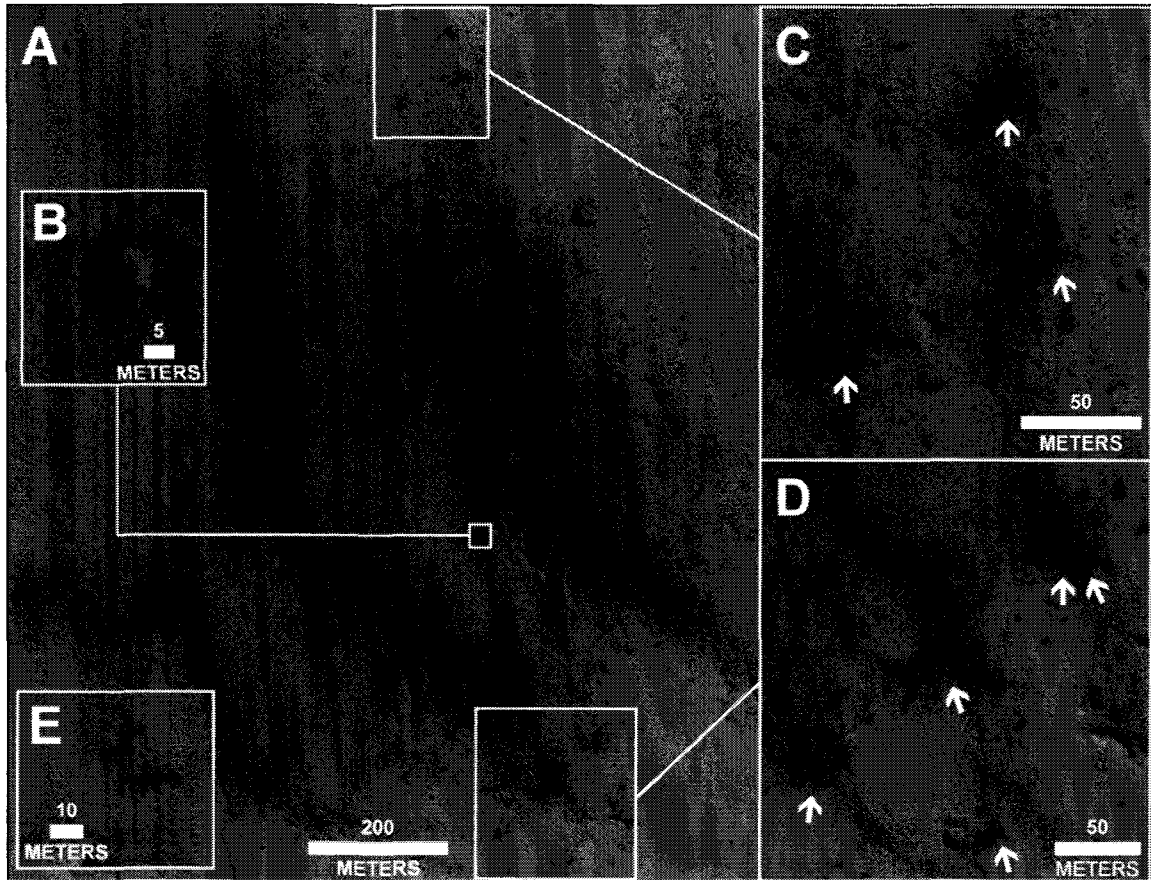


Figure 2.14: Crater field created by a primary impact. (A) This primary (ID 20) contains two craters $D = \sim 16$ m and (B) $D = \sim 13$ m, with tens of craters $5 \text{ m} \leq D \leq 10 \text{ m}$ and perhaps hundreds $D < 5 \text{ m}$ in or around the bright ejecta blanket (C and D). Tens of dark-rayed ejecta craters with $1 \text{ m} \leq D \leq 5 \text{ m}$ both north (Figure 2.14C) and south (Figure 2.14D) of the main ejecta field. White arrows denote the uprange azimuth of impact on the basis of the ejecta ray planform. These dark-rayed craters appear to be impacts created from the same meteor body that created the central bright ejecta in Figure 2.14A. (E) A cluster of three dark-rayed craters, $D < 3 \text{ m}$, located $\sim 1.7 \text{ km}$ north and $\sim 1.1 \text{ km}$ west of the main crater field. Background image PSP_003172_1870_RED courtesy NASA/JPL/University of Arizona.

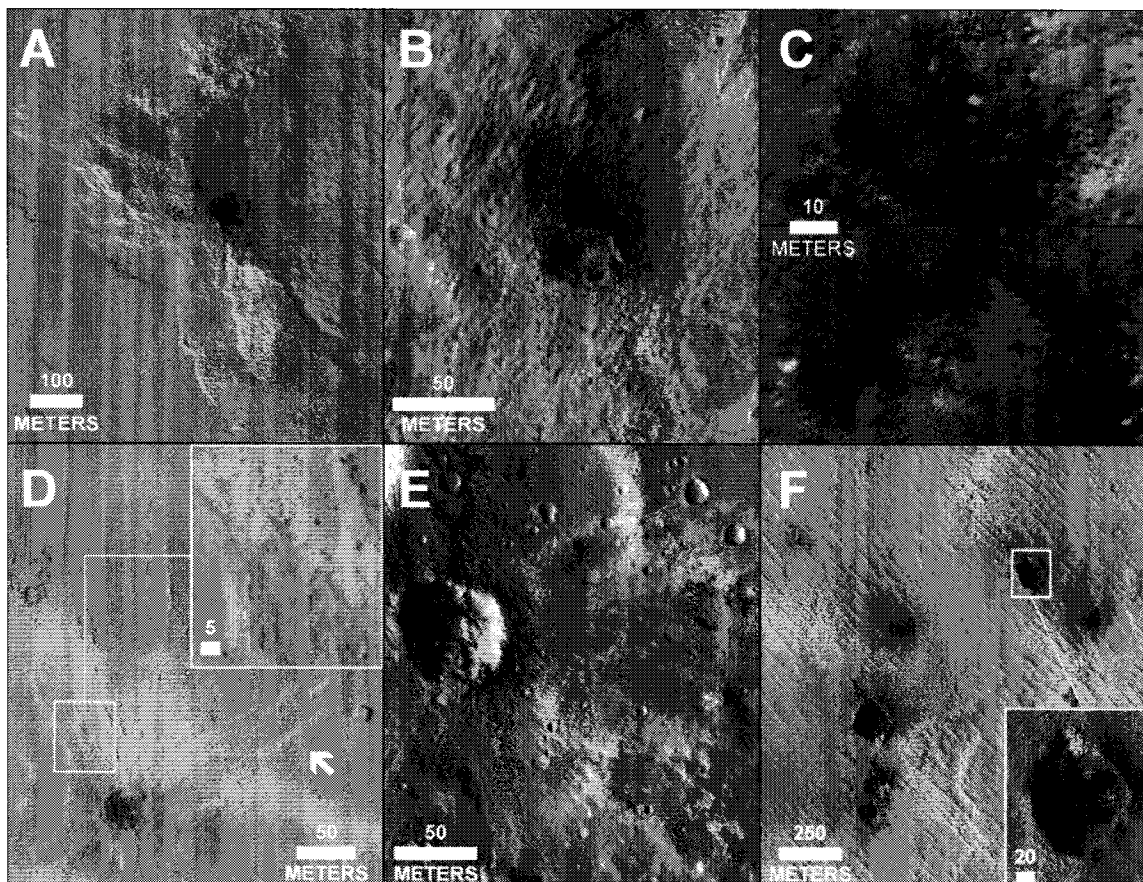


Figure 2.15: Examples of secondary SRC ejecta, crater rims and floors. (A) A typical Zuni secondary with bright ejecta, dark ejecta annulus and crater floor, somewhat circular rim, and axially asymmetric continuous ejecta. (B) A closer view of the dark ejecta annulus as well as an example of a double impact. (C) Two crater floors, one (top) dark and one (bottom) with bright, assumed aeolian deposits overlying the darker floor. Both crater in Figure 2.15C are within 100 m of each other. (D) Downrange ejecta (toward image top) inferred from the distal ejecta ray pattern. White arrow in Figure 2.15D denotes a discontinuous “island” of ejecta separated from the continuous ejecta blanket. Figure 2.15D provides a closer view of the sharp-edged, wind-eroded nature of the ejecta. (E) Draping of ejecta with no disruption over topographic features. (F) Seven examples of “sans-ejecta” secondaries with some dark ejecta near the crater rim, but no discernable bright ejecta. Inset in Figure 2.15F is a secondary crater with depth/diameter ratio = ~ 0.25 . Background images for Figure 2.15A and 2.15D (ID 300/160, PSP_004006_1900_RED), Figure 2.15B (PSP_002661_1895_RED), Figure 2.15C (ID 116 in lower half, PSP_003874_1815_RED), Figure 2.15E (ID 19, PSP_002820_1860_RED) and Figure 2.15F (PSP_002806_1870_RED) courtesy of NASA/JPL/University of Arizona.

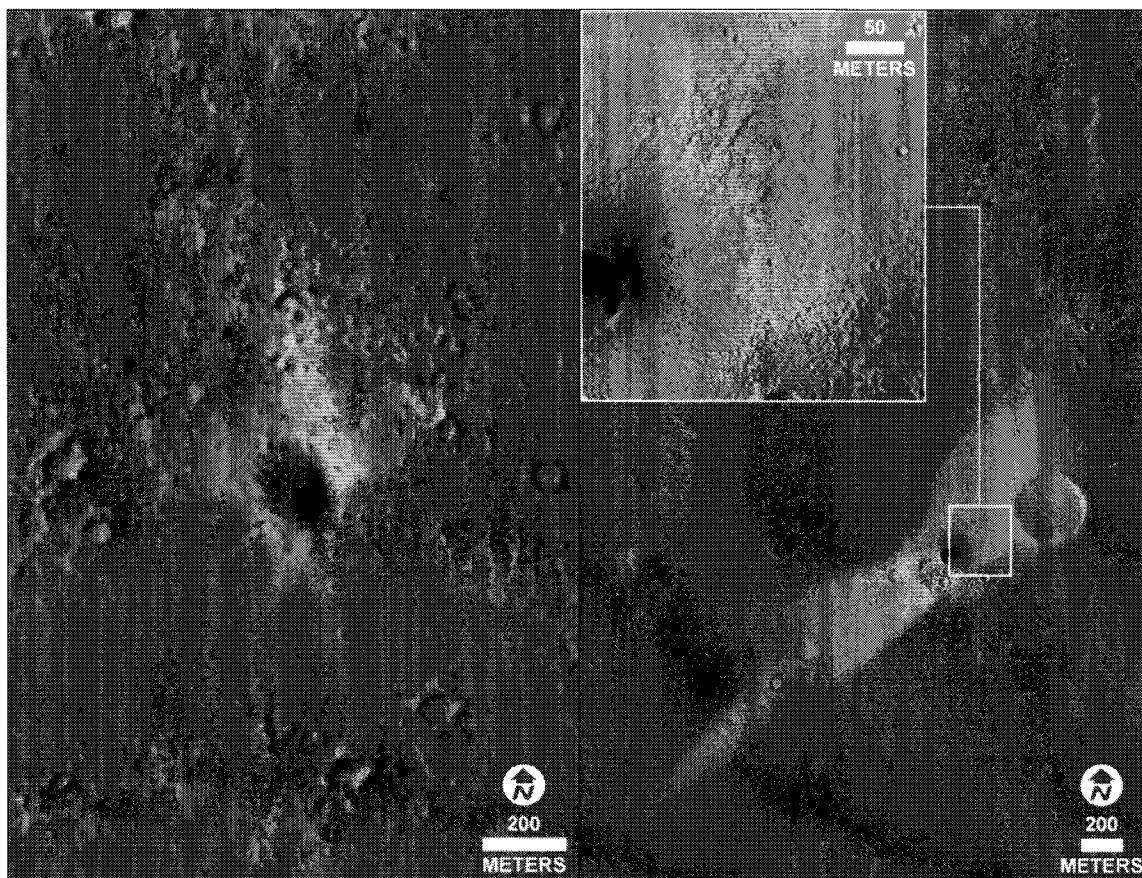


Figure 2.16: Wind-modified secondary craters. (left) Image (MOCNA R0600296) shows significant wind modification of dark and bright ejecta. (right) Image (HiRISE PSP_00681_1935_RED) also shows wind modification; however, the upper inset reveals that the bright wind deposit appears to overlay the ejecta and not modify it. In addition, another secondary to the northeast in Figure 2.16 (right), has no modification, but must have been subjected to the same wind regime, given its proximity. Other larger craters in the HiRISE image (not shown here) have bright crater “tails” which suggests rim (i.e. topographic) height plays a role in inducing bright wind streaks in this area. Background image R0600296 is courtesy NASA/JPL/MSSS and PSP_003172_1870_RED courtesy NASA/JPL/University of Arizona.

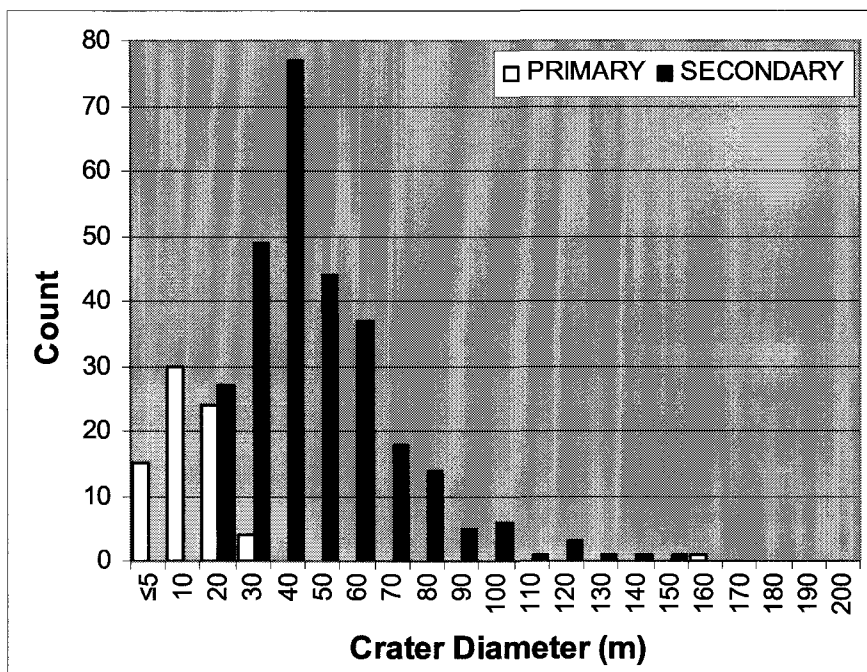
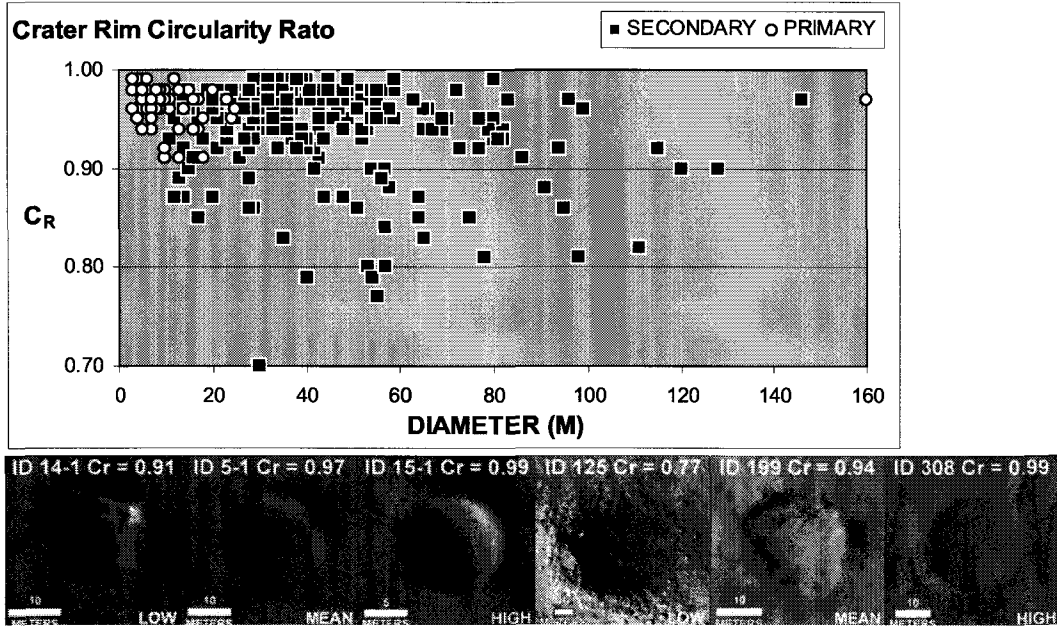


Figure 2.17: Total crater counts binned by crater diameter. These numbers do not represent cumulative numbers or densities of primaries or secondaries, only those selected for this study by diameter bin.

A



B

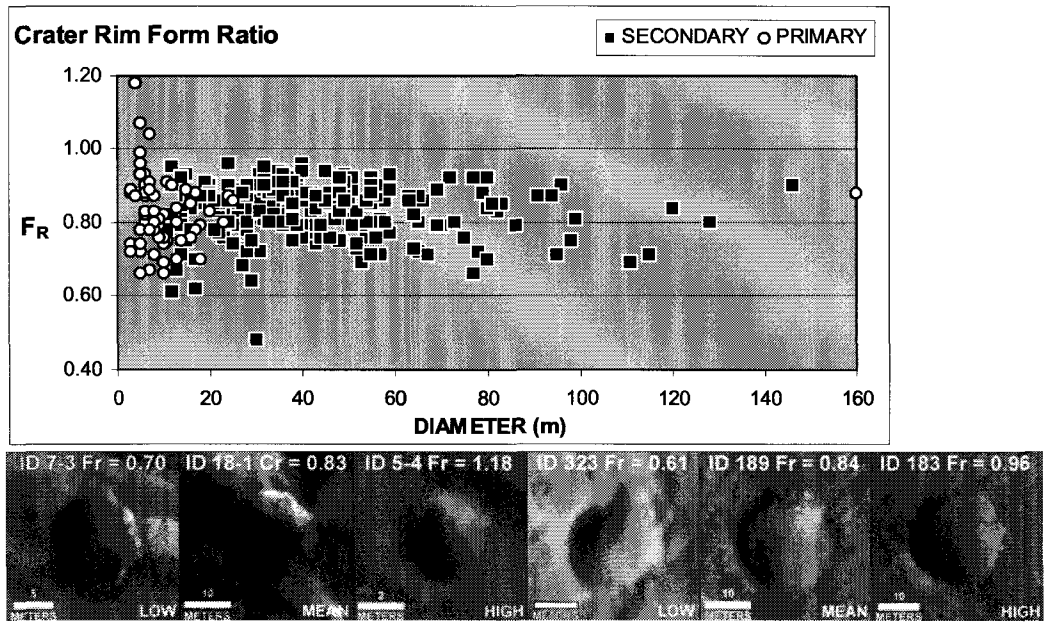


Figure 2.18: (A) Circularity (C_R) and (B) Form Ratio (F_R) results for primary and secondary crater rims. Both ratios have value 1.00 for a perfect circle and deviate from that value as does the planform. While the Circularity Ratio relies on area/perimeter relationships, the Form Ratio evaluates area versus the maximum horizontal length (L) of the planform. Examples for primary (top three crater rim ratios) and secondary (bottom three crater ratios) in Figures 2.18A and 2.18B follow the graphs.

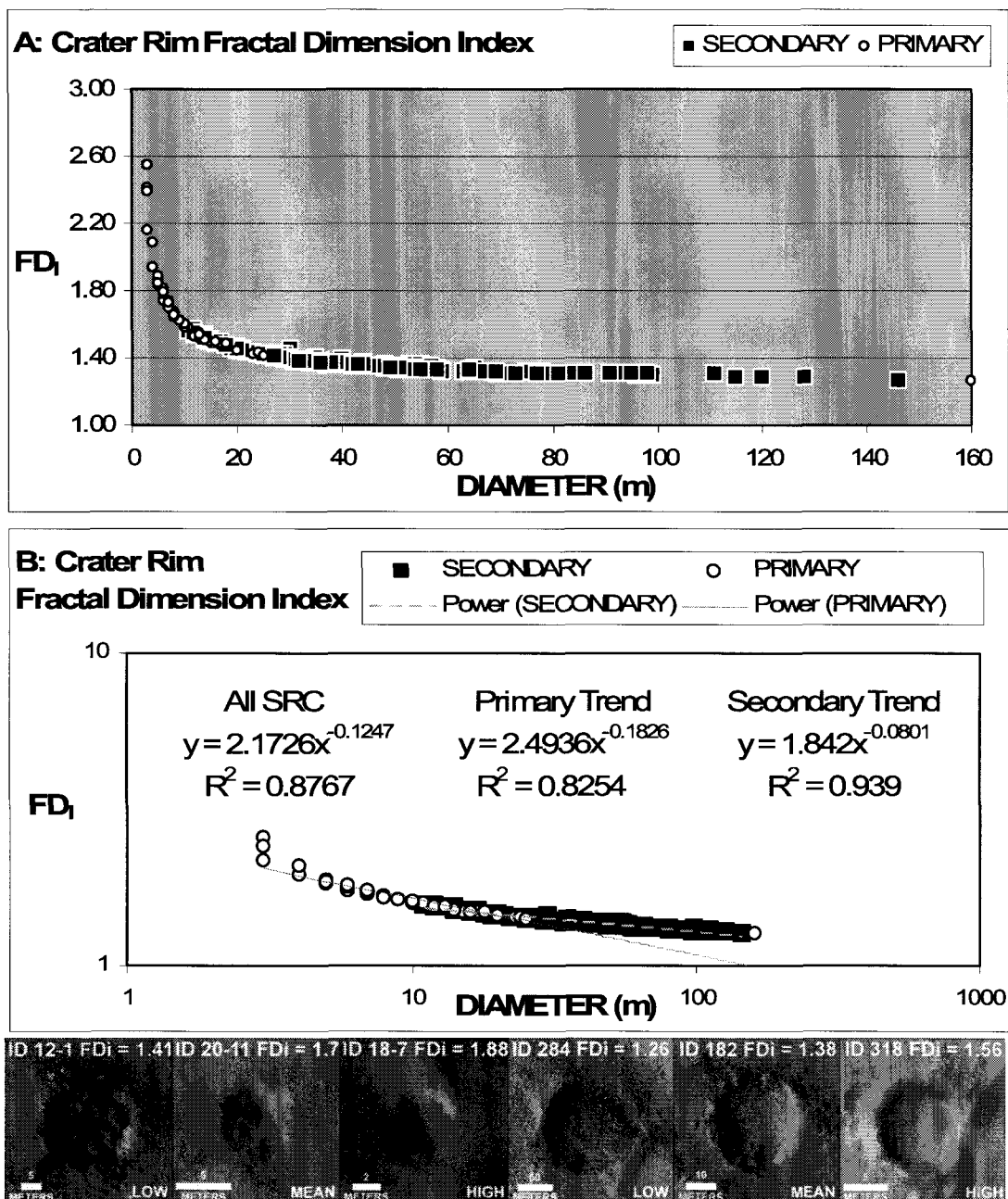


Figure 2.19: Fractal Dimension Index (FD_I) results for primary and secondary crater rims. (A) Note the exponential decay in the index with increasing crater diameter. (B) Graph has the same data plotted in a log-log plot with a power law fitted to the two crater populations. The r^2 values represent the correlation coefficient for the trends. Note the one primary at $D = 160$ m that follows the secondary crater rim FD_I trend. Examples for primary (left three crater rim indices) and secondary (right three crater rim indices) crater rim indices follow the graphs.

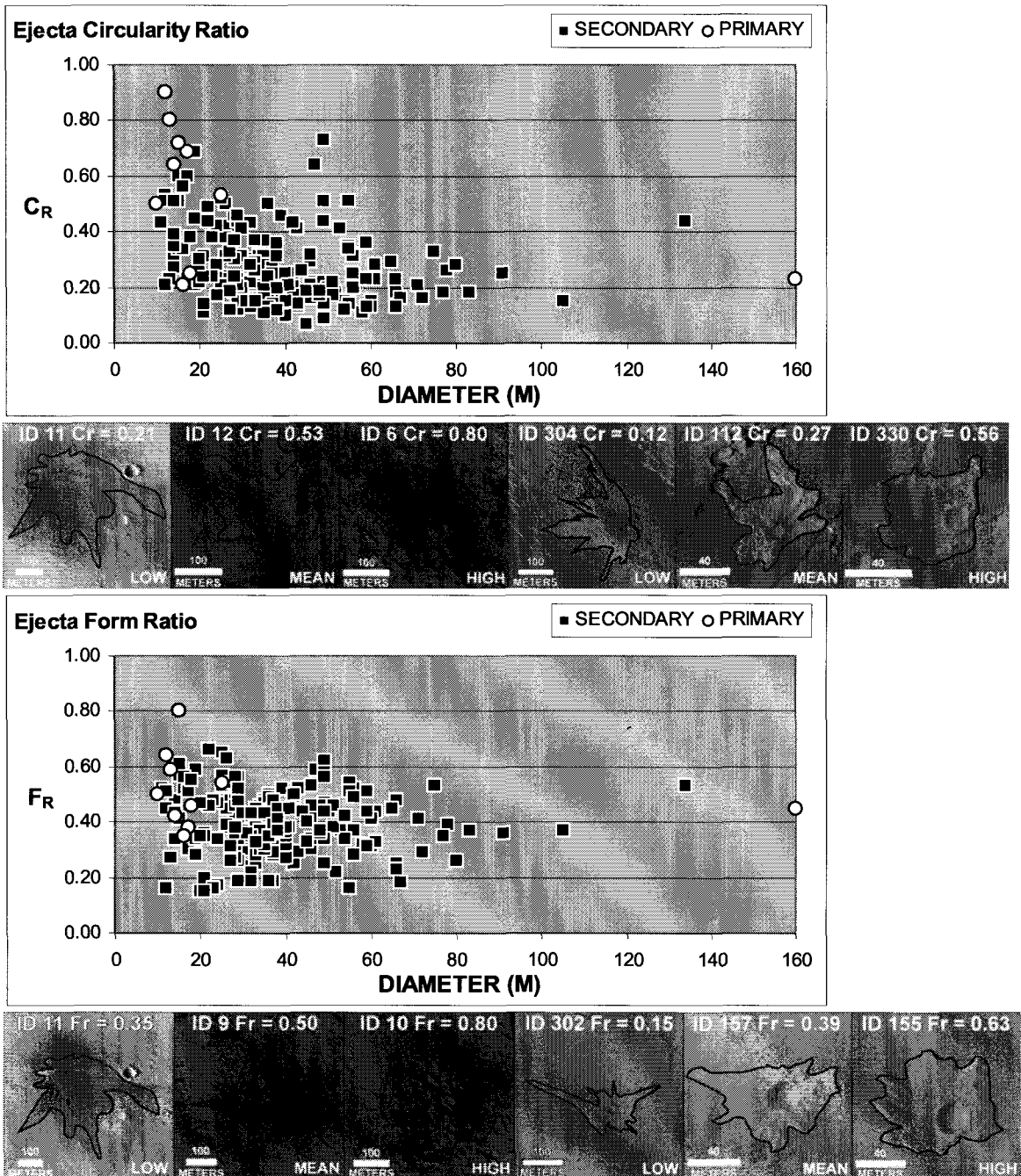


Figure 2.20: Circularity (C_R) and Form Ratio (F_R) results for primary and secondary ejecta planforms. Little to no difference can be distinguished between the two populations with either ratio, although primaries as a whole may have slightly more circular ejecta planforms. Examples for primary (left three ejecta planform ratios) and secondary (right three ejecta planform ratios) follow the graphs.

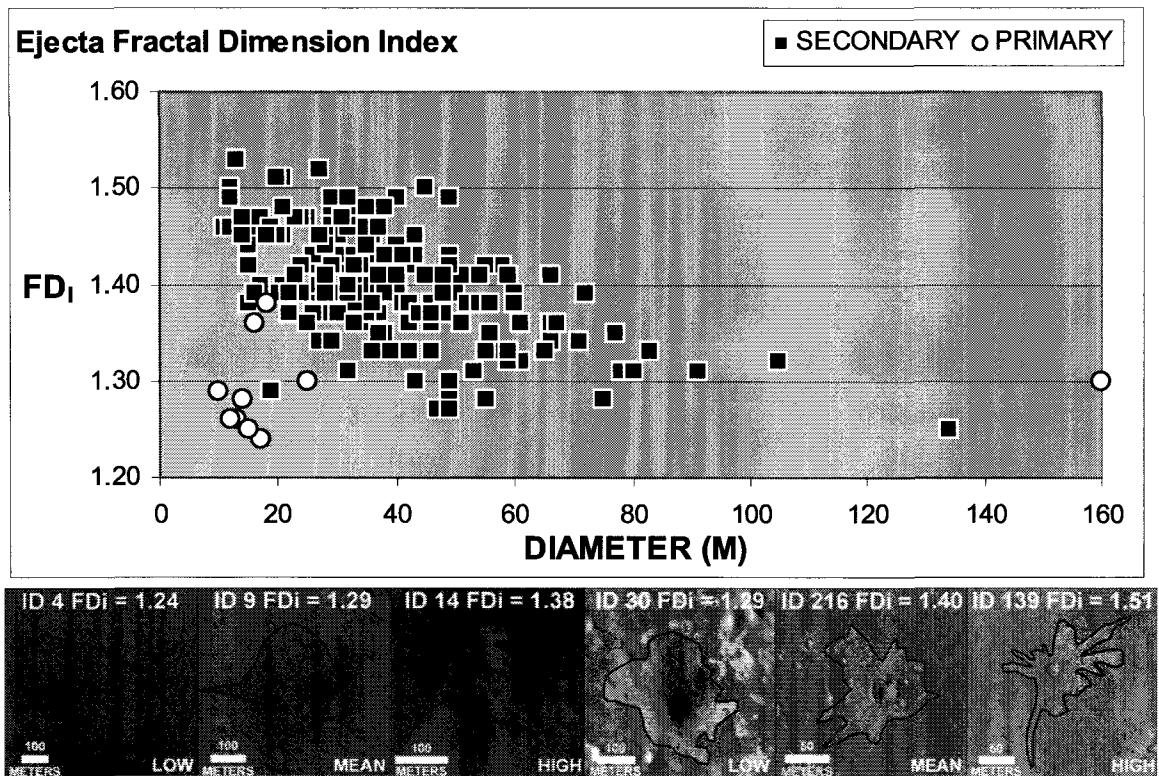


Figure 2.21: Fractal Dimension Index (FD_I) results for primary and secondary ejecta planforms. Note the broad negative trend in the secondary population from small to large diameter craters. Primaries appear to be less “fractal” (i.e., more “regular”) in their planform with the majority of the population below ~ 1.30 . Examples for primary (left three ejecta planform indices) and secondary (right three ejecta planform indices) follow the graphs.

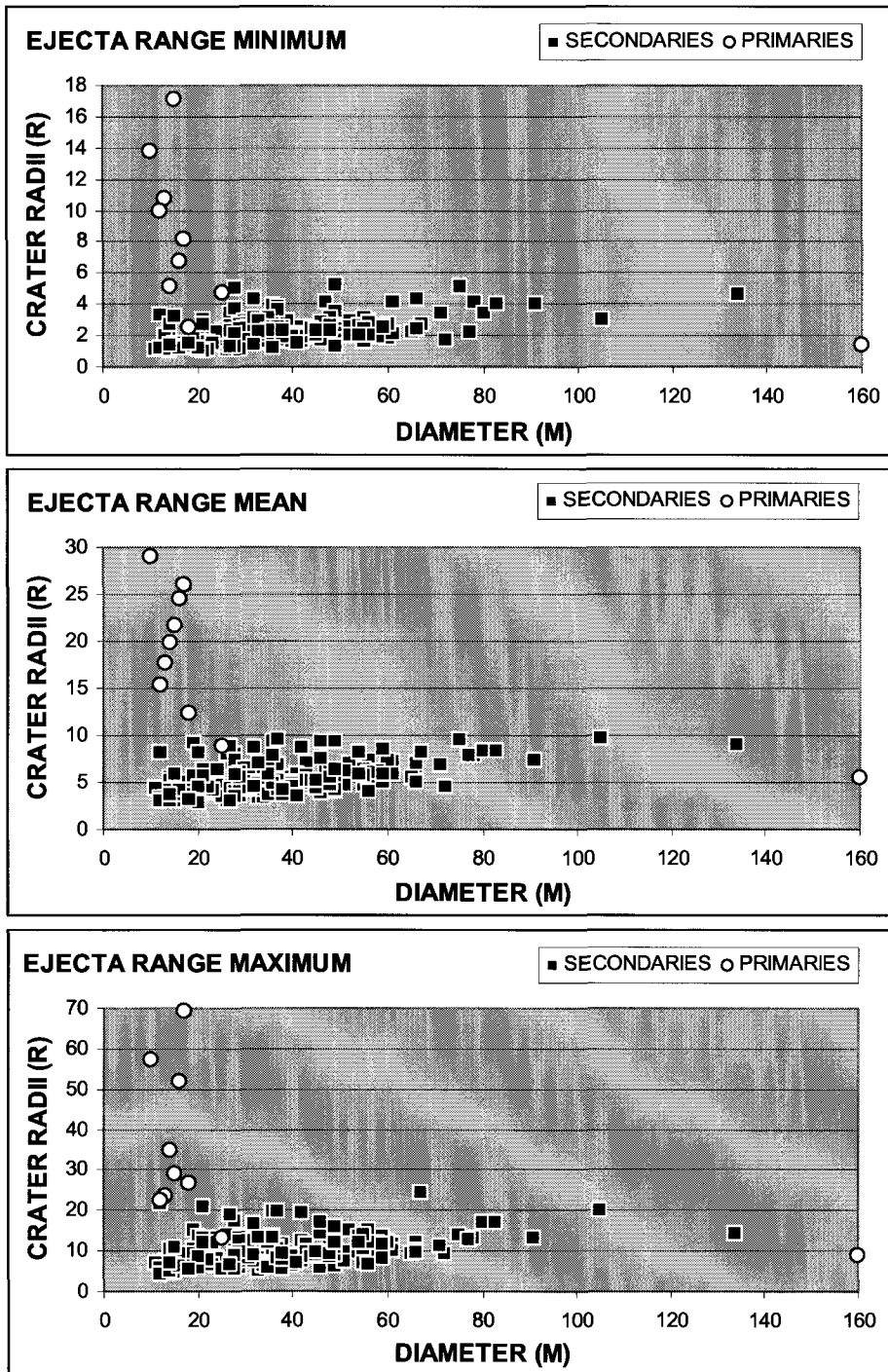


Figure 2.22: Distal ejecta range for primaries and secondaries, normalized by crater radii (R). Note the increased variation for the primaries and uniformity for secondaries at all diameters.

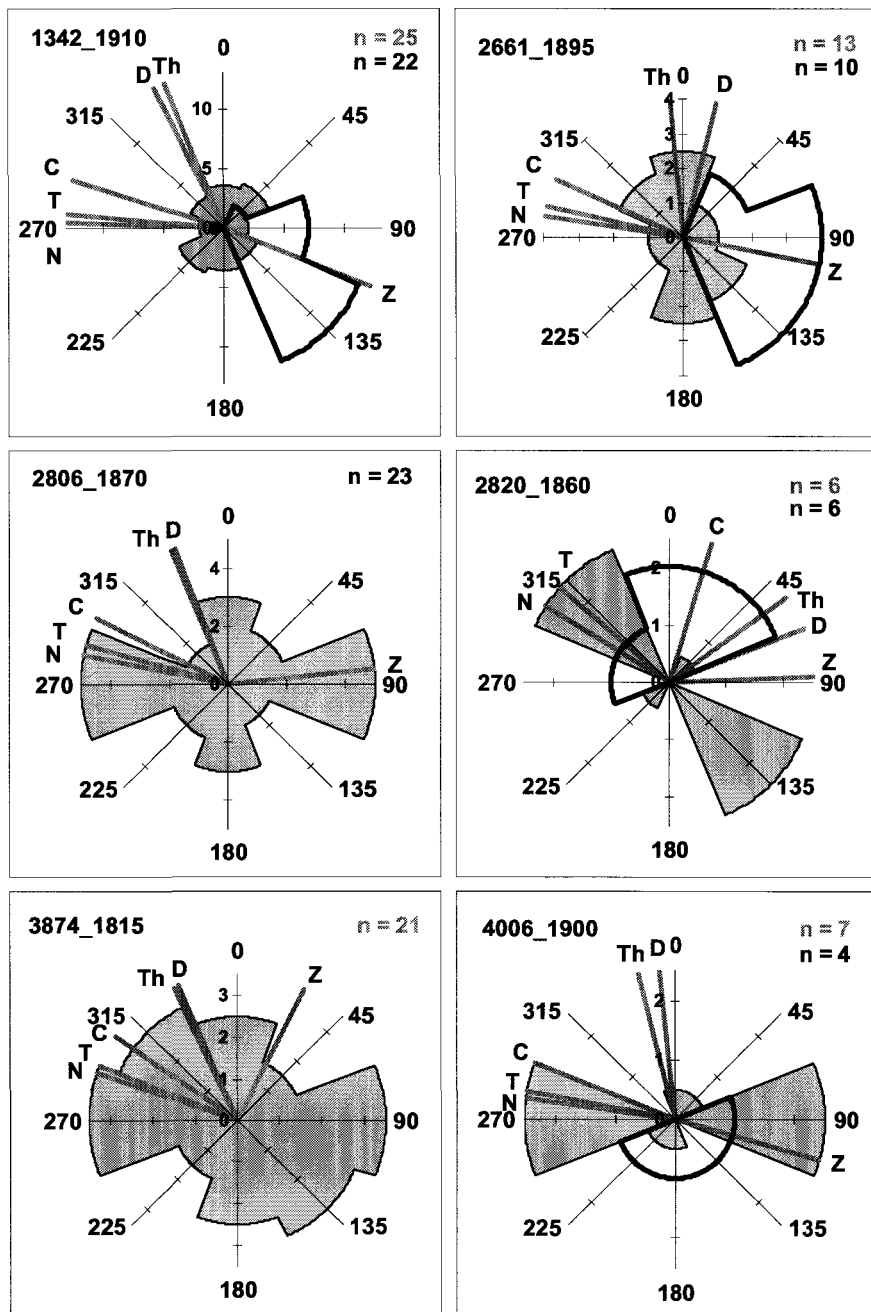


Figure 2.23A: Rose diagrams for crater rim long-axis orientation and ejecta uprange azimuth for secondary craters. Crater rim data in grey, and ejecta data in black. Note crater rim data is either parallel or orthogonal to Zunil, while ejecta predominately point uprange towards Zunil. C, Corinto, D, Dilly, N, Naryn, T, Tomilli, Th, Thila, and Z, Zunil. Image number recorded in the upper left corner of each graph (1234_5678 = HiRISE).

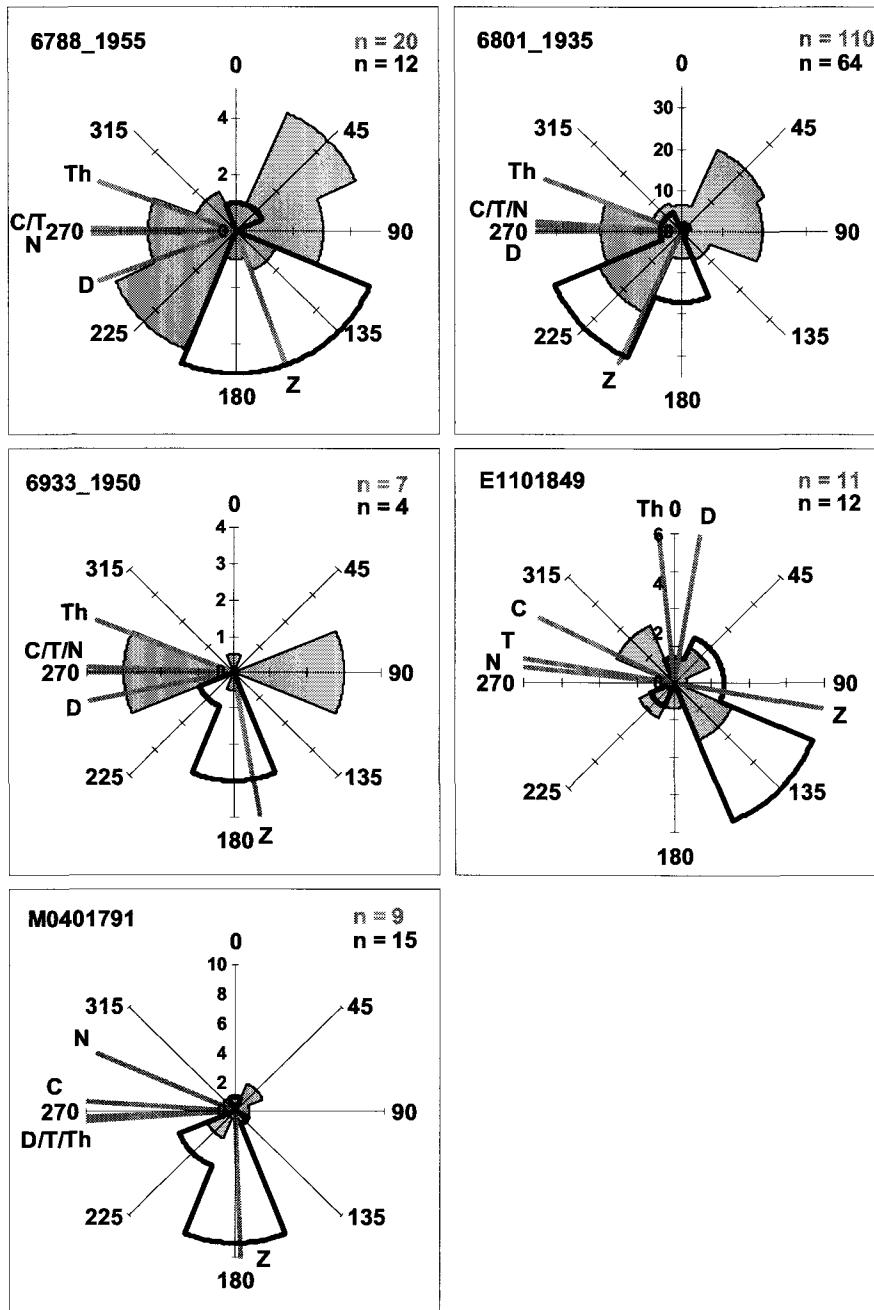


Figure 2.23B: Rose diagrams for crater rim long-axis orientation and ejecta uprange azimuth for secondary craters. Crater rim data are in gray, and ejecta data are in black. Note crater rim data are either parallel or orthogonal to Zunil, while ejecta predominately point uprange towards Zunil. C, Corinto, D, Dilly, N, Naryn, T, Tomilli, Th, Thila, and Z, Zunil. Image number recorded in the upper left corner of each graph (1234_5678 = HiRISE, M1234567 = MOCNA).

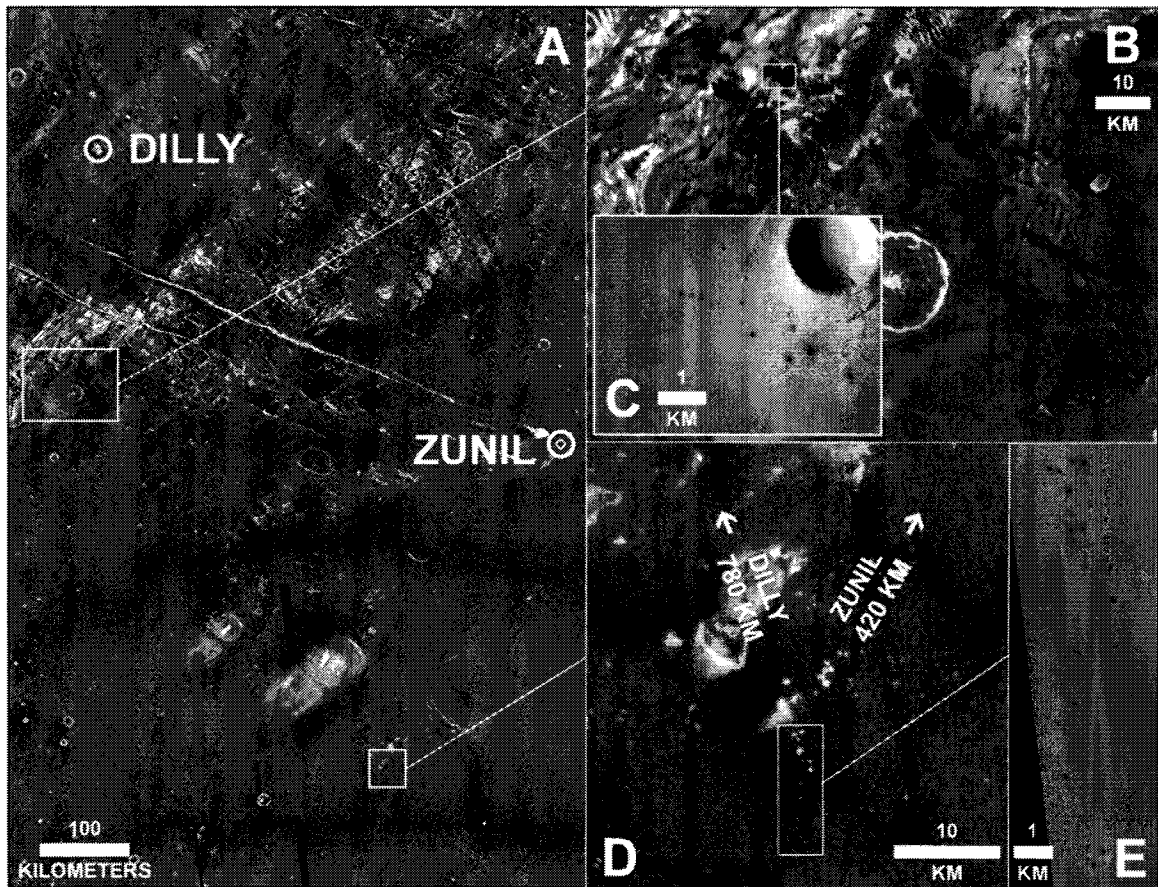


Figure 2.24: Linear orientation of secondary craters near Zunil. (A) Night-time infrared image rayed ejecta containing secondary craters (B and C) northwest and (D and E) southwest of Zunil. Secondary crater chains in Figure 2.24C point relatively in the direction of Zunil, while those in Figure 2.24E have a more ambiguous linear orientation, although they are closer to Zunil. Insets to Figures 2.24C (P06003294_1895_XI_09N203W) and 2.24E (PSP_003874_1815_RED) show details within the ray systems. Images courtesy NASA/JPL/MSSS/Arizona State University/University of Arizona.

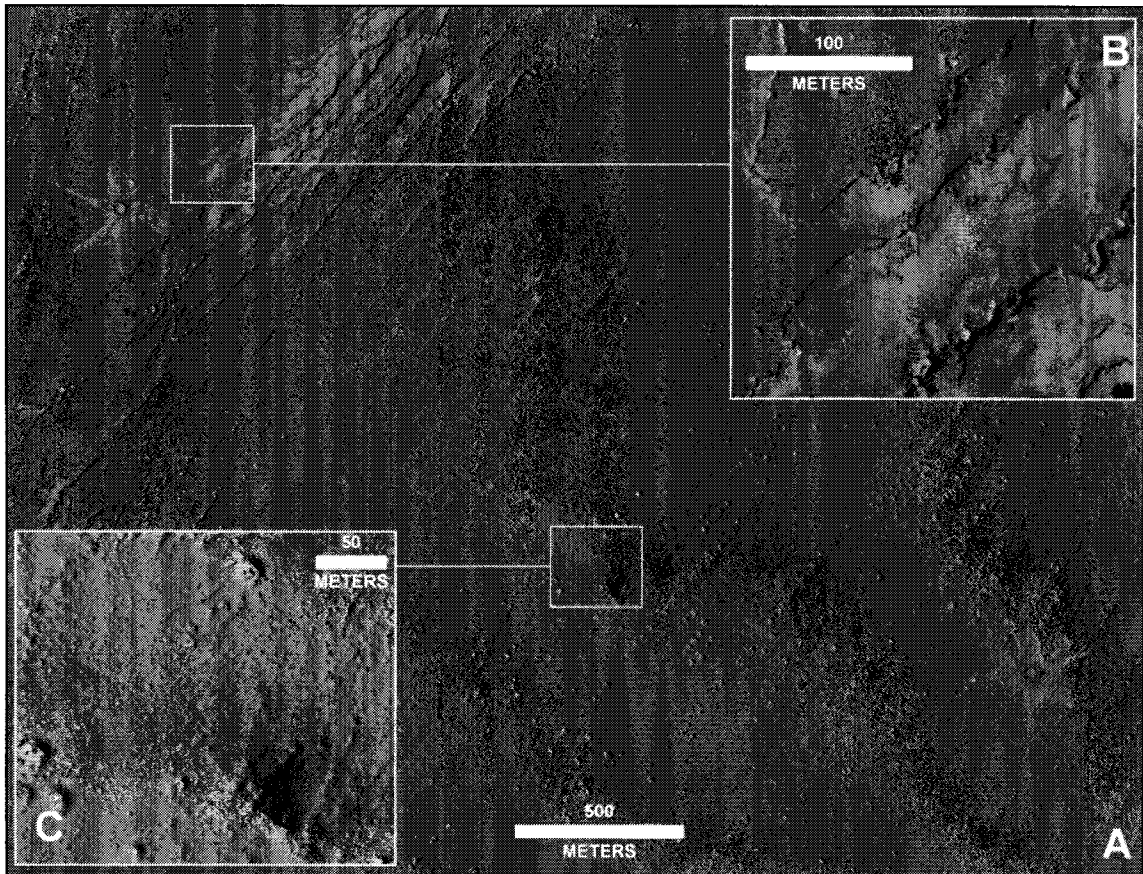


Figure 2.25: SRC of different ages in Elysium Planitia. (A) A darker-rayed crater, possibly a secondary, in proximity to two bright-rayed secondaries presumed from Zunil. All SRC occur over a horizontally uniform target (lava flow). (B) Cliff faces show erosion of bright material of similar tone as the bright ejecta. (C) Close-up of dark-rayed crater reveals ephemeral remnants of bright ejecta with rippled deposits in crater interior. Image PSP_002661_1895_RED courtesy NASA/JPL/University of Arizona.

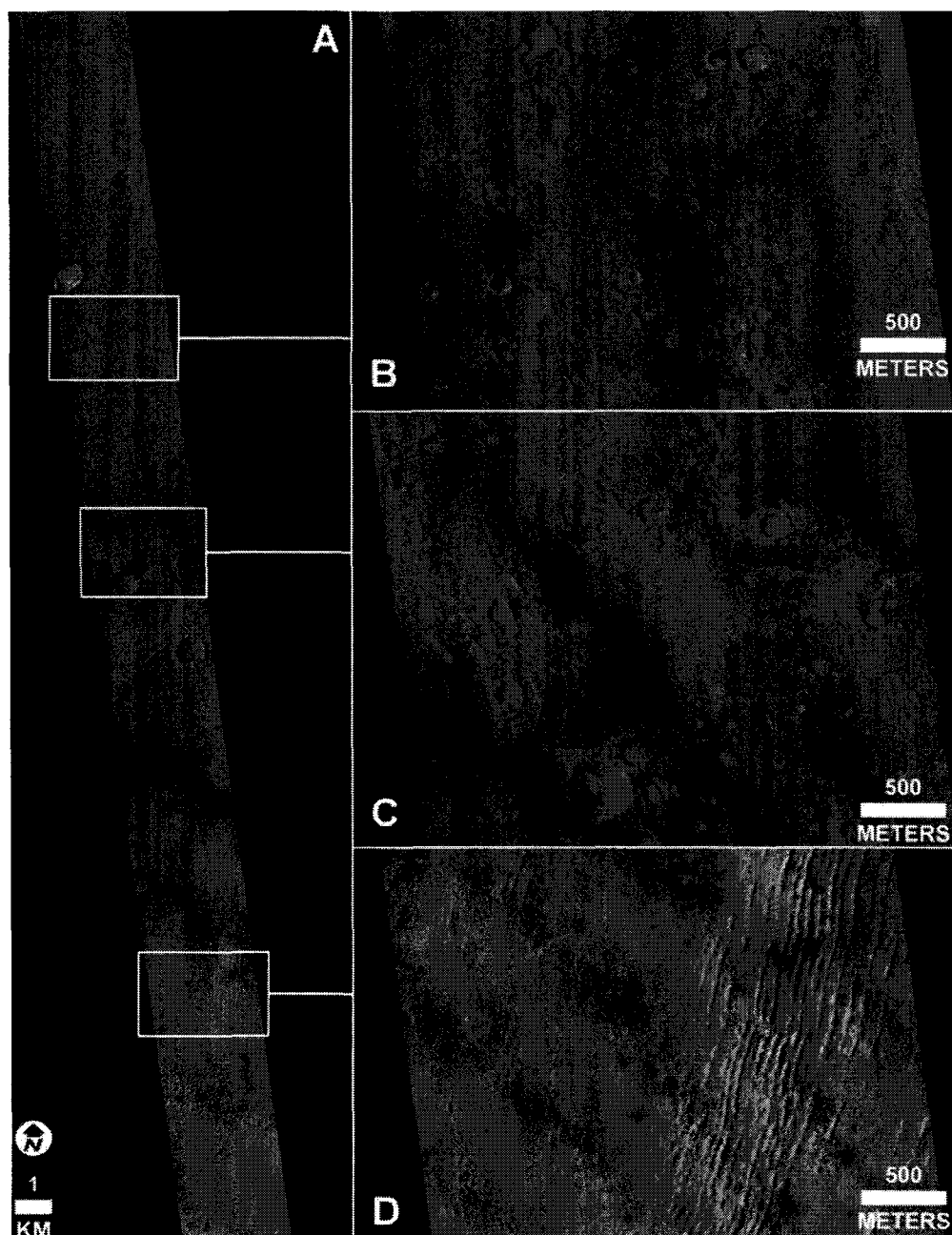


Figure 2.26: Transition from bright-rayed to dark-rayed craters in Athabasca Valles. (A) Several SRC, presumed to be of the same age, occur across a lava flow. (B) Location of dark-rayed craters on a cratered surface in the northern half of the image. A stratigraphically higher lava flow overlays an older basement (lava?) with (C) a diffuse dark-rayed crater right near the geologic boundary of the two units. (D) Bright-rayed secondaries cover the “younger” lava flow and several of its insipient features. Background image M0200581 courtesy NASA/JPL/MSSS.

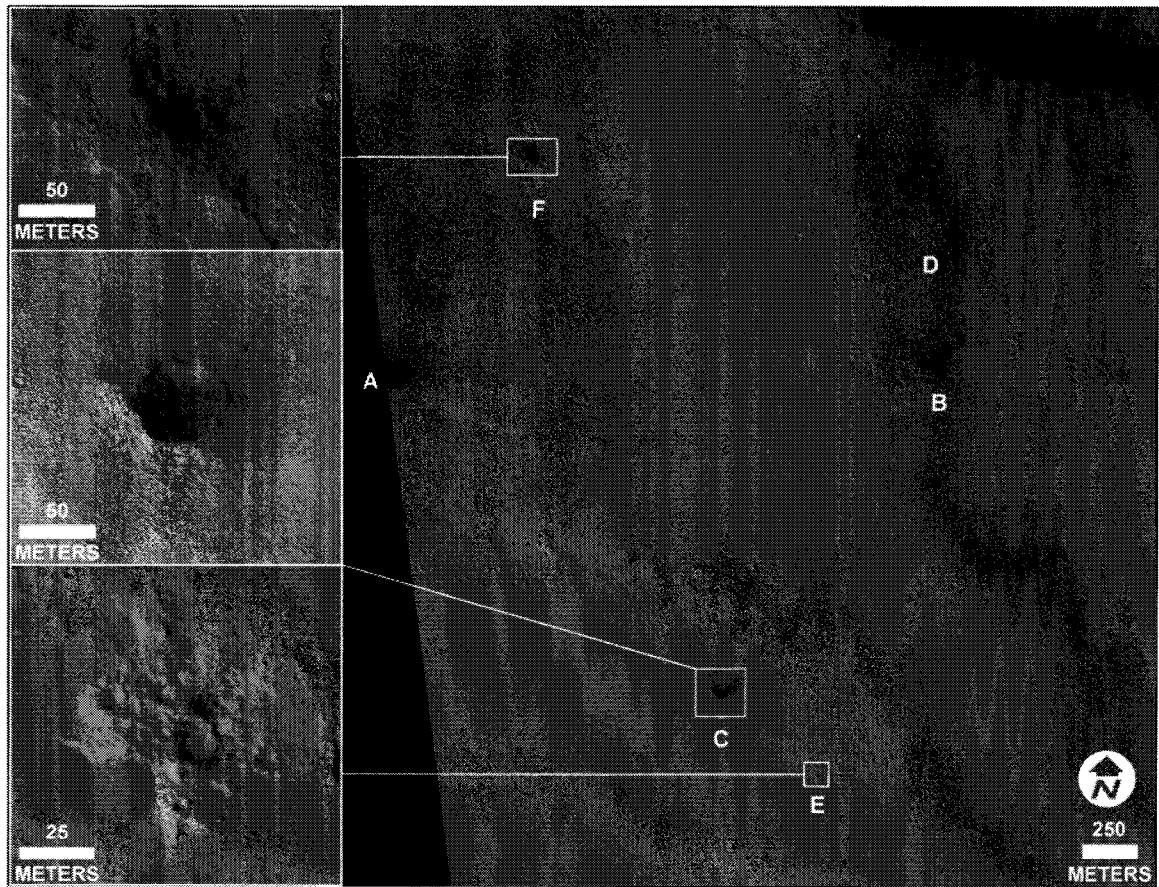


Figure 2.27: Dark and bright SRCs indicating two vertically distinct stratigraphic units. SRC A, B, and C represent craters with diameters $D > \sim 35$ m (60 m, 38 m, and 58 m), while SRC D and E have $D < \sim 25$ m (23 m, 15 m). SRC F, which has bright ejecta with a dark crater floor is $D = \sim 34$ m. Using a typical depth to diameter ratio of 0.2 for simple craters, the transition from bright to dark target material occurs at ~ 7 m. Image PSP_004006_1900_RED courtesy NASA/JPL/University of Arizona.

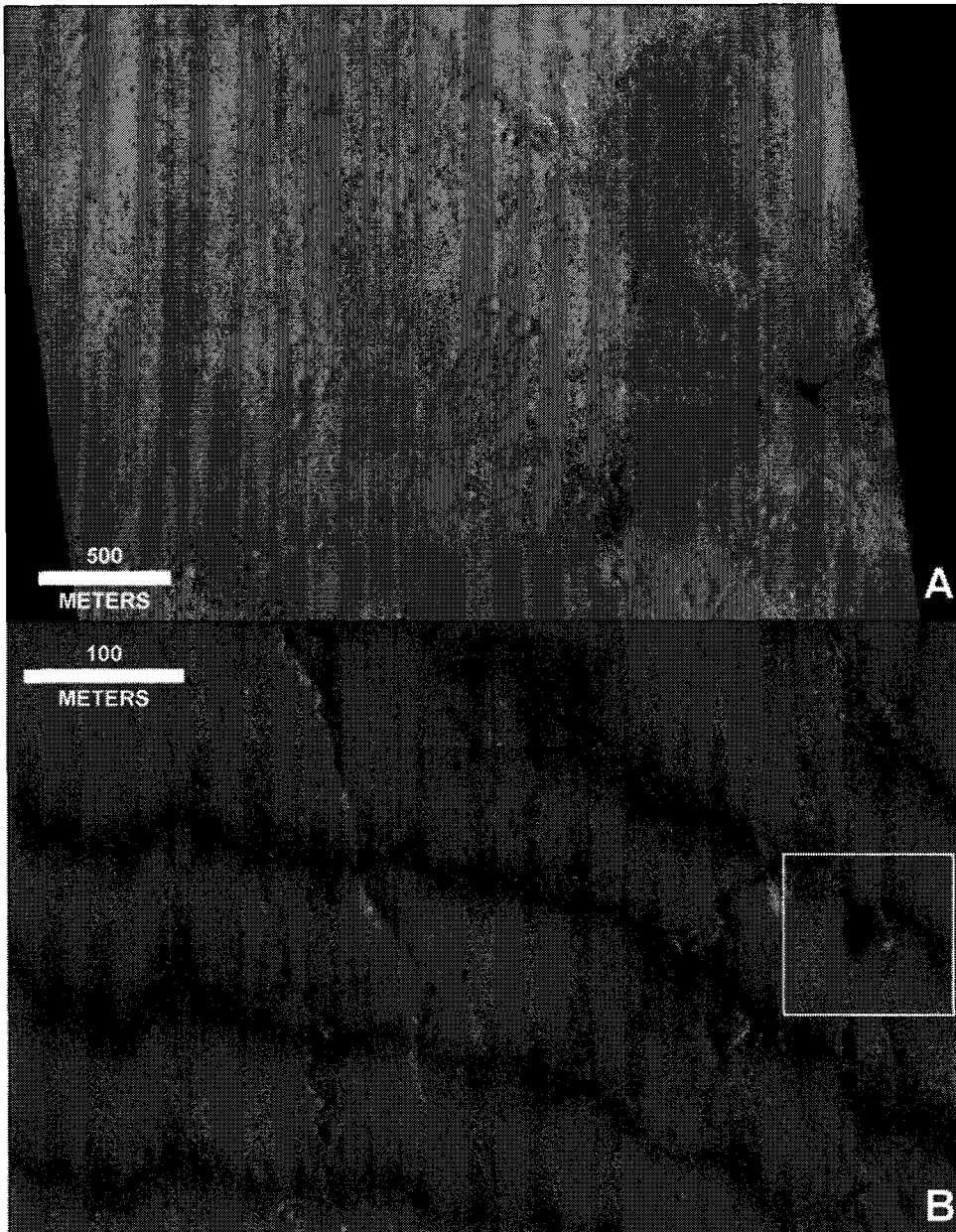


Figure 2.28: Two candidate primaries in the Elysium Planitia region, Mars. (A) A dark rayed crater in image MOCNA R0600296, located at approximately 150°E , 8.27°N . It has a diameter $D < \sim 40$ m and several long, ephemeral dark rays with one extending ~ 2.9 km or ~ 72.5 crater radii. (B) Image PSP_006801_1935 has a four crater cluster spread over ~ 280 m west-east and 120 m north-south. The main crater is at $D = \sim 6$ m and three “child” craters are at $D = \sim 3$ m; the largest crater is smaller than any of the primaries reported by Malin et al. [2006]. Image PSP_6801_1935_RED courtesy NASA/JPL/University of Arizona. Image R0600296 courtesy NASA/JPL/MSSS.

CHAPTER 3:

Global Distribution of Small Rayed Craters on Mars: Sequences of Ejecta Retention¹

ABSTRACT

Small rayed impact craters (SRC), whose diameter (D) is <1 km, should be randomly and monotonically distributed across Mars. Ejecta retention, the capacity of and time period impact excavated material remains in place around a crater, can serve as a proxy to understand global resurfacing rates and recent surficial processes. Ejecta retention depends on two factors: formation, where the target material is more conducive to creating ejecta, and retention, the erosion/deposition rate where ejecta are emplaced.

We surveyed 4,264 panchromatic Mars Orbiter Camera Narrow Angle (MOCNA) images from a global random sample resulting in 200 images with 631 SRC. With a mean $D = 71$ m, most SRC bound the equator between $\pm 30^\circ$ latitude. The paucity of SRC at higher latitudes correlates with near-surface ground ice affecting ejecta formation. Ejecta retention ages in these polar regions are likely an order of magnitude lower than crater retention ages of 1-2 Ma at $\sim 45^\circ$ to 1 ka above 70° latitude. To investigate equatorial retention processes, a t-test for statistical significance of SRC presence/absence versus albedo, dust occurrence, elevation, thermal inertia, and water equivalent hydrogen (WEH) was performed. Statistically significant values were found for albedo, dust, and

¹Calef, F. J. III, R. R. Herrick, and V. L. Sharpton (2010), Global distribution of small rayed craters on Mars: sequences of ejecta retention, prepared for submission in *Icarus*.

WEH. Since albedo is a surrogate for dust content on Mars, dust deposition is the dominant factor in ejecta retention in the equatorial latitudes. WEH's role in ejecta retention is debatable, but correlates with presence of a unique class of excess ejecta SRC.

Two ejecta retention sequences were observed: erosion and deposition. For the erosion sequence, ejecta rays progressively eroded back to the crater rim. In contrast, the deposition sequence preserves ray structure while reducing ejecta contrast over time. Each sequence has four stages representing increasing removal or burial of ejecta until only a few large remnant blocks remain along the crater rim. These sequences represent changing SRC morphology over an estimated hundreds of thousands of years.

SRC origin, as a meteoritic primary or as a low-velocity secondary impact, may affect ejecta retention age calculations. We studied secondary craters around the $D = 10.1$ km primary impact crater Zunil. From observations, we derived a simple power-law for a distance-diameter relationship for the maximum sized secondary crater, D_{maxsec} , as a function of distal radius from Zunil. This allowed us to select those SRC not associated with Zunil and therefore potential SRC primaries. Our results indicate an 11:1 ratio of Zunil secondaries to non-Zunil SRC. Estimates for SRC $D < 125$ m being 95% secondaries may be correct for this region on Mars. Defining diameter-distance functions for other large primaries could provide a key metric for sorting primaries and secondaries for more accurate crater and surface dating.

The global spatial distribution of ejecta retention suggests a change from depositional to erosional processes just south of the Martian equator in southern Arabia

Terra ≥ 100 ka ago that may be indicative of a climate change. Regional ejecta retention studies are warranted for a more controlled understanding of surface processes without target effects.

3.1 INTRODUCTION

3.1.1 Small Impact Craters as Tools for Understanding Current Surficial Processes

Craters predominate as geologic landforms on most terrestrial planets and satellites, including Mars. However, the majority of ejecta associated with both large and small craters on Mars has been reworked, buried or eroded to the point that only the crater rims remain. This is not surprising given the history of fluvial and volcanic processes active during Noachian and Hesperian times, as well as the surmised erosive capabilities of an ancient thicker Martian atmosphere [e.g. Howard, 2003]. In comparison to the first two billion years on Mars, current levels of fluvial and eolian activity are low.

Today, Mars is dominated by sub-kilometer scale geologic processes: mass wasting as seen in dark slope streaks and talus ramparts in steep cliff faces, eolian activity from dust storms to dust devils, the possible fluvial erosion from gullies on the interior of crater walls, patterned ground from near-surface ice, as well as excavation and emplacement of fresh ejecta from new small impacts. The extent of these features is partially determined by their occurrence interval and the erosional/depositional (i.e. retention) history on the surface which they overlie. For example, suspected melt-water gullies on crater rims are time constrained by secondary crater counts on their depositional fans in eastern Promethei Terra from ~1.25 Ma [Schon et al., 2009] to as early as 300 ka based on crater dating of intruding dunes in Nirgal Vallis [Reiss et al., 2004]. While all of these assorted processes provide insight into recent climate changes and current surficial processes [e.g. Head et al., 2003], each of them occurs in particular

geologic settings of limited geographic extent. Indeed, the distribution of gullies are geographically restricted in northern latitudes to 30° - 60° with peaks in occurrence at $\pm 45^{\circ}$ N and nearly exclusive to $>20^{\circ}$ slopes within interior crater rim walls [Kneissl et al., 2009]. This limits their use for broader surficial morphologic studies.

On the other hand, cratering is a ubiquitous geologic process across Mars. Ejecta from these craters, while extant, records the most recent erosive and depositional processes. As one can imagine, the time that ejecta remains visible around its originating crater (i.e. ejecta retention) must vary with substrate and changing climate conditions (e.g. wind speed) over time. As a direct result, ejecta morphology should be modified differentially with varying atmospheric states. Thus, ejecta morphology may serve as a proxy for changes in ejecta retention processes over time as it is transformed from its pristine initial ballistic emplacement to some degraded shape. Studying the spatial heterogeneity and subsequent degradation of small (diameters, $D < 1$ km) rayed impact craters (SRC) on Mars can provide unique insights into these surficial processes on a planet-wide scale. The absence or scarcity of SRC would indicate either rapid removal or a target surface not conducive to rayed ejected formation. In contrast, increased presence portends either increased ejecta retention (i.e. less erosion/deposition than other areas) or more favorable physical parameters for ejecta formation. One significant concern in extracting retention information is the origin of the SRC population, whether as spatially independent (i.e. random) meteorite impacts or as “statistically clustered” (i.e. non-random) secondary impacts from larger primary cratering events [McEwen et al., 2005]. Distinguishing between these two SRC populations would play a significant role in

deciphering ejecta retention in separate locations, deducing the responsible processes, and the timescales they operate on.

3.1.2 The Effects of Secondaries

Secondaries are those craters formed from the impact of large ejecta blocks from a larger diameter (several kilometer) primary crater. A population of secondaries from a recent large primary, such as the $D = 10.1$ km Zunil, can distort our assessment of SRC distribution by overpopulating a surface with numerous secondary-derived SRC. These SRC are all of one age and should have relatively uniform retention characteristics. In contrast, primary SRC collected on a surface may record changes in both the cratering rate and the temporal dynamics of retention (e.g. changing from a dust deposition to an erosion dominant process). However, identifying secondary impacts outside of the obvious ones within rays of known large primaries, like the impact crater Zunil, is a difficult task.

Several attempts have been made to identify secondaries from primaries based on their crater morphology. Secondary crater depth to diameter ratio (d/D) is approximately half the value compared to primaries on both the Moon [e.g. Pike and Wilhelms, 1978] and Mars (e.g. ~ 0.11 for assumed secondaries in McEwen et al. [2005]; 0.1 for ‘hollows’ in Golombek et al. [2006]; ~ 0.26 from shadow measurements of confirmed new primaries in Daubar and McEwen [2009]). However, target properties may greatly affect this ratio as it has been shown that some obvious secondaries are not so shallow [Calef et al., 2009]. Another geometric property like rim height to diameter (h_{rim}/D), while

appearing diagnostic of secondaries on the Moon (~ 0.02) [Pike and Wilhelms, 1978], is less so on Mars (~ 0.03 , just less than 0.04 for lunar primaries) [McEwen et al., 2005]. Ejecta thickness models for primaries based on experimental and lunar observational data [McGetchin and Settle, 1973], as well as from Martian elevation measurements [e.g. Garvin and Frawley, 1998], exist, but typically for $D > 1$ km craters. Some experimental work on low-velocity [e.g. Hartmann, 1985] and low-angle impacts [e.g. Gault and Wedekind, 1978] tend to indicate thicker, less distal ejecta and unique crater interiors (e.g. lower uprange rim elevation), that could be indicative of the lower velocity expected for secondary cratering (as argued by McEwen et al. [2005] and references therein). One caveat is target effects from different materials (e.g. regolith vs. bedrock) that appear to affect crater growth [e.g. Hartmann, 1985, Garvin et al., 2003]. For the Moon, it has been shown that the mean block size ejected from a crater should be greater around secondary crater rims as lower shock pressures (i.e. lower velocity impacts $< 2 \text{ km s}^{-1}$ compared to primaries at 19.2 km s^{-1}) generate smaller stress gradients resulting in larger fractures sets producing larger blocks for comparable crater sizes [Bart and Melosh, 2007]. However, when applied to Mars, differences in K values (the factor in the block size to crater diameter relationship) for secondaries were found to be only 30% higher than for primaries compared to a 60% difference on the Moon [Bart and Melosh, 2007]. Suspected explanations for the disparity includes a lower difference in peak shock pressures by a factor 3 greater for primaries than secondaries on Mars, but a factor of 40 difference on the Moon, and/or a difference between cratering in the strength regime for the craters studied on Mars versus gravity regime craters examined on the Moon [Bart

and Melosh, 2007]. Thus this metric was considered inconclusive as a useful parameter for distinguishing Martian crater origins.

Secondary cratering has also been shown to follow a size-velocity, hence diameter-distance, relationship on several terrestrial bodies. Melosh [1984] evaluated several ejection models to determine whether ejecta blocks could reach escape velocities without evidence of high-shock pressures, as are common in some Martian meteorite finds. It was found that spall, the earliest, largest and least shocked material ejected from the surface layer of a target, decreased in size (i.e. mass), but increased in velocity with distance away from the impactor [Melosh, 1984]. This was confirmed for twelve craters on Mercury, the Moon and Mars, collectively, by plotting ~25,000 secondary crater diameters converted to ejecta fragment sizes via scaling laws [e.g. Schmidt and Holsapple, 1982] versus velocities calculated via a ballistic range formula for spherical bodies from the secondaries to the suspected primary crater center [Vickery, 1987]. Results showed that the maximum secondary crater diameter (expressed as the fragment size) decreased with increasing distance (shown as velocity) from the primary crater according to a power-law:

$$D_{max} = v^{-\beta} \quad (3.1)$$

where D_{max} is the maximum fragment diameter, v is impact (and assumed launch) velocity and β is the power-law exponent that fit the data via a least-squares method [Vickery, 1987]. The maximum fragment size for Martian secondary craters, and hence

maximum crater diameter, decreased with increasing distance (i.e. velocity) for four different Martian craters ranging from the 227 km diameter Lyot down to the crater named Dv at $D = 26$ km with a concomitant increase in β (though not perfectly) from -2.57 to -1.46 [Vickery, 1987]. A similar example has been shown for Zunil where the largest mapped secondary craters decreased with increasing distance along Zunil's western ray system [Preblich et al., 2007]. This means that beyond a certain range from a primary, one can expect only secondary craters of a certain maximum diameter; further away any crater larger than this diameter must be from another source. We can use this relationship to filter SRC secondaries beyond a radial distance from a primary crater, if we know the primary crater's diameter-distance (i.e. size-velocity) parameters.

3.1.3 Research Goals

From our global survey of SRC on Mars (e.g. Figure 3.1), we plan to infer the general reasons behind SRC occurrence or absence, as well as to understand variations in their morphologic appearance. Where SRC are present, can we deduce the processes responsible for the spatial patterns observed? Ultimately, SRC may provide an understanding of active global surface processes and morphologic variability on Mars both today and in the recent past.

3.2 METHODOLOGY

3.2.1 Image Sampling

We searched a 5% random sample of Mars Orbiter Camera Narrow Angle (MOCNA) panchromatic images, 4,264 in total, covering the timespan of over two Martian years for all orbits up through and including Mars Global Surveyor (MGS) mapping subphase S10. Image pixel sizes ranged from 1.35m to 15.3m with an average of 4.8m, while image areas varied from 1km² to ~1400km² with an average of 77km². In terms of our sample size, the distribution of images by pixel size, longitude, and latitude for the sample and total MOCNA database are nearly identical (Figure 3.2). No filtering of images based on image pixel size or area were performed, assuming these variables will have a nominal effect on the number of rayed craters found over thousands of images viewed. In fact, the average sample pixel size and area for all MOCNA images were nearly identical to the smaller 5% sample. Using 4 pixels as the minimum for measuring crater diameters, we expect to be able to identify craters down to ~19m across in most images. Rayed ejecta allows us to identify some SRC below the pixel resolution of the crater diameter, but we've excluded those to provide more robust information in our database. Since MOCNA images are targeted and non-random at the global scale, we evaluated our 5% sample against the Martian surface by comparing both the global elevation (Figure 3.3) and geologic age unit distribution (Figure 3.4) versus the total footprint area from our selected images. On Mars, ~91% of surface elevations fall between -4km to 3km; our image areas averaged within ~11% of this range per kilometer bin. Elevations below -4km (e.g. the northern plains or Hellas Basin) and above 3km (e.g.

the Tharsis Bulge) were mostly oversampled. Consequentially, both Noachian and Hesperian units, which are emplaced mostly in the mid-elevations, were undersampled by ~18% and ~14%, respectively and Amazonian units oversampled by 38%. Due to this image distribution, there might be an oversampling of SRC in younger geologic units and extreme elevations with undersampling in older units within a few vertical kilometers of the zero elevation on Mars.

For each image in our sample, we recorded the presence or absence of a SRC. If an image contained a SRC, that image was radiometrically corrected (level 1) and map projected (level 2) in the Integrated Software for Imagers and Spectrometers (ISIS). Every SRC with a diameter down to the resolution limit (4 pixels or $D = 19$ m) of each image was counted. Each SRC had the following data recorded: longitude, latitude, crater diameter, minimum and maximum radial distance of the continuous ejecta, radial distance of the longest ray found, the ejecta contrast relative to the background surface (dark, bright, bimodal – two or more contrasts, or neutral – only the edge of ejecta was discernible from shading) and probable impact angle, using the same criteria as Calef et al. [2009] when possible. All distance measurements are in meters, though we will normalize ejecta data to crater radii.

The SRC image distribution, as well as the database of formation, crater, and ejecta parameters, should provide sufficient qualitative and statistical information on the spatial distribution and ejecta retention for SRC across Mars.

3.2.2 Hypothesized Ejecta Retention Models

Ejecta will persist at a crater for a time period that depends on two factors: formation, where the target material is more conducive to creating rayed ejecta; and retention, the erosion and/or deposition rate (i.e. resurfacing) at the ejecta location. Without a thorough understanding of the mineralogical and structural context of the target material on which an impact crater resides, hypothesizing the role of formation in ejecta retention can be difficult. As for retention, we infer two models for ejecta: a deposition model and erosion model. The deposition model assumes dust is deposited at a constant rate over the surface of the ejecta until such time that it is completely buried up to the crater rim. In this scenario, one would expect to see the ejecta tone uniformly brighten or darken to match the surrounding depositional dust reflectance. Any blocks larger than the dust thickness may create nunatak-like projections, especially near the rim where the largest blocks should reside. Asymmetries in ejecta thickness may produce similar ridges radial to the crater rim above the surrounding dust mimicking the once distal rays. Given the relatively shallow depth of the ejecta layer compared to crater depth, one would expect the ejecta to be buried well before the crater would infill to the crater rim, though the crater floor should be relatively flattened by this deposition. In the erosional model, ejecta erodes back towards the crater rim at a rate equivalent to the erosion rate as a function of ejecta layer thickness. Since ejecta layer thickness decreases rapidly (as a power law) with distance from the crater [McGetchin et al., 1973] and blocks become progressively smaller, more distal ejecta should erode more quickly, initially via wind uplift and saltation, followed by slower erosion of proximal near-rim

ejecta (i.e. the continuous ejecta blanket) by ventification (i.e. sand-blasted by sediments in the wind); wind being the dominate erosive process currently on the planet [Greeley, 2004]. Similar to the morphology model proposed by Moore et al. [1980] for small lunar craters, ejecta rays would shorten and thin over time until reaching back to the continuous ejecta blanket that would then erode to the crater rim. Fine, spikey ejecta would erode back to create more rounded forms where the ejecta are thicker and more resistant to the wind. Experiments have shown fine-sand is the dominant size for wind uplift, while smaller and larger particles are harder to move [e.g. Greeley et al., 1976], thereby this fraction of the ejecta would be expected to disappear before others. Dust devils can remove dust-sized particles due to their excessive negative pressure within the vortex core as they pass over dusty surfaces [e.g. Balme and Greeley, 2006]. Given that dust devils are prominent over many latitudes of Mars, we expect ejecta to rapidly erode back to the point where particles larger in size than fine-sand are dominant. Given this state, one would expect long rayed craters to be few with increasing numbers of SRC at the point where simple removal of ejecta transitions into downward erosion of larger ejecta blocks. This assumes produced craters are all of the same diameter range (i.e. similar impact energies), impact at similar angles, and have similar target properties (e.g. yield strength, particle size, etc.). With decreasing crater diameters, ejecta will be thinner closer to the rim; smaller craters can be expected to retain ejecta for shorter time spans. Again, large blocks near the rim will be the last remaining remnants to erode and leave a ring of blocky ejecta at the final stages of retention. At high latitudes, periglacial processes may cryoturbate ejecta in place. If ice was near the surface, ice-ejecta (where

the major constituent of ejecta is ice) may quickly sublimate and leave little solid material left after a short period of time (as seen in recent mid-latitude rayed craters by Byrne et al. [2009]).

We make the following additional assumptions: the cratering rate in the $D < 1$ km range is equivalent over all surfaces of Mars, the majority of impacting craters in this diameter range will be regolith-based, and impact velocities are all close to the average of 10 km s^{-1} for Mars. One can hypothesize that an older retention age denotes more preservation of rayed ejecta around smaller diameter craters (i.e. thinner ejecta experiences less reworking, because there is less erosion/deposition on average), while younger retention ages preserve only larger diameter rayed craters (i.e. only thick ejecta blankets will remain extant on the surface under high rates of erosion/deposition).

We examined our SRC images for these characteristics and attempt to verify our models by classifying the SRC to them. For validation, graphs of ejecta radii were created to visualize frequency of morphology types that fit our hypothetical models. One should expect to see shorter rays over time in an erosional environment or in a depositional dominant model, more consistent ray lengths with ejecta tone increasingly approaching the mean background tone.

3.2.3 Surface Property Statistics

For each image centroid, we recorded the geology (from Skinner et al., [2006]), thermophysical units (as defined by Mellon et al. [2000]), and gridded elevation from the Mars Orbiter Laser Altimeter (MOLA) [Smith et al., 1999]. Thermophysical units were

reconstructed with the most recent thermal inertia calculations from Putzig and Mellon [2007]. Three additional surface properties were measured from derived datasets from the Mars Global Surveyor Thermal Emission Spectrometer (MGS-TES): albedo (the calibrated radiance times the square of the Sun-Mars distance divided by the cosine of the incidence angle times the solar radiance integrated over the spectral response of the recording instrument) [Christensen et al., 2001], thermal inertia (in units of *tiu* defined in standard international units as $\text{J m}^{-2} \text{K}^{-1} \text{s}^{-1/2}$) [Putzig and Mellon, 2007], and a dust cover index (DCI) [Ruff and Christensen, 2002]. Our goal by sampling these properties is to gain an understanding of the role that the underlying target or formation may play in ejecta retention. To determine any significance of SRC occurrence in an image based on each of these parameters, we will conduct a Student's t-test to compare, for example, whether certain thermal inertia values tend to be more associated with SRC occurrence. This statistic requires a nominal variable (to parse out two sample groups) and a measurement variable (a numeric value, such as elevation). Means between the two sample groups are compared to determine whether they are similar (have comparable means) or represent different groups of values. Two sample groups were formed using SRC presence (1) or absence (0) as our nominal variable from images searched in this study. Our null hypothesis (H_0) will be that there is no difference in a physical property (e.g. mean albedo is the same) with SRC occurrence versus absence in an image. The alternative hypothesis (H_A) indicates a preference for a certain physical property value, in regards to the t-test, a significant difference in mean value for the SRC sample group compared to the non-SRC image group. We set our alpha equal to 0.05 for a 95%

confidence interval (i.e. only a 5% chance that we have a Type I/false positive significant result). The t-test requires an understanding of the variance of each population; therefore we checked each sample group using an F-test (alpha equal 0.05) to evaluate whether the two sample groups had equal or unequal variances. When the two population variances were equal, we used a pooled-variance t-test, otherwise a separate-variance t-test was performed. We generated boxplots comparing images with and without SRC to make non-parametric comparisons between the datasets to evaluate our statistical results.

3.2.4 Correcting for Secondary Impacts: a case study of the large primary crater Zunil

For the crater Zunil, the largest rayed secondary found was $D = \sim 230$ m. The largest mapped secondaries were found to follow an approximate inverse diameter-distance (and therefore fragment size-velocity) correlation out to ~ 1750 km where the largest secondary was 50 m in diameter [Preblich et al., 2007]. These diameters are well below the range of D_c values estimated by McEwen et al. [2005]. By fitting a line to measurements of the maximum secondary crater diameter versus radial distance from Zunil (data from Preblich et al. [2007]), we find a strong linear correlation between secondary crater maximum diameter, D_{maxsec} , and distance, r , from the crater rim (Figure 3.5):

$$D_{maxsec} = -0.1244r + 260.35, \quad R^2 = 0.94 \quad (3.2)$$

where r is in kilometers and D_{maxsec} is in meters. Solving for r , we can then calculate the maximum distance, r_{max} , beyond which a secondary of this diameter, according to the size-velocity law, should not be found:

$$r_{max} = (D_{maxsec} - 260.35)/-0.1244 \quad (3.3)$$

where $r_{max} \leq 0$ was ignored as the primary could not produce a secondary crater of this size. We calculated r_{max} for D_{maxsec} equal to the upper bin diameter for our SRC counts (Table 3.1). Using this data, we buffer an area around Zunil for each derived r_{max} for the diameter bins from 250 m down to 19 m (Figure 3.6). We then selected all SRC beyond each buffer zone that were greater in diameter than D_{maxsec} for that buffer, though less than the next larger D_{maxsec} buffer (e.g. if D_{maxsec} buffer = 22 m, select all SRC > 22 m in diameter, but \leq 31.2 m, the previous higher D_{maxsec} buffer); any SRC with a larger diameter must not have been produced from Zunil. This does not mean that these SRC are not secondaries, only that they are not secondaries from Zunil. Each successive buffer was summarized to form a population not to have originated from Zunil and was ultimately compared to all the SRC within the 19 m buffer as this zone is likely dominated by Zunil secondaries. From this data, we generated a maximum estimate of the primary to secondary ratio for SRC in this area and a new count of SRC that should not be Zunil secondaries.

3.2.5 Study Regions

We divide Mars into five distinct physiographic regions to analyze the spatial variation of SRC and their ejecta (Figure 3.7):

- 1) **Borealis:** Vastitas Borealis, Acidalia Planitia, Utopia Planitia, and Arcadia planitia. Extending from the northern pole down to 60°N and/or the ~3000m elevation contour that defines the crustal dichotomy. Composed primarily of Amazonian and Hesperian age units.
- 2) **Tharsis:** Including Tharsis Montes, Olympus Mons, Alba Patera, and Tempe Terra, Lunae Planum; This group also includes Chrysaë Planitia, Xanthe Terra, the eastern end of Valles Marineris and northwestern Margaritifer Terra; all runoff areas adjacent to the Tharsis Montes and composed almost equally of Amazonian and Hesperian aged units with some Noachian geologic units.
- 3) **Arabia:** Arabia Terra, Meridianni Terra, Terra Sabaea, Syrtis Major Planum. etc. bound by Terra Tyrrhena, 30°S and Chryse Planitia, Hellas Planitia and Terra Tyrrhena. Mostly a Noachian plateau with several Hesperian units mixed in.
- 4) **Amazonis-Elysium:** Elysium and Amazonis Planitia up to the Olympus Mons aureole, south of Vastitas Borealis and east of Utopia Planitia, but including the Elysium Mons volcanoes. Predominately Noachian and Amazonian units.
- 5) **Australis:** All the terra south of 30°S to the pole ignoring the Tharis Group and including Hellas and Argyre Planitia and Terra Tyrrhena and Hesperia Planum.

Mostly Noachian terrains, some contiguous Hesperian units and Amazonian polar deposits.

We chose regions that represented somewhat contiguous geologic and topographic features, ignoring Martian age units as our features measured resurfacing on surficial geology at what we expect to be $<10^6$ a timescales that would not affect bedrock ages. Our bias towards some age units has been noted (Figure 3.4).

3.3 OBSERVATIONS AND RESULTS

3.3.1 SRC Global Distribution

A total of 631 SRC were found in 200 images or 4.5% of our MOCNA database (Figure 3.7). Several distinct concentrations can be noted from the distribution of small rayed craters (SRC) across Mars. The first occurs in the mid to southern latitudes of Arabia Terra, distributed in an approximate arc over darker albedo material that borders this dusty region. A second cluster covers the Amazonis-Elysium Group, mostly southeast, south and southwest of Elysium Mons, then more dispersed in Amazonis Planitia. This is an area known for seven multi-diameter primary craters with well-defined ray systems recognizable in night-time thermal infrared imagery: Corinto, Dilly, Gratteri, Naryn, Thila, Tomini, Wiltz, and Zunil (with its abundant bright-rayed secondaries) (first recognized in Tornabene et al. [2006]). A third group forms along a positively sloped line across the southern edge of the Tharsis Montes with a few scattered mostly in the southern half of this region leaving the northern section nearly devoid of SRC. There are few (single digit) SRC in the polar Borealis and Australis regions. An

enigmatic paucity of SRC occurs along a 30° longitudinal band centered on ~100E in Isidis Planitia and Tyrrhena Terra; partially a factor of reduced MOCNA image coverage in our sample set. The MOCNA images are not randomly distributed, so we can't expect the observed distribution to represent a robust sampling of SRC on Mars (top, Figure 3.8). On the other hand, there is not a one-to-one correlation with image density and the SRC distribution. We created a simple normalized density index of SRC counts per image within a 5° radius (middle, Figure 3.8) and an image density of our total MOCNA image database using the image centroids:

$$\text{SRC-MOC Index} = \frac{(\#SRC \text{ Image Density} - \#MOCNA \text{ Image Density})}{(\#SRC \text{ Image Density} + \#MOCNA \text{ Image Density})} \quad (3.4)$$

creating a range of values between 1 and -1, where 1 equals more SRC counts than available MOCNA images, -1 equals more MOCNA images available than SRC and 0 is a balance between images available and SRC counts (i.e. some images, some SRC found, many images, many SRC found, etc.) (bottom, Figure 3.8). While there are cases where a sampling bias in SRC occurs because there are more images to observe, regions like northern Arabia Terra, where many MOCNA images occur still have a deficit of SRC counts. Thereby, the SRC we found are not merely due to increased probability in any one area because there is more image coverage, but must relate to the actual distribution of SRC on Mars.

There are clearly areas where SRC dominate in both latitude and longitude. SRC distribute as an approximate normal curve about the equator (top, Figure 3.9). Subordinate to a few SRC on the periphery of the polar regions, the majority of SRC fall within $\pm 40^\circ$ latitude. Indeed, $\sim 80\%$ of SRC are latitude bound between $\pm 20^\circ$ where a sharp break in frequency is evident. Two peaks in latitude frequency occur at the 15°N and 20°N bins. Longitudinal distribution is more even with a mean SRC count of ~ 17 ($1-\sigma = 23.2$) per bin (bottom, Figure 3.9). The dearth of SRC between 80°E and 110°E defies explanation and we offer none other than some lower image coverage in Isidus Planitia (80°E , 15°N) in our sample. Frequency peaks in longitude are observed in the 50°E , and 170°E longitudinal bins. We can explain the increased SRC frequency at the intersection of the 170°E and 15°N - 20°N bins and $\sim 150^\circ\text{E}$ and $\sim 5^\circ\text{N}$ bins to a predominance of secondaries from Zunil and the surrounding seven additional multi-kilometer diameter craters in the Elysium region. Increased SRC counts at 10°E and 60°E are not immediately assignable to known large primaries from Tornabene et al. [2006] that produce rayed secondaries. There may be unknown source primaries across Mars due to the limitations of identifying large fresh rayed primaries. The majority of these primaries (e.g. Tornabene et al. [2006]) are discovered in thermophysical units with intermediate albedo (0.19-0.27 from Christensen et al. [2001]), a minor silicate dust component (DCI 0.94-0.96 from Ruff and Christensen [2002]) and thermal inertia consistent with thermophysical Unit C (defined by Mellon et al. [2000] as 120-320 tiu). Recently, two new large rayed primaries have been identified in Arabia Terra, Ada (2 km diameter, http://hirise.lpl.arizona.edu/PSP_001678_1770) and Winslow (1 km,

http://hirise.lpl.arizona.edu/PSP_004313_1760) (Figure 3.7). Secondary fields for these primaries have not been delineated, but they are proximal (within a few low hundreds of kilometers) to some of our SRC.

To gain an understanding of possible sources for SRC, we have mapped readily identifiable fresh large primary craters from Tornabene et al. [2010] in concert with our SRC population. The large primaries were determined to be fresh if their crater rims were not degraded, showed little to no infilling or reworking of interior crater morphology and maintained ejecta rays identifiable in the thermal infrared from THEMIS data at 100m/pixel [Tornabene et al., 2010]. The 75 large fresh primaries appear randomly distributed (as one would expect) and have diameters ranging from 1 to greater than 40 km (Figure 3.10). Greater than 50% are 1 to 10 km in diameter, similar in size to Zunil and others primaries responsible for creating numerous secondaries in Elysium within 1000+ km of their crater rim [McEwen et al., 2005, Preblich et al., 2007]. In the Arabia region, eight large rayed craters with $D < 10$ km follow a similar southern arc of craters along the study region boundary, though the northeast section contains no obvious primary within one or two thousand km distance. In contrast, Tharsis has a more even distribution of nine large primaries (10 to 20 km diameter); however three primaries, two 1-10 km and one 10-20 km diameter, do fall within a one to two thousand km radius of the SRC. Primaries near Amazonis-Elysium tend towards the northern range of this study area near dense concentrations of SRC. An enigmatic group of large rayed primaries in a range of diameters exists near 120°E and -30°S in proximal vicinity to only one SRC. Similar to our SRC population, few large rayed craters rise poleward of $\pm 30^{\circ}$, including a

slight majority (~56%) in the southern hemisphere, though this dataset is preliminary and some sampling bias may take place.

The mean diameter of SRCs (Table 3.2) lends qualitative insight into the ejecta retention age of the five regions. Amazonis-Elysium, Arabia and Tharsis experience older retention ages with many small (<100 m) SRC, while both poles have younger retention ages with few craters at larger diameters (>100 m). Tharsis has somewhat older retention ages than Arabia and Amazonis-Elysium with mean diameters of 82 m compared to ~60 m for the other equatorial regions.

The SRC distribution tends to correlate with slightly southern equatorial areas including the lower halves of Tharis Terra, Arabia Terra and the Amazonis-Elysium region, excluding the spike of SRC related to the proximity of Zunil. Polar regions are practically devoid of any SRC and when they do occur are generally larger in diameter than the other regions.

3.3.2 SRC Ejecta and Crater Morphology

As one might expect, there is a variety of ejecta morphology for SRC (several examples cited here are in Figure 3.1). Images were examined under an initial 5% linear stretch of reflectance in I/F (a ratio of reflected to incoming light or irradiance/solar flux [Hapke, 1993]) to assess tone; many revealed ejecta in various stages of blending into the background tone (ID 078 or ID 581 as an extreme example). Ejecta tone varied from bright (ID 458) to dark (ID 606) and in some cases bimodal with dark or bright ejecta material annular to the crater rim and the opposite tone at farther distances (ID 015 and

ID 428). Ray structure varied from non-existent (ID 124) or ephemeral (ID 325 and ID 002) to extending tens of crater radii with well-defined morphology (ID 601). In areas with extensive feature softening from dust deposition, these SRC tended to have ejecta with less texture and tonal values approaching background levels. In contrast, areas with sharp features contained either well-defined, crisp ejecta delineations and/or strong tonal differences with the background. Ejecta distribution was frequently asymmetric with more downrange ejecta versus uprange, indicative of an impact angle $\sim <60^\circ$ [e.g. Gault and Wedekind, 1978] (ID 601 and extreme case). Only one example of a recent crater (ID 049, not shown) with an air blast zone was definitively identified after a more extreme linear contrast stretch in image E0400591. Although, several other images contained SRC with fresh extensive ejecta (e.g. ID 606 and ID 458).

From measuring ejecta morphology, we find the correlation of minimum and maximum distances for continuous ejecta follows a linear trend (slope = 1.8) dividing what we perceive as circular (i.e. even distribution of ejecta about the crater cavity) versus ‘butterfly’ ejecta blankets (having clear along-track and cross-track asymmetries) (Figure 3.11). Our data shows about 60% of our SRC ejecta morphology ($R^2 = 0.6$) falls in the middle ground of symmetry (neither circular nor highly elliptical), which is consistent with the expected majority of impact angles from Mars whether from cosmic or terrestrial sources [e.g. Gilbert, 1893; Anderson and Schultz, 2006]. A comparison of crater diameter to the radius of the continuous ejecta blanket (Figure 3.11) shows no strong correlation between the two parameters. However, less distal ejecta are noted for crater diameters $\sim <30$ m. In addition, there is a general trend of ejecta blankets retreating

with larger diameters. This is expected as larger craters should be relatively older, have experienced more erosion, and occur less often than smaller craters (i.e. lower production function).

3.3.3 Formation Properties and SRC Spatial Distribution

SRC are located predominately (50%) in Noachian units that make up a significant amount of area in the southern Martian hemisphere (top, Figure 3.12); Hesperian and Amazonian aged units had near equal amounts (26% and 21% respectively). Interestingly, the largest concentration of SRC in Amazonian units is in the Amazonis-Elysium region proximal to the large rayed craters Dilly, Thila, Wiltz and Zunil (Figure 3.7). Only a few SRC were found in Amazonian aged geologic units in the Tharsis region. A similar SRC distribution occurs in three thermophysical units identified by Mellon et al. [2000] (bottom, Figure 3.12). Each unit is defined by a unique density slice combination of albedo and thermal inertia values (see Table 4 in Mellon et al. [2000] for actual parameters). Unit A comprises an expansive region of the Tharsis rise and Amazonis Planitia, as well as the central region of Arabia. Unit B dominates the southern latitudes and constitutes a large part of the Borealis region including Chryse Planitia and Vastitas Borealis. Unit C tends to buffer Unit A from Unit B and extends to other contiguous areas in the north with one separate entity in and near the Hellas basin. Unit C, considered to be an indurated fine particle layer (perhaps dust), contains 47.5% of SRC, Unit B has 35.5%, and only 17% are in Unit A. Many of the SRC that fall within Unit A are close to its boundary with Unit C in both the Tharis and Arabia regions; SRC

counts may be higher in Unit C and perhaps lower in Unit A than are observed because of the resolution of the thermophysical data.

Night-time thermal inertia shows fewer SRC in low (<100 tiu) values that correspond to thermophysical Unit A (top, Figure 3.13). These low thermal inertia areas also show a consistent relationship with areas of high albedo and high dust cover. Values for the albedo and dust cover index (DCI) are near to a perfect inverse correlation (middle and bottom, Figure 3.13). Bright high albedo areas ($\sim >0.25$) represent areas of high dust content (DCI $\sim <0.92$), while areas of low dust content (DCI $\sim >0.96$) are mirrored with dark low albedo Zones ($\sim <0.15$). In general, the SRC qualitatively appear to occur in moderate to low albedo and similar levels of dust cover. Very high and very low elevations were mostly devoid of SRC, but the overall range of elevations covered anywhere from -5 km to 6.4 km from the Mars datum (top, Figure 3.14). As for water equivalent hydrogen (WEH), it appears the SRC are not readily retained in low WEH percentages ($\sim <2\%$) (bottom, Figure 3.14).

3.3.4 Statistical Correlations of SRC Occurrence and Formation Properties

We begin our statistical analysis by creating boxplots (Figure 3.15) of common statistical values (Table 3.3) for images with and without SRC for each of five formation parameters: albedo, dust cover (DCI), elevation, thermal inertia (tiu), and water equivalent hydrogen (WEH). Because these parameters are not recorded for every location on Mars, mostly due to limits of the image cross-track range and nominal sensor error, 199 out of 200 images with SRC and only 3213 out of 4264 images (75%) were

utilized for our statistics. However, given our large sample, this should still provide sufficient counts to adequately model the population.

For each parameter, the images without SRC mirrored the statistical distribution of the total population (labeled '5% SAMPLE' in Table 3.3). For albedo, the mean, maximum and minimum values were nearly identical; however the median rose from a value of 0.19 to 0.23 along with an increase of the 50% quartile to match the median. SRC DCI values had a similar shift in median and 50% quartile to nearly match the mean of 0.95. Elevation showed little differences in mean, median and quartile values for images with SRC, except less extremes in minimum (-4929 m compared to -7326 m) and maximum (6374 m compared to 20213 m) values. Night-time thermal inertia revealed little variation in mean and median values except an increase in the 25% quartile to 151 (versus 109) and a lower maximum value (449 tiu compared to 1658 tiu). Finally, WEH showed the largest divergence in its mean (5.6% compared to 10.3%) and a lower 75% quartile (7.2% versus 7.8%).

Our t-test statistics, with a 95% confidence interval ($\alpha = 0.05$), yield three physical parameters with statistically significant presence of SRC: albedo (moderately significant), DCI (slightly significant), and WEH (most significant) (Table 3.4). Albedo had a two-tail P-value of 0.007 ($t = 2.72$, $df = 3211$). DCI scored just below our α at $P = 0.015$ ($t = -2.43$, $df = 3211$), while WEH had the highest significance ($P < 0.001$, $t = -18.78$, $df = 1838$). Elevation ($P = 0.176$, $t = 1.36$, $df = 240$) and thermal inertia ($P = 0.67$, $t = 0.43$, $df = 239$) were revealed to be highly insignificant.

3.3.5 Identification of Erosional and Depositional Sequences

We established two ejecta retention sequences, one each for erosion and deposition, based on observations of unique SRC ejecta morphologies. These sequences appear to be the same regardless of whether rays are brighter or darker than the surrounding terrain. Each SRC was categorized into one of the two retention sequences and further subdivided into one of 4 stages (Figure 3.16). Each stage represents a progression from a recent impact to the complete removal or burial of ejecta.

The erosion sequence begins with the initial removal of the air blast associated with the most recent impacts [e.g. Malin et al., 2006]), but retains most of the fine ray structure with some distal disconnected ejecta segments (stage E1). Stage E2 removes the distal component and begins to erode ejecta rays back towards the continuous ejecta blanket, sharpening the ejecta transition with background target (i.e. less ephemeral ejecta). At stage E3, the rays have been reduced to the continuous ejecta, leaving only a few crater radii worth of the thickest part of the ejecta. The final part of the sequence, stage E4, leaves only the largest ejecta blocks in place with all other fine (<sand size?) ejecta having been preferentially removed, leaving the slow(er) ventifact process to eventually erode the blocks in-situ down to the level of the rim. In general, we consider the erosive process to be predominately eolian, though we cannot rule out periglacial processes approaching higher latitudes.

The deposition sequence progresses as a gradual decrease in ejecta tone as successive dust layers blend the visible ejecta with the surrounding target reflectance. Ray structure is retained up until the last stage (stage D4) where dust has effectively

buried the fine ejecta and only the largest blocks stick up out of the proximal ejecta blanket closest to the rim. These blocks are visible until such time as the dust depth matches the block height and eventually covers them. The crater floor should also be experiencing burial, but will still retain some depth as block sizes should be a couple factors smaller than crater depth.

In the last retention stage, there is an ambiguity in the classification as originating from an erosional or depositional process. However, general tonal qualities of the background (e.g. 'Is the background tone even and display softened morphologies indicative of a dust-laden surface?') assisted in placing an SRC into one sequence over the other. In general, both sequences converge on this final stage.

One set of craters existed outside our erosion classification system. For example, in Figure 3.1, crater ID 581 (middle column, third row) represented a type of crater that shows both erosional (ray structure more proximal to the continuous ejecta blanket) and depositional (no tonal contrast) properties. Another caveat to defining its sequence is the appearance of pedestal ejecta or retaining excess ejecta (as defined by Black and Stewart [2008] and Kadish and Head [2010]) that is unlike any of the other morphologies. These excess ejecta (EE) craters are found in the regions of higher WEH from ~4.5% to 7.4%, though it is hard to imagine that the ejecta thickness is sufficient to armor and preserve ice (ala the Kadish and Head [2010] model) given their small diameters and low latitude (all below $\pm 20^\circ$). They do eventually erode, as seen in EE ID 564 (Figure 3.1, center-bottom) that has nearly degraded down to the target surface. We have kept the counts of EE craters separate from our sequence, but in general consider them to represent a stage

somewhat between stage E3 and E4 on the erosion sequence. In fact, they may last longer (given their apparent dust cover) than those of stage E4 and no longer erode back towards the crater rim, but downward. Whatever induration mechanism maintains the ejecta thickness it must be sufficient to allow deflation of the surrounding target surface to produce the pedestal typical of this type (as appears to be the case for ID 564 in Figure 3.1). Given their induration state, we suspect these are some of the oldest SRC in their diameter range. However, we make no direct inference in formation properties with excess ejecta (also EE), perched (Pr) or pedestal (Pd) craters (i.e. Kadish and Head [2010]) as SRC have crater diameters that are one to two orders of magnitude smaller.

Counts of SRC by sequence stage are plotted in Figure 3.17A. We found 282 (45%) SRC in the depositional sequence and 350 (55%) SRC, including the EE type, cataloged as undergoing erosion. For both sequences, we see <10 SRC in the first stage, followed by increasing amounts, in stages 2 through 4, except the erosional sequence where we see a decline in counts in stage E4. However, if we include the EE craters in our erosional sequence as part of E4 (due to their perceived older characterization given the pedestal ejecta), then the two sequence distributions would have the same approximate negative skew to their histograms.

In Figure 3.17B, we plot statistics of ray length normalized to crater radii for each of the retention sequence categories. The ray length statistics have strikingly different numbers for each of the sequences. Stage D1 has the longest rays (~33 radii), highest mean (~11 radii), and most deviation about the mean. Ray lengths and means then remain fairly consistent through stages D2 through D4, albeit decreasing slightly in mean with

increasing stage number. For the erosion sequence, ray lengths decrease in mean and standard deviation with increasing stage number. Oddly, there are slightly longer rays associated with the E2 sequence than the E1, however the mean does decrease for E2 and continues to do so for the later erosion stages. EE craters are statistically similar to E2, nevertheless clear different in terms of ejecta tone and the transition from ejecta to surface morphology.

In the majority of images, the SRC retention sequence was of similar type (either erosion or deposition), though varied in stage for most SRC in each image. One clear example was in MOCNA image M1104273 (Figure 3.18). SRC ID 349 has a retention stage of E3 with only the continuous ejecta blanket retained at the level of the target surface, while SRC ID 350 is an EE type that has thicker pedestaled ejecta based on the sun angle and shadow cast around the northern edge of the ejecta. Given the downrange ejecta blanket morphology, we can determine that these two impacts occurred from at least different sources and likely different time intervals. We would argue that SRC ID 350 is older based on the fact that it has pedestal ejecta while the other SRC has undergone no deflation of the surrounding terrain. While separated in time, both appear to be undergoing an erosional sequence.

In some images, retention stages were nearly identical for all SRC, which may be interpreted as a cluster of SRC secondaries that impacted at the same time. However, no clear spatial pattern of these types of SRC clusters near known large primary was observed, except around Zunil.

3.3.6 Zunil and non-Zunil SRC

A total of 243 SRC fell within the D_{maxsec} 19 m buffer zone with only 22 greater than the diameter-distance relationship for Zunil summed over each of the diameter bins (Table 3.5). If these non-Zunil SRC are all primaries (though more analysis would be required to affirm this), the secondary to primary ratio in this area is at a maximum 11:1; a value in line with estimates of secondary cratering ratios on Europa [Bierhaus et al., 2005]. Indeed, we found only one crater with D smaller than 44.2 m as a possible non-Zunil SRC compared to over a hundred for all SRC in this area. The ratio of Zunil to non-Zunil SRC for bin diameters increased from 3.6:1 for $D = 88.3-125\text{m}$ to up to 26:1 for $D = 22.1-31.2$. Even if only one non-Zunil SRC was counted in the smaller diameter bins, the ratio would still favor Zunil SRC secondaries by an order of magnitude. From this data, the cross-over diameter, when Zunil secondaries begin to dominate the number of non-Zunil SRC (primaries?), occurs at ~ 125 m; a factor 2 smaller than the minimum estimated for secondaries by McEwen et al. [2005]. Additional SRC primaries may also be mixed in with Zunil secondaries when D is only a few tens of meters. Whether there are sufficient numbers to lower the cross-over diameter is unclear.

3.4. DISCUSSION

3.4.1 Spatial Variability of Ejecta Retention on Mars

We have shown that SRC are highly latitude dependent on Mars, being bound almost exclusively from $\pm 30^\circ$. Mustard et al. [2001] observed that the northern and southern $30^\circ-60^\circ$ latitude bands consist of dissected terrain indicative of an active ground

ice layer suspected to be 1×10^5 a old based on orbital obliquity models. Poleward of these locations, near surface water ice fraction increases to tens of percent by mass [Feldman et al., 2004]. However, recent impacts have excavated pure ice within decimeters of the surface at latitudes as low as 43°N [Byrne et al., 2009]. Bright ejecta from these impacts were visually and spectroscopically determined to be consistent with H_2O ice and in some cases a significant fraction thereof (see Figure 3, Site 3 in Byrne et al. [2009]) that sublimated over several months [Byrne et al., 2009]. These mid to high latitudes are also congruous with active thermal contraction crack polygons [Levy et al., 2009] from stresses induced by seasonal thermal deviations [Mellon et al., 2008], viscous flow features [Milliken et al., 2003], and lobate debris aprons composed of massive up to 100's m thick ice determined from radar studies [Holt et al., 2008]. All these morphologies share a genetic origin consistent with atmospheric deposition (i.e. snow) to form an ice-rich mantle during high obliquity excursions [e.g. Levy et al., 2009 and references therein]. Any impact creating ejecta within the past 2 Ma in the these latitudes must be subjected to near immediate degradation from patterned ground processes as was observed by Maine et al. [2010] for $D = 5\text{-}30$ m craters at $60^\circ\text{-}70^\circ\text{S}$. Initial results indicate more accelerated degradation rates for similar diameter craters in the north [Kreslavsky, 2009]. This asymmetry is also reflected in our counts with no SRC below ~ 30 m in Australis (south), while Borealis (north) had no craters up to twice that diameter (Table 3.2). As an alternative, excavated ice ejecta, with a high fraction of water ice, may rapidly sublimate on sub-annual timescales leaving a minor residual ejecta lag that is rapidly removed by eolian (e.g. dust devils) or other periglacial processes. These

observations indicate SRC ejecta retention may be an order of magnitude shorter (at a minimum) than crater retention rates in these regions.

Within the equatorial region ($\pm 30^\circ$), our statistics show some significant correlation of SRC locations with three formation parameters: dust content (DCI), albedo, and water equivalent hydrogen (WEH). DCI is a good proxy for the albedo as high dust content equates high albedo and vice versa, so both variables being significant is not surprising. WEH is more difficult to reconcile since it would appear that increasing WEH has some correspondence with SRC emplacement; perhaps partially explaining the gap in SRC from 80° - 120° E. Another caveat to the WEH values is that the spatial resolution is low; data is reduced to $5^\circ \times 5^\circ$ bins from a 300 km radius footprint [Feldman et al., 2004]. As a conjecture, the mineralogy at these locations (phyllosilicates?) might be more conducive to SRC formation due to mineral hydration, but there is no evidence of WEH as an indicator of any distinct geologic formations or bedding. One notable exception is the excess ejecta craters. These SRC indicate some degree of induration that while unlikely to be ice related, must represent some unique physical attribute of the regolith that coincides with higher WEH. Why these craters are found in equatorial latitudes and not higher in truly ice-rich polar regions is unclear. In these cases, formation dominates ejecta retention, though whether by mineralogy or ice content remains unknown at this time.

Dust content explains substantial amounts of the spatial variability in SRC distribution across the Martian equator. With a few exceptions, it seems likely that SRC become buried rapidly by increasing dust load in central Arabia and Tharsis. Modeling

has shown that wind stress decreases with surface brightening (i.e. dust load increases from less eolian erosion) [Fenton et al., 2007]. SRC are rapidly buried within high dust concentration areas, thus many SRC occur along their periphery. In contrast, intermediate albedo areas (correlative with thermophysical Unit C) represent a middle ground where winds are strong enough to keep dust aloft, but removing only a minimal amount of ejecta material. We do find several areas where SRC are numerous (just east of 60°E and below the equator from 0°-60°E). If we accept the premise that albedo-dark areas are experiencing greater ejecta erosion and albedo-bright regions are predominately undergoing deposition, given the SRC distribution about Arabia Terra and eastern Tharsis, dust is covering ejecta at a faster rate than erosion removes it.

A map of SRC in the erosion sequence ('E ALL', Figure 3.19) is in good agreement with the dust distribution across Mars. Most SRC fall in regions with less dust (high DCI values). The one exception is in the Zunil area with many SRC (likely Zunil secondaries) being classified in an erosional sequence, but residing in a dust-laden area at 15°N, 160°E, albeit with a small pocket of lower dust concentrations. This leads us to two interpretations: 1) experimental results have shown that low-velocity impacts, like secondaries, emplace ejecta more proximal to the crater rim as less energy is partitioned into ejecta (~1%) at impact speeds <1000 km/s [Hartmann 1985], indicating secondary ejecta may have characteristics similar to the erosion sequence just by the nature of their emplacement, or 2) these SRC are particularly old and have undergone a brief erosion sequence that only removed the most distal ejecta followed by a deposition sequence. Estimates of Zunil's age, which is equivalent to the age of its secondaries, have been

calculated from counts of small impacts on its proximal ejecta blanket (itself, free of secondaries) placing its impact time anywhere from 180 ka using a Neukum production function [Neukum et al., 2001], to an upper limit based on recent production values from new impacts observed by Malin et al. [2006] at ~540 ka [Kreslavsky, 2008]. During that period of time, modeling reveals several substantial orbital obliquity variations on ~100 ka timescales [e.g. Mellon and Jakowsky, 1995], so it is conceivable that certain sections of Mars have changed in terms of dominant ejecta retention processes in the 500 ka timeframe. We do not have a specific conclusion at this time, only that these craters, even if reclassified as belonging to the deposition sequence, would only modify the counts and not the shape of the sequence histogram; hence we are still confident in our classification scheme.

As for the deposition sequence distribution ('D ALL', Figure 3.19), we again have general agreement, but the spatial variability is more diverse with dusty SRC located in high DCI (low dust) areas. In collecting our imagery, we did not subset our data according to seasonal variations or by Mars year; hence, some of our data may show evidence of dust collection from recent dust storms such as the hemispheric event in 2007 [detailed in Kass et al., 2007]. The fact remains that Mars is a dusty planet and local heterogeneities in dust collection may be evident in some of our results. For comparison, 13 SRC initially identified by the Mars Global Surveyor [Malin et al., 2006] showed little to no modification after the 2007 global dust storm in HiRISE imagery [Geissler et al., 2010] despite residing in some of the dustiest areas of the planet.

Each progressive ejecta retention stage appears to represent an increase in SRC morphologic age. For the erosional sequence, it makes perfect sense that ejecta rays will never increase in length (ignoring obvious wind-modified patterns around some craters). All initial parameters like impact speed and angle, target, and projectile size being equal, shorter rayed ejecta craters are more degraded by erosion along the sequence and hence are expected to be older. As seen in Figure 3.17B, the mean and deviation about the mean decreases for ejecta ray length with each progressive erosion stage (E1 to E4), concomitant with our classification scheme. The counts per stage (Figure 3.17A) indicate a quick removal of long thin rays from most SRC (low numbers in stage E1), followed by longer retention of ejecta as ray length becomes shorter and ejecta becomes thicker proximal to the crater rim (SRC frequency increasing from E2 to E3). A comparison of ray length between the depositional and erosional sequence indicates SRC in erosion dominated environments have ejecta removed much more rapidly in all stages than in areas of deposition, as expected. For the depositional sequence, increasing age with increasing stage (D1 to D4) is not necessarily true. Changes in wind speed and atmospheric density over million year timescales could easily lead to variable amounts of dust deposition and/or deflation in one location. However, given that the counts in the depositional sequence (Figure 3.17A) increase from D1 to D4, it appears safe to assume that the retention sequence type has not changed appreciably (i.e. switched from deposition to erosion) since the formation of these SRC. It also implies the current wind regime has been stable over the same time period. Ray length reinforces this inference, as mean and standard deviation of this measurement (Figure 3.17B) is high in the first stage,

though nearly constant from stage D2 to D4. Otherwise, some previous dust-laden SRC would have been deflated or darkened resulting in counts with more variation between stages. Our results indicate that the current climatic regimes that dictate erosion and deposition on Mars have been globally stable for the existence of the SRC; as they go along the retention sequence, their age increases. Putting an absolute age to any of the stages is difficult. Given the rapidity of dust deposition on Mars, stage D1 would be the youngest stage of either sequence, perhaps in the thousand year time frame. This would be followed by stage E1 at a few tens of thousands of years given the ephemeral nature of distal rays, but incredibly slow erosion rates seen thus far at several landing sites [e.g. Golombek et al., 2006]. The rest of the stages are hard to gauge and would be guesswork at best, but assumed to be in the hundreds of thousands of years. Of course, these timelines must take into account crater diameter as ejecta thickness scales with crater size [McGetchin and Settle, 1973]. Another aspect in placing a SRC into any one stage is the influence of target type. Some regions may by nature of their formation be more conducive to greater or lesser amounts of ejecta upon initial impact due to target bulk strength, faults, or depth-to-bedrock, not to mention variance in impact angle or velocity, which all affect ejecta excavation [e.g. Carlson and Jones, 1965; Dillon, 1972; Gault and Wedekind, 1978]. Some SRC, simply due to the above differences in formation, enter either sequence at a later stage than would be expected. For example, if an SRC does not produce ejecta because it lands in a dusty or icy region, it could be designated D4/E4 without other clarifying evidence. In this regard, these retention stages are probably best

used at a smaller regional scale where the effects of formation can be more easily ruled out.

While this appears generically true for all surfaces, a closer examination of each stage's spatial distribution is warranted. Due to the nature of our data collection, spatial statistics such as a Nearest Neighbor or Ripley's k-function to analyze clustering are not useful. From a qualitative standpoint, we can see SRC undergoing the erosional and depositional sequence in similar locations near the equator (Figure 3.19, D1-D4 and E1-E4). This could hint at microtopographic variations in erosion and deposition or variation in target/bedrock material. Different physical and structural properties as well as regolith depth could influence ray length and hence skew our interpretation of retention sequence and stage. One exceptional area emerges where the retention sequence appears to change between deposition and erosion. At 0-30° east and south of the coordinate grid origin (center of map) in southern Arabia Terra (Figure 3.19), SRC counts are more abundant in the last depositional stage (D4) and absent in E4-type SRC. However, in the next earlier stage SRC increase significantly in stage E3, with less counts in stage D3 in the same area. If we assume dust deposition is always at an order of magnitude faster rate than erosion (at least in the past 1 Ma on Mars), then it is logical to assume that in this location, the depositional sequence occurred before the erosional sequence. If the reverse were true, dust would have rapidly buried earlier erosional stages (E1 and E2, which still exist in this area) leaving only the later E3 and some presumed E4 stage SRC. However, the lack of E4 SRC indicates that none have reached this stage nor could they have been buried (otherwise, all other stages would have been buried too). The various depositional

stages are probably in the process of being exhumed and entering the erosional sequence. In fact, this scenario explains all SRC in the D4 retention sequence in non-dusty areas (i.e. high DCI values). This further explains the reduction in the E4 stage (Figure 3.17B) as only a few are located in the non-dusty areas south of the equator ('E4', Figure 3.19). This might indicate a major shift from dust deposition to erosion processes from just south of the Martian equator towards northern latitudes. Placing an absolute age to this shift is difficult, though estimated at >100 ka given that it occurs during the later stages of each sequence.

3.4.2 Estimated Primary to Secondary Ratio around Zunil

The fraction of SRC not accountable as Zunil secondaries is significantly small. As would be expected, most non-Zunil SRC are towards the periphery of the distal zones where D_{maxsec} is smaller. Within the zones closer to Zunil, it is impossible via the diameter-distance metric to declare a tens-of-meter diameter SRC as a primary or secondary. In addition, five multi-kilometer diameter rayed primaries fall within or near the 19 m zone. While Dilly, Thila, and Wiltz are in close proximity to SRC closest to Zunil's rim, they are also less than half the diameter of Zunil and thus likely produced far fewer and smaller diameter secondaries over shorter distances. Gratteri is ~500 km distal to the very edge of the Zunil study area, though its larger diameter (6.9 km) may make it a contributor to SRC in the south-southeast quadrant. The large primary Corinto (13.5 km) on the other hand, assuming similar target properties and impact velocities, would have also contributed significant numbers of secondaries, with larger diameters, at greater

distances. What contribution each of these other primaries made to our counts is inconclusive, though we cannot discount the possibility that even these non-Zunil SRC are secondaries from another primary too. However, we have shown that only a small fraction of SRC within 2000 km of Zunil could not have been secondaries from it. If the ratio of Zunil to non-Zunil SRC approximates the secondary to primary ratio, this would imply ejecta (and crater) retention age estimates may be off by an order of magnitude.

3.5 Conclusions

Observations from a global sampling of MOCNA images have revealed a spatial distribution of SRC constrained by active surface processes. This survey demonstrated that mid to high latitudes are nearly devoid of ejecta from sub-kilometer diameter craters, except for a few in the 100s of meters range. This absence of SRC is likely due to the presence of near-surface ground ice. Either icy ejecta is created and sublimated on annual timescales or periglacial processes rapidly rework ejecta while generating patterned ground landforms. Thus, properties of formation in the polar regions play a substantial role in ejecta retention. In the equatorial regions, ejecta retention is controlled primarily by active dust accumulation in the Amazonis-Elysium, Arabia and Tharsis regions. The increase in water equivalent hydrogen with SRC occurrence proved statistically significant in some areas, especially for excess ejecta craters with pedestal-like ejecta scarps, though the true nature of this correlation needs further exploration.

We developed two retention sequences from ejecta morphology: erosion and deposition. Erosion sequence craters display a decrease in ray length (hence, ejecta

thickness) with increasing stage of degradation. Deposition sequence craters brightened with increase dust load, but maintained visible ray structure throughout most of the stages. Both stages culminate in only the largest proximal ejecta blocks remaining visible around the crater rim. One set of craters, with excess ejecta and morphologically similar to pedestal craters do not fit entirely into either sequence, but more closely resemble the erosion craters with shorter rays that by some induration mechanism retain structure for more extended periods of time. We suspect these SRC are the oldest rayed craters identified. The influence of secondary cratering in terms of evaluating ejecta retention could prove problematic in accurately measuring retention ages. Around primaries like Zunil, the frequency of secondary craters may outnumber primaries by an order of magnitude. For that reason, caution is warranted when deriving any absolute age estimates with $D < 125$ m craters.

A major shift in ejecta retention from a depositional to erosional environment may indicate a possible change in the climatic regime at ~ 100 ka just south of the Martian equator. Further exploration of ejecta retention at regional scales would be more functional in evaluating surface processes across Mars.

REFERENCES

Anderson, J. L. B., and P. H. Schultz (2006), Flow-field center migration during vertical and oblique impacts, *International Journal of Impact Engineering*, 33, 35-44, doi:10.1016/j.ijimpeng.2006.09.022.

Balme, M., and R. Greeley (2006), Dust devils on Earth and Mars, *Rev. Geophys.*, 44, RG3003, doi:10.1029/2005RG000188.

Bart, G. D., and H. J. Melosh (2007), Using lunar boulders to distinguish primary from distant secondary impact craters, *Geophys. Res. Lett.*, 34, L07203, doi:10.1029/2007GL029306.

Bierhaus, E. B., C. R. Chapman, and W. J. Merline (2005), Secondary craters on Europa and implications for cratered surfaces, *Nature*, 437, 1125– 1127, doi:10.1038/nature04069.

Black, B. A. and S. T. Stewart (2008), Excess ejecta craters record episodic ice-rich layers at middle latitudes on Mars, *J. Geophys. Res.*, 113, E02015, doi:10.1029/2007JE002888.

Byrne, S., C. M. Dundas, M. R. Kennedy, M. T. Mellon, A. S. McEwen, S. C. Cull, I. J. Daubar, D. E. Shean, K. D. Seelos, S. L. Murchie, B. A. Cantor, R. E. Arvidson, K. S. Edgett, A. Reufer, N. Thomas, T. N. Harrison, L. V. Posiolova, and F. P. Seelos (2009), Distribution of Mid-Latitude Ground-Ice on Mars from New Impact Craters, *Science*, 325, 1674.

Calef, F. J., III, R. R. Herrick, and V. L. Sharpton (2009), Geomorphic analysis of small rayed craters on Mars: Examining primary versus secondary impacts, *J. Geophys. Res.*, 114, E10007, doi:10.1029/2008JE003283.

Carlson, R.H. and G.D. Jones (1965), Distributions of ejecta from Cratering explosions in soils, *J. Geophys. Res.* 70, 1897.

Christensen, P. R. and 25 colleagues (2001), Mars Global Surveyor Thermal Emission Spectrometer experiment: Investigation description and surface science results, *J. Geophys. Res.*, 106, pp. 23,823 - 23,872.

Daubar, I. J., and A. S. McEwen (2009), Depth to diameter ratios of recent primary impact craters on Mars, *Lunar Planet. Sci. Conf.*, XXXX, abstract #2419.

Dillon, L.A. (1972), The influence of soil and rock properties on the dimensions of explosion-produced craters, *Tech. Rept. AFWL-TR-71-144*, Air Force Weapons Lab., Kirtland Air Force Base, New Mexico.

Feldman, W. C., and 14 colleagues (2004), Global distribution of near-surface hydrogen on Mars, *J. Geophys. Res.*, 109, E09006, doi:10.1029/2003JE002160.

Fenton, L. K., P. E. Geissler, and R. M. Haberle (2007), Global warming and climate forcing by recent albedo changes on Mars, *Nature*, 446, 646-649, doi:10.1038/nature05718.

Garvin, J. B. and J. J. Frawley (1998), Geometric properties of Martian impact craters: Preliminary results from Mars Orbiter Laser Altimeter, *Geophys. Res. Lett.*, 25, 4405–4408.

Garvin, J. B., S. E. H. Sakimoto and J. J. Frawley (2003), Craters on Mars: global geometric properties from gridded MOLA topography, *6th Int. Conf. on Mars*, #3277.

Gault, D. E., and J. Wedekind (1978), Experimental studies of oblique impact, *Lunar Planet. Sci. Conf.*, IX, 3843–3875.

Geissler, P. E., I. J. Daubar, A. S. McEwen, N. T. Bridges, and C. M. Dundas (2010), Eolian degradation of young Martian craters, *Lunar Planet. Sci. Conf.*, XXXXI, abstract #2591.

Gilbert, G. K. (1893), The Moon's face: a study of the origin of its features, *Philosophical Society of Washington Bulletin*, 12, 241–292.

Golombek, M. P., and 10 colleagues (2006), Erosion rates at the Mars Exploration Rover landing sites and long-term climate change on Mars, *J. Geophys. Res.*, 111, E12S10, doi:10.1029/2006JE002754.

Greeley, R., B. White, R. Leach, J. Iversen, and J. Pollack (1976), Mars: wind friction speeds for particle movement, *Geophysical Research Letters*, 3, 8, 417-420.

Greeley, R. and 19 colleagues (2004), Coordinated observations of Aeolian features from the Mars Exploration Rover (MER) and the Mars Express High Resolution Stereo Camera and other orbiters, *Lunar Planet. Sci. Conf. XXXV*, abstract #2162.

Hapke, B. (1993), *Theory of Reflectance and Emittance Spectroscopy*, Cambridge University Press, Cambridge, 455p.

Hartmann, W. K. (1985), Impact experiments: 1. Ejecta velocity distributions and related results from regolith targets, *Icarus*, 63, 69 – 98, doi:10.1016/0019-1035(85)90021-1.

Head, J.W., J. F. Mustard, M. A. Kreslavsky, R. E. Milliken, and D. R. Marchant (2003), Recent ice ages on Mars, *Nature*, 426, 797-802.

Holt, J. W. and 11 colleagues (2008), Radar sounding evidence for buried glaciers in the southern mid-latitudes of Mars, *Science*, 322, 1235-1238, DOI: 10.1126/science.1164246.

Howard, A. D. (2003), Erosional history of Mars during the Noachian, EGS - AGU - EUG Joint Assembly meeting, abstract #1352.

Kadish, S. J. and J. W. Head (2010), Impacts into ice-rich deposits on Mars: excess ejecta craters, perched craters, and pedestal craters, *Lunar Planet. Sci. Conf.*, XXXXI, abstract #1017.

Kass, D. M., D. McCleese, T. Schofield, A. Kleinboehl, R. Zurek, and N. Bowles (2007), MCS Views of the 2007 Global Dust Storm, *Bulletin of the American Astronomical Society*, Vol. 39, p.441.

Kneissl, T., D. Reiss, S. van Gasselt and G. Neukum (2009), Distribution and orientation of northern-hemisphere gullies on Mars from the evaluation of HRSC and MOC-NA data, *Earth and Planetary Science Letters*, Article in Press, doi:10.1016/j.epsl.2009.05.018.

Kreslavsky, M. (2008), Young populations of small craters on Mars: A case study, paper presented at 3rd European Planetary Science Congress, Abstract EPSC2008-A-00237, Eur. Geosci. Union, Münster, Germany, 21–26 September.

Kreslavsky, M. (2009), Dynamic landscapes at high latitudes on Mars: constraints from populations of small craters, *Lunar Planet. Sci. Conf. XXXXI*, abstract #2311.

Levy, J., J. Head, and D. Marchant (2009), Thermal contraction crack polygons on Mars: Classification, distribution, and climate implications from HiRISE observations, *J. Geophys. Res.*, 114, E01007, doi:10.1029/2008JE003273.

Maine, A., M. A. Kreslavsky, T. C. Orloff, E. Asphaug, and H. Gray (2010), Degradation of small craters in the high latitudes of Mars, *Lunar Planet. Sci. Conf. XXXXI*, abstract #1556.

Malin, M. C., K. S. Edgett, L. V. Posiolova, S. M. McColley, and E. Z. Noe Dobrea (2006), Present-day impact cratering rate and contemporary gully activity on Mars, *Science*, 314(5805), 1573 – 1577, doi:10.1126/science.1135156.

McEwen, A. S., B. S. Preblich, E. P. Turtle, N. A. Artemieva, M. P. Golombek, M. Hurst, R. L. Kirk, D. M. Burr, and P. R. Christensen (2005), The rayed crater Zunil and interpretations of small impact craters on Mars, *Icarus*, 176, 351–381, doi:10.1016/j.icarus.2005.02.009.

McGetchin, T. R., and M. Settle (1973), Radial thickness variation in impact crater ejecta: implications for lunar basin deposits, *Earth and Planet. Sci. Let.*, 20, 226-236.

Mellon, M. T., and B. M. Jakosky (1995), The distribution and behavior of Martian ground ice during past and present epochs, *J. Geophys. Res.*, 100, 11,781–11,799, doi:10.1029/95JE01027.

Mellon, M. T., B. M. Jakosky, H. H. Kieffer and P. R. Christensen (2000), High-resolution thermal inertia mapping from the Mars Global Surveyor Thermal Emission Spectrometer, *Icarus*, 148, 2, 437-455.

Mellon, M. T., W. V. Boynton, W. C. Feldman, R. E. Arvidson, T. N. Titus, J. L. Bandfield, N. E. Putzig, and H. G. Sizemore (2008), A prelanding assessment of the ice table depth and ground ice characteristics in Martian permafrost at the Phoenix landing site, *J. Geophys. Res.*, 113, E00A25, doi:10.1029/2007JE003067.

Melosh, H. J. (1984), Impact ejection, spallation, and the origin of meteorites, *Icarus*, 59, 234-260.

Milliken, R. E., J. F. Mustard, and D. L. Goldsby (2003), Viscous flow features on the surface of Mars: Observations from high-resolution Mars Orbiter Camera (MOC) images, *J. Geophys. Res.*, 108(E6), 5057, doi:10.1029/2002JE002005.

Moore, H. J., J. M. Boyce, and D. A. Hahn (1980), Small impacts in the lunar regolith – their morphologies, relative ages, and rates of formation, *The Moon and the Planets*, 23, 231-252.

Mustard, J. F., C. D. Cooper, and M. K. Rifkin (2001), Evidence for recent climate change on Mars from the identification of youthful near-surface ground ice, *Nature*, 412, 411-414.

Neukum, G., B. A. Ivanov, and W. K. Hartmann (2001), Cratering records in the inner solar system in relation to the lunar reference system, *Space Sci. Rev.*, 96(1–4), 55–86, doi:10.1023/A:1011989004263.

Pike, R. J., and D. E. Wilhelms (1978), Secondary-impact craters on the Moon: topographic form and geologic process, *Lunar and Planet. Sci. Conf. 9th*, 907–909

Preblich, B. S., A. S. McEwen, and D. M. Studer (2007), Mapping rays and secondary craters from the Martian crater Zunil, *J. Geophys. Res.*, 112, E05006, doi:10.1029/2006JE002817.

Putzig, N. E. and M. T. Mellon (2007), Apparent thermal inertia and the surface heterogeneity of Mars, *Icarus*, 191, 68-94, doi: 10.1016/j.icarus.2007.05.013.

Reiss, D., S. van Gasselt, G. Neukum, R. Jaumann (2004), Absolute dune ages and implications for the time of formation of gullies in Nirgal Vallis, Mars. *J. Geophys. Res.* 109, E06007.

Ruff, S. W. and P. R. Christensen (2002), Bright and dark regions on Mars: Particle size and mineralogical characteristics based on Thermal Emission Spectrometer data, *J. Geophys. Res.*, 107, E12, 5127, doi:10.1029/2001JE001580.

Schmidt, R.M. and K.A. Holsapple (1982), Estimates of Crater Size for Large-Body Impact: Gravity-Scaling Results, *Geo. Soc. Am., Special Paper No. 190*.

Schon, S. C., J. W. Head, C. I. Fassett (2009), Unique chronostratigraphic marker in depositional fan stratigraphy on Mars: Evidence for ca. 1.25 Ma gully activity and surficial meltwater origin, *Geology*, 37, 3, 207–210, doi: 10.1130/G25398A.1.

Skinner, J. A., T. M. Hare, and K. L. Tanaka (2006), Digital renovation of the atlas of Mars 1:15,000,000-scale global geologic series maps, *Lunar Planet. Sci. Conf., XXXVII*, Abstract 2331.

Smith, D. E., and 11 colleagues (1999), The global topography of Mars and implications for surface evolution, *Science*, 284, 1495 – 1503, doi:10.1126/science.284.5419.1495.

Tornabene, L. L., J. E. Moersch, H. Y. McSween Jr., A. S. McEwen, J. L. Piatek, K. A. Milam, and P. R. Christensen (2006), Identification of large (2– 10 km) rayed craters on Mars in THEMIS thermal infrared images: Implications for possible Martian meteorite source regions, *J. Geophys. Res.*, 111, E10006, doi:10.1029/2005JE002600.

Tornabene, L. L., Bray, V., McEwen, A. S., Osinski, G. R., Mouginis-Mark, P. and Boyce, J (2010) Recognition of fresh & well-preserved Martian craters & their general interior morphologic aspects as observed by HiRISE & CTX, *J. Geophys. Res.*, in prep.

Vickery, A. M. (1987), Variation in ejecta size with ejection velocity, *Geophys. Res. Lett.*, 14, 7, 726-729.

TABLES

Table 3.1: Diameter-distance relationship for Zunil SRC.

<u>Dmaxsec (m)</u>	<u>Distance (km)</u>
250	83
176	678
125	1088
88.3	1383
62.5	1590
44.2	1738
31.2	1842
22.1	1915
19	1940

Table 3.2: Crater diameter statistics for SRC by region on Mars.

	AMAZONIS- ELYSIUM	ARABIA	THARSIS	AUSTRALIS	BOREALIS	ALL SRC
MIN	19	19	21	36	63	19
MAX	725	592	449	823	702	823
AVERAGE	64	59	82	165	245	71
GEOMEAN	51	51	67	92	211	54
MEDIAN	46	41	63	72	177	47
STDEV	64	61	66	220	332	95

Table 3.3: Statistics for 5% MOCNA image sample and presence/absence of SRC for five formation parameters.

ALBEDO	5% SAMPLE	WITH SRC	WITHOUT SRC	DCI	5% SAMPLE	WITH SRC	WITHOUT SRC
Mean	0.20	0.21	0.20	Mean	0.96	0.96	0.96
STDEV	0.05	0.05	0.05	STDEV	0.02	0.02	0.02
Median	0.19	0.23	0.19	Median	0.96	0.95	0.96
Minimum	0.09	0.09	0.09	Minimum	0.88	0.92	0.88
Maximum	0.32	0.32	0.32	Maximum	0.99	0.99	0.99
25th Pct	0.15	0.16	0.15	25th Pct	0.94	0.94	0.95
50th Pct	0.19	0.23	0.19	50th Pct	0.96	0.95	0.96
75 Pct	0.24	0.25	0.24	75 Pct	0.97	0.97	0.97

ELEVATION	5% SAMPLE	WITH SRC	WITHOUT SRC	TIU	5% SAMPLE	WITH SRC	WITHOUT SRC
Mean	-389	-170	-404	Mean	195	198	195
STDEV	2841	2316	2872	STDEV	103	85	104
Median	159	-125	216	Median	200	196	200
Minimum	-7326	-4929	-7326	Minimum	10	23	10
Maximum	20213	6374	20213	Maximum	1658	449	1658
25th Pct	-2700	-2248	-2752	25th Pct	111	151.5	109
50th Pct	2859	2123	2968	50th Pct	200	196	200
75 Pct	4194	3748	4246	75 Pct	260	252	260

WEH%	5% SAMPLE	WITH SRC	WITHOUT SRC
Mean	10.0	5.6	10.3
STDEV	11.4	1.8	11.7
Median	5.3	5.3	5.3
Minimum	2.0	2.1	2.0
Maximum	46.9	13.6	46.9
25th Pct	4.2	4.3	4.2
50th Pct	5.3	5.3	5.3
75 Pct	7.7	7.2	7.8

TABLE 3.4: F-Test and T-Test statistics for MOCNA images with and without SRC.

<i>ALBEDO</i>	<i>With SRC</i>	<i>Without SRC</i>	<i>Dust Cover Index</i>	<i>With SRC</i>	<i>Without SRC</i>
Mean	0.21	0.20	Mean	0.96	0.96
Variance	0.00	0.00	Variance	0.00	0.00
Observations	199	3014	Observations	199	3014
F-Test df	198	3013	F-Test df	198	3013
^a F value	1.05		^a F value	0.97	
P(F<=f) one-tail	0.322	Equal. Vari.	P(F<=f) one-tail	0.415	Equal. Vari.
F Critical one-tail	1.18		F Critical one-tail	0.84	
Pooled Variance	0.00		Pooled Variance	0.00	
T-Test df	3211		T-Test df	3211	
^{ab} t value	2.72		^{ab} t value	-2.43	
P(T<=t) two-tail	0.007	Significant	P(T<=t) two-tail	0.015	Significant
t Critical two-tail	1.96		t Critical two-tail	1.96	
<i>ELEVATION</i>	<i>With SRC</i>	<i>Without SRC</i>	<i>THERMAL INERTIA</i>	<i>With SRC</i>	<i>Without SRC</i>
Mean	-170	-404	Mean	198	195
Variance	5365602	8246878	Variance	7268	10853
Observations	199	3014	Observations	199	3014
F-Test df	198	3013	F-Test df	198	3013
^a F value	0.65		^a F value	0.67	
P(F<=f) one-tail	0.000	Uneq. Vari.	P(F<=f) one-tail	0.00	Uneq. Vari.
F Critical one-tail	0.84		F Critical one-tail	0.84	
T-Test df	240		T-Test df	239	
^{ab} t value	1.36		^{ab} t value	0.43	
P(T<=t) two-tail	0.176	Insignificant	P(T<=t) two-tail	0.67	Insignificant
t Critical two-tail	1.97		t Critical two-tail	1.97	
<i>H₂O Equiv. Hyd.</i>	<i>With SRC</i>	<i>Without SRC</i>			
Mean	5.6	10.3			
Variance	3.3	137.4			
Observations	199	3014			
F-Test df	198	3013			
^a F value	0.02				
P(F<=f) one-tail	0.000	Uneq. Vari.			
F Critical one-tail	0.84				
T-Test df	1838				
^{ab} t value	-18.78				
P(T<=t) two-tail	0.000	Significant			
t Critical two-tail	1.96				

^aTests use a significance level (α) = 0.05 for a 95% confidence level.

^bT-Test adjusted based on F-Test results of variance equality between the samples.

Table 3.5: Zunil SRC and non-Zunil SRC Counts

D (m)	All Zunil SRC	Non-Zunil SRC	Ratio
15.6-22.1	6	0	6?
22.1-31.2	26	1	26
31.2-44.2	76	0	76?
44.2-62.5	74	4	18.5
62.5-88.3	39	6	6.5
88.3-125	18	5	3.6
125-176	6	4	1.5
176-250	6	5	1.2
250-353	3	3	1
353-500	1	1	1
500-707	2	2	1
707-1000	1	1	1

FIGURES

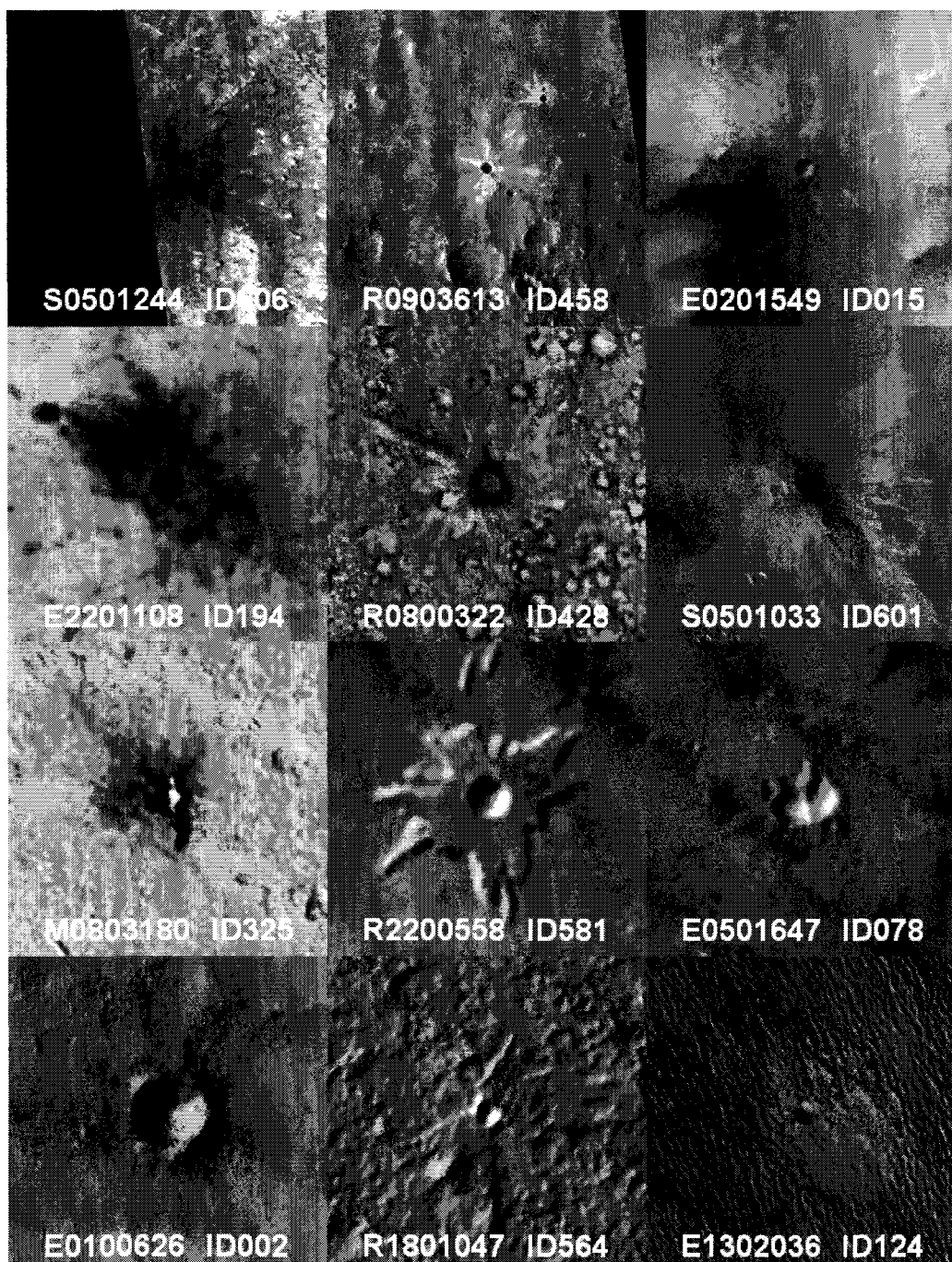


Figure 3.1: Twelve examples of small (sub-kilometer diameter) rayed craters (SRC) on Mars. Original MOCNA image name and identification number, for this study, in white lettering. Crater diameters are from 20 m to 100 m.

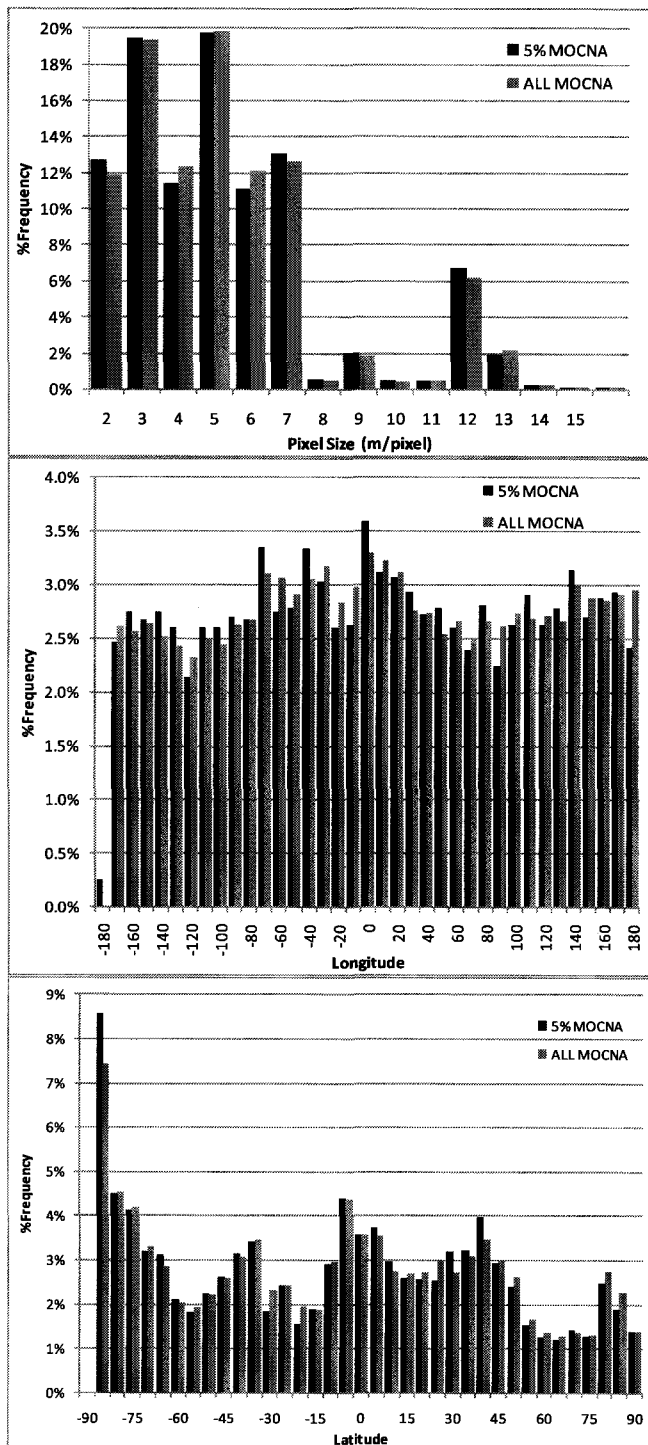


Figure 3.2: Comparison of spatial distribution and resolution for a 5% sample and complete MOCNA image database.

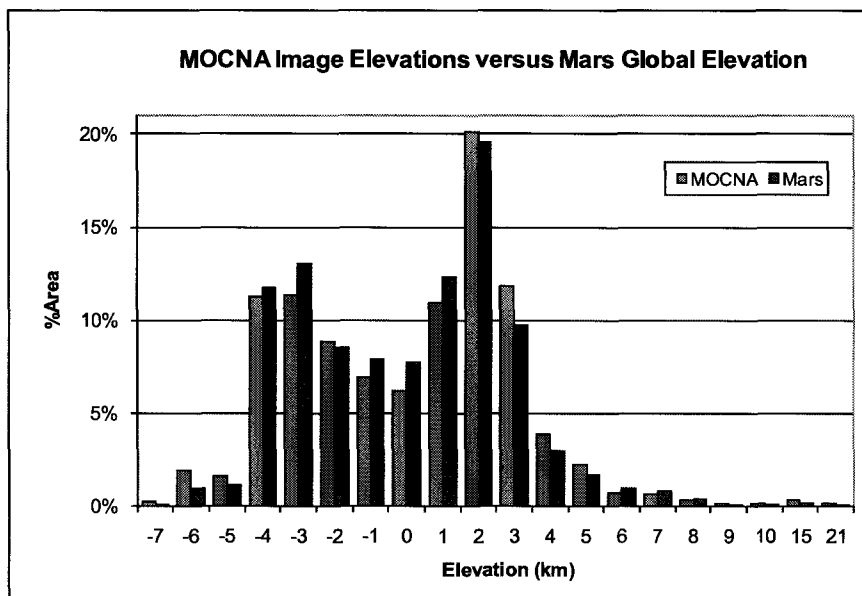


Figure 3.3: Percent surface area covered by elevations in 1km bins for Mars and our sample of MOCNA images. Our total image areas are within ~11% of actual elevation areas for ~91% of the Martian surface. Elevations greater than 3km and below -4km are mostly oversampled.

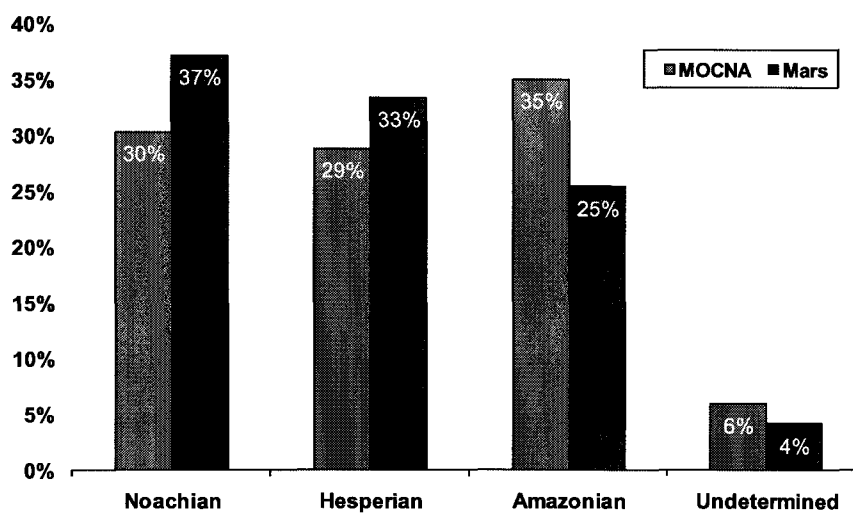


Figure 3.4: Percent surface area covered by age units for Mars and out sample of MOCNA images. Older Noachian and Hesperian units are undersampled by 18% and 14% respectively. Younger Amazonian units are oversampled by 38%.

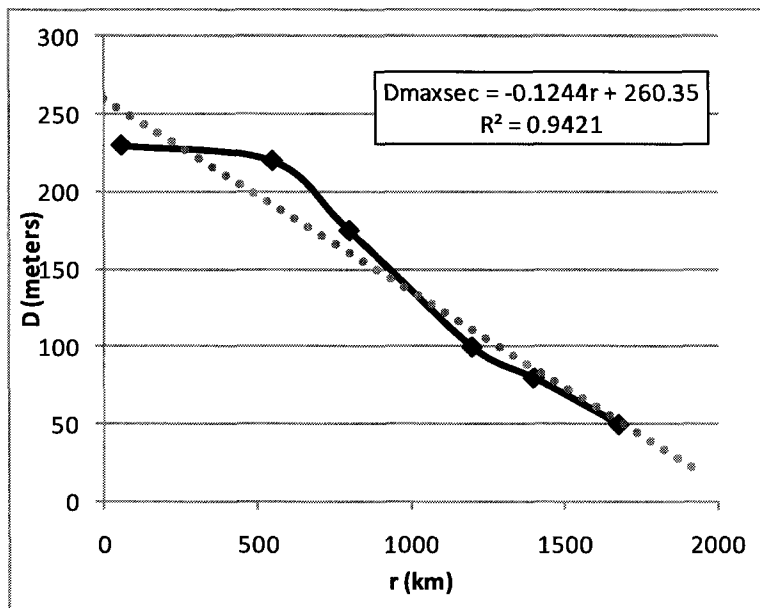


Figure 3.5: Size-diameter relationship for maximum secondary size distal to Zunil. The maximum diameter Zunil secondary from Preblich et al. [2007] is plotted versus its radial distance from Zunil expressing a size-diameter (i.e. size-velocity [e.g. Melosh, 1984. Vickery et al. 1987]) relationship; secondary craters get smaller with distance from the parent primary crater that they were ejected from. Secondary craters of a maximum size should not exist beyond a predicted radial distance (e.g. 50 m in diameter secondaries should not be found farther than ~1700 km from Zunil).

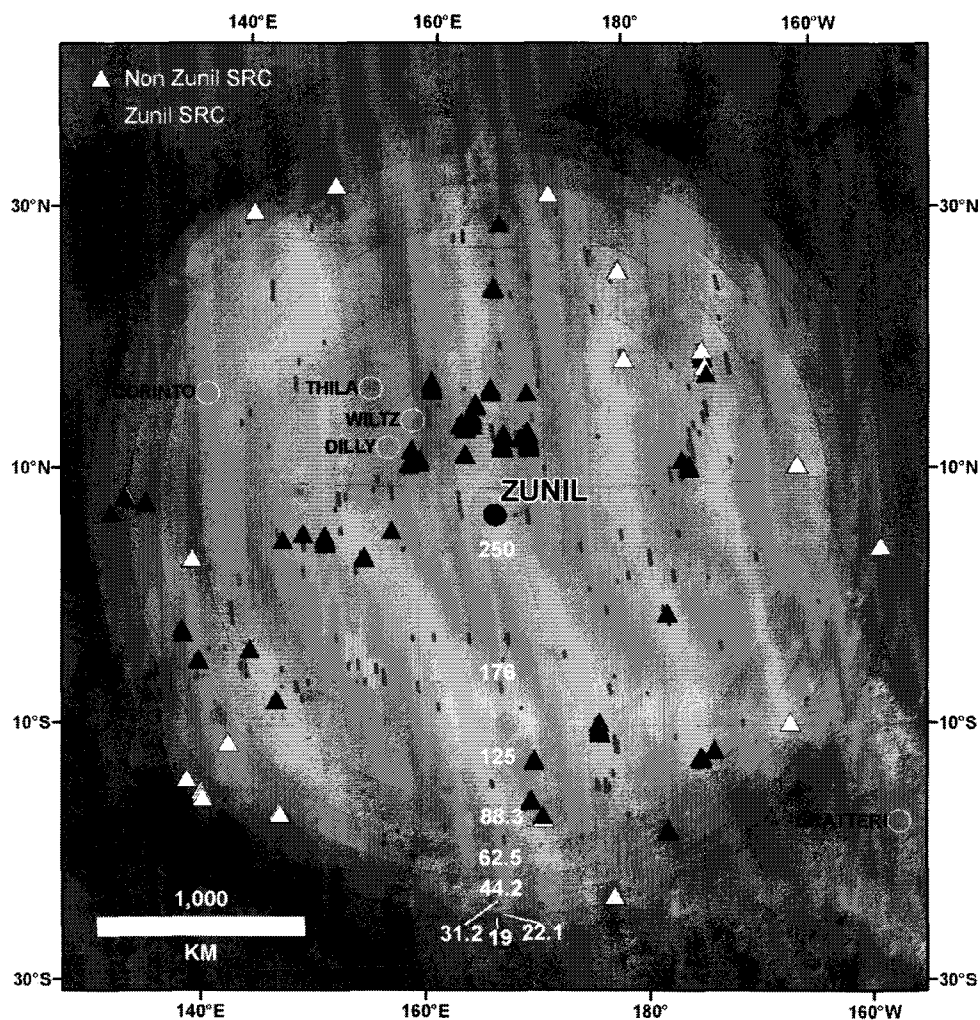


Figure 3.6: SRC within the secondary field of Zunil. White triangles represent those SRC that do not follow the diameter-distance (size-velocity) relationship; these must either be primaries or secondaries from another unidentified primary crater. Each concentric ring represents the maximum distance a secondary of a given diameter, D_{maxsec} , will be produced; past this distance all secondaries will have smaller diameters for the source primary. White circles denote large multi-kilometer in diameter primaries whose size-velocity relationship is unknown that may have contributed SRC secondaries to this region. White numbers indicate the D_{maxsec} diameter and boundary for secondaries from Zunil. Long grey boxes are MOCNA footprints used in the search for SRC from Calef et al. [2009] within the D_{maxsec} 19 m buffer. This map is in a polar azimuthal equidistant projection centered on Zunil.

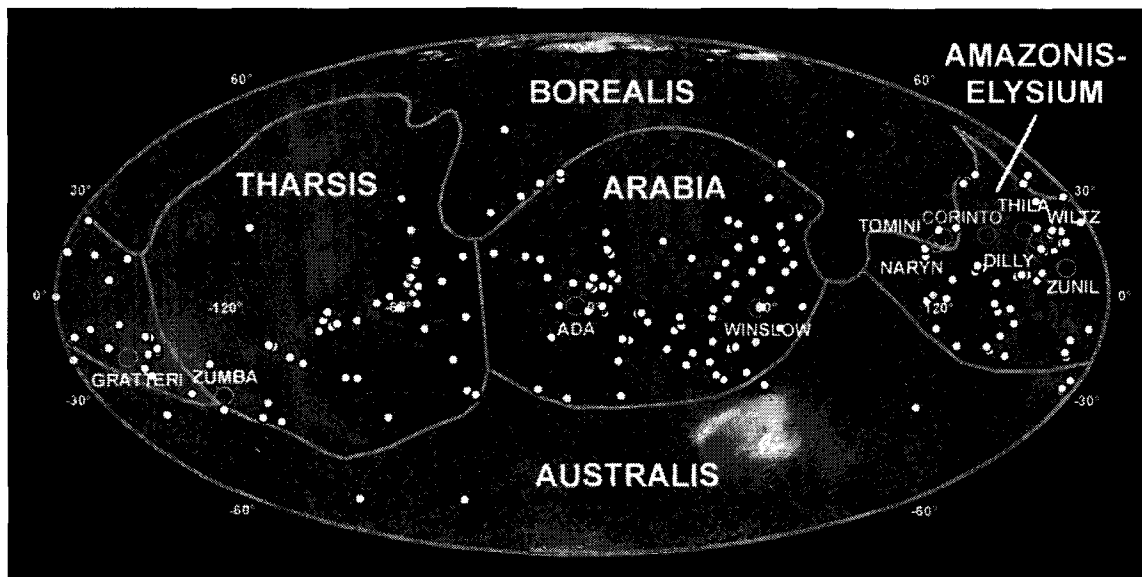


Figure 3.7: Five generalized physiographic regions for our study. (top) Main groups include Tharis (center left) and Amazonis-Elysius (far left and right): the two main volcanic centers on Mars, Arabia Terra (center): a mid-latitude Noachian plateau, and Australis (bottom) and Borealis (top): the southern and northern high-latitude polar areas, respectively. White points indicate 631 individual SRC found in MOCNA images from this study. Grey dots represent centroids of the 4264 images evaluated for SRC presence. White circles represent known large (>1 km diameter) rayed craters.

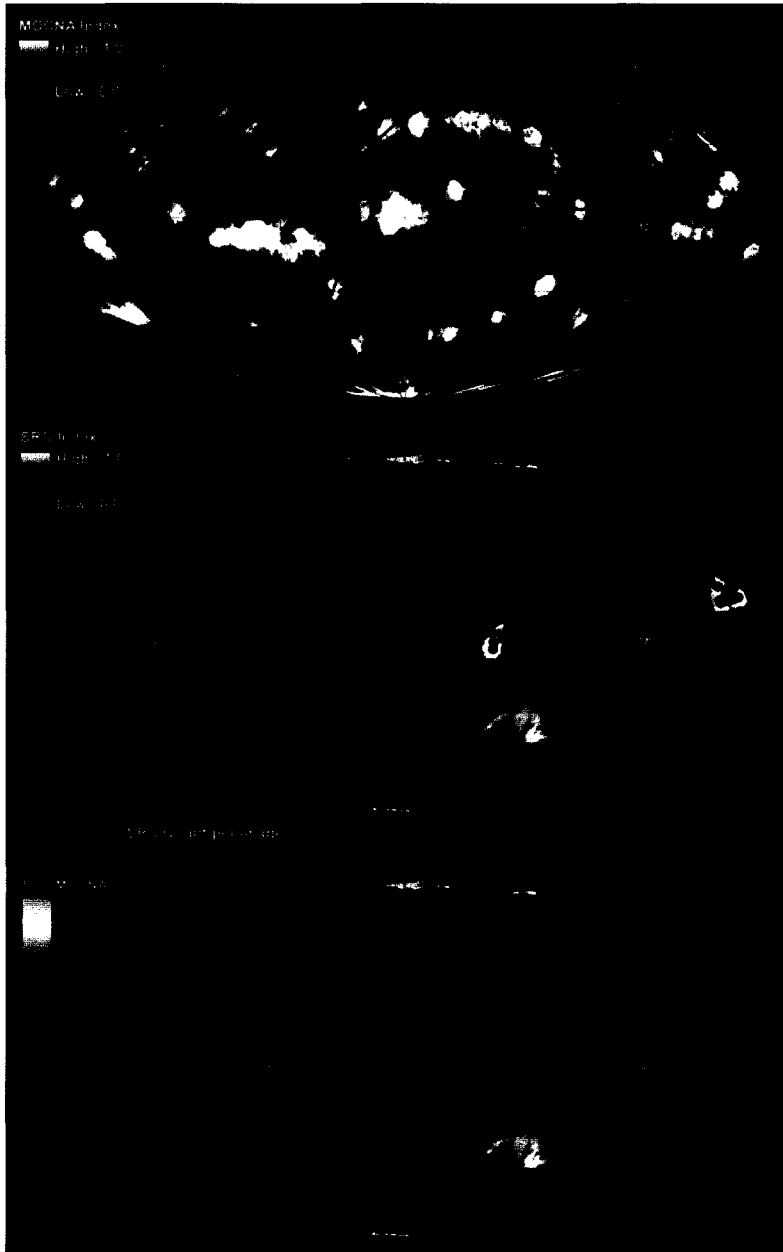


Figure 3.8: Small rayed crater indices for Mars. (top) Density of MOCNA image centroids within a 5 degree radius. (middle) Actual small rayed crater counts per image overlaid on normalized SRC point density estimates over a 5 degree radius circle. (bottom) Normalized difference index between SRC density and MOCNA image density. Blue areas represent higher counts of SRC compared to lower counts of MOCNA images. Red areas have many images, but low SRC counts. Tan areas have about equal normalized ‘densities’ of images and SRC counts.

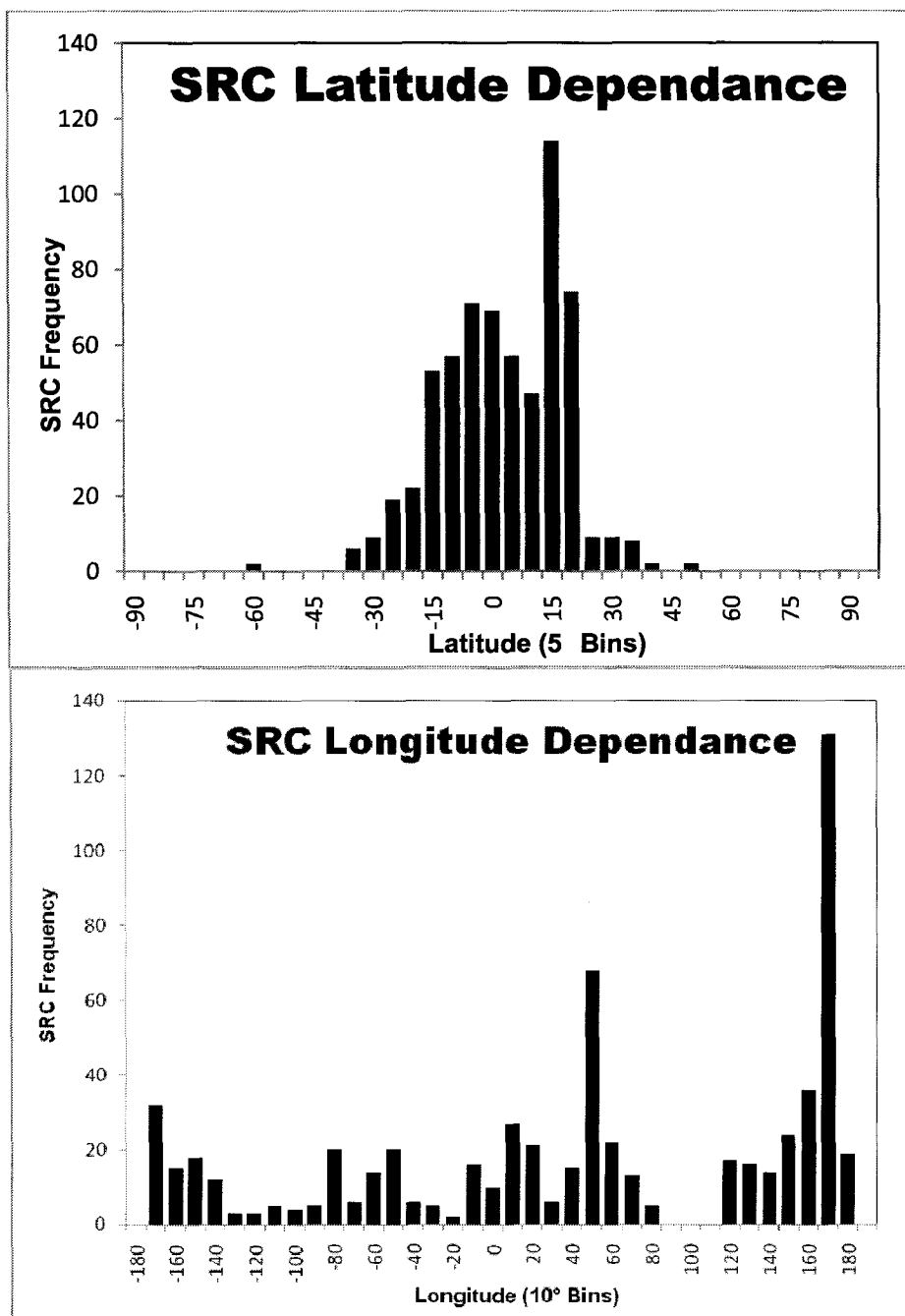


Figure 3.9: Latitude and longitude dependence of the global SRC population. Note the peak of SRC at $\sim 15^{\circ}$ - 20° N (top) and 170° E bins; this coincides approximately with Zunil, a large primary known to have produced an extensive secondary cratering field. (bottom) An additional prominent peak occurs at 50° E longitude that does not correlate with the known position of any large rayed primary craters from Tornabene et al., [2006].

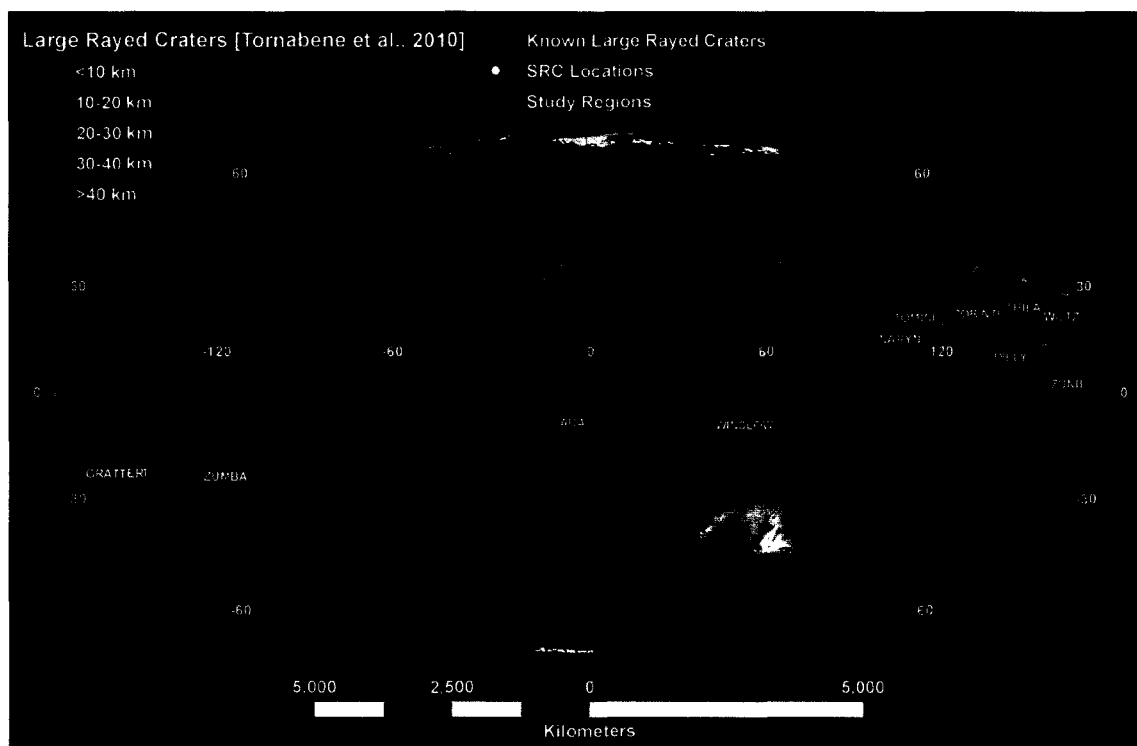


Figure 3.10: Large rayed craters on Mars. Besides the nine well known large (>1km in diameter) rayed craters identified by Tornabene et al. [2006] and two ~1km diameter rayed craters in Arabia (Ada and Winslow), 78 additional large rayed craters have been identified by Tornabene et al. [2010] with ‘fresh’ morphology and rays appearing in THEMIS night-time thermal infrared imagery. It is possible that these newly identified rayed craters are responsible for generating some (if not many) of the SRC in this study in the form of secondary cratering events. Colors represent classes by crater diameter.

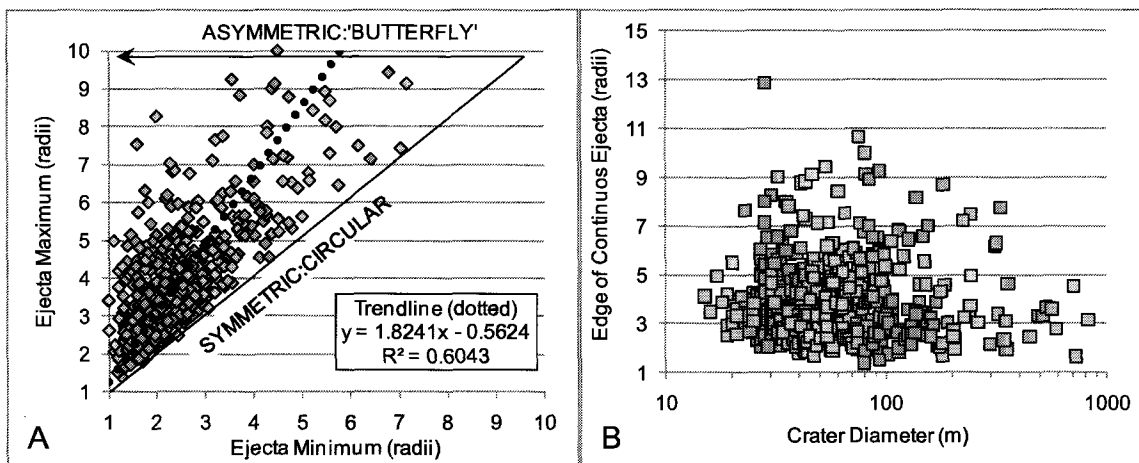


Figure 3.11: SRC continuous ejecta morphology across Mars. (a) Approximately 60% ($R^2=0.6$) of the variability in the ejecta blanket morphology can be described as 'elliptical', between being 'circular' (a feature of vertical impacts) and having a 'butterfly' pattern typical of the lowest impact angles. (b) Crater diameter does not appear to have a strong correlation with the radius of continuous ejecta near the crater rim. However, craters less than 30 m in diameter appear to erode more quickly than larger craters (note the sharp increase in radii from ~ 4.5 to 7 at ~ 30 m in diameter) and there is a weak reciprocal relationship with decreasing ejecta radius as crater diameter increases; older craters, with thicker ejecta blankets, retain ejecta longer.

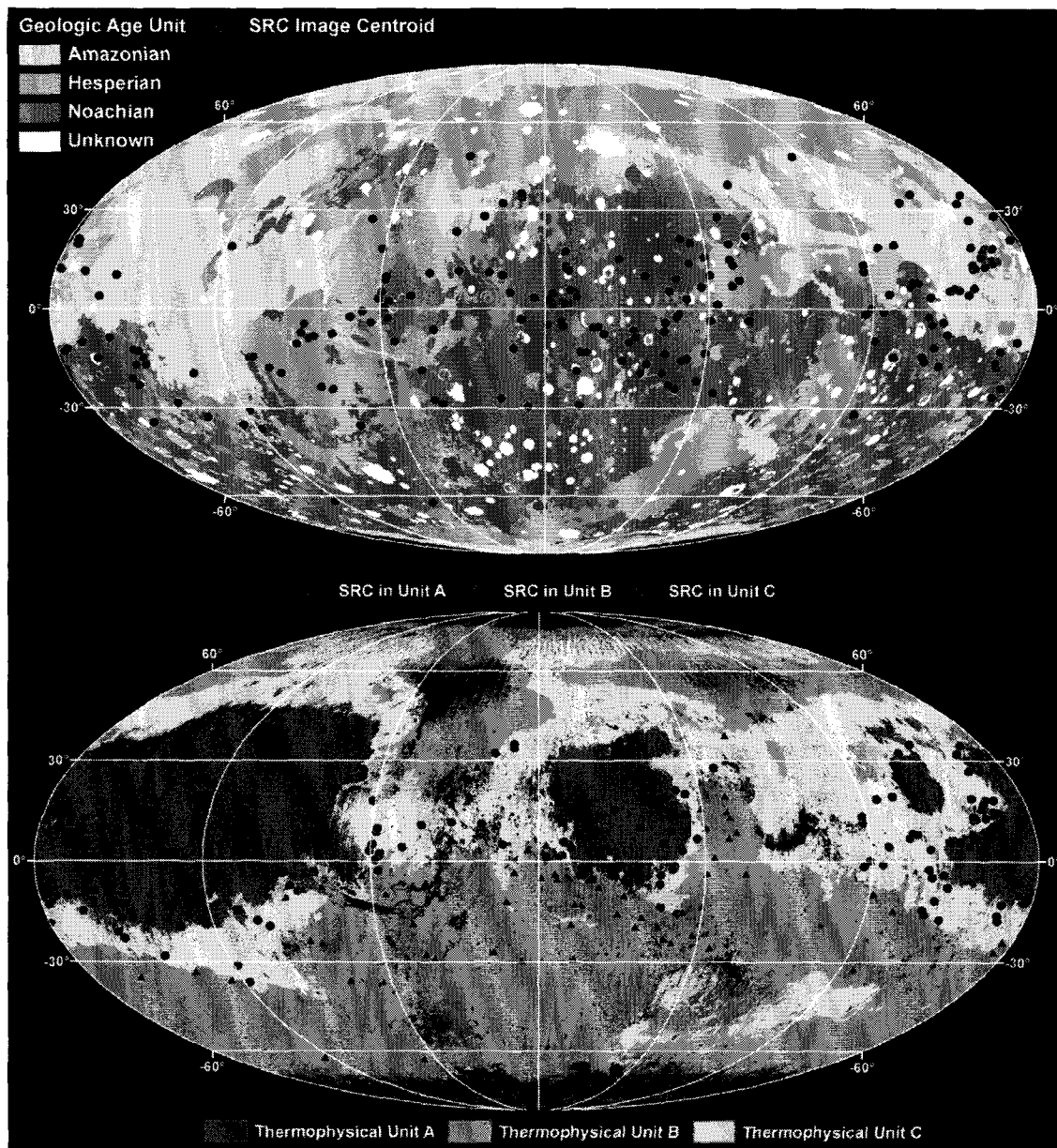


Figure 3.12: Geologic age unit distribution, thermophysical units and SRC occurrence on Mars. 50% of SRC images fell on Noachian units (predominately Npl1, Npl2, and Npld), while mostly Hesperian ridge plain units (Hr) and Amazonian units of the Elysium Formation (Ae11 along with Achu and Apk) had near equals numbers (26% and 21% respectively). 47.5% of SRC images fell on Unit C, while 35.5% were located on Unit B and 17.0% on Unit A. Black thermophysical areas represent areas that did not fall into one of the three thermophysical unit descriptions. Original thermophysical unit designations were established by Mellon et al. [2000] and updated here with night-time thermal inertia data from Putzig et al. [2007].

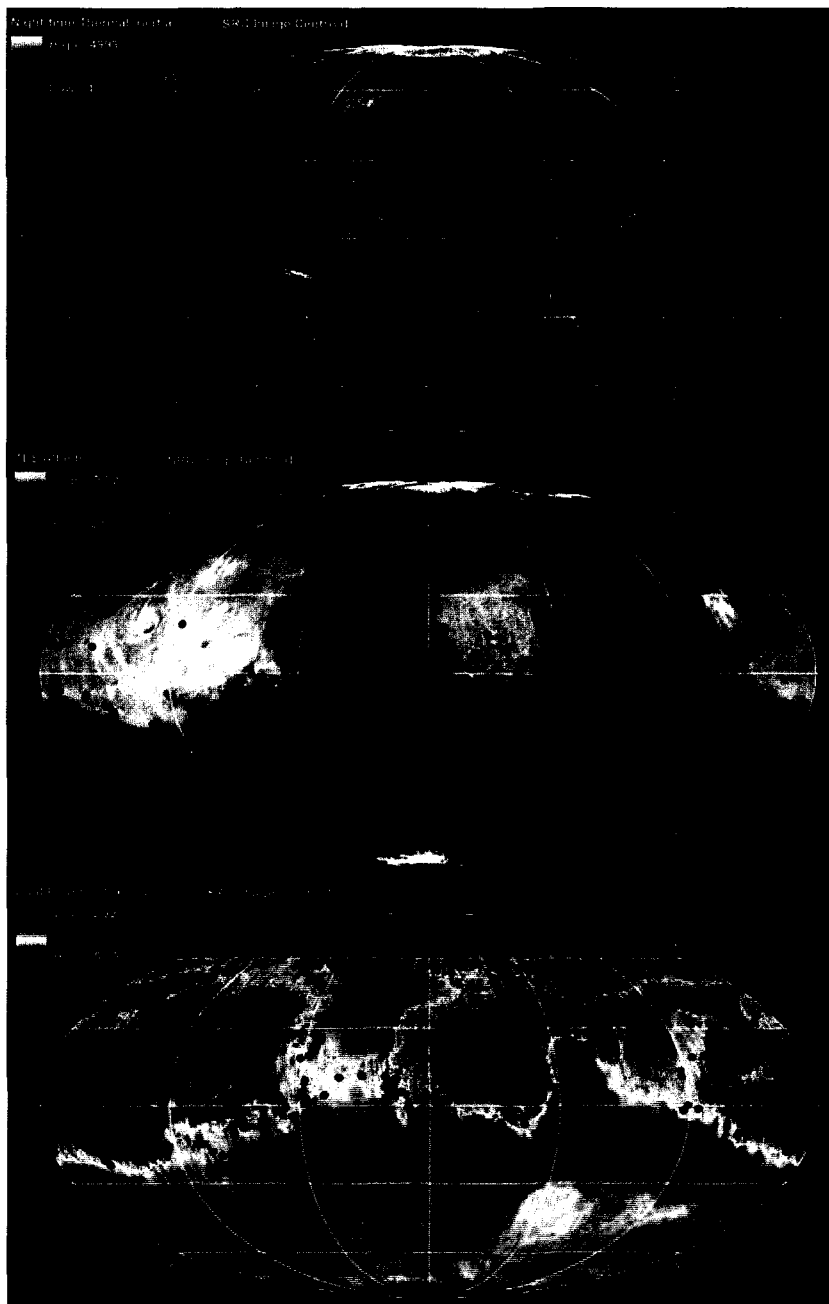


Figure 3.13: Night-time thermal inertia values, albedo and dust cover with SRC occurrence on Mars. SRC appear to be somewhat absent in low thermal inertia (i.e. dust covered) areas that correlate with Unit A (Figure 10). SRC occurrences versus high albedo regions correspond directly to high dust concentrations (low DCI values), while albedo dark areas are indicative of less dust deposition (high DCI values). SRC appear absent in 'bright and dusty' regions. Thermal inertia units are in $\text{tiu} (\text{J m}^{-2} \text{K}^{-1} \text{s}^{-1/2})$.

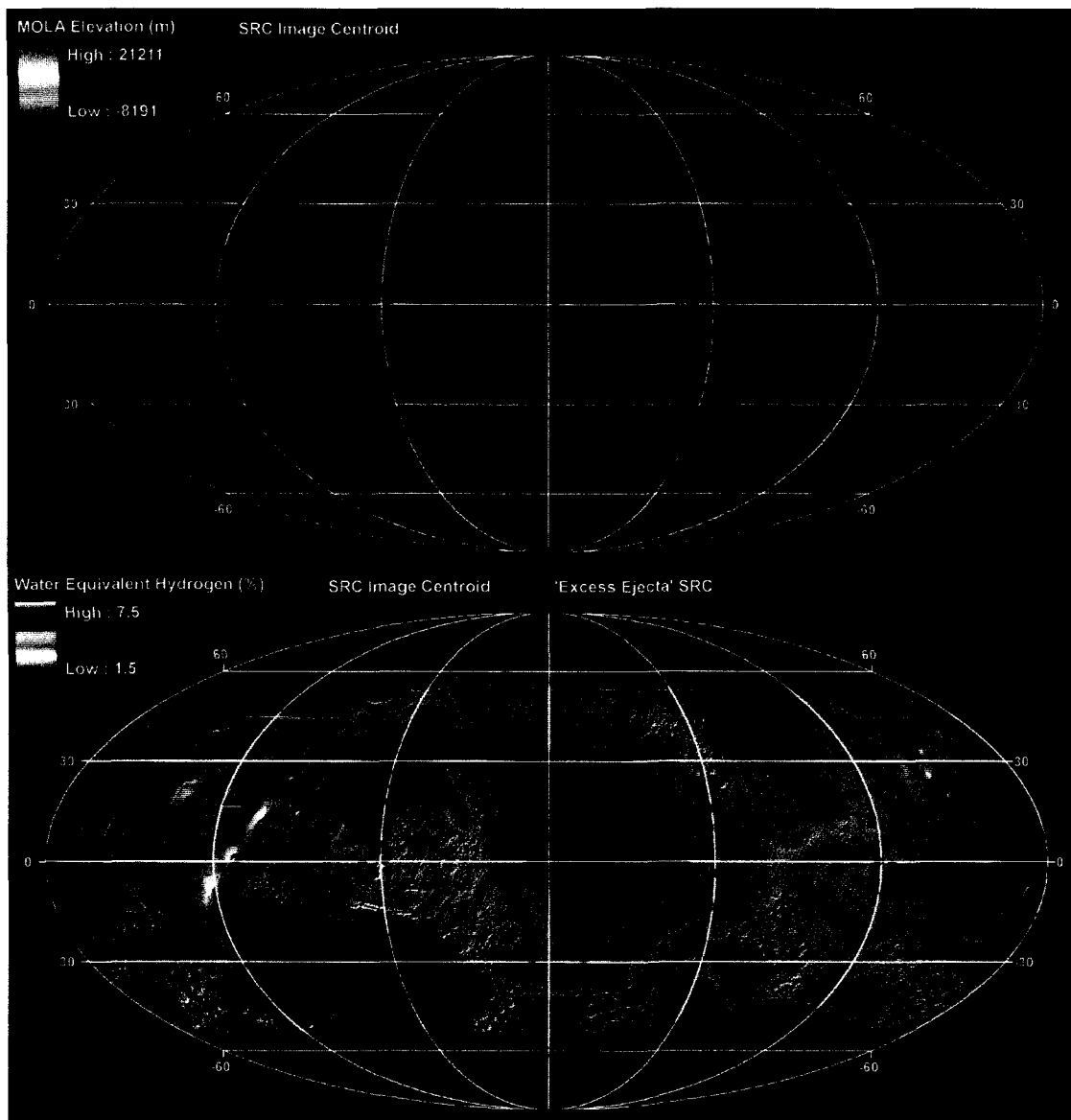


Figure 3.14: SRC occurrences versus MOLA elevation and water equivalent hydrogen. Most SRC occupy a range of elevation values (~ 3750 m to ~ 6000 m). SRC appear deficient in the lowest WEH values ($< 2.5\%$), except 'excess ejecta' craters (triangles) that favor higher WEH values. WEH above $\pm 45^\circ$ approaches tens of percent (northern and southern border values are interpolation error), but generally was outside of the majority SRC distribution.

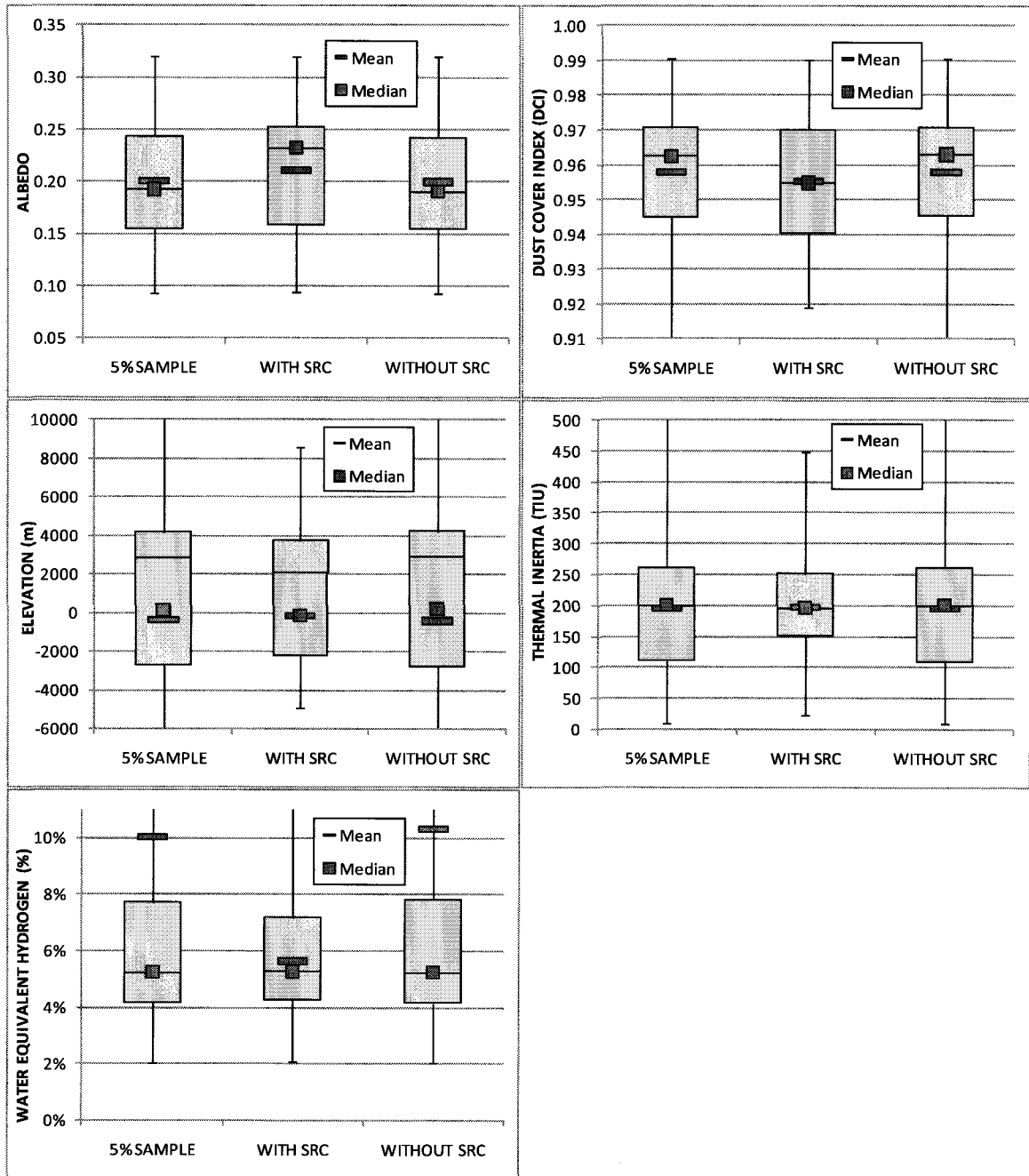


Figure 3.15: Box plots of SRC occurrence and non-occurrence from our study images. Upper grey box represents the 75% Percentile range and the lower grey box the 50% Percentile of the samples. Error bars represent the minimum and maximum range of values. Maximum values much greater than the mean (i.e. large variance) are cut off to preserve quantile ranges. Please see Table 3.3 for the actual statistic values.

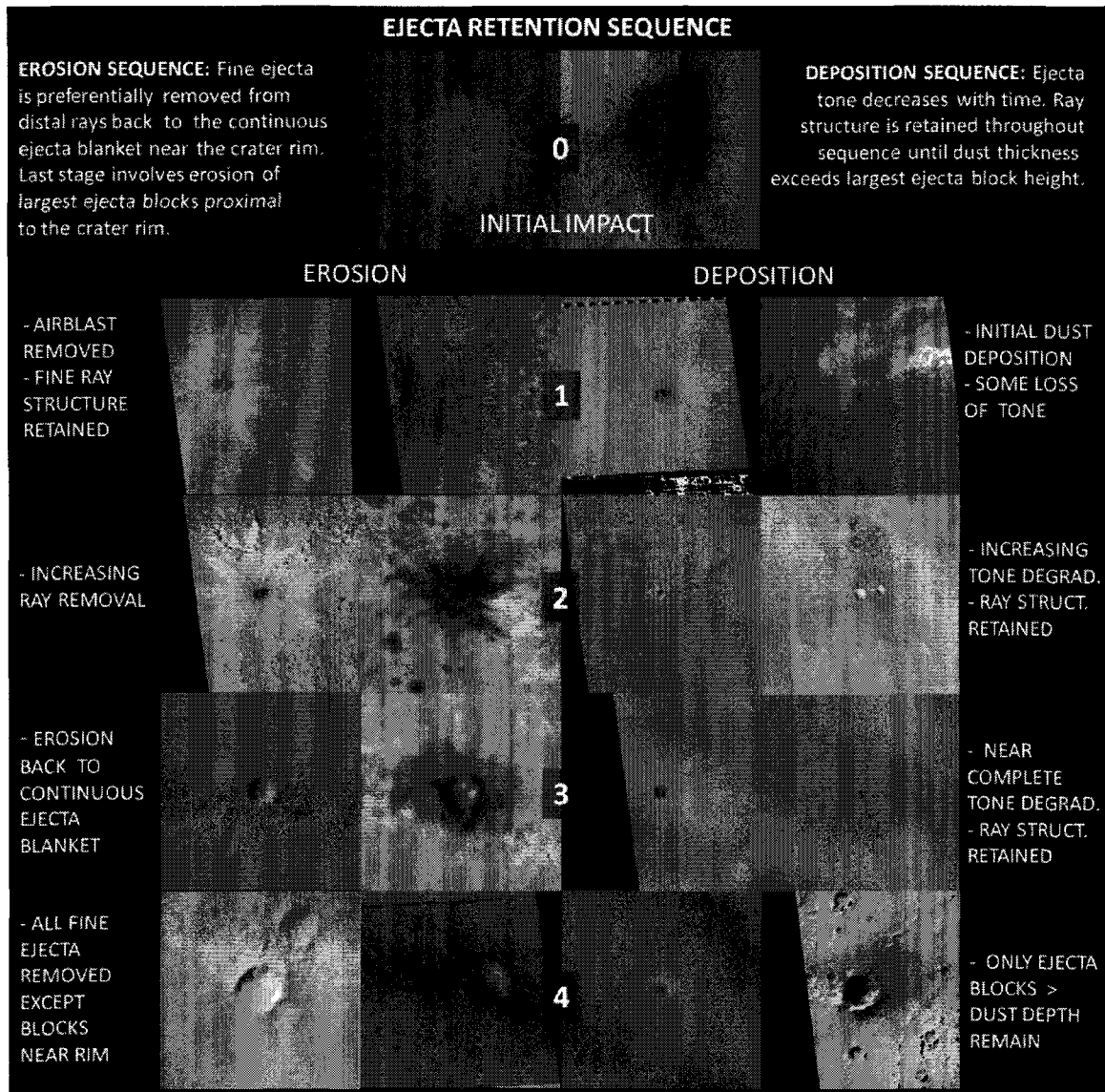


FIGURE 3.16: Observed SRC ejecta retention sequence on Mars. Both bright and dark rayed craters appear to experience the same morphologic changes of retention for both erosion and deposition. SRC at ‘stage 0’ were first discovered by Malin et al [2006] and are not incorporated into our study.

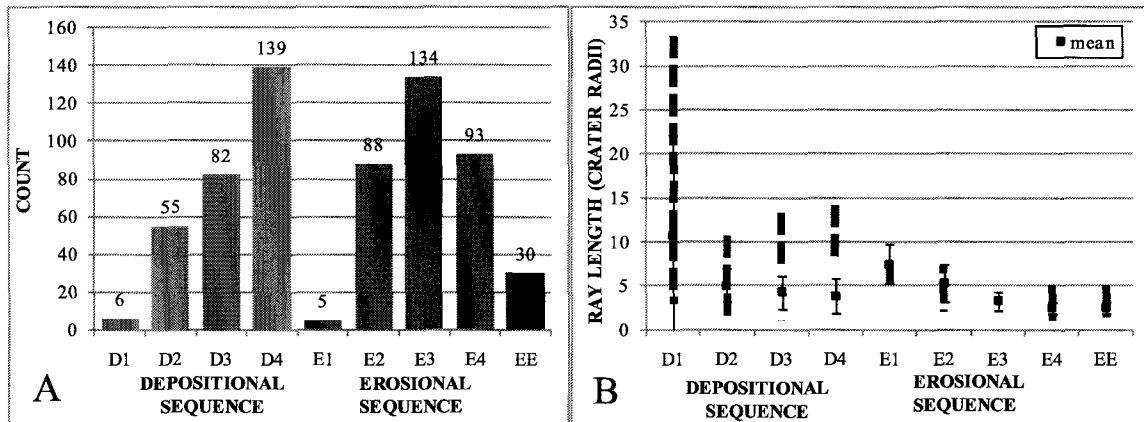


FIGURE 3.17: Ejecta retention sequence statistics for SRC. (A) Total counts for each sequence and (B) mean, minimum, and maximum ray lengths for the most distal rays from each SRC. Error bars in (B) represent one standard deviation from the mean.

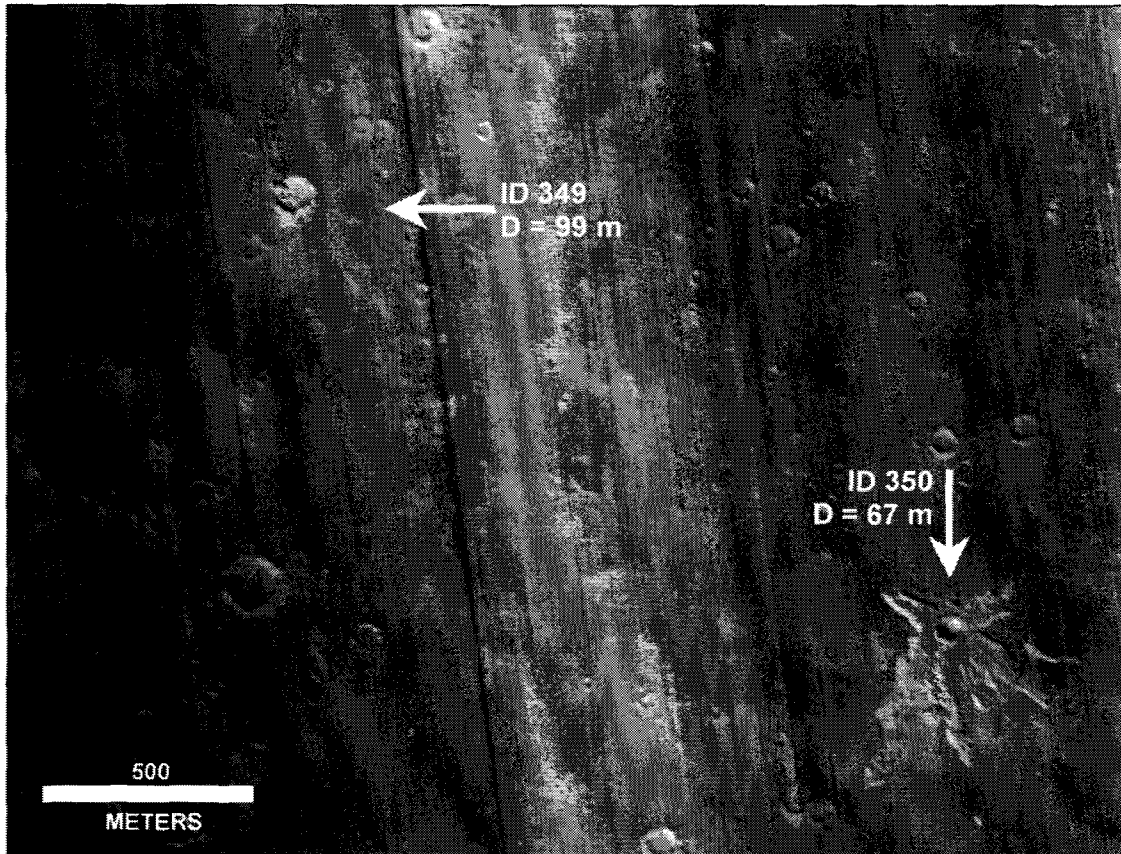


FIGURE 3.18: SRC from different events. This image, MOCNA M1104273, contains several craters (two shown here) that are at two different erosional stages. Uprange impact angles (white arrows), based on the downrange azimuth of the ejecta and uprange forbidden zone, between the craters is orthogonal and indicate impacts at different times. Sun angle in the image is from lower left half of the image. Image is courtesy of NASA/JPL/MSSS.

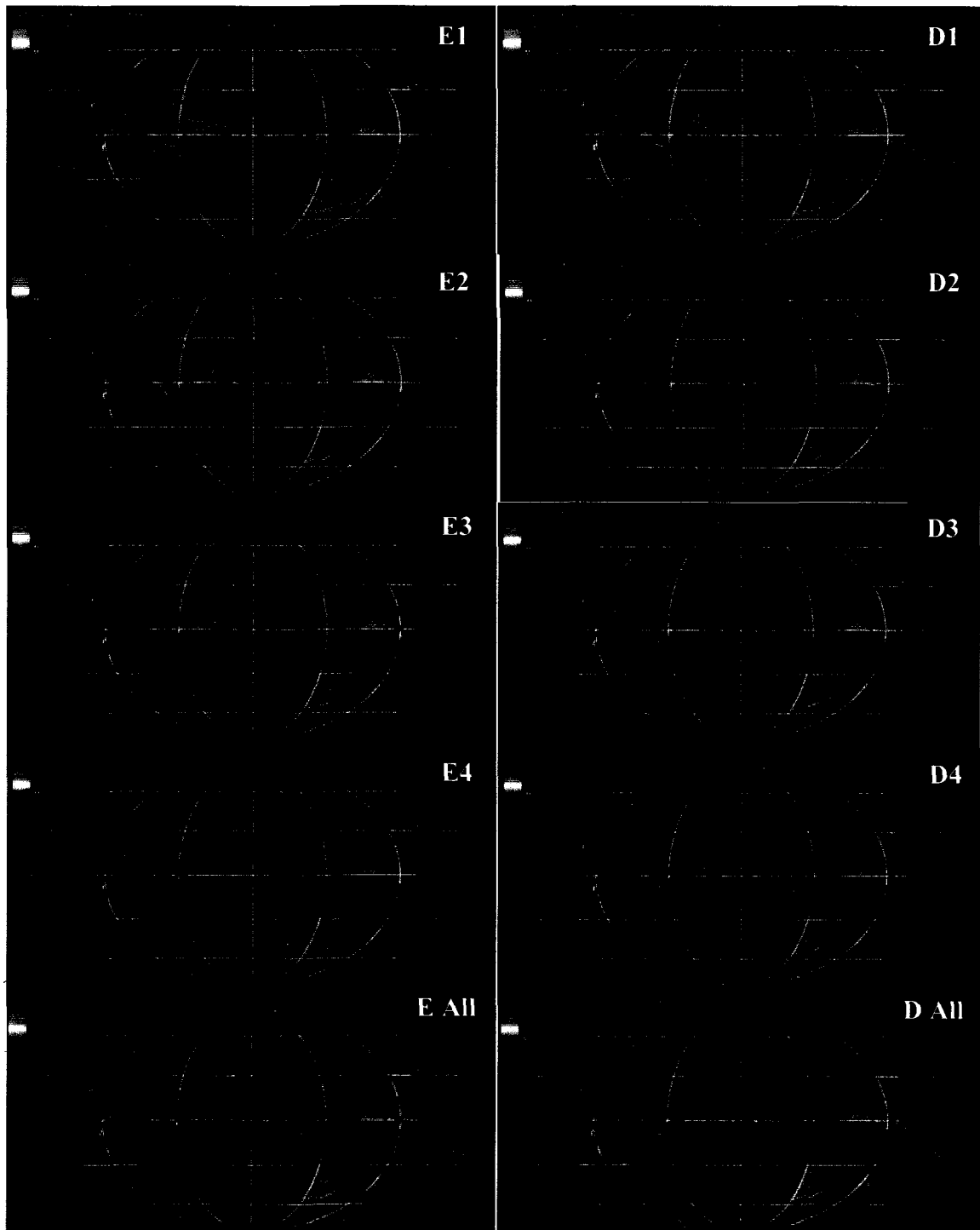


Figure 3.19: SRC images classified by the erosion or deposition ejecta retention sequence on Mars. Retention sequence stages are marked in the upper right-hand corner.

CHAPTER 4:

Small Rayed Crater Ejecta Retention Age Calculated from Current Crater Production Rates on Mars¹

ABSTRACT

Small (diameter <1 km) rayed primary impact craters are spatially and temporally random, creating ejecta over all surfaces on Mars. Estimating ejecta retention age, the time span when ejecta remains in place around a crater, can be applied to estimate the timescale that surface processes operate on, thereby obtaining a history of geologic activity. However, the abundance of sub-kilometer diameter (D) craters identifiable in high-resolution imagery (down to ~25cm/pixel on Mars) has led to questions of accuracy in absolute crater dating and estimating ejecta retention ages (E_{ret}). This research calculated the ejecta retention age for small (diameter <1 km) rayed impact craters (SRC) on Mars using current estimates of the Martian impactor flux adjusted for meteorite ablation losses in the atmosphere. Utilizing published model results for atmospheric filtering of impactors in a 6mb atmosphere, we correct for asymmetries in the asteroidal impactor population, meteorite loss from burn up in the atmosphere, and reductions in crater frequency for $D < 30$ m craters. Retention ages for three equatorial regions and both polar latitudes on Mars were constructed based on crater counts plotted in standardized

¹Calef, F. J. III, R. R. Herrick, and V. L. Sharpton (2010), Small rayed crater ejecta retention age calculated from the current crater production rate, prepared for submission in the Journal of Geophysical Research – Planets edition.

Hartmann production function (HPF) and the current production function (CPF), both corrected for atmospheric filtering, in log-incremental diagrams. The corrected estimates of the martian impact flux increase from 1.28×10^{-7} upwards to 6.29×10^{-7} craters $\text{km}^{-2} \text{a}^{-1}$, increasing the power-law slope of the CPF to -2. Calculated ejecta retention ages exploiting new Martian isochrons developed from the CPF generate E_{ret} on the order of 10 ka to 25 ka for $D = 30\text{-}500$ m SRC in equatorial ($\pm 30^\circ$) Mars. Ejecta from Arabian and Tharsis SRC retained ejecta from ~ 20 ka to 50 ka for a similar D range before an increase in retention to ~ 100 ka for $D \geq 500$ m. Amazonis-Elysium SRC retain ejecta from $\sim 60\text{-}100$ ka for $D = 30\text{-}500\text{m}$ and up to 350 ka for larger diameters, though these estimates are considered to be skewed by secondary cratering contaminating counts. In general, CPF isochrons estimate SRC ages an order of magnitude younger than the HPF. All equatorial SRC decrease in retention ages below 50 m diameters for Arabia and Amazonis-Elysium and 100 m diameters for Tharsis; interpreted as a decrease in retention time with decreasing D (i.e. thinner ejecta blankets).

Dust deposition and periglacial erosion operate at a maximum on thousand year timescales. Equatorial eolian erosion are much slower mechanisms for reworking ejecta at upwards of 100 ka. Based on our ejecta retention ages, a major increase in erosion and/or deposition processes may have occurred across Mars at ~ 100 ka, removing most subsequent traces of SRC ejecta. This date may mark the end of the last major obliquity excursion and significant climate change on Mars.

4.1 INTRODUCTION

4.1.1 Understanding Small Rayed Crater Ejecta Retention

Small rayed craters (SRC) (Figure 4.1), those with diameters (D) <1 km, occur over many different terrains on Mars. Some SRC represent new meteorite impacts (i.e. primaries) formed over the last 3 or 4 Martian (6 to 8 Earth) years [Malin et al., 2006, Byrne et al. 2009]. Others are secondary cratering events (i.e. secondaries) created from ballistically ejected blocks from a larger impact that spatially cluster around primary craters like Zunil (Figure 4.2) [McEwen et al., 2005; Tornabene et al., 2006]. One common feature for both types of SRC is the retention of ejecta. In contrast, many small craters have since lost their ejecta to surface processes working over millions to billions of years. While impact rates from asteroid populations and crater retention times are well constrained by crater counting and radiometric dating from samples returned from the Moon, we know little about ejecta retention and the timescales it operates on. Ejecta retention serves as a proxy for dynamic surface processes that bury new features, exhume older ones, and generally shape the surface of Mars within the recent past. We can define an ejecta retention time, E_{Ret} , as the time it takes to erode or bury ejecta to the point that only the rim of the crater remains visible. If we understood the distribution of rayed craters and their age since formation, we could estimate E_{Ret} for various regions on Mars. Areas with increased or decreased retention ages could elucidate target properties, timescales of active surface processes, and possibly recent climate variations in the last few million years. To estimate E_{Ret} , one needs to know the SRC formation time, which

correlates to impact origin. This is because a family of secondaries share a common formation time (i.e. the impact time of the primary that ejected them), yet are displaced over a range of azimuths and distances. In contrast, primaries impact Mars as a Poisson process with continuous and independent formation times. If a region is dominated by secondaries, a retention time would be overestimated (a maximum) based on a pure count of SRC per unit area, much as argued by McEwen et al. [2005] for crater retention ages. Extracting the origins of these SRC, either as primary or secondary impacts, can be accomplished via their ejecta morphology [Calef et al., 2009] or from image change detection [Malin et al., 2006] with moderate to good success. However, those secondaries outside the ray structure from their primary of origin, background secondaries [Shoemaker, 1965] or far-field secondaries [Werner et al., 2009], present a unique case for identification on Mars due to their emplacement at near-escape impact velocities (approaching 5 km s^{-1}) that are a significant fraction of meteor impact velocities ($\sim 10 \text{ km s}^{-1}$) in this region of space. Another caveat in either identification method is time. Secondaries are upwards of 5.4×10^5 years in age (e.g. the estimated age of the most recent known large primary crater Zunil [Kreslavsky, 2008]), while primaries impacted earlier than Viking I imaging may not retain the original ephemeral ejecta planform features, such as air-blast zones and distal ray structure, that are unique to them [Calef et al., 2009]. If counts of secondaries can be removed from the primary population, even partially, this would improve ejecta retention rate estimates as SRC are used to establish timelines for recent geologic surface processes on Mars.

Rayed craters represent a young set of geologic features on Mars [e.g. Tornabene et al., 2006]. Recently discovered SRC primaries (Figure 4.1A) [Malin et al., 2006; Kennedy and Malin, 2009; Daubar et al., 2010] and SRC secondaries of Zunil (Figure 4.1B) [McEwen et al., 2005; Preblich et al., 2007] embody a fresh crater population with minimal eolian modification and infilling, compared to degraded and ejecta-less craters. Dating SRC using production rates extrapolated down from billions to single years as done by Hartmann [2007] and based on rates from impacts into bedrock as opposed to regolith (as argued by Daubar et al. [2010]) may produce erroneous conclusions. Current crater production estimates appear to be well within an order of magnitude within the past 10^6 years as secondary cratering production of decameter diameter craters are suspected not to have been globally active during that time [Hartmann, 2007]. An initial census of SRC on Mars was conducted using a 5% sample of MOCNA images (e.g. Figure 4.1C, 4.1D) [Calef et al., 2010] revealing some latitudinal and longitudinal clustering that coincided with known large rayed primaries (e.g. Zunil) and many were within close proximity to other multi-kilometer rayed craters recently identified by Tornabene et al., [2010]. The SRC population could lend insight on the efficacy of absolute dating with small diameter craters and the suspected recent activity of some geologic processes on Mars. To access this knowledge, primary and secondary rayed crater populations need to be separated and more accurately dated with current crater production values.

4.1.2 Dating small D craters on Mars

Based on crater counts and absolute dating of rocks from lunar cratered surfaces, researchers [e.g. Hartmann, 1999] have extrapolated a dating methodology (i.e. isochrons) to date Mars' surfaces and hence surface age from the Noachian (>3 Ga) to the very late Amazonian (<1 Ma). Hartmann [1999] established isochrons, lines of equal age corresponding to crater production rates, for Mars by:

- (1) comparing the cratering rate for Mars to the Moon (R_{bolide} estimated at $\sim 2.6 \pm 0.7$ [Hartmann, 2005]),
- (2) comparing the number of lunar craters (binned by rim diameter) per unit area to an absolute radiometric date of lunar samples at 3.5 Ga, 3 Ga and 1 Ga,
- (3) fitting a power-law to the lunar crater population in the form of log number of craters per area, N , versus log crater diameter, D :

$$\log N = -b \log D, \quad (4.1)$$

where b is the power-law exponent (i.e. slope), and finally,

- (4) calculating the size/frequency distribution (corrected for R_{bolide} , diameter scaling due to different gravity and impact velocities as well as atmospheric filtering of small meteoroids on Mars) for a theoretical martian surface of the same age.

From this methodology, additional isochrons are extrapolated to other time periods. With this data, counting the number of craters per unit area by diameter bins can be graphed to see which linear power-law isochron the data aligns with and thereby determine an approximate age of the surface (Figure 4.3). A similar production function fits a

polynomial to N generating a better fitted curve than simple straight-line segments [Neukum et al., 2001], though results from both are similar with a factor of a few. Recently, a record of new rayed impacts over the last five Martian years appears to corroborate this technique using Hartmann and Neukum production functions [Neukum et al., 2001; Hartmann 2005] to be accurate within a small factor down to single years in absolute age estimation using craters whose D measure ≤ 80 meters [Malin et al., 2006; Kreslavsky, 2007; Dauber et al., 2010]. However, both the Hartmann (HPF) and Neukum (NPF) functions are derived from multi-kilometer diameter craters governed by the gravity regime of cratering (i.e. where gravity is the driving force in crater formation), excavating bedrock and extrapolate ages down from billions of years to thousands. In contrast, current cratering rates produce sub-kilometer diameter craters predominately in the strength regime (i.e. target bulk strength is more important in determining crater growth) or at the most a transitional strength-gravity regime, excavate mostly regolith targets, average tens of meters in diameter, and are estimated to be within a few to tens of years of age.

With the rapid increase of new satellite imagery with pixel sizes in the single to sub-meter widths, a controversy has developed over the efficacy of using small craters for determining surface ages. Earlier studies had purported that an increase in the size-frequency distribution slope at $D < 1$ km on the Moon, the so-called “steep branch” of the isochrons (Figure 4.3), was directly related to an increase in secondary cratering events (i.e. new craters from ejected blocks from a primary, not directly from meteorite impacts) being recorded along with similarly sized primaries [e.g. Shoemaker, 1965]. With the

discovery of a large ($D = \sim 10$ km) rayed crater, Zunil, that is linked to $\sim 10^8$ small (10 m $< D < 200$ m) bright-rayed secondary craters (Figure 4.1B) [McEwen et al., 2005; Preblich et al., 2007], it has been proposed that many, if not the majority of craters on Mars with $D < 1$ km are in fact secondaries. Modeling has shown that a large primary similar to Zunil impacting into a basaltic target (i.e. lava flow) may create upwards of 10^6 - 10^8 10 cm diameter fragments capable of re-impacting with enough force to create a $D \geq 15$ m crater similar to a primary [McEwen et al., 2005]. To date, seven multi-kilometer diameter Martian primaries with rays visible in the thermal infrared have been recognized [Tornabene et al., 2006]. The cross-over diameter, D_c (where counts of secondaries begin to dominate the number of primaries in the same D), is estimated to be between ~ 250 m to 500 m [McEwen et al., 2005]. However, proponents of the crater dating system have argued that while this may be true for “statistically clustered” secondary crater fields near the primary crater rim, “background” or “far field” secondaries are more homogeneously distributed and would not greatly contribute to the overall counts used to measure surface ages [e.g. Hartmann, 2007, Hartmann et al., 2008, Werner et al., 2009]. Indeed, even if secondaries are counted along with primaries, the difference in surface age versus a purely primary surface has been demonstrated in the Cerberus plains (a location with Zunil secondaries that are recognized by their unique ejecta blanket morphology) to be different only within the same order of magnitude (from 14 Ma to 25 Ma; less than a factor of two) [Werner et al., 2009]. In contrast, observations from extensive secondary fields on Europa indicated that 95% of sub-kilometer diameter craters there were secondaries and crater populations of this diameter on any large rocky

body are dominated by secondary impacts [Bierhaus et al., 2005]. If true for Mars, dating surfaces with small $D < 1$ km craters would yield unrealistic ages that currently predict very young active surfaces; e.g. in Nirgal Vallis, gully depositional fans intruding dunes have been dated to as recent as 300 ka using small D craters [Reiss et al., 2004].

Preblich et al. [2007] mapped unambiguous bright rayed secondaries out to 1700 km both on and between thermally distinct rays radial to the 10.1 km diameter primary Zunil; a total of $\sim 10^8$ secondaries $D \geq 15$ m were estimated. A power-law slope (i.e., b) of this population ranged from -3.4 down to -5 inside Zunil rays [Preblich et al., 2007]. This is similar to the steep branch of isochrons for craters of this size from Hartmann [2005]. Qualitative observations of small craters conclude that most are spatially clustered, have experienced similar degradation, and are shallow [McEwen et al., 2005]. However, non-clustered far-field secondaries, hundreds of km distant from the primary, may share several or all physical traits of primary impacts due to their higher impact velocities (approaching Mars' 5 km s^{-1} escape velocity). Therefore, secondaries may change the expected age of a surface by either: a) ageing a surface unit by increasing the number of craters generating an older date, or b) obscure the true $-b$ production slope, thereby creating younger units (counts should fall above an older isochron, but the slope is too steep).

4.1.3 Estimating the Current Cratering Rate for Small Rayed Craters on Mars

Several estimates of the current cratering rate based on rayed craters with diameters of a few to few tens of meters have recently been published for Mars. The first

estimate by Malin et al. [2006], found 19 confirmed new SRC (though one has been reconsidered as not recent) based on the existence of blast features in the ephemeral dust layer surrounding distinct ejecta deposits. In these locations, no such tonal feature existed in earlier imagery. Their counts and imaged areas over the dusty volcanic Tharis region and the cratered uplands of Arabia Planitia with a time delta of 6.9 Earth years gives a cratering rate of 1.28×10^{-7} craters $\text{km}^{-2} \text{a}^{-1}$ [Malin et al., 2006]. Corrections for spatial randomness within this population reduced the measured sample area by a factor of 1/2.9, increasing the given rate to 3.72×10^{-7} craters $\text{km}^{-2} \text{a}^{-1}$ [Kreslavsky, 2007]. With the advent of new instruments with broader fields of view covering a greater percentage of the planet at meter-scale resolution (i.e. the Mars Reconnaissance Orbiter (MRO) Context camera (CTX)), a new estimate from 100 impacts sampled from 62% of the surface area of Mars puts the cratering rate at $8 \pm 6 \times 10^{-7}$ craters $\text{km}^{-2} \text{a}^{-1}$ [Kennedy and Malin, 2009], over a factor of two greater than the Kreslavsky [2007] estimate, though within its wide error margin. A slightly more conservative estimate using 69 impacts confirmed by HiRISE over 3.9 years from 2006 to 2009 gives an intermediate estimate at 5.30×10^{-7} craters $\text{km}^{-2} \text{a}^{-1}$ [Daubar et al., 2010].

Each of these cratering rates comes with two general caveats. The first is that these new impacts are predominately found in dust-laden areas which produce a distinctive air blast zone. This zone represents an imprint of the atmospheric shock wave interaction with the surrounding millimeter thick dust layer [Ivanova et al., 2010]. It can extend tens to hundreds of crater radii beyond the continuous ejecta blanket [Malin et al., 2006], thereby making the zone readily noticeable in lower resolution imagery. However,

some recent cratering events may not have produced this distinctive signature or it may not have lasted very long. The true crater production rates in this diameter range are likely higher than what is observed. Though, some researchers consider these estimates are off by less than a factor of two [Malin et al., 2006]. A second problem is the issue of atmospheric filtering. Craters in this diameter range are within the size-frequency population of impactors that are expected to be filtered by the Martian atmosphere [e.g. Popova et al., 2003]. Based on modeling results for the current mean 6 mb atmosphere, craters $D < 30$ m are subject to a depleted crater production function as many impactors either burn up before reaching the surface or “bin hop” to a smaller diameter crater size than expected due to significant ablation of the original meteorite body [e.g. Chappelow and Sharpton, 2005]. Therefore, the overall production functions for low decameter or smaller D craters needs to be corrected for atmospheric effects to extend crater count estimates to larger D craters in the sub-kilometer range. This would allow us to estimate E_{Ret} for all SRC across Mars.

4.2 METHODOLOGY

4.2.1 Estimating Ejecta Retention Age

To estimate the ejecta retention age (E_{ret}) for a surface, we need to determine the current cratering rate production function (CPF) and the distribution of SRC over a known surface area. The assumption is SRC primaries must be the source for the global SRC population over time, assuming all SRC are primaries. The crater production rate is typically expressed within a defined range of crater size (i.e. diameter) by the number of

craters (N) impacting a square kilometer of surface over a given time period, typically one Earth year (e.g. $N \text{ km}^{-2} \text{ a}^{-1}$). We calculated this CPF from the published data of Malin et al. [2006] for SRC primaries, adjusted for both spatial randomness [Kreslavsky, 2007] and atmospheric filtering [Chappelow and Sharpton, 2005] as discussed below in section 4.2.2. The ejecta retention age for a surface from small rayed craters is found by utilizing standard crater dating techniques [e.g. Crater Analysis Techniques Working Group, 1978] with new isochrons extrapolated from the CPF as discussed in section 4.2.2 and 4.2.3. For our SRC population, we employed the observations and study areas of Calef et al. [2010] for three equatorial regions (Amazonis-Elysium, Arabia, and Tharsis) where the cratering rates are most applicable because of their proximity to dust-laden areas, and the polar regions (Australis and Borealis) (Figure 4.2, Table 4.1). All 630 SRC in this population are between 19 m and 1000 m in diameter and represent a sample of 4264 MOCNA images across Mars (see Calef et al. [2010] for a thorough description of the observations).

4.2.2 Correcting for Atmospheric Filtering

As previously discussed in section 4.1.3, all the current estimates of crater production based on observations of primary SRC are in the diameter range subject to extensive atmospheric filtering, even through the relatively thin ~ 6 mb atmosphere on Mars. This leads to a decrease in counts and slope of the production function by decreasing the number of meteorites that form impacts and by ablating meteorites to smaller masses, thus causing bin hopping of crater diameters to small diameter bins. We

attempted to resurrect the lost and degraded counts by applying a correction from the modeling work of Chappelow and Sharpton [2005] to the production rates by Malin et al. [2006] and Kreslavsky [2007] as they provide actual numbers and diameters for new primary SRC with their estimates. For each diameter bin, a certain percentage amount of craters is lost due to either burn up of the meteorite, soft land without creating a crater, or breakup into smaller sized impactors (though their affect on the counts is negligible). An additional number of meteorites bin hop to smaller diameter bins either one or multiple times as ablation increases depending on initial cross-sectional size, impact angle (i.e. amount of atmosphere passed through) and incoming velocity [Chappelow and Sharpton, 2005]. For our purposes, we are unconcerned how the ultimate counts are affected; only the percentage that remains in their original bin. Actual loss from burn up or bin hopping is inconsequential.

There are four categories of possible asteroidal impactor types, each with a certain percentage relating to the parent source in the main asteroid belt between Mars and Jupiter [Tholen, 1989]: carbonaceous chondrites (cc) (75%), stony (16%), irons (9%) or icy (i.e. cometary material). We ignore the icy component as it has been shown to have a negligible effect on the production rate of sub-kilometer diameter craters in a 6mb atmosphere [Chappelow and Sharpton, 2005]. As well, migration of crater counts into bins from larger diameters is also ignored as it is considered a lesser amount than that initially lost, though does portend that our counts will slightly overestimate the total production population. From these parameters, and the estimates of crater survival per diameter bin, we reconstituted the original population for a given size range by

multiplying the counts, $N(D)_{src}$, times the mass fraction of meteorite type (A_{type} after Chappelow and Sharpton, [2005]), then divided by the fraction of meteorites from the total impacting population expected to impact (Table 4.2) and create a crater count in that diameter bin, $N(D)$:

$$N(D)_{cp} = (A_{cc}N(D)_{src})/N_{cc} + (A_{stony}N(D)_{stony})/N_{stony} + (A_{iron}N(D)_{iron})/N_{iron} \quad (4.2)$$

thereby recreating the crater population that would have occurred in the absence of an atmosphere. This correction nearly doubles the crater counts from $N = 19$ to $N = 32$ and increases the production function slope from -1.68 to -2.093 (Figure 4.4). With the new population taking into account spatial randomness from Kreslavsky [2007] and atmospheric filtering, we estimate the current crater production function at 6.29×10^{-7} craters $\text{km}^{-2} \text{a}^{-1}$ for craters $D > 10$ m. This value is intermediate from estimates by Daubar et al. [2010] and Kennedy and Malin [2009], though takes into account corrections they do not. Since this new cratering rate (CPF) is corrected for atmospheric loss, we assume the slope of the production function can be extended to large D craters with some confidence up to $D = 1$ km. The new CPF can be represented as a power-law:

$$N = 0.0008D^{-2.093}, R^2 = 0.83 \quad (4.3)$$

where N represents the crater density in craters km^{-2} over 6.9 years and crater diameter D is in meters. This can be written in the more traditional form in terms of $\log(N)$ and $\log(D)$:

$$\log(N) = -2.093\log(D) - 3.09691 \quad (4.4)$$

for plotting on a log-incremental diagram. E_{ret} estimates are calculated for each SRC D bin utilizing both the HPF and this new production function to develop new isochrons based on this CPF (Table 4.3).

4.2.3 Rayed Crater Counting

The retention age was estimated using both the HPF and CPF isochrons for our rayed crater counts in each of our five study regions. Not only does the crater count denote the last resurfacing event in an area, but it also represents the ejecta retention age since the ejecta have yet to be removed from around the SRC. We characterized rayed crater counts using a log-incremental approach for each size-frequency distribution plot as standardized by the Crater Analysis Techniques Working Group [1978]. The HPF isochrons account for changes in R_{bolide} and atmospheric filtering at small D to establish dating functions [Hartmann, 2005]. The CPF isochrons account for the aforementioned spatial randomness and atmospheric filtering, and do not rely on R_{bolide} values as rates are derived directly from observed Mars impacts. Both production functions assume a monotonic constant cratering rate allowing a simple order of magnitude multiplier to

calculate later (HPF) or earlier (CPF) isochrons (i.e. if the 10 year isochron had $N = 10^{-6}$, the 100 year isochron would have $N = 10^{-5}$ and so on). One of the larger possible errors in calculating the HPF involves an order of magnitude extrapolation of the cratering rate down from billions of years to less than a million. We are more confident in the cratering rate being constant over the last 10^6 years versus over the last 10^9 . Another caveat to the HPF is the evaluation of R_{bolide} . This value is based on telescopic counts of asteroids as well as crater counts on asteroids and itself an extrapolation from the Moon cratering rate to Mars. The CPF relies on actual evidence of new impacts on Mars and not estimates of impacting rates. Other scaling factors involving crater size, gravity differences and impact velocity can also be ignored since we are generating our cratering rate from direct observations. One often underappreciated error may come from the rather limited spatial diversity of radiometrically dated samples from the Moon which underlie the whole HPF system. The CPF is highly constrained by images taken both before and after new meteorite impacts with a time delta of only a few years in most cases. Both production functions do model expected atmospheric filtering based on estimates of the impacting meteorite population. Chappelow and Sharpton [2005] consider their filtering estimates to be slightly conservative to Popova et al. [2003], so some differences in age between the two dating systems can be assumed to come from this disparity.

Counts were compiled in standard $\sqrt{2}$ bins (D to $\sqrt{2}D$) starting with all craters less than or equal $D = 1$ km, down to the next $\sqrt{2}$ bin (707 m as $\sqrt{2} \cdot 707 = \sim 1$ km). Because our effective diameter resolution is ~ 19 m, the last bin (15.6-22.1 m) may be undercounted by ~ 0.5 . However, because ejecta typically extends several factors farther

than the crater diameter, initial identification is consider high and few systematic errors are expected in this regard. We cannot discount some sampling error due to poor image contrast or the rare low resolution (>10 m/pixel) image. Error is presented at $1-\sigma$ as $\pm(\sqrt{N})/A$, with A equal to the sampled area in kilometers squared for all the images examined in Calef et al., [2010].

4.3 RESULTS AND DISCUSSION

4.3.1 Hartmann Production Function Ejecta Retention Ages across Mars

Global and regional log-incremental size-frequency plots of small rayed craters with HPF isochrons can be found in Figure 4.5. A breakdown of SRC N by bin and region, along with density and $1-\sigma$ error can be found in Tables 4.1, 4.4 and 4.5, respectively. In Table 4.4, the sum total of image footprint area examined for SRC occurrence in each region is listed at the top of the columns under the region name. SRC counts by bin and region from Table 4.1 were divided by these area measurements to generate the SRC density as listed in Table 4.4.

At the global scale, the largest D SRCs (>500 - 1000 m) appear to retain ejecta for 7-10 Ma (Table 4.6). Then, a steep break occurs in retention age from 1 Ma for $D = 250$ - 500 m SRC followed by a change in the retention age slope to an approximately -1.6 power law down to the $D = 44.2$ m bin (down to and including $D = 31.2$ m) and ~ 30 ka ejecta retention time. Finally, a roll-off (i.e. reduction) in counts begins and continues to the smallest D bin for a retention age of 350 a. Again, our lowest D bin is undercounted

by ~50%, so the retention age for 15.6 m to 22.1 m diameter SRC is in all likelihood closer to 1 ka.

All three equatorial regions produce similar crater size-frequency trends. Amazonis-Elysium dominates in the SRC crater counts at nearly 50% of the sample population (Table 4.1), indicating a higher retention age than the global average. SRC from 176 to 500 m diameters retained ejecta for ~3.5-4 Ma, followed by a sharp break in retention to 1 Ma down to 500 ka, bracketing the Zunil estimated age (540 ka), before rolling-off after the 62.5 m bin down to 1.5 ka. Bins larger than 500 m have poor sampling (only two craters in the 500 m and 1000 m bin at 725 m), but are represented in the other regions too; for this reason we do not believe they are anomalous. Arabia follows this pattern, although retention ages are ~2/3 younger in comparison; SRC in the $D = 50$ m to 100 m range have a ~150-300 ka retention age, though smaller SRC still have lower ages with decreasing D . In contrast, Tharsis is in between Arabia and Amazonis-Elysium with regard to retention ages down to $D = 62.5$ m before it begins steadily decreasing in retention age with smaller D , though more sharply than the other regions. Both the Australis and Borealis polar study regions have too few counts to make any clear observations, except that the mean diameter of SRC in these areas is a factor of 3 to 4 greater than the other regions.

With few counts in the polar regions, an estimation of E_{ret} in these areas is difficult, though we can rely on some maximum bounds by looking at small crater degradation. Small sub-kilometer craters on thermal contraction crack polygons and mantled terrain poleward of $\pm 30^\circ$ have latitude dependent ages [Kostama et al., 2006;

Levy et al., 2009; Kreslavsky, 2009]. Patterned ground has the following surface ages by latitude [Kostama et al., 2006; Levy et al., 2009; Kreslavsky, 2009]: 1-2 Ma at mid-latitude ($\sim 45^\circ$), ~ 100 -300 ka at $\sim 55^\circ$, <100 ka at $\sim 65^\circ$, and 1-3 ka above 70°S (though probably higher for equivalent northern latitudes [Kreslavsky, 2009]). These ages would represent a maximum ejecta retention time, perhaps by an order of magnitude as ejecta must erode faster than the crater itself. From our log-incremental plots (Figure 4.5), we can see that near the equator, retention time decreases rapidly with crater diameters <50 m, but decreases sooner for craters near Tharsis when $D < 100$ m. Above these diameters, an equilibrium in retention is reached until about $D = 125$ m (250 m in Tharsis), before achieving another constant age up to $D = 500$ m. Beyond the 500 m bin, counts are too few to draw any definitive conclusions, though our age estimate may be accurate to within an order of magnitude. In general, ejecta retention ages run between 10 ka - 1 Ma for the majority of SRC based on the HPF; this would be consistent with the aforementioned maximum retention times for higher latitude SRC.

4.3.2 Current Production Function Ejecta Retention Ages across Mars

In general, retention ages with the CPF isochrons are an order of magnitude younger than those estimated with the HPF (Figure 4.6). At the global scale, the largest D SRCs (>500 -1000 m) appear to retain ejecta for only ~ 80 ka (Table 4.7). Then, a break occurs in retention age down to ~ 25 ka at $D = 250$ -500 m SRC with little change in E_{ret} down to the $D = 44.2$ m bin with a ~ 15 ka ejecta retention age. A roll-off in counts follows, continuing to the smallest D bin for a retention age of 150 a. With the exception

of the polar regions, the equatorial SRC now produce parallel to the isochrons through a larger range of D , with Amazonis-Elysium SRC retaining ejecta for ~ 100 ka, Arabia SRC for ~ 30 -50 ka, and Tharsis at ~ 30 ka for slightly larger D . Both polar regions appear to experience a near constant erosion cycle with no consistent age of ejecta preservation.

4.3.3 Ejecta Retention Ages for Mars

Our calculations show that SRC on Mars are very young geologic features. Ejecta retention age changes with both spatial location and crater diameter and may approach a state where the ejecta retention process is very slow once most of the ephemeral distal material is removed. Experimental and observational work have shown that ejecta layer thickness is a function of crater radius (factor 0.04 at the crater rim for radii < 500 m) and decreases by a power-law with distance from the crater rim [e.g. McGetchin and Settle, 1973]; all things being equal, small D craters will retain ejecta for shorter timespans. On Mars, most SRC have a mean D of ~ 71 m with a median of 47 m [Calef et al., 2010], consistent with thin ejecta blankets and brief retention ages. However, measurements of landing site deflation (i.e. erosion) rates from Gusev crater and Meridiani Planum are as little as 0.03 nm a^{-1} to $1\text{-}10 \text{ nm a}^{-1}$, respectively. This deflation rate is lower than the minimum erosion rates on Earth removing only a single meter of surface material over 1 Ga [Golombek et al., 2006]. However, dust deposition by comparison is 3 to 5 orders of magnitude higher on Mars, with estimates in the Chryse Planitia region at the Carl Sagan Memorial Station (i.e. Mars Pathfinder) from $20\text{-}45 \text{ } \mu\text{m a}^{-1}$ [Johnson et al., 2003]. A back-of-the-envelope calculation with the dust deposition rates would bury these SRC in

tens of thousands of years up to the rim. However, this is not necessary as experimental results indicate a modest $1.5 \times 10^{-4} \text{ g cm}^{-2}$ of dust particles that are 1 to 5 μm in diameter, which is an order of magnitude less than produced by one dust storm season ($\sim 2 \times 10^{-3} \text{ g cm}^{-2}$), can reduce visible reflectance by 70% [Wells et al., 1984]. This would visibly erase the presence of SRC ejecta within a modest number of years. Therefore, dust deposition is likely the dominating process in ejecta retention, as has been shown through statistical analysis of dust cover and SRC occurrence [e.g. Calef et al., 2010]. Our E_{ret} ages should be considered reliable for those diameters close to the production functions size-frequency craters (low tens of meters) and a lower limit for increasing crater radius.

The current driving surface processes across two-thirds of Mars today are dust deposition and periglaciation that operate on thousand year timescales, based on our ejecta retention ages and SRC distribution from Calef et al. [2010]. The other one third is regulated to eolian erosion and other related processes (dust devils, planet-wide dust storms, etc.) along the Martian equator. However, the timescales on which they operate in terms of erosion are miniscule (fractions of a nanometer per year) in comparison to periglacial or dust depositional processes. From our measurements, periglaciation and dust deposition must be eroding or burying close to whole millimeters per year of ejecta in the most active areas, as observed from SRC counts. We tend to think of Mars as a dry planet, though its presence in the form of ice continues to shape the surface from mid to high latitudes in both northern and southern hemispheres regardless of underlying topography, based on observed distribution of SRC [Calef et al., 2010] and the very young retention ages for $D < 100 \text{ m}$ SRC. The initial heavy bombardment, volcanic, and

fluvial environment in the Noachian and Hesperian (4.6-1.8 Ga) made the first mark on Mars' topography [e.g. Head et al., 2002]. Over the last 2 Ga, the resurfacing of Mars appears to occur only in the upper few meters of the regolith surface. In the past, Mars was gaining surface roughness from large impacts creating high ridges, being carved in chasms by massive floods, and occasionally wrinkled by lava flows. Today, the surface of Mars is slowly being molded along the equator by a never-ending stream of dust and constantly disassembled by ice-wedge polygons and other patterned ground features in northern and southern polar latitudes. However, we have seen possible evidence of a change from depositional to erosional dominate processes in the southern equatorial region [Calef et al., 2010], that based on our retention age calculations in Arabia Terra, must have transgressed at $\sim 50 \pm 30$ ka ago. Given that only a handful of SRC have retention ages > 100 ka, one could consider that some global event, perhaps the predicted cyclical changes in obliquity [Mellon and Jakosky, 1995], augments one or several surface processes. During an event such as this, SRC ejecta may conceivably be more rapidly obliterated on briefer time scales along with other similar regolith-based features.

4.4 CONCLUSION

Retention ages, E_{ret} , based on SRC counts in each of three equatorial regions with the CPF yielded dates ranging from a few ka for craters $D = 30$ m up to 100 ka for $D = 500$ m craters between $\pm 30^\circ$ latitude. Deficits in SRC counts for high northern and southern latitudes preclude accurate dating, but retention ages are assumed to be < 30 ka and decreasing with increasing latitude based on crater retention times in these areas.

SRC with $D < 50$ m (< 100 m in Tharsis) are subject to less retention (i.e. shorter timespans) with decreasing D , assumed due to decreasing ejecta thickness with crater diameter. HPF isochrons do not reflect SRC densities and estimate retention ages an order of magnitude greater than the CPF. Current crater production rates for SRC are an important new metric for dating young surfaces and calibrating the cratering record for sub-kilometer diameter craters in the past several to tens of thousands of years. These rates, when corrected for atmospheric filtering yield slopes of ~ -2 that are shallower than the standard -3.8 for isochrons from Hartmann [2005] which may prove more accurate for measurements in the past 1 Ma before secondaries begin to dominate the landscape [Hartmann, 2007]. SRC retain ejecta on average from 10 ka to 30 ka across equatorial Mars. Further cataloguing of SRC in all regions and with greater image coverage could improve these retention ages and allow calculations for smaller geographic units. Despite sediment deflation rates of fractions of a nanometer per year, ejecta retention is low for the majority of SRC currently on Mars.

The dominant processes of dust deposition and periglacial erosion remove SRC on thousand year timescales. Equatorial southern highlands have longer ejecta retention ages up to 100 ka, but under the nascent erosional environment ejecta would be maintained for longer timespans if suspected obliquity variations did not modify the rate of global retention processes. Mars surface processes are confined to affecting only the upper few meters of regolith, but are dynamic across the majority of the Martian surface. SRC have proven to be a practical tool for understanding the recent surface history and identifying the pertinent erosional and depositional processes on Mars.

REFERENCES

Bierhaus, E. B., C. R. Chapman, and W. J. Merline (2005), Secondary craters on Europa and implications for cratered surfaces, *Nature*, 437, 1125–1127, doi:10.1038/nature04069.

Byrne, S., C. M. Dundas, M. R. Kennedy, M. T. Mellon, A. S. McEwen, S. C. Cull, I. J. Daubar, D. E. Shean, K. D. Seelos, S. L. Murchie, B. A. Cantor, R. E. Arvidson, K. S. Edgett, A. Reufer, N. Thomas, T. N. Harrison, L. V. Posiolova, and F. P. Seelos (2009), Distribution of Mid-Latitude Ground-Ice on Mars from New Impact Craters, *Science*, 325, 1674.

Calef, F. J., III, R. R. Herrick, and V. L. Sharpton (2009), Geomorphic analysis of small rayed craters on Mars: Examining primary versus secondary impacts, *J. Geophys. Res.*, 114, E10007, doi:10.1029/2008JE003283.

Calef, F. J., III, R. R. Herrick, and V. L. Sharpton (2010), Global distribution of small rayed craters on Mars: sequences of ejecta retention, *Icarus*, *in prep.*

Chappelow J. E., and Sharpton V. L. (2005), Influences of atmospheric variations on Mars' record of small craters, *Icarus*, 178, 40–55.

Crater Analysis Techniques Working Group (1978), Standard Techniques for Presentation and Analysis of Crater Size-Frequency Data, NASA Technical Memorandum, 79730.

Daubar, I. J., A. S. McEwen, S. Byrne, C. M. Dundas, M. Kennedy, and B. A. Ivanov (2010), The current Martian cratering rate, *Lunar and Planet. Sci. Conf. XXXXI*, #1978.

Golombek, M. P., and 10 colleagues (2006), Erosion rates at the Mars Exploration Rover landing sites and long-term climate change on Mars, *J. Geophys. Res.*, 111, E12S10, doi:10.1029/2006JE002754.

Hartmann, W.K. (1999), Martian cratering. VI. Crater count isochrons and evidence for recent volcanism from Mars Global Surveyor. *Meteorit. Planet. Sci.* 34, 167–177.

Hartmann, W. K. (2005), Martian cratering 8: Isochron refinement and the chronology of Mars, *Icarus*, 174, 294 – 320, doi:10.1016/j.icarus.2004.11.023.

Hartmann, W. K. (2007), Martian cratering: 9. Toward resolution of the controversy about small craters, *Icarus*, 189, 274 – 278, doi:10.1016/j.icarus.2007.02.011.

Hartmann, W. K., G. Neukum, and S. Werner (2008), Confirmation and utilization of the “production function” size-frequency distributions of Martian impact craters, *Geophys. Res. Lett.*, 35, L02205, doi:10.1029/2007GL031557.

Head, J. W., M. A. Kreslavsky, and S. Pratt (2002), Northern lowlands of Mars: Evidence for widespread volcanic flooding and tectonic deformation in the Hesperian Period, *J. Geophys. Res.*, 107, E1, 5004, 10.1029/2000JE001445.

Ivanova, B. A., H. J. Melosh, A. S. McEwen and the HiRISE team (2010), New small impact craters in high resolution HiRISE images - III, *Lunar and Planet. Sci. Conf. XXXXI*, abstract #2020.

Johnson, R. J., W. M. Grundy, and M. T. Lemmon (2003), Dust deposition at the Mars Pathfinder landing site: observations and modeling of visible/near-infrared spectra, *Icarus*, 163, 2, 330-346, doi:10.1016/S0019-1035(03)00084-8.

Kennedy, M. R. and M. C. Malin (2009), 100 new impacts crater sites found on Mars, 969 *American Geophysical Union, Fall Meeting 2009*, abstract #P43D-1455.

Kostama, V.P., M. A. Kreslavsky, and J. W. Head (2006), Recent high-latitude icy mantle in the northern plains of Mars: Characteristics and ages of emplacement, *Geophys. Res. Lett.*, 33, L11201, doi:10.1029/2006GL025946.

Kreslavsky, M. (2007), Statistical characterization of spatial distribution of impact craters: implications to present-day cratering rate on Mars, *Seventh International Conference on Mars*, abstract #3325.

Kreslavsky, M. (2008), Young populations of small craters on Mars: A case study, paper presented at 3rd European Planetary Science Congress, Abstract EPSC2008-A-00237, Eur. Geosci. Union, Münster, Germany, 21– 26 September.

Kreslavsky, M. (2009), Dynamic landscapes at high latitudes on Mars: constraints from populations of small craters, Lunar Planet. Sci. Conf. XXXXI, abstract #2311.

Levy, J., J. Head, and D. Marchant (2009), Thermal contraction crack polygons on Mars: Classification, distribution, and climate implications from HiRISE observations, *J. Geophys. Res.*, 114, E01007, doi:10.1029/2008JE003273.

Malin, M. C., K. S. Edgett, L. V. Posiolova, S. M. McColley, and E. Z. Noe Dobrea (2006), Present-day impact cratering rate and contemporary gully activity on Mars, *Science*, 314, 5805, 1573 – 1577, doi:10.1126/science.1135156.

McEwen, A. S., B. S. Preblich, E. P. Turtle, N. A. Artemieva, M. P. Golombek, M. Hurst, 1003 R. L. Kirk, D. M. Burr, and P. R. Christensen (2005), The rayed crater Zunil and interpretations of small impact craters on Mars, *Icarus*, 176, 351– 381, doi:10.1016/j.icarus.2005.02.009.

McGetchin, T. R., and M. Settle (1973), Radial thickness variation in impact crater ejecta: implications for lunar basin deposits, *Earth and Planet. Sci. Let.*, 20, 226-236.

Mellon, M. T., and B. M. Jakosky (1995), The distribution and behavior of Martian ground ice during past and present epochs, *J. Geophys. Res.*, 100, 11,781–11,799, doi:10.1029/95JE01027.

Neukum, G., Ivanov, B. A., and Hartmann, W. K. (2001), Cratering records in the inner Solar System in relation to the lunar reference system. In: Kallenbach, R., Geiss, J., Hartmann, W.K. (Eds.), *Chronology and Evolution of Mars*, Int. Space Science Institute, Bern, pp. 87–104.

Popova, O. P., I. Nemtchinov, and W. K. Hartmann (2003), Bolides in the present and past Martian atmosphere and effects on cratering processes, *Meteorit. Planet. Sci.*, 38, 905– 925.

Preblich, B. S., A. S. McEwen, and D. M. Studer (2007), Mapping rays and secondary craters from the Martian crater Zunil, *J. Geophys. Res.*, 112, E05006, doi:10.1029/2006JE002817.

Reiss, D., S. van Gasselt, G. Neukum, and R. Jaumann (2004), Absolute dune ages and implications for the time of formation of gullies in Nirgal Vallis, Mars. *J. Geophys. Res.* 109, E06007.

Shoemaker, E. M. (1965), Preliminary analysis of the fine structure of the lunar surface in Mare Cognitum, in *The Nature of the Lunar Surface*, JPL Tech. Rep. 32-700, edited by W. N. Hess, D. H. Menzel, and J. A. O'Keefe, pp. 23– 77, Johns Hopkins Press, Baltimore, Md.

Tholen, D.J. (1989), Asteroid Taxonomy classifications. In: Binzel, R.P., Gehrels, T., Matthews, M.S. (Eds.), *Asteroids II*. Univ. of Arizona Press, Tucson, pp. 1139–1150.

Tornabene, L. L., J. E. Moersch, H. Y. McSween Jr., A. S. McEwen, J. L. Piatek, K. A. 1075 Milam, and P. R. Christensen (2006), Identification of large (2– 10 km) rayed craters on Mars in THEMIS thermal infrared images: Implications for possible Martian meteorite source regions, *J. Geophys. Res.*, 111, E10006, doi:10.1029/2005JE002600.

Tornabene, L. L., Bray, V., McEwen, A. S., Osinski, G. R., Mouginis-Mark, P. & Boyce, 1081 J (2010) Recognition of fresh & well-preserved Martian craters & their general interior 1082 morphologic aspects as observed by HiRISE & CTX, *J. Geophys. Res.*, in prep.

Wells, E. M., J. Veverka, and P. Thomas (1984), Mars: Experimental study of albedo changes caused by dust fallout, *Icarus*, 58, 3, 331-338.

Werner, S. C., B. A. Ivanov, and G. Neukum (2009), Theoretical analysis of secondary cratering on Mars and an image-based study on the Cerberus plains, *Icarus*, 200, 406–417, doi:10.1016/j.icarus.2008.10.011.

TABLES

Table 4.1: Crater counts by study region.

Diameter Bin (m) ^a	Amazonis-Elysium	Arabia	Australis	Borealis	Tharsis	ALL SRC
15.6 - 22.1	6	8	0	0	1	15
22.1 - 31.2	44	49	0	0	7	100
31.2 - 44.2	94	60	6	0	13	173
44.2 - 62.5	86	40	2	0	19	147
62.5 - 88.3	40	14	3	3	21	81
88.3 - 125	21	11	3	1	12	48
125 - 176	8	12	0	3	7	30
176 - 250	9	3	0	3	2	17
250 - 353	3	2	2	0	2	9
353 - 500	1	1	0	0	1	3
500 - 707	0	1	1	3	0	5
707 - 1000	1	0	1	0	0	2
TOTALS^b	49.7%	31.9%	2.9%	2.1%	13.5%	630^c

^aBins are $D + D2^{(1/2)}$ [Crater Analysis Techniques Working Group, 1978].

^bPercent total of SRC by region compared to all SRC in this study.

^cSum total of all SRC for each region and all diameter bins.

Table 4.2: Atmospheric correction factors for the crater production

Bin (D) m	^a Bin (D) _{Chap}	^b Meteor _{cc}	^b Meteor _{stony}	^b Meteor _{iron}	^c N _{original}	^d N _{atmos}
7.81 - 11	mean(8+12)	0.43	0.58	0.71	1	2.1
11 - 15.6	mean(12+19)	0.48	0.62	0.75	7	13.6
15.6 - 22.1	mean(19+27)	0.58	0.72	0.82	5	8.1
22.1 - 31.2	mean(27+37)	0.69	0.80	0.88	5	7.0
31.2 - 44.2	mean(37+55)	0.77	0.86	0.92	1	1.3

^aBin diameters used from Chappelow and Sharpton [2005] to estimate atmospheric correction factors.

^bModelled fraction of meteorites that impacted the surface and created a crater in this diameter bin after passing through a 6mb atmosphere, by meteor composition [Chappelow and Sharpton, 2005].

^cNumber of SRC primaries observed by Malin et al. [2006].

^dCorrected for atmospheric filtering from N_{original}.

Table 4.3: Martian isochrons extrapolated from the CPF.

D (m)	6.9 a ^b	1 a	10 a	100 a	1 ka	10 ka	100 ka	1 Ma
7.8 ^a	6.34E-06	9.19E-07	9.19E-06	9.19E-05	9.19E-04	9.19E-03	9.19E-02	9.19E-01
11 ^a	3.56E-06	5.16E-07	5.16E-06	5.16E-05	5.16E-04	5.16E-03	5.16E-02	5.16E-01
15.6 ^a	1.98E-06	2.87E-07	2.87E-06	2.87E-05	2.87E-04	2.87E-03	2.87E-02	2.87E-01
22.1 ^a	1.10E-06	1.60E-07	1.60E-06	1.60E-05	1.60E-04	1.60E-03	1.60E-02	1.60E-01
31.2	5.97E-07	8.65E-08	8.65E-07	8.65E-06	8.65E-05	8.65E-04	8.65E-03	8.65E-02
44.2	2.88E-07	4.17E-08	4.17E-07	4.17E-06	4.17E-05	4.17E-04	4.17E-03	4.17E-02
62.5	1.39E-07	2.02E-08	2.02E-07	2.02E-06	2.02E-05	2.02E-04	2.02E-03	2.02E-02
88.3	6.76E-08	9.80E-09	9.80E-08	9.80E-07	9.80E-06	9.80E-05	9.80E-04	9.80E-03
125	3.27E-08	4.74E-09	4.74E-08	4.74E-07	4.74E-06	4.74E-05	4.74E-04	4.74E-03
176	1.60E-08	2.31E-09	2.31E-08	2.31E-07	2.31E-06	2.31E-05	2.31E-04	2.31E-03
250	7.66E-09	1.11E-09	1.11E-08	1.11E-07	1.11E-06	1.11E-05	1.11E-04	1.11E-03
353	3.72E-09	5.39E-10	5.39E-09	5.39E-08	5.39E-07	5.39E-06	5.39E-05	5.39E-04
500	1.80E-09	2.60E-10	2.60E-09	2.60E-08	2.60E-07	2.60E-06	2.60E-05	2.60E-04
707	8.69E-10	1.26E-10	1.26E-09	1.26E-08	1.26E-07	1.26E-06	1.26E-05	1.26E-04
1000	4.21E-10	6.10E-11	6.10E-10	6.10E-09	6.10E-08	6.10E-07	6.10E-06	6.10E-05

^aCalculated to the -1.68 power. Larger diameters use a -2.093 exponent.

^bThis and all subsequent crater densities are in craters/km².

Table 4.4: Craters per km² by study region.

Diameter Bin (m) ^a	Amazonis- Elysium (6846 km ²)	Arabia (6754 km ²)	Australis (1080 km ²)	Borealis (1166 km ²)	Tharsis (3877 km ²)	ALL SRC (19723 km ²)
15.6 - 22.1	8.76E-04	1.18E-03	0.00E+00	0.00E+00	2.58E-04	7.61E-04
22.1 - 31.2	6.43E-03	7.26E-03	0.00E+00	0.00E+00	1.81E-03	5.07E-03
31.2 - 44.2	1.37E-02	8.88E-03	5.55E-03	0.00E+00	3.35E-03	8.77E-03
44.2 - 62.5	1.26E-02	5.92E-03	1.85E-03	0.00E+00	4.90E-03	7.45E-03
62.5 - 88.3	5.84E-03	2.07E-03	2.78E-03	2.57E-03	5.42E-03	4.11E-03
88.3 - 125	3.07E-03	1.63E-03	2.78E-03	8.58E-04	3.10E-03	2.43E-03
125 - 176	1.17E-03	1.78E-03	0.00E+00	2.57E-03	1.81E-03	1.52E-03
176 - 250	1.31E-03	4.44E-04	0.00E+00	2.57E-03	5.16E-04	8.62E-04
250 - 353	4.38E-04	2.96E-04	1.85E-03	0.00E+00	5.16E-04	4.56E-04
353 - 500	1.46E-04	1.48E-04	0.00E+00	0.00E+00	2.58E-04	1.52E-04
500 - 707	0.00E+00	1.48E-04	9.26E-04	2.57E-03	0.00E+00	2.54E-04
707 - 1000	1.46E-04	0.00E+00	9.26E-04	0.00E+00	0.00E+00	1.01E-04

^aRepresents the upper bound of craters counted from D to D2^(1/2) (the stated bin diameter) [Crater Analysis Techniques Working Group, 1978].

Table 4.5: 1- σ crater count error as $\pm N^{(1/2)}$ /area of study region.

Diameter Bin (m) ^a	Amazonis- Elysium	Arabia	Australis	Borealis	Tharsis	ALL SRC
15.6 - 22.1	3.58E-04	4.19E-04	0.00E+00	0.00E+00	2.58E-04	1.96E-04
22.1 - 31.2	9.69E-04	1.04E-03	0.00E+00	0.00E+00	6.82E-04	5.07E-04
31.2 - 44.2	1.42E-03	1.15E-03	2.27E-03	0.00E+00	9.30E-04	6.67E-04
44.2 - 62.5	1.35E-03	9.36E-04	1.31E-03	0.00E+00	1.12E-03	6.15E-04
62.5 - 88.3	9.24E-04	5.54E-04	1.60E-03	1.49E-03	1.18E-03	4.56E-04
88.3 - 125	6.69E-04	4.91E-04	1.60E-03	8.58E-04	8.94E-04	3.51E-04
125 - 176	4.13E-04	5.13E-04	0.00E+00	1.49E-03	6.82E-04	2.78E-04
176 - 250	4.38E-04	2.56E-04	0.00E+00	1.49E-03	3.65E-04	2.09E-04
250 - 353	2.53E-04	2.09E-04	1.31E-03	0.00E+00	3.65E-04	1.52E-04
353 - 500	1.46E-04	1.48E-04	0.00E+00	0.00E+00	2.58E-04	8.78E-05
500 - 707	0.00E+00	1.48E-04	9.26E-04	1.49E-03	0.00E+00	1.13E-04
707 - 1000	1.46E-04	0.00E+00	9.26E-04	0.00E+00	0.00E+00	7.17E-05

^aBins are $D + D2^{(1/2)}$ [Crater Analysis Techniques Working Group, 1978].

Table 4.6: HPF Ejecta Retention (E_{ret}) estimates for five regions on Mars.

Diameter Bin (m) ^a	Amazonis-Elysium	Arabia	Tharsis	Australis	Borealis	ALL SRC
15.6 - 22.1	1.5 ka	1.5 ka	150 a	<2.5 ka	<20 ka	350 a
22.1 - 31.2	35 ka	25 ka	3 ka	<2.5 ka	<20 ka	8 ka
31.2 - 44.2	200 ka	80 ka	15 ka	2.5 ka	<20 ka	30 ka
44.2 - 62.5	500 ka	150 ka	60 ka	2.5 ka	<20 ka	75 ka
62.5 - 88.3	600 Ma	150 ka	175 ka	10 ka	20 ka	100 ka
88.3 - 125	800 Ma	300 ka	300 ka	25 ka	20 ka	175 ka
125 - 176	1 Ma	1 Ma	500 ka	>25 ka	175 ka	300 ka
176 - 250	3.5 Ma	750 ka?	450 ka?	<550 Ka	500 ka	600 ka
250 - 353	3.5 Ma	1.5 Ma	1.5 Ma	550 ka	>500 ka	1 Ma
353 - 500	4 Ma	2.5 Ma	2.5 Ma	>550 ka	<20 Ma	1 Ma
500 - 707	4-50 Ma	10 Ma	>2.5 Ma	3 Ma	20 Ma	7 Ma
707 - 1000	50 Ma	>10 Ma	>2.5 Ma	11 Ma	>20 Ma	10 Ma

^aBins are $D + D2^{(1/2)}$ [Crater Analysis Techniques Working Group, 1978].

Table 4.7: CPF Ejecta Retention (E_{ret}) estimates for five regions on Mars.

Diameter Bin (m) ^a	Amazonis-Elysium	Arabia	Tharsis	Australis	Borealis	ALL SRC
15.6 - 22.1	900 a	800 a	90 a	≥800 a	< 3ka	150 a
22.1 - 31.2	10 ka	9 ka	1 ka	≥800 a	< 3ka	2 ka
31.2 - 44.2	60 ka	20 ka	3.5 ka	800 a	< 3ka	9 ka
44.2 - 62.5	100 ka	25 ka	12 ka	600 a?	< 3ka	15 ka
62.5 - 88.3	95 ka	20 ka	25 ka	1.5 ka	3 ka	15 ka
88.3 - 125	100 ka	25 ka	30 ka	3 ka	2.5 ka	20 ka
125 - 176	80 ka?	70 ka?	30 ka	3-15 ka	15 ka	25 ka
176 - 250	150 ka	35 ka	20 ka?	3-15 ka	30 ka	25 ka
250 - 353	125 ka	50 ka	50 ka	15 ka	30-200 ka	25 ka
353 - 500	90 ka?	50 ka	50 ka	15-40 ka	30-200 ka	20 ka?
500 - 707	90-350 ka	100 ka	≥50 ka	40 ka	200 ka	80 ka
707 - 1000	350 ka	≥100 ka	≥50 ka	80 ka	≥200 ka	70 ka?

^aBins are $D + D2^{(1/2)}$ [Crater Analysis Techniques Working Group, 1978].

FIGURES

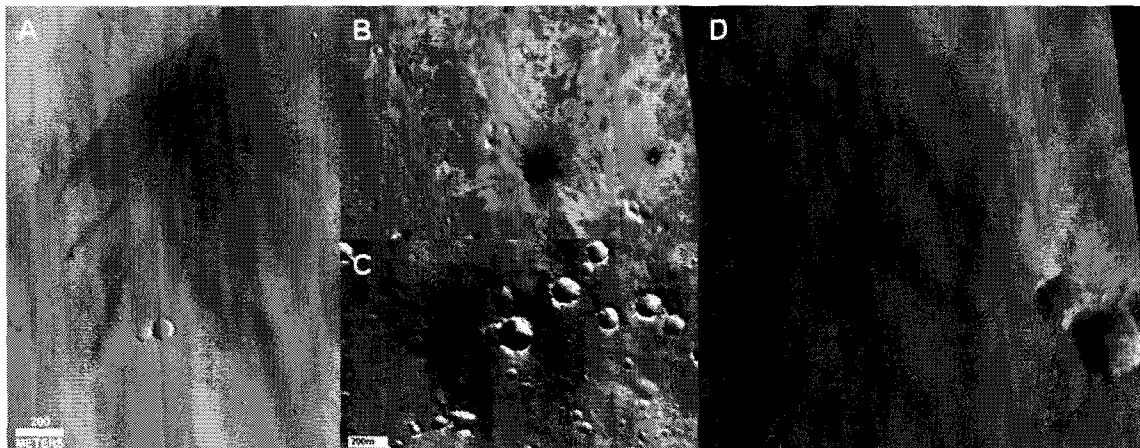


Figure 4.1: Small rayed craters on Mars. A) A new primary crater from the survey of Malin et al., [2006] (HiRISE image PSP_003101_2065_RED). B) Field of bright-rayed secondaries originating from Zunil (MOCNA image M0401791). C) Dark-rayed 182m diameter SRC also from Arabia Terra (MOCNA image R0902935). D) Bright-rayed 318m diameter SRC from Arabia Terra (MOCNA image E0402293). HiRISE images courtesy NASA/JPL/University of Arizona and MOCNA images courtesy NASA/JPL/MSSS. Images 2A and 2B, 2C and 2D are at approximately the same scale, respectively.

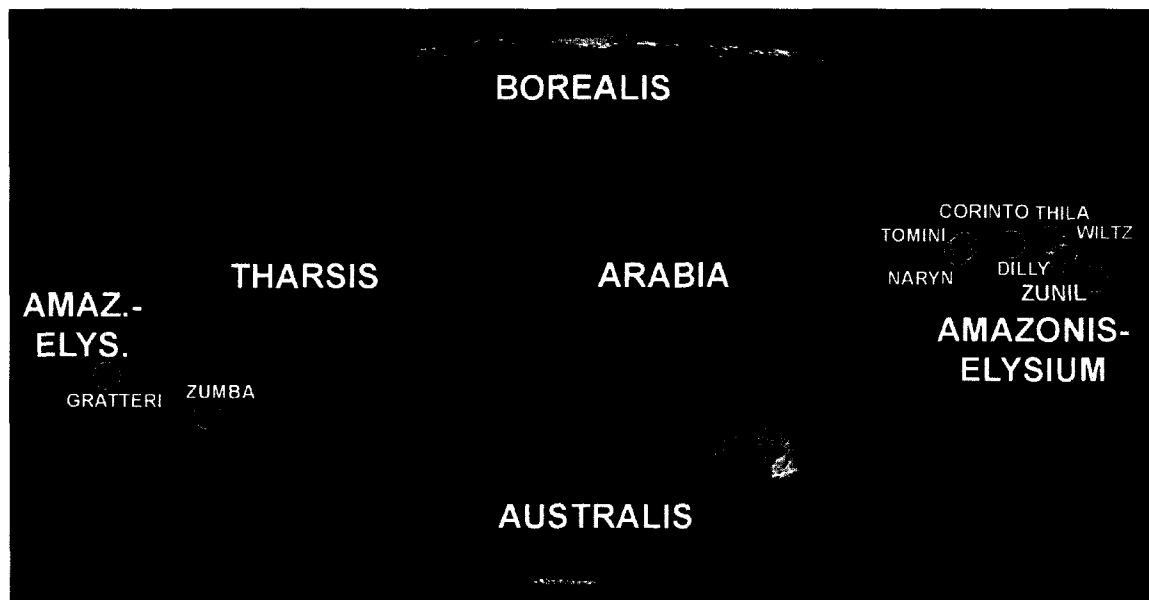


Figure 4.2: Mars location map for study areas from Calef et al. [2010]. Known large rayed primary craters ($D > 1$ km), including Zunil, are shown with white circles.

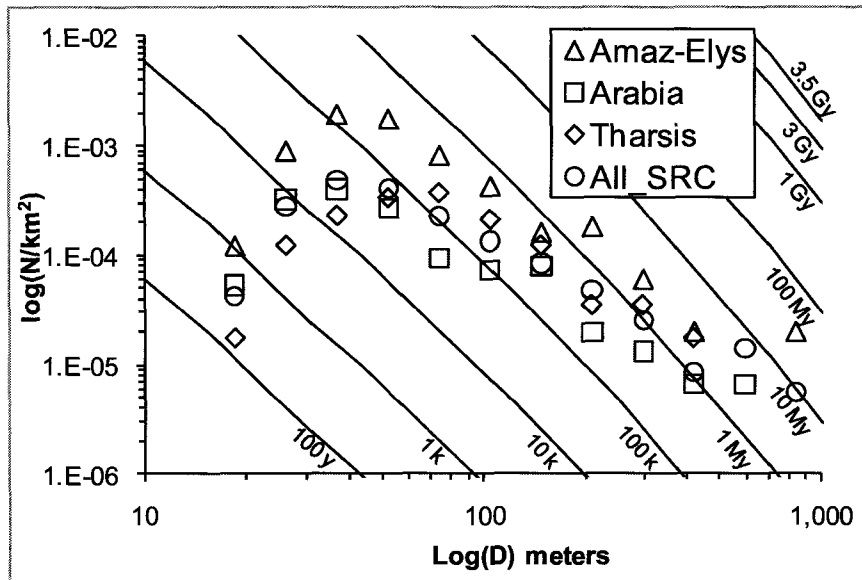


Figure 4.3: Example of an isochron dating plot using data from Calef et al. [2010]. Lines represent Hartmann production function isochrons for crater retention ages within the “steep branch” slope of -3.82 compared to ~ -2 for diameters > 1 km [Hartmann, 2005]. Error bars have been removed for clarity. Binned SRC counts and areas for generating this plot are in Table 4.1.

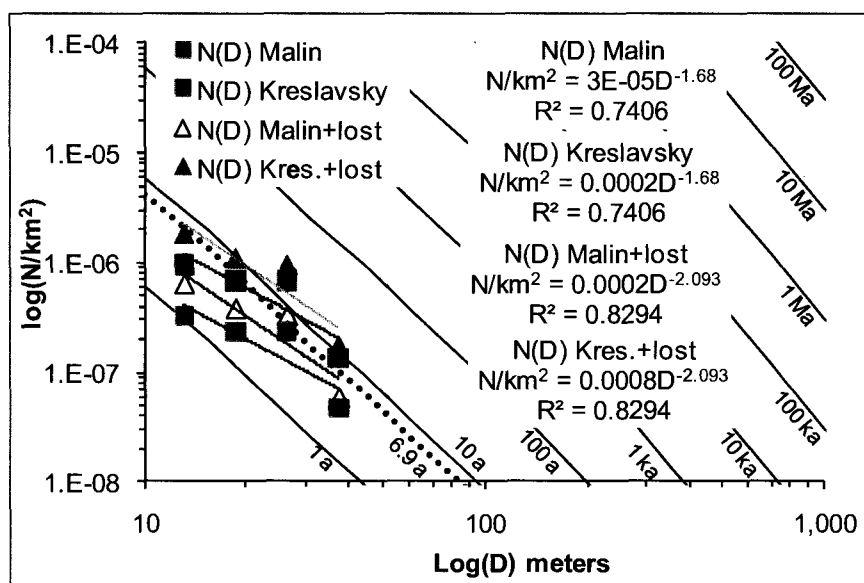


Figure 4.4: Corrections to the Malin et al. [2006] current crater production function on Mars. Initial spatial randomness correction by Kreslavsky [2007] adjusted the area surveyed by a factor of $1/2.9$, raising values by decreasing the sampling region denominator. Further adjustments for atmospheric filtering based on the modeling work of Chappelow and Sharpton [2005] decreases the slope of the line from -1.68 to -2.09 , thereby becoming a better 'fit' to the Hartmann production function [e.g. Neukum et al., 2001]. Dotted line represents the timespan when the Malin et al. [2006] SRC primaries were estimated to have impacted.

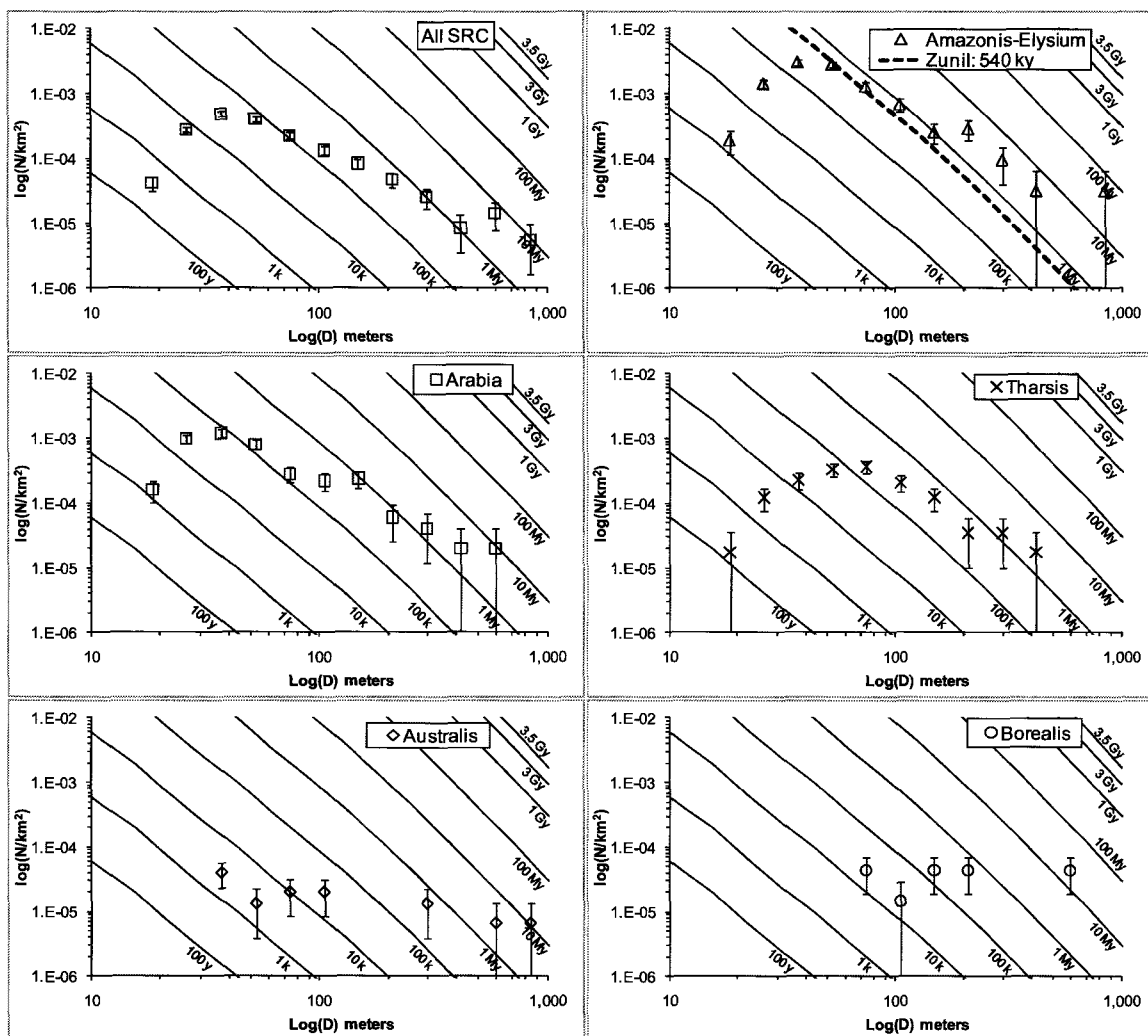


Figure 4.5: Hartmann production function (HPF) ejecta retention ages for SRC on Mars. These plots show the number of crater per units area that have retained ejecta (i.e. ejecta is still visible) per crater bin across several regions. The isochrons represent not only the age of the crater, but in addition the time period over which ejecta are retained by craters in this diameter range. Smaller craters (~ 50 m in diameter) appear to only retain ejecta over 10^4 year timescales; larger craters (> 100 m in diameter) potentially maintain ejecta for 10^5 - 10^6 years. Notice that SRC in Amazonis-Elysium, known for extensive secondaries from the 10.1 km diameter primary Zunil, has a retention age for 50-100m diameter craters within a small factor of Zunil's estimated age of 540k determined by Kreslavsky [2008]. Error bars are $N^{0.5} \text{ km}^{-2}$ per bin.

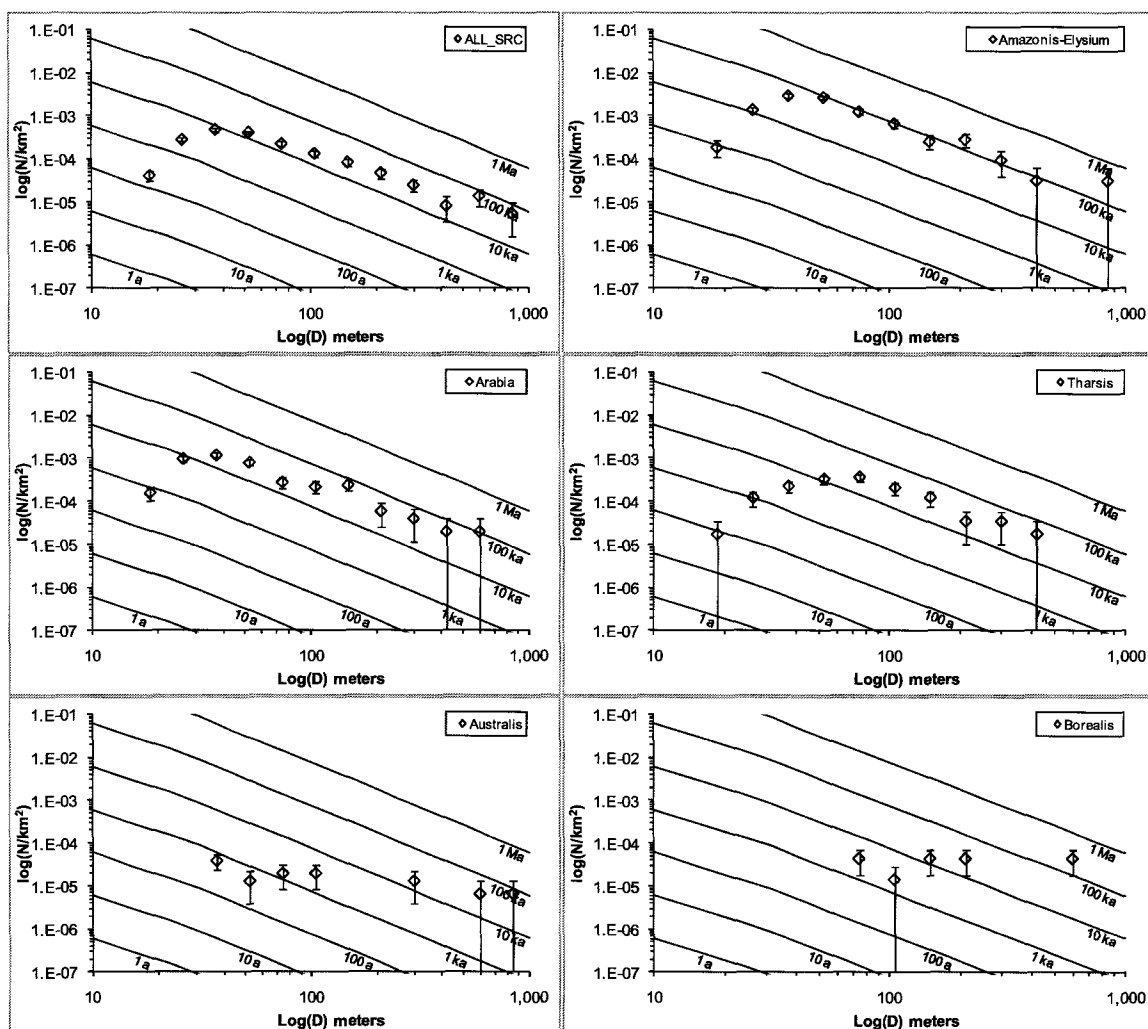


Figure 4.6: Current production function (CPF) ejecta retention ages for SRC on Mars. These new isochrons fit better to the counts and are an order of magnitude younger than the HPF isochrons due to a change in cratering rate and a shallower slope to the power-law. While retention estimates for smaller craters ($< \sim 50$ m in diameter) still retain ejecta over 10^4 year timescales, this remains true out to larger diameters within a factor of 2 or 3. Notice that SRC in Amazonis-Elysium, known for extensive secondaries from the 10.1 km diameter primary Zunil, has a 100 ka retention age for 50-500m diameter craters within a factor of 0.5 of the lowest age estimate for Zunil's impact at 180 ka determined by Kreslavsky [2008]. This implies a very young age for Zunil.

GENERAL CONCLUSIONS

From this thesis, we have learned about ejecta retention processes across Mars in terms of spatial extent, mechanisms, and duration. From this research, we can begin to answer the original questions regarding SRC ejecta retention:

- Ejecta are more readily retained near the Martian equator and are rapidly removed at high latitudes.
- Along the equator, dust deposition is the major process dictating ejecta retention, followed by presence of near-surface ice (i.e. target/formation properties control ejecta retention) as one exceeds $\pm 45^\circ$ towards either pole.
- Two retention sequences were identified: one for erosion and deposition. While the erosional sequence recedes ejecta back towards the crater rim over time, the depositional sequence retains ejecta structure while increasingly burying and reducing ejecta contrast till it matches the background.
- Ejecta are retained for ≤ 100 ka for most SRC along the equator. At higher latitudes or diameters < 50 m, ejecta retention times are at a maximum < 10 ka.
- Horizontal ejecta and crater rim planforms are morphologically similar enough between primary and secondary SRC that no one metric proved useful to distinguish between the two populations. Ejecta planform did serve as an indicator of the direction of origin via the uprange/downrange ejecta shape. The diameter-distance relationship for secondaries near Zunil established a methodology to discriminate those SRC that could not be secondaries from a source primary. Counts of non-Zunil SRC are orders of magnitude less than Zunil secondaries in

the same area. If such a ratio held for primaries to secondaries, crater dating ages would also be orders of magnitude younger in age.

Mars' surface, even along the equator, has been reworked at least within the past ~100 ka by eolian and periglacial processes. Evidence from ejecta retention studies indicate a possible shift from depositional to erosional processes south of the Martian equator within in the past hundred thousand years. Given that large obliquity transgressions occur during similar intervals resulting in ice redistribution from the poles to the equator, it is not surprising that SRC may bear witness to such a major event. SRC are one of the few geologic features capable of yielding a global perspective on surface processes over time on Mars.

SRC also serve as proxies for understanding primary and secondary cratering, crucial to providing limits and guidelines to absolute crater dating. Unlike the Moon, secondaries on Mars share many morphologic similarities to primaries and would be indistinguishable from either population minus their fresh ejecta. Whether this is strictly a result of target properties or the Martian atmosphere is not entirely clear. Dust deposition and reworking by eolian forces is a strong mechanism in shaping crater morphology post-impact. One can also expect that new SRC imaged by high-resolution cameras orbiting the Moon and Mars will lead to a reevaluation of primary and secondary morphology, further blurring and defining the distinctions between these two crater populations.

New regional ejecta retention estimates and secondary crater ejecta emplacement studies are a logical next step to understanding SRC and surface processes on Mars.

APPENDIX

Table A-1: Primary crater diameter(s) and rim measurements from MOCNA and HIRISE imagery.

ID	D _{crater} (m)	Radius (m)			Area (m ²)	Perimeter (m)	L (m)	C _R	F _R	F _D	Location _c	Image Name
		Min.	Mean	Max.								
1a	11	-	-	-	-	-	-	-	-	-	AT	S1502128
1-1	13	5	7	8	137	43	15	0.94	0.78	1.53	AT	3925-1940
1-2	11	5	5	6	87	34	11	0.96	0.91	1.58	AT	3925-1940
1-3	11	4	5	6	82	34	12	0.92	0.73	1.59	AT	3925-1940
1-4	11	5	5	6	90	35	12	0.91	0.80	1.58	AT	3925-1940
1-5	11	4	5	7	93	35	13	0.93	0.70	1.57	AT	3925-1940
1-6	10	4	5	6	80	33	12	0.92	0.70	1.60	AT	3925-1940
1-7	10	4	5	6	77	33	12	0.90	0.68	1.61	AT	3925-1940
1-8	8	4	4	5	50	25	9	0.96	0.78	1.66	AT	3925-1940
1-9	7	2	4	5	38	25	9	0.80	0.60	1.76	AT	3925-1940
1-10	7	3	4	4	40	24	9	0.89	0.62	1.72	AT	3925-1940
1-11	7	3	3	4	34	21	8	0.94	0.67	1.74	AT	3925-1940
1-12	6	3	3	3	31	20	7	0.98	0.80	1.74	AT	3925-1940
1-13	5	2	3	3	22	17	6	0.96	0.78	1.83	AT	3925-1940
2a	16	-	-	-	-	-	-	-	-	-	AR	S1502322
3a	16	-	-	-	-	-	-	-	-	-	AT	S1502488
4b	13	-	-	-	-	-	-	-	-	-	AR	S1502522
4-1	17	8	9	9	225	54	18	0.97	0.88	1.47	AR	3812-2035
5b	17	-	-	-	-	-	-	-	-	-	AR	S1502724
5-1	23	10	12	14	422	74	26	0.97	0.80	1.42	AR	4038-2005
5-2	5	2	2	3	19	16	5	0.99	0.99	1.86	AR	4038-2005
5-3	5	2	3	3	20	16	6	0.98	0.72	1.85	AR	4038-2005
5-4	4	2	2	2	15	14	4	0.99	1.18	1.94	AR	4038-2005
6b	11	-	-	-	-	-	-	-	-	-	AT	S1600097
6-1	13	6	6	7	129	41	14	0.98	0.84	1.52	AT	3780-2000
6-2	6	2	3	3	26	18	6	0.96	0.90	1.79	AT	3780-2000
6-3	3	1	1	1	5	8	3	0.98	0.74	2.55	AT	3780-2000
7a	22	-	-	-	-	-	-	-	-	-	AT	S1600667
7-1	21	8	11	12	353	69	23	0.94	0.85	1.44	AT	2764-1800
7-2	17	7	8	10	224	55	19	0.91	0.79	1.48	AT	2764-1800
7-3	13	6	6	8	123	41	15	0.91	0.70	1.55	AT	2764-1800
7-4	12	5	6	7	107	39	14	0.89	0.70	1.57	AT	2764-1800
7-5	12	4	6	8	103	39	15	0.86	0.59	1.58	AT	2764-1800
7-6	7	3	4	4	40	23	7	0.97	1.04	1.69	AT	2764-1800
7-7	5	2	2	3	19	16	5	0.97	0.96	1.87	AT	2764-1800
7-8	3	1	1	2	6	9	3	0.96	0.88	2.41	AT	2764-1800

ID	Diameter (m)	Radius (m)			Area (m ²)	Perimeter (m)	L (m)	C _R	F _R	FD _I	Location	Image Name
		Min.	Mean	Max.								
7-9	3	1	1	2	6	9	3	0.96	0.89	2.39	AT	2764-1800
8a	30	-	-	-	-	-	-	-	-	-	AT	S1600855
8-1	24	10	12	13	426	75	25	0.95	0.87	1.43	AT	5942-1825
8-2	18	8	9	11	247	57	20	0.95	0.79	1.47	AT	5942-1825
8-3	17	7	9	10	221	54	19	0.94	0.78	1.48	AT	5942-1825
8-4	11	5	5	6	85	33	12	0.97	0.75	1.58	AT	5942-1825
8-5	10	4	5	5	71	30	11	0.98	0.74	1.60	AT	5942-1825
8-6	9	4	5	5	62	29	10	0.96	0.79	1.62	AT	5942-1825
8-7	6	3	3	3	25	18	6	0.98	0.87	1.80	AT	5942-1825
8-8	6	3	3	3	32	20	7	0.99	0.82	1.74	AT	5942-1825
8-9	6	3	3	3	26	18	6	0.98	0.93	1.78	AT	5942-1825
8-10	6	3	3	3	24	17	6	0.99	0.83	1.81	AT	5942-1825
8-11	5	2	3	3	21	16	6	0.98	0.74	1.84	AT	5942-1825
9b	14	-	-	-	-	-	-	-	-	-	AT	S1601063
9-1	10	4	5	5	78	32	11	0.98	0.82	1.59	AT	4123-1915
10b	14	-	-	-	-	-	-	-	-	-	AR	S1601105
10-1	15	7	8	8	179	48	16	0.98	0.89	1.49	AR	3958-2025
11b	19	-	-	-	-	-	-	-	-	-	AT	S1601140
11-1	16	6	8	9	194	51	18	0.94	0.76	1.49	AT	2736-2075
12b	27	-	-	-	-	-	-	-	-	-	AR	S1601199
12-1	25	11	13	14	495	80	27	0.96	0.86	1.41	AR	3075-2020
13b	25	-	-	-	-	-	-	-	-	-	AT	S1601331
14b	26	-	-	-	-	-	-	-	-	-	AR	S1601674
14-1	18	7	9	11	241	58	21	0.91	0.70	1.48	AR	3101-2065
15a	13	-	-	-	-	-	-	-	-	-	AT	S1700774
15-1	12	6	6	7	120	39	13	0.99	0.90	1.53	AT	3754-1815
16b	19	-	-	-	-	-	-	-	-	-	AT	S1700998
16-1	13	6	6	7	130	41	14	0.98	0.84	1.53	AT	3527-1940
16-2	14	6	7	8	152	44	16	0.96	0.75	1.51	AT	3527-1940
17b	177	-	-	-	-	-	-	-	-	-	AT	S1701187
17-1	160	70	80	87	19809	507	169	0.97	0.88	1.26		2039-1545
18b	15	-	-	-	-	-	-	-	-	-	AR	S1701561
18-1	20	9	10	11	316	64	22	0.98	0.83	1.44	AR	3602-2085
18-2	11	5	6	6	96	35	12	0.98	0.85	1.56	AR	3602-2085
18-3	10	5	5	6	86	33	12	0.97	0.76	1.58	AR	3602-2085
18-4	9	4	4	5	60	28	10	0.98	0.76	1.62	AR	3602-2085
18-5	8	3	4	4	45	24	9	0.97	0.71	1.67	AR	3602-2085
18-6	6	3	3	3	25	18	6	0.98	0.88	1.79	AR	3602-2085

ID	D _{crater} (m)	Radius (m)			Area (m ²)	Perimeter (m)	L (m)	C _R	F _R	FD _I	Location ^c	Image Name
		Min.	Mean	Max.								
18-7	5	2	2	3	18	15	5	0.98	0.93	1.88	AR	3602-2085
18-8	5	2	3	3	22	17	6	0.95	0.79	1.83	AR	3602-2085
18-9	4	2	2	2	11	12	4	0.95	0.87	2.08	AR	3602-2085
18-10	3	2	2	2	9	11	4	0.99	0.72	2.16	AR	3602-2085
19 ^a	10	-	-	-	-	-	-	-	-	-	AT	S1701972
20 ^a	17	-	-	-	-	-	-	-	-	-	AT	S1800492
20-1	16	7	8	9	193	50	17	0.97	0.85	1.49	AT	3172-1870
20-2	13	6	6	7	123	41	14	0.94	0.80	1.54	AT	3172-1870
20-3	10	4	5	6	78	33	12	0.91	0.69	1.60	AT	3172-1870
20-4	10	4	5	6	75	32	12	0.92	0.66	1.60	AT	3172-1870
20-5	9	4	5	5	63	29	10	0.97	0.81	1.62	AT	3172-1870
20-6	8	4	4	5	50	25	9	0.96	0.78	1.66	AT	3172-1870
20-7	8	4	4	5	51	26	9	0.98	0.80	1.65	AT	3172-1870
20-8	8	4	4	5	55	27	9	0.96	0.87	1.64	AT	3172-1870
20-9	8	4	4	5	53	26	9	0.96	0.83	1.65	AT	3172-1870
20-10	7	3	3	4	35	21	7	0.96	0.91	1.72	AT	3172-1870
20-11	7	3	4	4	39	23	8	0.95	0.78	1.70	AT	3172-1870
20-12	7	3	3	4	34	21	7	0.97	0.89	1.73	AT	3172-1870
20-13	5	2	3	3	19	16	6	0.94	0.66	1.88	AT	3172-1870
20-14	5	2	3	3	21	16	5	0.98	1.07	1.84	AT	3172-1870

^aLargest crater diameter, rounded to the nearest meter, as published in Malin et al., 2006.

^bLargest crater diameter using two-point method in this study with MOCNA ROTO image.

^cAR = Arabia Terra, AT = Amazonis/Tharsis Montes

Text A-2: Primary rayed crater ejecta measurements from MOCNA and HIRISE imagery.

ID	D _{crater}	Ejecta Radius (m)			Area (m ²)	Perim. (m)	L (m)	C _R	F _R	F _D	Uprange		Location ^d	Image Name
	Max (m)	Min.	Mean	Max.							Azimuth (°) ^c			
1 _a	11	22	64	102	11681	631	166	0.37	0.54	1.38	-	AT	S1502128	
1	13	45	86	135	23851	740	217	0.55	0.64	1.31	40	AT	3925-1940	
2 _a	16	-	-	-	-	-	-	-	-	-	-	AR	S1502322	
3 _a	16	221	364	506	390193	2327	754	0.91	0.87	1.20	-	AT	S1502488	
4 _b	13	65	113	166	36319	806	256	0.70	0.71	1.27	-	AR	S1502522	
4	17	69	221	588	146661	1638	703	0.69	0.38	1.24	125	AR	3812-2035	
5 _b	17	130	260	391	187640	1797	556	0.73	0.77	1.23	-	AR	S1502724	
5	23	121	313	479	246235	4603	861	0.15	0.42	1.36	10	AR	4038-2005	
6 _b	11	70	125	190	41836	884	289	0.67	0.64	1.28	-	AT	S1600097	
6	13	70	115	154	35432	745	277	0.80	0.59	1.26	999	AT	3780-2000	
7 _a	22	-	-	-	-	-	-	-	-	-	-	AT	S1600667	
7	21	56	147	289	62861	1256	370	0.50	0.58	1.29	95	AT	2764-1800	
8 _a	30	-	-	-	-	-	-	-	-	-	-	AT	S1600855	
8	24	59	228	376	126279	2041	546	0.38	0.54	1.30	999	AT	5942-1825	
9 _b	14	92	176	333	87192	1394	471	0.56	0.50	1.27	-	AT	S1601063	
9	10	69	145	287	64419	1269	404	0.50	0.50	1.29	175	AT	4123-1915	
10 _b	14	117	161	205	79685	1060	356	0.89	0.80	1.23	-	AR	S1601105	
10	15	128	163	217	85226	1219	368	0.72	0.80	1.25	120	AR	3958-2095	
11 _b	19	56	114	224	34913	990	344	0.45	0.38	1.32	-	AR	S1601140	
11	16	29	120	362	47552	2654	557	0.08	0.20	1.46	340	AT	2736-2075	
12 _b	27	85	113	143	39940	844	267	0.70	0.71	1.27	-	AR	S1601199	
12	25	57	90	133	24431	862	240	0.41	0.54	1.34	999	AR	3075-2020	
13 _b	25	129	312	446	290965	1960	703	0.95	0.75	1.21	-	AT	S1601331	
14 _b	26	25	88	175	23295	658	207	0.68	0.69	1.29	-	AR	S1601674	
14	18	23	88	196	28186	1046	275	0.32	0.47	1.36	320	AR	3101-2065	
15 _a	13	54	79	105	18558	515	194	0.88	0.63	1.27	-	AT	S1700774	
15	12	60	92	134	24843	590	222	0.90	0.64	1.26	90	AT	3754-1815	
16 _b	19	31	115	212	38307	894	345	0.60	0.41	1.29	-	AT	S1700998	
16	14	36	139	243	48701	976	384	0.64	0.42	1.28	-	AT	3527-1940	
17 _b	177	153	352	447	404999	2390	830	0.89	0.75	1.20	999	AT	S1701187	
17	160	119	430	757	527513	3680	1077	0.49	0.58	1.25	-	AT	2039-1545	
18 _b	15	82	107	148	33102	681	237	0.90	0.75	1.25	255	AR	S1701561	
18	20	75	104	143	32326	699	249	0.83	0.66	1.26	999	AR	3602-2085	
19 _a	10	-	-	-	-	-	-	-	-	-	-	AT	S1701972	
20 _a	17	-	-	-	-	-	-	-	-	-	-	AT	S1800492	
20	16	24	155	326	64822	1447	422	0.39	0.46	1.31	340	AT	3172-1870	

^aLargest crater diameter, rounded to the nearest meter, as published in Malin et al., 2006.

^bLargest crater diameter using two-point method in this study with MOCNA ROTO image.

^cEstimate based on downrange ejecta and uprange forbidden zone. No preferred azimuth = 999.

^dAR = Arabia Terra, AT = Amazonis/Tharsis Montes

Table A-3: Secondary crater diameter(s) and rim measurements from MOCNA and HIRISE imagery.

ID	D _{crater} (m)	Radius (m)			Area (m ²)	Perimeter (m)	L (m)	C _R	F _R	FD _I	Long-Axis Angle (°) _a	Image Name
		Min.	Mean	Max								
1	28	-	-	-	630	89	-	-	-	-	130	E1101849
2	37	-	-	-	1076	116	-	-	-	-	130	E1101849
3	32	-	-	-	797	100	-	-	-	-	125	E1101849
4	32	-	-	-	774	99	-	-	-	-	999	E1101849
5	61	-	-	-	2936	192	-	-	-	-	150	E1101849
6	38	-	-	-	1156	121	-	-	-	-	130	E1101849
7	36	-	-	-	1043	115	-	-	-	-	160	E1101849
8	78	-	-	-	4808	246	-	-	-	-	10	E1101849
9	30	-	-	-	697	94	-	-	-	-	999	E1101849
10	36	16	18	21	988	114	40	0.95	0.79	1.37	92	E1301939
11	41	-	-	-	1341	130	-	-	-	-	130	E1301939
12	38	-	-	-	1153	121	-	-	-	-	999	E1301939
13	34	-	-	-	927	108	-	-	-	-	999	E1301939
14	75	-	-	-	4376	235	-	-	-	-	999	M0200581
15	66	-	-	-	3459	209	-	-	-	-	35	M0200581
16	55	-	-	-	2401	174	-	-	-	-	155	M0200581
17	56	-	-	-	2409	174	-	-	-	-	999	M0200581
18	47	-	-	-	1753	149	-	-	-	-	999	M0200581
19	72	-	-	-	4110	227	-	-	-	-	125	M0204182
19	66	29	33	37	3396	211	71	0.96	0.86	1.32	143	2820-1860
20	53	-	-	-	2202	167	-	-	-	-	999	M0204182
20	46	20	23	26	1589	145	48	0.95	0.88	1.35	119	2820-1860
21	39	-	-	-	1174	122	-	-	-	-	999	M0204182
21	34	15	17	19	891	107	36	0.98	0.88	1.38	122	2820-1860
22	56	-	-	-	2453	176	-	-	-	-	999	M0204182
23	134	-	-	-	13993	420	-	-	-	-	999	M0204182
24	49	-	-	-	1876	154	-	-	-	-	999	M0401791
25	42	-	-	-	1353	131	-	-	-	-	999	M0401791
26	48	-	-	-	1765	149	-	-	-	-	50	M0401791
27	32	-	-	-	816	101	-	-	-	-	999	M0401791
28	60	-	-	-	2836	189	-	-	-	-	135	M0401791
29	32	-	-	-	790	100	-	-	-	-	125	M0401791
30	61	-	-	-	2915	192	-	-	-	-	999	M0401791
31	105	-	-	-	8567	328	-	-	-	-	40	M0401791
32	46	-	-	-	1684	146	-	-	-	-	999	M0401791
33	55	-	-	-	2373	173	-	-	-	-	40	M0401791
34	60	-	-	-	2853	190	-	-	-	-	85	M0401791
35	49	-	-	-	1898	155	-	-	-	-	999	M0802130
36	67	-	-	-	3514	210	-	-	-	-	85	R0600296
37	43	-	-	-	1426	134	-	-	-	-	999	E0401721

ID	D _{crater} (m)	Radius (m)			Area (m ²)	Perimeter (m)	L (m)	C _R	F _R	FD _I	Long-Axis Angle (°) _a	Image Name
		Min.	Mean	Max.								
38	52	20	26	30	2056	166	60	0.93	0.73	1.34	25	R1100286
39	25	-	-	-	476	77	-	-	-	-	40	E1101849
40	27	-	-	-	565	84	-	-	-	-	40	E1101849
41	36	-	-	-	1018	113	-	-	-	-	85	E1101849
42	35	-	-	-	960	110	-	-	-	-	45	E1101849
43	30	-	-	-	704	94	-	-	-	-	130	E1301939
44	71	-	-	-	3913	222	-	-	-	-	105	M0401791
45	66	-	-	-	3365	206	-	-	-	-	999	M0401791
46	38	-	-	-	1101	118	-	-	-	-	50	M0401791
47	46	-	-	-	1628	143	-	-	-	-	999	M0401791
48	65	-	-	-	3294	204	-	-	-	-	180	M0401791
49	42	-	-	-	1360	131	-	-	-	-	999	M0401791
100	70	30	35	40	3863	226	79	0.95	0.79	1.31	154	2147-1875
101	82	37	41	47	5255	265	90	0.94	0.83	1.30	26	2147-1875
102	49	22	25	28	1858	157	54	0.95	0.81	1.34	67	2147-1875
103	58	26	29	33	2584	185	62	0.95	0.86	1.33	13	2661-1895
104	26	10	13	15	548	87	29	0.91	0.83	1.42	127	2661-1895
105	35	16	18	19	954	112	38	0.95	0.84	1.38	131	2661-1895
106	37	16	19	21	1065	119	41	0.94	0.81	1.37	174	2661-1895
107	28	10	14	16	552	87	31	0.92	0.73	1.41	177	2661-1895
108	19	8	9	10	268	59	20	0.98	0.85	1.46	145	2661-1895
109	28	12	14	16	589	89	31	0.94	0.78	1.41	14	2661-1895
110	31	14	15	17	743	99	33	0.96	0.87	1.39	104	2661-1895
111	20	7	10	12	322	68	22	0.87	0.85	1.46	120	2661-1895
112	14	5	7	9	143	45	16	0.87	0.71	1.54	20	2661-1895
113	21	9	11	12	359	68	23	0.96	0.86	1.44	86	2661-1895
114	35	14	17	20	928	118	38	0.83	0.82	1.40	62	2661-1895
115	53	19	26	32	2138	183	63	0.80	0.69	1.36	27	2661-1895
116	80	36	40	44	4881	253	86	0.95	0.84	1.30	62	3874-1815
117	57	22	28	36	2499	193	67	0.84	0.71	1.35	90	3874-1815
118	65	22	32	40	3188	220	75	0.83	0.72	1.34	56	3874-1815
119	128	57	64	75	12632	420	142	0.90	0.80	1.28	12	3874-1815
120	111	44	56	68	9378	379	132	0.82	0.69	1.30	96	3874-1815
121	54	18	27	31	2213	187	61	0.79	0.76	1.36	96	3874-1815
122	86	39	43	50	5684	281	96	0.91	0.79	1.30	103	3874-1815
123	82	37	41	48	5172	264	88	0.93	0.85	1.30	175	3874-1815
124	75	28	37	45	4326	252	85	0.85	0.76	1.32	6	3874-1815
125	55	22	28	35	2342	195	65	0.77	0.71	1.36	113	3874-1815
126	78	30	39	48	4601	267	90	0.81	0.72	1.32	132	3874-1815
127	120	50	60	67	11129	393	130	0.90	0.84	1.28	115	3874-1815
128	64	22	32	39	3140	216	74	0.85	0.73	1.33	106	3874-1815
129	43	17	21	25	1445	141	50	0.91	0.74	1.36	120	3874-1815

ID	Derater (m)	Radius (m)			Area (m ²)	Perimeter (m)	L (m)	C _R	F _R	FD _I	Long-Axis Angle (°) _a	Image Name
		Min.	Mean	Max.								
130	48	19	24	29	1787	161	55	0.87	0.75	1.36	107	3874-1815
131	54	24	27	31	2279	178	58	0.90	0.86	1.34	158	3874-1815
132	57	23	28	33	2532	188	63	0.90	0.81	1.34	149	3874-1815
133	53	23	26	31	2157	170	59	0.94	0.79	1.34	27	3874-1815
134	65	29	33	37	3332	211	70	0.94	0.87	1.32	94	3874-1815
135	77	30	39	47	4322	242	91	0.92	0.66	1.31	166	3874-1815
136	40	13	20	24	1248	141	45	0.79	0.78	1.39	120	3874-1815
137	30	6	15	21	635	107	41	0.70	0.48	1.45	79	6788-1955
138	28	11	14	16	605	91	31	0.92	0.80	1.41	156	6788-1955
139	21	8	11	12	345	69	23	0.92	0.83	1.45	48	6788-1955
140	29	11	15	19	620	95	35	0.86	0.64	1.42	132	6788-1955
141	17	7	9	10	221	54	20	0.95	0.70	1.48	125	6788-1955
142	13	5	7	8	134	43	16	0.89	0.67	1.54	5	6788-1955
143	12	6	6	7	120	39	13	0.96	0.90	1.54	45	6788-1955
144	33	14	16	19	823	105	36	0.95	0.81	1.39	47	6788-1955
145	19	9	10	10	285	60	20	0.98	0.91	1.45	44	6788-1955
146	49	23	25	26	1875	155	51	0.99	0.92	1.34	50	6788-1955
147	27	13	14	15	582	86	29	0.98	0.88	1.40	81	6788-1955
148	16	7	8	9	191	50	17	0.96	0.84	1.49	60	6788-1955
149	12	5	6	7	107	37	12	0.97	0.95	1.55	55	6788-1955
150	25	11	12	13	471	78	26	0.96	0.89	1.42	95	6788-1955
151	14	6	7	8	149	44	15	0.96	0.84	1.51	69	6788-1955
152	49	23	24	26	1866	155	53	0.97	0.85	1.34	98	6788-1955
153	46	21	23	25	1659	147	49	0.97	0.88	1.35	49	6788-1955
154	33	16	16	17	837	103	34	0.99	0.92	1.38	105	6788-1955
155	26	12	13	15	524	82	28	0.98	0.85	1.41	61	6788-1955
156	36	16	18	22	1024	116	40	0.95	0.81	1.37	169	6788-1955
157	26	12	13	14	505	81	27	0.97	0.88	1.41	87	6933-1950
158	34	16	17	18	896	107	35	0.98	0.93	1.37	73	6933-1950
159	24	11	12	13	450	76	26	0.97	0.85	1.42	73	6933-1950
160	37	16	19	21	1096	122	41	0.93	0.83	1.37	77	6933-1950
161	36	17	18	19	1010	113	38	0.99	0.89	1.37	108	6933-1950
162	25	11	13	15	485	80	28	0.96	0.79	1.42	159	6933-1950
163	29	14	15	16	653	92	31	0.98	0.87	1.39	76	6933-1950
164	26	11	13	14	501	81	27	0.97	0.88	1.41	171	6801-1935
165	20	9	10	11	313	63	21	0.98	0.90	1.44	74	6801-1935
166	50	23	25	27	1906	157	53	0.97	0.86	1.34	39	6801-1935
167	29	13	14	16	638	91	31	0.97	0.84	1.40	62	6801-1935
168	19	9	10	10	286	61	20	0.98	0.91	1.45	57	6801-1935
169	42	16	21	23	1314	134	45	0.92	0.83	1.36	60	6801-1935
170	30	13	15	17	677	94	32	0.96	0.84	1.39	32	6801-1935
171	52	23	26	31	2037	165	59	0.94	0.74	1.34	102	6801-1935

ID	Derater (m)	Radius (m)			Area (m ²)	Perimeter (m)	L (m)	C _R	F _R	FD _I	Long-Axis Angle (°) _a	Image Name
		Min.	Mean	Max								
172	35	16	18	20	954	111	39	0.97	0.80	1.37	85	6801-1935
173	30	13	15	16	683	94	32	0.97	0.85	1.39	174	6801-1935
174	80	33	40	49	4945	259	95	0.93	0.70	1.31	110	6801-1935
175	33	15	17	18	851	105	36	0.98	0.84	1.38	31	6801-1935
176	47	21	23	26	1654	147	51	0.96	0.81	1.35	75	6801-1935
177	55	24	28	31	2327	175	59	0.96	0.85	1.33	180	6801-1935
178	31	13	16	19	730	99	36	0.94	0.72	1.39	123	6801-1935
179	51	24	26	27	2050	162	54	0.98	0.89	1.33	5	6801-1935
180	36	16	18	19	983	112	37	0.98	0.91	1.37	58	6801-1935
181	24	11	12	13	442	75	25	0.98	0.90	1.42	90	6801-1935
182	31	15	16	16	746	97	32	0.99	0.93	1.38	9	6801-1935
183	24	11	12	13	435	75	24	0.98	0.96	1.42	20	6801-1935
184	39	18	19	20	1158	122	40	0.98	0.92	1.36	102	6801-1935
185	40	18	20	21	1221	125	42	0.98	0.88	1.36	56	6801-1935
186	42	18	21	24	1385	139	48	0.90	0.77	1.36	117	6801-1935
187	43	19	21	24	1397	136	46	0.94	0.84	1.36	137	6801-1935
188	32	13	16	18	783	102	35	0.94	0.81	1.39	125	6801-1935
189	23	10	12	13	411	74	25	0.93	0.84	1.43	17	6801-1935
190	28	11	14	17	619	93	33	0.89	0.72	1.41	61	6801-1935
191	25	12	13	14	499	81	27	0.97	0.87	1.41	71	6801-1935
192	29	12	15	17	638	93	33	0.93	0.75	1.40	23	6801-1935
193	44	15	22	27	1490	147	50	0.87	0.76	1.37	126	6801-1935
194	59	27	29	32	2678	186	62	0.98	0.89	1.32	91	6801-1935
195	33	14	17	19	848	106	36	0.94	0.83	1.38	84	6801-1935
196	54	23	27	30	2180	170	59	0.95	0.80	1.34	129	6801-1935
197	24	10	12	13	456	78	27	0.95	0.80	1.42	43	6801-1935
198	22	10	11	12	379	70	24	0.98	0.84	1.43	68	6801-1935
199	23	10	11	14	403	73	26	0.94	0.76	1.43	137	6801-1935
200	91	37	45	52	6454	303	97	0.88	0.87	1.30	57	6801-1935
201	32	15	16	17	782	101	34	0.97	0.86	1.38	105	6801-1935
202	58	23	29	33	2623	193	65	0.88	0.79	1.34	31	6801-1935
203	56	22	28	34	2370	183	63	0.89	0.76	1.34	164	6801-1935
204	36	15	18	20	963	113	39	0.94	0.81	1.38	148	6801-1935
205	29	12	14	16	654	93	31	0.95	0.87	1.40	109	6801-1935
206	32	14	16	17	765	100	34	0.95	0.84	1.39	63	6801-1935
207	40	16	20	24	1202	128	44	0.92	0.79	1.37	142	6801-1935
208	30	14	15	16	675	94	32	0.96	0.84	1.40	26	6801-1935
209	51	20	26	32	1936	168	56	0.86	0.79	1.35	38	6801-1935
210	40	18	20	22	1245	127	43	0.97	0.86	1.36	13	6801-1935
211	43	19	22	24	1462	138	47	0.96	0.84	1.35	45	6801-1935
212	59	26	29	34	2634	187	66	0.95	0.77	1.33	92	6801-1935
213	63	29	32	34	3061	199	67	0.97	0.87	1.32	53	6801-1935

ID	D _{crater} (m)	Radius (m)			Area (m ²)	Perimeter (m)	L (m)	C _R	F _R	FD _I	Long-Axis Angle (°) _a	Image Name
		Min.	Mean	Max.								
214	43	18	21	25	1379	135	47	0.95	0.79	1.36	77	6801-1935
215	33	14	16	18	827	104	35	0.96	0.86	1.38	57	6801-1935
216	27	13	14	15	572	86	29	0.97	0.87	1.40	97	6801-1935
217	41	19	21	22	1335	131	44	0.97	0.88	1.36	12	6801-1935
218	22	10	11	12	386	70	24	0.98	0.85	1.43	107	6801-1935
219	39	17	20	23	1146	124	43	0.94	0.79	1.37	46	6801-1935
220	69	30	35	39	3770	224	78	0.94	0.79	1.31	123	6801-1935
221	65	28	33	37	3250	206	72	0.96	0.80	1.32	27	6801-1935
222	28	13	14	16	624	89	30	0.98	0.88	1.40	173	6801-1935
223	40	16	20	23	1206	128	45	0.93	0.76	1.37	83	6801-1935
224	48	22	24	27	1764	151	52	0.97	0.83	1.34	107	6801-1935
225	29	13	14	16	637	91	31	0.96	0.84	1.40	30	6801-1935
226	34	16	17	18	917	108	36	0.99	0.90	1.37	19	6801-1935
227	52	23	26	29	2109	165	57	0.97	0.83	1.33	63	6801-1935
228	31	15	15	17	735	97	33	0.98	0.86	1.39	66	6801-1935
229	83	37	41	46	5301	262	89	0.97	0.85	1.30	96	6801-1935
230	55	25	28	29	2386	175	58	0.98	0.90	1.33	76	6801-1935
231	32	15	16	18	810	102	34	0.98	0.89	1.38	116	6801-1935
232	34	14	17	19	885	110	37	0.92	0.82	1.38	1	6801-1935
233	44	20	22	23	1502	140	47	0.97	0.87	1.35	71	6801-1935
234	49	23	24	25	1834	153	50	0.98	0.93	1.34	85	6801-1935
235	40	20	20	21	1266	127	41	0.99	0.96	1.36	50	6801-1935
236	56	25	28	30	2386	175	59	0.98	0.87	1.33	54	6801-1935
237	72	33	36	38	4068	228	75	0.98	0.92	1.31	79	6801-1935
238	33	15	17	18	847	105	35	0.97	0.88	1.38	85	6801-1935
239	46	21	23	25	1597	144	49	0.97	0.85	1.35	50	6801-1935
240	55	25	27	30	2336	174	57	0.97	0.92	1.33	44	6801-1935
241	37	18	19	20	1085	118	39	0.98	0.91	1.36	78	6801-1935
242	39	18	19	21	1176	122	41	0.99	0.89	1.36	80	6801-1935
243	37	17	18	19	1043	116	38	0.98	0.92	1.37	58	6801-1935
244	46	21	23	25	1598	144	48	0.97	0.88	1.35	79	6801-1935
245	56	26	28	30	2457	178	59	0.98	0.90	1.33	28	6801-1935
246	37	17	18	20	1055	117	39	0.96	0.88	1.37	43	6801-1935
247	51	23	26	28	2031	163	53	0.96	0.92	1.34	86	6801-1935
248	49	23	24	26	1824	153	51	0.98	0.89	1.34	79	6801-1935
249	34	16	17	19	924	109	36	0.98	0.91	1.37	63	6801-1935
250	35	17	18	19	965	111	37	0.98	0.90	1.37	65	6801-1935
251	38	18	19	21	1153	122	40	0.98	0.92	1.36	143	6801-1935
252	24	11	12	13	457	77	26	0.98	0.86	1.42	72	6801-1935
253	34	16	17	18	906	108	36	0.98	0.89	1.37	72	6801-1935
254	80	38	40	42	4995	252	83	0.99	0.92	1.30	41	6801-1935
255	42	19	21	23	1403	134	45	0.98	0.88	1.35	72	6801-1935

ID	D _{crater} (m)	Radius (m)			Area (m ²)	Perimeter (m)	L (m)	C _R	F _R	FD _I	Long-Axis Angle (°) _a	Image Name
		Min.	Mean	Max.								
256	37	17	19	21	1082	118	41	0.98	0.82	1.37	155	6801-1935
257	40	19	20	21	1239	126	41	0.98	0.94	1.36	75	6801-1935
259	37	17	18	20	1042	115	38	0.99	0.92	1.37	58	6801-1935
260	38	17	19	22	1140	122	44	0.97	0.75	1.36	132	6801-1935
261	32	15	16	17	798	101	33	0.99	0.93	1.38	58	6801-1935
262	54	24	27	29	2278	171	58	0.98	0.86	1.33	109	6801-1935
263	45	21	22	23	1563	141	46	0.99	0.94	1.35	72	6801-1935
264	35	17	17	18	954	110	36	0.98	0.94	1.37	33	6801-1935
265	31	14	16	17	751	98	34	0.98	0.83	1.39	65	6801-1935
266	37	17	18	19	1039	115	38	0.98	0.92	1.37	58	6801-1935
267	45	21	22	24	1560	142	48	0.98	0.86	1.35	68	6801-1935
268	49	23	24	26	1865	154	51	0.98	0.91	1.34	46	6801-1935
269	36	17	18	19	999	113	37	0.98	0.93	1.37	96	6801-1935
270	59	28	30	31	2725	186	61	0.99	0.93	1.32	60	6801-1935
271	41	19	20	22	1275	128	43	0.98	0.88	1.36	59	6801-1935
272	48	22	24	26	1807	152	50	0.98	0.92	1.34	24	6801-1935
273	38	18	19	21	1145	121	40	0.99	0.91	1.36	95	6801-1935
274	35	16	18	19	982	112	37	0.98	0.91	1.37	6	6801-1935
275	96	45	48	52	7245	307	101	0.97	0.90	1.29	13	2806-1870
276	73	31	37	42	4122	237	81	0.92	0.80	1.31	146	2806-1870
277	48	22	24	26	1803	152	51	0.98	0.88	1.34	93	2806-1870
278	63	27	32	35	3113	201	68	0.97	0.86	1.32	105	2806-1870
279	115	49	57	69	9956	369	134	0.92	0.71	1.28	169	2806-1870
280	79	33	40	44	4851	255	84	0.94	0.88	1.31	53	2806-1870
281	67	27	33	39	3298	210	77	0.94	0.71	1.32	60	2806-1870
282	46	19	23	26	1557	143	51	0.95	0.76	1.35	103	2806-1870
283	94	35	47	54	6825	306	100	0.92	0.87	1.30	77	2806-1870
284	146	65	73	81	16272	459	152	0.97	0.90	1.26	69	2806-1870
285	99	44	49	56	7429	311	108	0.96	0.81	1.29	78	2806-1870
286	95	39	48	59	6853	316	111	0.86	0.71	1.30	155	2806-1870
287	81	36	41	46	5171	265	88	0.93	0.85	1.30	105	2806-1870
288	57	18	28	33	2485	197	63	0.80	0.80	1.35	163	2806-1870
289	98	38	49	58	7541	342	113	0.81	0.75	1.31	149	2806-1870
290	39	15	20	23	1198	127	44	0.93	0.79	1.37	25	2806-1870
291	69	30	34	37	3617	219	72	0.95	0.89	1.32	21	2806-1870
292	44	19	22	26	1483	142	49	0.93	0.79	1.36	61	2806-1870
293	64	26	32	38	3076	211	69	0.87	0.82	1.33	78	2806-1870
294	43	19	22	23	1444	138	46	0.95	0.87	1.36	22	2806-1870
295	36	16	18	19	990	113	38	0.97	0.87	1.37	73	2806-1870
296	55	25	28	30	2297	172	57	0.98	0.90	1.33	72	2806-1870
297	25	11	13	15	492	81	29	0.95	0.74	1.42	173	2806-1870
298	58	26	29	32	2576	184	64	0.96	0.80	1.33	90	4006-1900

ID	D _{crater} (m)	Radius (m)			Area (m ²)	Perimeter (m)	L (m)	C _R	F _R	FD _i	Long-Axis Angle (°) ^a	Image Name
		Min.	Mean	Max.								
299	38	15	19	21	1118	124	41	0.92	0.85	1.37	92	4006-1900
300	33	15	17	19	863	107	37	0.95	0.80	1.38	89	4006-1900
301	36	16	18	20	1001	114	40	0.96	0.80	1.37	32	4006-1900
302	21	9	10	12	327	66	22	0.95	0.86	1.45	7	4006-1900
303	15	7	8	9	174	48	16	0.96	0.87	1.50	98	4006-1900
304	27	11	14	16	551	86	32	0.93	0.68	1.41	109	4006-1900
305	28	11	14	15	614	95	30	0.86	0.87	1.42	132	2820-1860
306	48	21	24	27	1770	154	52	0.94	0.83	1.35	66	2820-1860
307	38	16	19	22	1116	123	42	0.92	0.81	1.37	157	2820-1860
308	29	14	14	15	634	90	30	0.99	0.90	1.39	21	1342-1910
309	49	23	25	27	1903	156	53	0.99	0.86	1.34	6	1342-1910
310	32	14	16	17	772	99	33	0.98	0.90	1.38	137	1342-1910
311	22	10	11	12	378	70	25	0.97	0.77	1.43	60	1342-1910
312	77	36	39	41	4615	247	80	0.95	0.92	1.31	130	1342-1910
313	28	13	14	15	593	87	29	0.98	0.90	1.40	4	1342-1910
314	32	15	16	17	814	103	33	0.97	0.95	1.38	94	1342-1910
315	36	16	18	19	974	113	37	0.97	0.91	1.37	99	1342-1910
316	55	23	28	30	2417	178	59	0.95	0.88	1.33	27	1342-1910
317	15	7	7	8	165	46	15	0.98	0.93	1.50	89	1342-1910
318	11	5	6	7	103	37	13	0.93	0.78	1.56	156	1342-1910
319	21	10	11	12	351	67	24	0.97	0.78	1.44	56	1342-1910
320	16	7	8	9	198	51	17	0.97	0.87	1.48	32	1342-1910
321	14	6	7	8	143	44	15	0.92	0.81	1.53	18	1342-1910
322	15	6	7	9	171	49	17	0.90	0.75	1.51	141	1342-1910
323	12	5	6	8	107	39	15	0.87	0.61	1.57	26	1342-1910
324	27	11	13	15	542	84	28	0.96	0.88	1.41	47	1342-1910
325	12	5	6	7	109	38	13	0.95	0.82	1.55	5	1342-1910
326	20	9	10	11	304	63	21	0.96	0.88	1.45	42	1342-1910
327	14	6	7	8	159	45	16	0.97	0.79	1.51	179	1342-1910
328	20	9	10	11	300	62	21	0.97	0.87	1.45	158	1342-1910
329	17	6	8	11	213	56	21	0.85	0.62	1.50	117	1342-1910
330	16	7	8	9	197	52	18	0.91	0.78	1.50	57	1342-1910
331	14	6	7	8	142	43	14	0.96	0.92	1.52	81	1342-1910
332	18	8	9	10	245	58	19	0.93	0.87	1.47	147	1342-1910

^aEstimate from Standard Deviation Ellipse (SDE) semi-major axis orientation. No data value = 999.

Table A-4: Secondary rayed crater ejecta measurements from MOCNA and HIRISE imagery.

ID	D _{crater} (m)	Ejecta Radius (m)			Area (m ²)	Perimeter (m)	L (m)	C _R	F _R	F _D	Uprange		Image Name
		Min.	Mean	Max.							Azimuth (°) _a		
1	43	54	152	246	76385	1534	433	0.41	0.52	1.30	10	E0401721	
2	28	71	113	177	34444	1071	318	0.38	0.43	1.34	999	E1101849	
3	37	36	91	184	22836	1177	324	0.21	0.28	1.41	140	E1101849	
4	32	40	83	159	21562	953	261	0.30	0.40	1.37	105	E1101849	
5	32	47	97	166	25022	1116	306	0.25	0.34	1.39	210	E1101849	
6	61	126	221	349	139361	2502	633	0.28	0.44	1.32	40	E1101849	
7	38	52	90	169	23544	909	276	0.36	0.39	1.35	10	E1101849	
8	36	70	167	354	72769	1717	505	0.31	0.36	1.33	50	E1101849	
9	78	159	306	514	284897	3712	962	0.26	0.39	1.31	90	E1101849	
10	30	42	93	204	18842	1182	282	0.17	0.30	1.44	150	E1101849	
11	25	29	58	91	8247	520	148	0.38	0.48	1.39	145	E1101849	
12	27	46	95	181	21605	808	239	0.42	0.48	1.34	140	E1101849	
13	36	44	81	113	17149	656	209	0.50	0.50	1.33	120	E1101849	
14	35	36	88	153	19170	809	226	0.37	0.48	1.36	125	E1101849	
15	37	71	177	364	85647	2117	548	0.24	0.36	1.35	25	E1301939	
16	41	49	120	199	39079	1470	361	0.23	0.38	1.38	999	E1301939	
17	38	30	95	171	26078	1372	321	0.17	0.32	1.42	35	E1301939	
18	34	33	95	185	22139	1084	291	0.24	0.33	1.40	40	E1301939	
19	30	34	68	131	12375	707	196	0.31	0.41	1.39	130	E1301939	
20	75	194	354	516	376860	3812	949	0.33	0.53	1.28	30	M0200581	
21	66	81	221	393	112788	2788	754	0.18	0.25	1.36	100	M0200581	
22	55	60	130	251	48108	1319	347	0.35	0.51	1.33	130	M0200581	
23	56	73	153	253	56998	1489	374	0.32	0.52	1.33	90	M0200581	
24	47	96	147	228	72301	1193	394	0.64	0.59	1.27	999	M0200581	
25	72	60	163	333	66726	2264	540	0.16	0.29	1.39	355	M0204182	
26	53	74	160	255	67514	1436	479	0.41	0.37	1.31	30	M0204182	
27	39	57	87	154	20719	751	225	0.46	0.52	1.33	50	M0204182	
28	56	82	206	419	122442	2766	648	0.20	0.37	1.35	999	M0204182	
29	134	307	607	947	880742	5026	1450	0.44	0.53	1.25	150	M0204182	
30	49	87	139	206	63829	1250	361	0.51	0.62	1.29	190	M0401791	
31	42	52	181	410	79071	2152	630	0.21	0.25	1.36	200	M0401791	
32	48	74	154	281	57038	1800	454	0.22	0.35	1.37	160	M0401791	
33	32	69	140	266	48596	1195	422	0.43	0.35	1.31	999	M0401791	
34	60	55	194	376	79841	2584	577	0.15	0.31	1.39	20	M0401791	
35	32	39	104	193	22337	1011	342	0.27	0.24	1.38	190	M0401791	
36	61	64	180	305	79870	2097	551	0.23	0.33	1.36	205	M0401791	
37	105	157	505	1065	821756	8177	1686	0.15	0.37	1.32	130	M0401791	
38	46	64	172	331	63977	1894	517	0.22	0.30	1.36	185	M0401791	
39	55	87	173	260	94430	1526	473	0.51	0.54	1.28	180	M0401791	
40	60	80	219	359	140930	3671	663	0.13	0.41	1.38	999	M0401791	

ID	D _{crater} (m)	Ejecta Radius (m)			Area (m ²)	Perimeter (m)	L (m)	C _R	F _R	FD _I	Uprange Azimuth (°) _a	Image Name
		Min.	Mean	Max.								
41	71	121	243	398	163253	3132	710	0.21	0.41	1.34	195	M0401791
42	66	142	229	334	151581	2882	632	0.23	0.48	1.34	195	M0401791
43	38	47	105	223	27790	1412	336	0.18	0.31	1.42	200	M0401791
44	46	53	117	225	42396	1852	360	0.16	0.42	1.41	230	M0401791
45	65	73	181	307	85319	1915	489	0.29	0.45	1.33	230	M0401791
46	42	44	96	154	27256	894	267	0.43	0.49	1.33	240	M0401791
47	49	127	227	385	154484	2091	645	0.44	0.47	1.28	999	M0802130
48	67	91	271	818	156204	3467	1042	0.16	0.18	1.36	95	R0602961
49	59	78	146	237	66603	1515	406	0.36	0.51	1.32	215	R1102861
19	66	78	163	323	63318	2482	588	0.13	0.23	1.41	25	2820-1860
20	46	41	120	206	42703	1568	344	0.22	0.46	1.38	30	2820-1860
21	34	48	84	132	19616	875	244	0.32	0.42	1.37	20	2820-1860
104	26	32	103	183	30376	1268	293	0.24	0.45	1.38	75	2661-1895
105	35	37	98	173	26769	1493	333	0.15	0.31	1.43	48	2661-1895
106	37	67	126	201	41849	1457	343	0.25	0.45	1.37	150	2661-1895
107	28	52	103	245	28784	1401	353	0.18	0.29	1.41	115	2661-1895
108	19	15	87	142	19023	588	203	0.69	0.59	1.29	120	2661-1895
109	28	29	49	83	6737	430	133	0.46	0.48	1.38	42	2661-1895
110	31	31	78	144	16022	948	236	0.22	0.37	1.42	80	2661-1895
111	20	23	82	135	16150	835	209	0.29	0.47	1.39	75	2661-1895
112	14	13	38	69	3759	419	100	0.27	0.48	1.47	140	2661-1895
113	21	32	63	109	11317	683	201	0.31	0.36	1.40	100	2661-1895
114	35	55	122	200	41781	1479	395	0.24	0.34	1.37	999	2661-1895
137	30	43	98	194	28208	1677	323	0.13	0.34	1.45	999	6788-1955
138	28	21	56	103	7604	569	145	0.30	0.46	1.42	160	6788-1955
139	21	19	61	137	9662	1035	248	0.11	0.20	1.51	999	6788-1955
140	29	33	86	189	18220	1357	298	0.12	0.26	1.47	999	6788-1955
141	17	10	42	80	4485	492	138	0.23	0.30	1.47	185	6788-1955
142	13	13	27	48	1888	319	94	0.23	0.27	1.53	180	6788-1955
143	12	20	49	131	3902	486	175	0.21	0.16	1.50	25	6788-1955
144	33	43	110	191	27723	1193	376	0.24	0.25	1.38	116	6788-1955
145	19	16	54	100	7102	651	179	0.21	0.28	1.46	145	6788-1955
146	49	45	118	176	44341	876	311	0.73	0.58	1.27	165	6788-1955
147	27	35	60	107	9782	728	182	0.23	0.38	1.43	999	6788-1955
150	25	25	49	70	7472	498	121	0.38	0.65	1.39	999	6788-1955
151	14	19	36	72	3096	350	108	0.32	0.34	1.46	355	6788-1955
152	49	62	128	214	47947	2019	366	0.15	0.46	1.41	999	6788-1955
153	46	44	215	389	91040	1970	534	0.29	0.41	1.33	999	6788-1955
154	33	34	93	141	21903	1147	260	0.21	0.41	1.41	140	6788-1955
155	26	15	47	70	5944	386	110	0.50	0.63	1.37	150	6788-1955
156	36	39	97	169	22983	1229	289	0.19	0.35	1.42	125	6788-1955
157	26	22	40	75	4230	374	118	0.38	0.39	1.42	999	6788-1955

ID	D _{crater} (m)	Ejecta Radius (m)			Area (m ²)	Perimeter (m)	L (m)	C _R	F _R	FD _I	Uprange	Image Name
		Min.	Mean	Max.							Azimuth (°) _a	
158	34	33	56	94	9942	640	165	0.31	0.46	1.40	999	6933-1950
159	24	24	47	76	5903	423	126	0.42	0.47	1.39	180	6788-1955
160	37	34	86	193	17998	1127	279	0.18	0.29	1.43	185	6933-1950
161	36	45	91	185	18177	918	257	0.27	0.35	1.39	180	6933-1950
162	25	17	59	96	6724	403	123	0.52	0.57	1.36	185	6933-1950
163	29	27	51	82	7600	465	135	0.44	0.53	1.37	220	6933-1950
164	26	21	49	88	5785	487	137	0.31	0.39	1.43	165	6801-1935
165	20	14	42	88	2898	411	156	0.22	0.15	1.51	243	6801-1935
166	50	53	116	207	36802	1530	326	0.20	0.44	1.39	999	6801-1935
167	29	39	77	132	15180	641	186	0.46	0.56	1.34	195	6801-1935
168	19	17	40	88	4876	371	135	0.45	0.34	1.39	999	6801-1935
169	42	33	104	263	27322	1406	370	0.17	0.25	1.42	305	6801-1935
170	30	37	66	132	11518	595	185	0.41	0.43	1.37	165	6801-1935
171	52	77	181	392	69716	2193	630	0.18	0.22	1.38	215	6801-1935
172	35	26	67	105	14317	760	196	0.31	0.47	1.39	305	6801-1935
173	30	31	71	133	13047	891	211	0.21	0.37	1.43	320	6801-1935
174	80	136	331	684	256275	3384	1116	0.28	0.26	1.31	205	6801-1935
175	33	41	73	119	15447	813	226	0.29	0.39	1.39	220	6801-1935
179	51	64	156	247	68526	1978	436	0.22	0.46	1.36	165	6801-1935
180	36	42	71	131	15314	831	200	0.28	0.49	1.40	205	6801-1935
181	24	25	56	98	8534	614	179	0.28	0.34	1.42	185	6801-1935
186	42	42	100	177	27322	1181	265	0.25	0.50	1.38	190	6801-1935
187	43	43	123	246	28863	1677	353	0.13	0.29	1.45	30	6801-1935
188	32	25	74	150	12313	847	267	0.22	0.22	1.43	355	6801-1935
189	23	24	44	74	5755	438	124	0.38	0.48	1.41	220	6801-1935
190	28	27	61	112	9571	756	211	0.21	0.27	1.45	999	6801-1935
191	25	21	43	69	5332	559	113	0.21	0.53	1.47	165	6801-1935
192	29	23	78	182	9914	905	259	0.15	0.19	1.48	230	6801-1935
194	59	78	252	404	161005	2952	685	0.23	0.44	1.33	215	6801-1935
195	33	28	77	157	16324	1171	274	0.15	0.28	1.46	999	6801-1935
196	54	70	219	366	106149	3003	629	0.15	0.34	1.38	999	6801-1935
197	24	26	76	157	10202	881	278	0.17	0.17	1.47	135	6801-1935
198	22	18	44	90	5073	379	118	0.44	0.46	1.39	225	6801-1935
199	23	17	48	137	4620	494	190	0.24	0.16	1.47	225	6801-1935
200	91	185	336	591	319521	4024	1068	0.25	0.36	1.31	999	6801-1935
201	32	34	87	198	18572	1309	349	0.14	0.19	1.46	215	6801-1935
202	58	55	181	346	79017	2964	565	0.11	0.32	1.42	200	6801-1935
203	56	80	168	340	64448	1606	539	0.31	0.28	1.33	225	6801-1935
204	36	27	84	169	19663	1292	239	0.15	0.44	1.45	270	6801-1935
205	29	29	61	108	9404	897	187	0.15	0.34	1.49	315	6801-1935
207	40	43	101	163	21907	1083	278	0.23	0.36	1.40	999	6801-1935
208	30	33	71	120	14255	938	205	0.20	0.43	1.43	285	6801-1935

ID	D _{crater} (m)	Ejecta Radius (m)			Area (m ²)	Perimeter (m)	L (m)	C _R	F _R	FD ₁	Uprange	Image Name
		Min.	Mean	Max.							Azimuth (°) _a	
210	40	43	94	174	22880	1178	303	0.21	0.32	1.41	175	6801-1935
211	43	40	112	212	33932	1760	386	0.14	0.29	1.43	999	6801-1935
215	33	31	55	82	8919	655	159	0.26	0.45	1.43	999	6801-1935
216	27	31	58	90	9077	586	146	0.33	0.54	1.40	999	6801-1935
222	28	30	55	100	8595	689	175	0.23	0.36	1.44	999	6801-1935
223	40	40	98	176	23270	1408	313	0.15	0.30	1.44	215	6801-1935
225	29	35	69	120	14845	908	198	0.23	0.48	1.42	25	6801-1935
226	34	35	96	204	29583	1502	345	0.16	0.32	1.42	205	6801-1935
229	83	165	346	701	359478	5005	1116	0.18	0.37	1.33	225	6801-1935
230	55	67	127	192	48355	1328	346	0.34	0.51	1.33	215	6801-1935
231	32	50	79	137	19214	928	242	0.28	0.42	1.39	999	6801-1935
233	44	54	112	186	36047	1331	322	0.26	0.44	1.37	220	6801-1935
234	49	59	98	151	27553	1527	281	0.15	0.44	1.43	175	6801-1935
235	40	34	75	120	14907	870	223	0.25	0.38	1.41	215	6801-1935
238	33	48	80	136	18435	793	248	0.37	0.38	1.36	225	6801-1935
239	46	51	90	130	23938	977	240	0.32	0.53	1.37	999	6801-1935
240	55	45	154	383	43277	1949	582	0.14	0.16	1.42	290	6801-1935
243	37	46	95	165	19647	965	229	0.27	0.48	1.39	210	6801-1935
244	46	40	110	192	23296	1188	296	0.21	0.34	1.41	195	6801-1935
245	56	56	110	179	34656	1324	299	0.25	0.49	1.38	200	6801-1935
246	37	32	80	154	13646	821	205	0.25	0.41	1.41	225	6801-1935
247	51	52	117	184	33602	1588	337	0.17	0.38	1.41	205	6801-1935
248	49	51	125	218	42972	1971	402	0.14	0.34	1.42	225	6801-1935
249	34	27	66	121	11337	951	221	0.16	0.30	1.47	210	6801-1935
250	35	37	63	113	11218	835	219	0.20	0.30	1.44	999	6801-1935
253	34	36	58	107	9400	890	181	0.15	0.37	1.48	215	6801-1935
256	37	35	78	171	15031	1147	314	0.14	0.19	1.46	220	6801-1935
257	40	38	90	168	20666	1614	312	0.10	0.27	1.49	999	6801-1935
260	38	31	71	105	14357	757	201	0.31	0.45	1.39	220	6801-1935
261	32	24	66	119	11377	1061	204	0.13	0.35	1.49	195	6801-1935
262	54	54	157	327	70882	2689	464	0.12	0.42	1.41	250	6801-1935
263	45	46	99	203	26728	1331	321	0.19	0.33	1.41	305	6801-1935
264	35	36	65	100	12738	998	194	0.16	0.43	1.46	220	6801-1935
265	31	26	67	125	12559	1026	212	0.15	0.36	1.47	195	6801-1935
266	37	32	77	153	15914	1188	229	0.14	0.39	1.46	195	6801-1935
267	45	53	116	220	31827	2398	319	0.07	0.40	1.50	200	6801-1935
268	49	43	103	262	24239	1814	352	0.09	0.25	1.49	220	6801-1935
269	36	33	87	246	14630	1211	311	0.13	0.19	1.48	215	6801-1935
270	59	75	174	340	78220	2792	570	0.13	0.31	1.41	250	6801-1935
271	41	31	72	139	14155	919	201	0.21	0.45	1.43	220	6801-1935
272	48	63	114	205	36080	1610	355	0.17	0.36	1.41	210	6801-1935
273	38	36	80	148	16806	1351	229	0.12	0.41	1.48	210	6801-1935

ID	D _{crater} (m)	Ejecta Radius (m)			Area (m ²)	Perimeter (m)	L (m)	C _R	F _R	FD _I	Uprange	Image Name
		Min.	Mean	Max.							Azimuth (°) _a	
274	35	41	101	212	21680	1589	296	0.11	0.32	1.48	185	6801-1935
300	33	36	115	216	36223	1745	374	0.15	0.33	1.42	215	4006-1900
301	36	22	142	236	37873	1417	373	0.24	0.35	1.38	115	4006-1900
302	21	29	66	221	12725	1072	324	0.14	0.15	1.48	175	4006-1900
303	15	24	44	82	5020	430	125	0.34	0.41	1.42	999	4006-1900
304	27	19	120	258	28425	1701	374	0.12	0.26	1.45	95	4006-1900
305	28	30	50	77	7718	509	133	0.37	0.56	1.39	275	2820-1860
306	48	56	133	221	49705	1833	415	0.19	0.37	1.39	310	2820-1860
307	38	43	78	173	14765	952	226	0.20	0.37	1.43	18	2820-1860
308	29	16	80	142	17231	1023	205	0.21	0.52	1.42	120	1342-1910
309	49	33	155	290	69325	1402	397	0.44	0.56	1.30	110	1342-1910
310	32	23	73	143	14270	804	206	0.28	0.43	1.40	55	1342-1910
311	22	12	49	87	6661	414	113	0.49	0.66	1.37	110	1342-1910
312	77	86	303	488	233335	4090	925	0.18	0.35	1.35	135	1342-1910
313	28	19	81	125	13522	834	214	0.24	0.38	1.41	125	1342-1910
317	15	9	32	50	2783	242	79	0.60	0.57	1.38	120	1342-1910
318	11	6	24	38	1528	212	61	0.43	0.52	1.46	125	1342-1910
319	21	11	60	125	6410	582	152	0.24	0.35	1.45	140	1342-1910
320	16	12	34	50	3208	344	89	0.34	0.52	1.45	120	1342-1910
321	14	7	29	48	1944	265	75	0.35	0.44	1.47	120	1342-1910
322	15	11	23	34	1492	191	56	0.51	0.61	1.44	100	1342-1910
323	12	7	20	34	913	147	51	0.53	0.45	1.46	110	1342-1910
324	27	17	41	87	3355	474	117	0.19	0.31	1.52	55	1342-1910
325	12	7	18	25	706	132	42	0.51	0.51	1.49	110	1342-1910
326	20	11	28	58	1822	286	82	0.28	0.35	1.51	120	1342-1910
327	14	8	21	35	1222	174	60	0.51	0.43	1.45	105	1342-1910
328	20	12	45	87	4115	417	106	0.30	0.47	1.45	145	1342-1910
329	17	11	31	54	2144	211	73	0.60	0.51	1.40	120	1342-1910
330	16	10	33	49	2747	249	79	0.56	0.56	1.39	100	1342-1910
331	14	10	26	48	1600	227	69	0.39	0.43	1.47	130	1342-1910
332	18	14	29	50	2442	285	75	0.38	0.55	1.45	270	1342-1910

^aEstimate based on downrange ejecta and uprange forbidden zone. No preferred azimuth = 999.

Table A-5: Small rayed crater (SRC) database.

SRC Id	Image Name	Longitude	Latitude	Crater	Min. Ejecta	Max Ejecta	Max. Ray	Ejecta Tone	Study Region	Retention
				Diameter (m)	Blanket Radius (m)	Blanket Radius (m)	Length (m)			Sequence Stage
1	E0100365	1.717862	2.612378	18	18	35	110	DARK	ARABIA	D2
2	E0100626	7.616360	17.310926	205	150	200	400	DARK	ARABIA	D4
3	E0101088	-148.390356	-15.377304	30	30	40	170	BRIGHT	AMAZ.-ELYS.	EE
4	E0101088	-148.421122	-15.249352	52	65	120	140	BRIGHT	AMAZ.-ELYS.	D2
5	E0200546	-86.309354	-8.934634	54	72	100	275	BRIGHT	THARSIS	D3
6	E0200546	-86.281553	-9.380993	63	80	120	200	BRIGHT	THARSIS	D4
7	E0201028	152.268934	5.176344	63	70	120	220	BRIGHT	AMAZ.-ELYS.	E2
8	E0201028	152.264906	5.068712	26	24	46	57	BRIGHT	AMAZ.-ELYS.	E3
9	E0201028	152.225669	5.442890	27	25	28	104	BRIGHT	AMAZ.-ELYS.	E2
10	E0201028	152.251601	5.437407	33	33	44	54	BRIGHT	AMAZ.-ELYS.	E4
11	E0201028	152.214640	5.554780	46	58	86	95	BRIGHT	AMAZ.-ELYS.	E4
12	E0201028	152.180801	5.770521	38	48	67	115	BRIGHT	AMAZ.-ELYS.	E4
13	E0201549	-165.296586	-15.012597	152	185	350	925	BIMODAL	AMAZ.-ELYS.	D2
14	E0201549	-165.293905	-15.007272	46	60	80	270	BIMODAL	AMAZ.-ELYS.	D2
15	E0201549	-165.291304	-15.045851	95	98	153	650	BIMODAL	AMAZ.-ELYS.	D2
16	E0201549	-165.262562	-15.153081	44	46	55	210	BIMODAL	AMAZ.-ELYS.	D3
17	E0201549	-165.270673	-15.172649	56	47	75	200	BRIGHT	AMAZ.-ELYS.	D3
18	E0201549	-165.282467	-15.105219	44	64	98	110	BIMODAL	AMAZ.-ELYS.	D3
19	E0201900	-177.512401	11.328616	118	125	160	195	DARK	AMAZ.-ELYS.	E4
20	E0201900	-177.501610	11.317381	115	70	105	310	DARK	AMAZ.-ELYS.	E4
21	E0201900	-177.535087	11.291801	90	80	90	175	DARK	AMAZ.-ELYS.	E4
22	E0201900	-177.502071	11.300475	102	65	90	140	DARK	AMAZ.-ELYS.	E4
23	E0201900	-177.501102	11.308144	79	50	55	95	DARK	AMAZ.-ELYS.	E4
24	E0201900	-177.543074	11.594573	79	61	84	155	DARK	AMAZ.-ELYS.	E4
25	E0202487	164.205861	16.154793	60	47	89	130	BIMODAL	AMAZ.-ELYS.	E2
26	E0202487	164.181146	16.152009	39	39	56	85	BIMODAL	AMAZ.-ELYS.	E2
27	E0202487	164.202143	16.105764	29	20	47	158	BIMODAL	AMAZ.-ELYS.	E2
28	E0202487	164.201217	16.054049	53	50	65	210	BIMODAL	AMAZ.-ELYS.	E2
29	E0202487	164.211750	16.013339	43	47	75	185	BIMODAL	AMAZ.-ELYS.	E2
30	E0202487	164.208040	16.003699	45	40	58	250	BIMODAL	AMAZ.-ELYS.	E2
31	E0202487	164.210887	15.934520	56	50	79	280	BIMODAL	AMAZ.-ELYS.	E2
32	E0202487	164.223368	15.874910	56	70	85	178	BIMODAL	AMAZ.-ELYS.	E3
33	E0202487	164.235983	15.835601	64	56	115	155	BIMODAL	AMAZ.-ELYS.	E3
34	E0202487	164.244662	15.828573	54	44	90	140	BIMODAL	AMAZ.-ELYS.	E3
35	E0202487	164.229876	15.735672	41	37	43	95	BIMODAL	AMAZ.-ELYS.	E4
36	E0202487	164.247392	15.684725	54	37	71	205	BIMODAL	AMAZ.-ELYS.	E3
37	E0202487	164.242691	15.648595	76	70	124	330	BIMODAL	AMAZ.-ELYS.	E2
38	E0202487	164.327807	15.172274	74	74	190	370	BIMODAL	AMAZ.-ELYS.	E2
39	E0300904	-16.642434	31.961855	180	140	198	463	DARK	BOREALIS	D3
40	E0300904	-16.690234	31.967455	121	95	166	330	DARK	BOREALIS	D3

SRC Id	Image Name	Longitude	Latitude	Crater Diameter (m)	Min. Ejecta Blanket Radius (m)	Max. Ejecta Blanket Radius (m)	Max. Ray Length (m)	Ejecta Tone	Study Region	Retention Sequence Stage
41	E0300904	-16.671945	31.958967	176.0	108.00	183.00	290.00	DARK	BOREALIS	D4
42	E0302069	-98.951067	-19.289904	125.0	94.00	159.00	240.00	DARK	THARSIS	D4
43	E0400083	-159.284355	-8.669607	33.0	22.00	39.00	105.00	NEUTRAL	AMAZ.-ELYS.	EE
44	E0400083	-159.280035	-8.600648	42.0	34.00	42.00	80.00	NEUTRAL	AMAZ.-ELYS.	EE
45	E0400083	-159.287837	-8.600161	33.0	30.00	38.00	49.00	NEUTRAL	AMAZ.-ELYS.	D4
46	E0400504	-39.939902	-29.105944	74.0	53.00	82.00	212.00	DARK	THARSIS	D4
47	E0400504	-39.963498	-28.734835	44.0	35.00	41.00	87.00	DARK	THARSIS	D4
48	E0400504	-40.021521	-28.603705	50.0	42.00	60.00	230.00	BRIGHT	THARSIS	D4
49	E0400591	27.762959	14.467714	28.0	120.00	180.00	375.00	BIMODAL	ARABIA	D3
50	E0400591	27.694800	15.033079	53.0	90.00	100.00	195.00	BRIGHT	ARABIA	D4
51	E0400653	74.839755	-3.338512	172.0	127.00	182.00	500.00	BRIGHT	ARABIA	D3
52	E0401780	6.206674	2.378045	25.0	30.00	50.00	135.00	DARK	ARABIA	D2
53	E0401780	6.208312	2.199344	154.0	124.00	240.00	385.00	BRIGHT	ARABIA	E3
54	E0401780	6.197893	2.202504	136.0	114.00	177.00	417.00	BRIGHT	ARABIA	E3
55	E0402293	18.031976	-5.366364	318.0	560.00	1000.00	1800.00	BRIGHT	ARABIA	D1
56	E0402514	-118.124228	-31.088355	88.0	95.00	110.00	200.00	BRIGHT	THARSIS	D3
57	E0402514	-118.122612	-30.992885	48.0	50.00	80.00	120.00	BRIGHT	THARSIS	D3
58	E0402514	-118.168159	-30.878811	43.0	30.00	45.00	95.00	BRIGHT	THARSIS	D3
59	E0500492	60.838571	-3.556189	115.0	260.00	300.00	640.00	BIMODAL	ARABIA	D2
60	E0500492	60.888563	-3.823143	43.0	44.00	56.00	98.00	BRIGHT	ARABIA	D4
61	E0500782	77.158839	21.880766	31.0	25.00	47.00	330.00	DARK	ARABIA	D2
62	E0500995	166.061031	26.721256	351.0	318.00	345.00	1100.00	DARK	AMAZ.-ELYS.	D4
63	E0500995	166.064776	26.705911	43.0	52.00	70.00	120.00	DARK	AMAZ.-ELYS.	D4
64	E0500995	166.105536	26.594759	98.0	110.00	130.00	330.00	BIMODAL	AMAZ.-ELYS.	D4
65	E0501229	-81.479177	-23.784163	93.0	85.00	120.00	215.00	DARK	THARSIS	D4
66	E0501229	-81.470189	-23.790492	114.0	100.00	115.00	265.00	DARK	THARSIS	D4
67	E0501229	-81.482311	-23.866730	131.0	120.00	140.00	230.00	DARK	THARSIS	D4
68	E0501229	-81.457971	-23.879353	160.0	110.00	200.00	365.00	DARK	THARSIS	D4
69	E0501229	-81.469730	-24.005613	69.0	50.00	75.00	100.00	DARK	THARSIS	D4
70	E0501229	-81.444374	-24.050171	70.0	65.00	70.00	105.00	DARK	THARSIS	D4
71	E0501229	-81.453260	-24.009681	47.0	34.00	40.00	80.00	DARK	THARSIS	D4
72	E0501229	-81.460951	-23.999207	48.0	45.00	50.00	125.00	DARK	THARSIS	D4
73	E0501229	-81.474987	-23.973500	80.0	65.00	75.00	140.00	DARK	THARSIS	D3
74	E0501378	36.217981	-19.778956	49.0	40.00	80.00	155.00	BIMODAL	ARABIA	D4
75	E0501378	36.256931	-20.136868	43.0	80.00	190.00	300.00	DARK	ARABIA	D4
76	E0501647	170.220633	-17.720931	42.0	40.00	50.00	215.00	BIMODAL	AMAZ.-ELYS.	E2
77	E0501647	170.237426	-17.732409	75.0	115.00	120.00	315.00	BIMODAL	AMAZ.-ELYS.	D3
78	E0501647	170.240700	-17.694350	180.0	115.00	150.00	210.00	BIMODAL	AMAZ.-ELYS.	D3
79	E0501647	170.174213	-17.423106	32.0	40.00	50.00	98.00	BIMODAL	AMAZ.-ELYS.	D2
80	E0501853	144.323662	-11.360306	44.0	28.00	45.00	160.00	DARK	AMAZ.-ELYS.	D4
81	E0501853	144.325891	-11.445166	94.0	80.00	90.00	430.00	DARK	AMAZ.-ELYS.	D4
82	E0502141	32.677323	-6.242346	49.0	90.00	130.00	375.00	NEUTRAL	ARABIA	D4
83	E0502141	32.732558	-6.663522	47.0	75.00	85.00	185.00	BIMODAL	ARABIA	D3
84	E0503203	15.701848	-12.799494	33.0	78.00	90.00	215.00	BIMODAL	ARABIA	D3

SRC Id	Image Name	Longitude	Latitude	Crater	Min. Ejecta	Max. Ejecta	Max Ray	Ejecta Tone	Study Region	Retention
				Diameter (m)	Blanket Radius (m)	Blanket Radius (m)	Length (m)			Sequence Stage
85	E0503203	15.700458	-12.809398	33.0	60.00	75.00	130.00	BIMODAL	ARABIA	D3
86	E0503203	15.706192	-12.820225	40.0	38.00	44.00	80.00	DARK	ARABIA	D4
87	E1102251	50.299813	-24.093798	146.0	130.00	200.00	900.00	DARK	ARABIA	E2
88	E1103342	61.117595	9.849172	47.0	80.00	120.00	250.00	DARK	ARABIA	D4
89	E1103621	-45.904483	-18.229716	136.0	190.00	240.00	750.00	DARK	THARSIS	E2
90	E1200502	-109.260665	-14.153408	68.0	67.00	80.00	155.00	BRIGHT	THARSIS	E3
91	E1201113	-175.868945	20.629062	59.0	76.00	105.00	275.00	NEUTRAL	AMAZ.-ELYS.	D4
92	E1201113	-175.812464	20.286429	97.0	90.00	130.00	225.00	DARK	AMAZ.-ELYS.	D4
93	E1201113	-175.871355	20.950950	725.0	490.00	600.00	1800.00	NEUTRAL	AMAZ.-ELYS.	D3
94	E1201471	-151.432207	-11.995336	23.0	30.00	40.00	90.00	DARK	AMAZ.-ELYS.	D3
95	E1201471	-151.430420	-11.997518	33.0	50.00	80.00	228.00	DARK	AMAZ.-ELYS.	D3
96	E1201471	-151.405969	-12.125011	184.0	320.00	420.00	775.00	DARK	AMAZ.-ELYS.	D3
97	E1201471	-151.381636	-12.229719	240.0	215.00	390.00	485.00	DARK	AMAZ.-ELYS.	D4
98	E1201471	-151.369376	-12.480555	68.0	55.00	195.00	550.00	NEUTRAL	AMAZ.-ELYS.	D4
99	E1201500	125.433655	-32.042979	93.0	55.00	70.00	250.00	DARK	AUSTRALIS	D3
100	E1201687	-66.903509	27.213465	123.0	90.00	145.00	190.00	DARK	THARSIS	D4
101	E1201687	-66.879258	27.043681	63.0	70.00	90.00	200.00	DARK	THARSIS	D4
102	E1202659	77.737834	37.722485	151.0	150.00	190.00	300.00	DARK	BOREALIS	E2
103	E1203445	165.823348	18.385825	38.0	36.00	42.00	175.00	BRIGHT	AMAZ.-ELYS.	E2
104	E1203445	165.846065	18.043015	38.0	50.00	60.00	150.00	BRIGHT	AMAZ.-ELYS.	E2
105	E1203445	165.874018	18.026386	47.0	60.00	70.00	175.00	BRIGHT	AMAZ.-ELYS.	D3
106	E1203445	165.866428	17.974167	78.0	80.00	140.00	350.00	BRIGHT	AMAZ.-ELYS.	D2
107	E1300423	49.183511	-1.249913	46.0	35.00	75.00	270.00	DARK	ARABIA	D2
108	E1300423	49.206683	-1.292433	62.0	100.00	130.00	320.00	DARK	ARABIA	D3
109	E1300423	49.204701	-1.292879	73.0	100.00	110.00	550.00	DARK	ARABIA	D3
110	E1300423	49.211295	-1.350883	52.0	55.00	85.00	350.00	DARK	ARABIA	D3
111	E1300423	49.264594	-1.568247	65.0	110.00	140.00	200.00	BRIGHT	ARABIA	D4
112	E1300423	49.240535	-1.565151	42.0	45.00	60.00	95.00	BRIGHT	ARABIA	D3
113	E1300423	49.264544	-1.646514	29.0	25.00	30.00	70.00	DARK	ARABIA	D4
114	E1300423	49.242424	-1.653635	101.0	150.00	180.00	500.00	BIMODAL	ARABIA	D2
115	E1300423	49.247987	-1.662957	47.0	45.00	50.00	75.00	BIMODAL	ARABIA	D3
116	E1300423	49.255599	-1.671316	56.0	36.00	55.00	165.00	DARK	ARABIA	D3
117	E1300423	49.274497	-1.685805	42.0	45.00	50.00	70.00	BIMODAL	ARABIA	D4
118	E1300423	49.264929	-1.772647	36.0	30.00	40.00	105.00	DARK	ARABIA	D3
119	E1300423	49.291555	-1.899061	34.0	30.00	40.00	115.00	DARK	ARABIA	D3
120	E1300423	49.303712	-1.912497	52.0	85.00	115.00	260.00	DARK	ARABIA	D3
121	E1300423	49.304277	-1.915775	43.0	50.00	55.00	110.00	BIMODAL	ARABIA	D3
122	E1300423	49.303387	-1.946664	28.0	25.00	35.00	95.00	DARK	ARABIA	D3
123	E1300740	11.312589	4.589323	24.0	30.00	40.00	80.00	BRIGHT	ARABIA	D3
124	E1302036	-162.045619	4.123299	80.0	180.00	400.00	575.00	BRIGHT	AMAZ.-ELYS.	D3
125	E1400750	-84.499812	-8.075262	28.0	90.00	100.00	180.00	DARK	THARSIS	D4
126	E1400750	-84.482955	-8.100756	31.0	55.00	60.00	135.00	DARK	THARSIS	D4
127	E1400750	-84.501037	-8.143641	95.0	150.00	225.00	530.00	BRIGHT	THARSIS	D4
128	E1401574	131.940172	18.972610	227.0	310.00	370.00	475.00	DARK	BOREALIS	D3

SRC Id	Image Name	Longitude	Latitude	Crater Diameter (m)	Min. Ejecta Blanket Radius (m)	Max Ejecta Blanket Radius (m)	Max Ray Length (m)	Ejecta Tone	Study Region	Retention Sequence Stage
129	E1600700	168.879540	14.752915	54.0	55.00	80.00	130.00	BIMODAL	AMAZ.-ELYS.	E3
130	E1600700	168.877702	14.721811	49.0	55.00	85.00	145.00	BIMODAL	AMAZ.-ELYS.	E3
131	E1600700	168.929292	14.568252	40.0	45.00	90.00	175.00	BIMODAL	AMAZ.-ELYS.	E3
132	E1600700	168.944884	14.555319	35.0	75.00	140.00	350.00	BIMODAL	AMAZ.-ELYS.	E3
133	E1600700	168.910824	14.557434	48.0	70.00	80.00	190.00	BIMODAL	AMAZ.-ELYS.	E3
134	E1600700	168.913065	14.522316	37.0	35.00	50.00	95.00	BIMODAL	AMAZ.-ELYS.	E3
135	E1600700	168.953189	14.522584	42.0	50.00	60.00	135.00	BIMODAL	AMAZ.-ELYS.	E3
136	E1600700	168.922500	14.500482	31.0	25.00	45.00	130.00	BIMODAL	AMAZ.-ELYS.	E3
137	E1600700	168.956145	14.473831	49.0	60.00	80.00	275.00	BIMODAL	AMAZ.-ELYS.	E3
138	E1600700	168.957397	14.441102	45.0	70.00	85.00	220.00	BIMODAL	AMAZ.-ELYS.	E2
139	E1600700	168.956242	14.440421	30.0	40.00	50.00	90.00	BIMODAL	AMAZ.-ELYS.	E3
140	E1600700	168.949705	14.405407	58.0	70.00	85.00	310.00	BIMODAL	AMAZ.-ELYS.	E2
141	E1600700	168.926198	14.396224	53.0	180.00	250.00	480.00	BIMODAL	AMAZ.-ELYS.	E2
142	E1600700	168.920425	14.399535	47.0	60.00	80.00	160.00	BIMODAL	AMAZ.-ELYS.	E2
143	E1600700	168.946728	14.369444	65.0	75.00	150.00	375.00	BIMODAL	AMAZ.-ELYS.	E2
144	E1600700	168.959433	14.360081	49.0	60.00	80.00	235.00	BIMODAL	AMAZ.-ELYS.	E2
145	E1600700	168.925939	14.363301	75.0	120.00	150.00	320.00	BIMODAL	AMAZ.-ELYS.	E2
146	E1600700	168.956933	14.329028	59.0	75.00	120.00	250.00	BIMODAL	AMAZ.-ELYS.	E2
147	E1600700	168.975649	14.289261	85.0	105.00	170.00	500.00	BIMODAL	AMAZ.-ELYS.	E2
148	E1600700	168.981261	14.276051	40.0	50.00	80.00	185.00	BIMODAL	AMAZ.-ELYS.	E2
149	E1600700	168.971198	14.161926	28.0	35.00	75.00	80.00	BIMODAL	AMAZ.-ELYS.	E2
150	E1600700	168.956564	14.139695	54.0	60.00	95.00	230.00	BIMODAL	AMAZ.-ELYS.	E2
151	E1600700	168.983658	14.035078	95.0	175.00	250.00	875.00	BIMODAL	AMAZ.-ELYS.	E2
152	E1600700	169.022309	13.902607	68.0	90.00	120.00	195.00	BIMODAL	AMAZ.-ELYS.	E3
153	E1600700	169.010182	13.888985	51.0	45.00	65.00	310.00	BIMODAL	AMAZ.-ELYS.	E2
154	E1600700	168.999115	13.843177	39.0	50.00	55.00	160.00	BIMODAL	AMAZ.-ELYS.	E2
155	E1600700	169.033502	13.818145	58.0	70.00	130.00	275.00	BIMODAL	AMAZ.-ELYS.	E2
156	E1600700	169.041913	13.750959	95.0	145.00	190.00	490.00	BIMODAL	AMAZ.-ELYS.	E2
157	E1600700	169.049601	13.746031	36.0	75.00	105.00	230.00	BIMODAL	AMAZ.-ELYS.	E2
158	E1600700	169.049430	13.666227	32.0	45.00	55.00	100.00	BIMODAL	AMAZ.-ELYS.	E3
159	E1600700	169.060793	13.669908	33.0	40.00	50.00	90.00	BIMODAL	AMAZ.-ELYS.	E3
160	E1600700	169.034826	13.587485	63.0	45.00	85.00	130.00	BIMODAL	AMAZ.-ELYS.	E3
161	E1600700	169.047761	13.514095	145.0	190.00	250.00	375.00	DARK	AMAZ.-ELYS.	E3
162	E1600700	169.086642	13.445906	60.0	65.00	100.00	155.00	BIMODAL	AMAZ.-ELYS.	E3
163	E1600700	169.078970	13.466073	42.0	40.00	80.00	120.00	BIMODAL	AMAZ.-ELYS.	E3
164	E1600700	169.075695	13.428352	39.0	50.00	75.00	150.00	BIMODAL	AMAZ.-ELYS.	E3
165	E1600700	169.092109	13.300216	88.0	120.00	200.00	280.00	BIMODAL	AMAZ.-ELYS.	E2
166	E1600700	169.092418	13.316623	53.0	55.00	110.00	135.00	BIMODAL	AMAZ.-ELYS.	E2
167	E1600700	169.084479	13.271847	64.0	65.00	140.00	215.00	BIMODAL	AMAZ.-ELYS.	E2
168	E1601557	148.741635	5.286039	79.0	50.00	65.00	140.00	DARK	AMAZ.-ELYS.	E4
169	E1601635	163.740079	15.377719	93.0	150.00	280.00	490.00	BIMODAL	AMAZ.-ELYS.	E2
170	E1601635	163.748112	15.058156	81.0	290.00	370.00	960.00	BIMODAL	AMAZ.-ELYS.	E2
171	E1601635	163.738131	15.351108	38.0	48.00	70.00	140.00	BIMODAL	AMAZ.-ELYS.	E3
172	E1601635	163.714386	15.349177	34.0	37.00	40.00	80.00	BIMODAL	AMAZ.-ELYS.	E4

SRC Id	Image Name	Longitude	Latitude	Crater		Min. Ejecta	Max Ejecta	Max. Ray	Ejecta Tone	Study Region	Retention
				Diameter (m)	Radius (m)	Blanket Radius (m)	Blanket Radius (m)	Length (m)			Sequence Stage
173	E1601635	163.711911	15.374937	36.0	27.00	47.00	91.00	BIMODAL	AMAZ.-ELYS.	E4	
174	E1601635	163.723652	15.341767	33.0	28.00	35.00	75.00	BIMODAL	AMAZ.-ELYS.	E4	
175	E1601635	163.747119	15.238492	39.0	26.00	45.00	95.00	BIMODAL	AMAZ.-ELYS.	E4	
176	E1601635	163.736124	15.229993	56.0	46.00	70.00	235.00	BIMODAL	AMAZ.-ELYS.	E3	
177	E1601635	163.748253	15.149714	45.0	50.00	70.00	175.00	BIMODAL	AMAZ.-ELYS.	E3	
178	E1601635	163.770253	14.868452	61.0	65.00	145.00	500.00	BIMODAL	AMAZ.-ELYS.	E2	
179	E1701362	177.331286	20.534990	84.0	115.00	220.00	480.00	BIMODAL	AMAZ.-ELYS.	D2	
180	E1701362	177.309968	20.530001	491.0	610.00	810.00	3560.00	DARK	AMAZ.-ELYS.	D2	
181	E1800267	-8.511031	-3.165020	20.0	20.00	30.00	90.00	DARK	ARABIA	E2	
182	E1800267	-8.494366	-3.221356	23.0	30.00	42.00	115.00	DARK	ARABIA	E2	
183	E1800267	-8.519785	-3.007076	20.0	42.00	55.00	100.00	BIMODAL	ARABIA	E1	
184	E1801385	168.286843	14.151646	242.0	190.00	600.00	1350.00	BRIGHT	AMAZ.-ELYS.	D2	
185	E1801385	168.302248	14.157360	97.0	200.00	220.00	645.00	BRIGHT	AMAZ.-ELYS.	D2	
186	E1801465	70.187516	13.085681	32.0	80.00	90.00	175.00	BIMODAL	ARABIA	D3	
187	E1900525	166.910552	14.534568	87.0	145.00	255.00	500.00	BIMODAL	AMAZ.-ELYS.	E2	
188	E1900525	166.915107	14.481364	40.0	20.00	68.00	155.00	BRIGHT	AMAZ.-ELYS.	E3	
189	E1900525	166.931851	14.463678	47.0	33.00	114.00	200.00	BIMODAL	AMAZ.-ELYS.	E3	
190	E1900525	166.973655	14.197197	61.0	52.00	72.00	94.00	BIMODAL	AMAZ.-ELYS.	D2	
191	E2000661	-3.770454	3.442453	43.0	45.00	62.00	185.00	DARK	ARABIA	E3	
192	E2201108	3.033158	1.557515	98.0	138.00	287.00	565.00	DARK	ARABIA	E2	
193	E2201108	3.021925	1.566811	21.0	20.00	38.00	85.00	DARK	ARABIA	E3	
194	E2201108	3.023464	1.573341	28.0	25.00	68.00	98.00	DARK	ARABIA	E3	
195	E2300479	-175.711618	19.565851	130.0	147.00	190.00	250.00	DARK	AMAZ.-ELYS.	D4	
196	E2300479	-175.633653	19.007658	40.0	38.00	95.00	185.00	BRIGHT	AMAZ.-ELYS.	E3	
197	FHA01584	148.326590	-7.927331	17.0	26.00	42.00	51.00	BIMODAL	AMAZ.-ELYS.	E3	
198	FHA01584	148.315348	-7.932329	16.0	19.00	28.00	51.00	BIMODAL	AMAZ.-ELYS.	E3	
199	FHA01584	148.312389	-7.932845	15.0	20.00	31.00	48.00	BIMODAL	AMAZ.-ELYS.	E3	
200	FHA01584	148.313712	-7.941099	27.0	21.00	40.00	66.00	BIMODAL	AMAZ.-ELYS.	E3	
201	FHA01584	148.323754	-7.948313	29.0	31.00	48.00	84.00	BIMODAL	AMAZ.-ELYS.	E3	
202	FHA01584	148.315036	-7.953774	20.0	23.00	33.00	61.00	BIMODAL	AMAZ.-ELYS.	E3	
203	FHA01584	148.329791	-7.946047	19.0	21.00	24.00	36.00	BIMODAL	AMAZ.-ELYS.	E3	
204	M0000120	-168.509511	11.196981	207.0	210.00	245.00	750.00	BRIGHT	AMAZ.-ELYS.	D4	
205	M0000120	-168.533491	11.181318	321.0	460.00	545.00	775.00	BRIGHT	AMAZ.-ELYS.	D4	
206	M0000120	-168.517426	11.180840	152.0	170.00	250.00	460.00	BRIGHT	AMAZ.-ELYS.	D4	
207	M0000120	-168.501621	11.171438	206.0	180.00	225.00	725.00	BRIGHT	AMAZ.-ELYS.	D4	
208	M0001078	30.974066	-10.032610	21.0	19.00	27.00	42.00	BRIGHT	ARABIA	E3	
209	M0001078	30.980518	-10.074306	31.0	24.00	43.00	80.00	BRIGHT	ARABIA	D4	
210	M0001078	30.972308	-9.998814	22.0	24.00	45.00	76.00	BRIGHT	ARABIA	D4	
211	M0001273	159.071016	11.938275	75.0	75.00	140.00	175.00	BRIGHT	AMAZ.-ELYS.	D2	
212	M0001273	159.064563	11.923405	25.0	23.00	53.00	97.00	BRIGHT	AMAZ.-ELYS.	D2	
213	M0001273	159.045943	11.913499	39.0	33.00	59.00	105.00	BRIGHT	AMAZ.-ELYS.	D2	
214	M0001273	159.051881	11.907772	50.0	63.00	114.00	277.00	BRIGHT	AMAZ.-ELYS.	D2	
215	M0001273	159.088948	11.915224	35.0	42.00	66.00	203.00	BRIGHT	AMAZ.-ELYS.	D2	
216	M0001273	159.090796	11.917184	37.0	40.00	52.00	144.00	BRIGHT	AMAZ.-ELYS.	D2	

SRC Id	Image Name	Longitude	Latitude	Crater		Min. Ejecta	Max Ejecta	Max Ray	Ejecta Tone	Study Region	Retention
				Diameter (m)	Radius (m)	Blanket Radius (m)	Blanket Radius (m)	Length (m)			Sequence Stage
217	M0001273	159.054211	11.890084	33.0	36.00	54.00	89.00	BRIGHT	AMAZ.-ELYS.	D2	
218	M0001273	159.056495	11.887981	56.0	38.00	73.00	165.00	BRIGHT	AMAZ.-ELYS.	D2	
219	M0001273	159.068034	11.877296	37.0	58.00	78.00	220.00	BRIGHT	AMAZ.-ELYS.	D2	
220	M0001273	159.077960	11.874136	33.0	43.00	55.00	135.00	BRIGHT	AMAZ.-ELYS.	D2	
221	M0001273	159.077135	11.871915	35.0	33.00	51.00	107.00	BRIGHT	AMAZ.-ELYS.	D2	
222	M0001273	159.060135	11.861590	36.0	50.00	85.00	159.00	BRIGHT	AMAZ.-ELYS.	D2	
223	M0001273	159.080071	11.851070	51.0	43.00	80.00	150.00	BRIGHT	AMAZ.-ELYS.	D2	
224	M0001273	159.085862	11.832964	26.0	21.00	42.00	162.00	BRIGHT	AMAZ.-ELYS.	D3	
225	M0001273	159.083858	11.826867	26.0	18.00	31.00	100.00	BRIGHT	AMAZ.-ELYS.	D3	
226	M0001273	159.079215	11.819569	32.0	36.00	44.00	90.00	BIMODAL	AMAZ.-ELYS.	D2	
227	M0100906	-178.152653	12.017179	95.0	90.00	124.00	220.00	DARK	AMAZ.-ELYS.	E4	
228	M0102906	171.220132	34.471429	131.0	120.00	190.00	273.00	DARK	BOREALIS	E4	
229	M0200289	124.169516	-0.943311	30.0	30.00	50.00	160.00	DARK	AMAZ.-ELYS.	D4	
230	M0200289	124.189603	-0.972997	23.0	27.00	45.00	65.00	DARK	AMAZ.-ELYS.	E4	
231	M0200289	124.190297	-0.972952	36.0	37.00	60.00	90.00	DARK	AMAZ.-ELYS.	E4	
232	M0200289	124.188374	-0.972682	40.0	40.00	65.00	95.00	DARK	AMAZ.-ELYS.	E4	
233	M0200289	124.189158	-0.972916	28.0	40.00	55.00	70.00	DARK	AMAZ.-ELYS.	E4	
234	M0200289	124.197949	-1.048123	26.0	24.00	30.00	54.00	BRIGHT	AMAZ.-ELYS.	E4	
235	M0200289	124.189874	-1.058072	53.0	85.00	110.00	180.00	BIMODAL	AMAZ.-ELYS.	D4	
236	M0200289	124.185764	-1.101872	77.0	112.00	176.00	508.00	BIMODAL	AMAZ.-ELYS.	E2	
237	M0200508	-60.325406	3.068072	90.0	115.00	215.00	430.00	DARK	THARSIS	D4	
238	M0200703	69.120670	14.577350	25.0	24.00	38.00	103.00	BRIGHT	ARABIA	E4	
239	M0200886	-154.965619	-23.005112	31.0	22.00	45.00	82.00	BRIGHT	AMAZ.-ELYS.	E4	
240	M0201483	53.034732	-14.790988	41.0	97.00	180.00	265.00	DARK	ARABIA	D4	
241	M0201483	53.036376	-14.809426	39.0	22.00	40.00	78.00	DARK	ARABIA	D4	
242	M0203784	160.868450	18.008344	41.0	25.00	60.00	155.00	DARK	AMAZ.-ELYS.	D3	
243	M0203784	160.865816	18.076586	107.0	100.00	195.00	420.00	DARK	AMAZ.-ELYS.	D3	
244	M0203784	160.871697	18.096906	41.0	40.00	61.00	91.00	BIMODAL	AMAZ.-ELYS.	E4	
245	M0203784	160.870370	18.096593	41.0	34.00	54.00	72.00	BIMODAL	AMAZ.-ELYS.	E4	
246	M0203784	160.858589	18.175489	60.0	40.00	82.00	173.00	BRIGHT	AMAZ.-ELYS.	E4	
247	M0203784	160.844452	18.219662	55.0	70.00	120.00	305.00	DARK	AMAZ.-ELYS.	D4	
248	M0203784	160.844323	18.320107	46.0	88.00	125.00	162.00	DARK	AMAZ.-ELYS.	D4	
249	M0203784	160.831154	18.338318	30.0	39.00	49.00	74.00	DARK	AMAZ.-ELYS.	E4	
250	M0203784	160.832445	18.342610	39.0	34.00	49.00	63.00	BRIGHT	AMAZ.-ELYS.	E4	
251	M0203784	160.815701	18.422366	29.0	27.00	33.00	52.00	DARK	AMAZ.-ELYS.	E4	
252	M0203784	160.811530	18.481056	47.0	58.00	110.00	165.00	DARK	AMAZ.-ELYS.	D3	
253	M0203784	160.806384	18.501329	19.0	22.00	40.00	68.00	DARK	AMAZ.-ELYS.	E4	
254	M0203784	160.792503	18.704374	53.0	83.00	96.00	130.00	BRIGHT	AMAZ.-ELYS.	E3	
255	M0203784	160.765658	18.752507	32.0	27.00	48.00	130.00	DARK	AMAZ.-ELYS.	E4	
256	M0203784	160.773357	18.755353	25.0	22.00	35.00	66.00	DARK	AMAZ.-ELYS.	E4	
257	M0203784	160.777033	18.781140	33.0	48.00	56.00	90.00	DARK	AMAZ.-ELYS.	E4	
258	M0203784	160.764628	18.780150	32.0	29.00	42.00	60.00	BRIGHT	AMAZ.-ELYS.	E4	
259	M0203784	160.769609	18.811465	25.0	25.00	38.00	125.00	DARK	AMAZ.-ELYS.	E4	
260	M0203784	160.753332	18.859487	24.0	24.00	35.00	58.00	DARK	AMAZ.-ELYS.	E4	

SRC Id	Image Name	Longitude	Latitude	Crater	Min. Ejecta	Max Ejecta	Max Ray	Ejecta Tone	Study Region	Retention Sequence Stage
				Diameter (m)	Blanket Radius (m)	Blanket Radius (m)	Length (m)			
261	M0204302	-89.060500	-7.194413	25.0	30.00	39.00	49.00	DARK	THARSIS	D4
262	M0204302	-89.048488	-7.236606	21.0	28.00	35.00	55.00	DARK	THARSIS	D4
263	M0204806	-41.819227	10.685352	87.0	70.00	95.00	410.00	DARK	THARSIS	D3
264	M0300754	51.499864	20.871073	40.0	42.00	68.00	105.00	BRIGHT	ARABIA	E4
265	M0300754	51.491156	20.907405	33.0	38.00	44.00	104.00	BRIGHT	ARABIA	E4
266	M0302816	125.740777	-32.041374	514.0	450.00	850.00	1900.00	BRIGHT	AUSTRALIS	E4
267	M0303364	166.581937	32.016740	1232.0	1270.00	1985.00	4570.00	DARK	BOREALIS	E4
268	M0303701	47.391236	-22.749300	74.0	60.00	73.00	290.00	DARK	ARABIA	D4
269	M0304228	150.392718	5.868520	44.0	55.00	85.00	200.00	DARK	AMAZ.-ELYS.	D4
270	M0304228	150.407071	5.849569	25.0	30.00	35.00	65.00	DARK	AMAZ.-ELYS.	E4
271	M0305751	-48.474316	3.724433	89.0	82.00	117.00	320.00	DARK	THARSIS	D4
272	M0307416	69.619145	19.097560	28.0	30.00	42.00	87.00	BRIGHT	ARABIA	E3
273	M0307416	69.580407	19.301571	45.0	40.00	56.00	100.00	BRIGHT	ARABIA	E3
274	M0400362	-77.678565	-7.407951	64.0	65.00	80.00	145.00	BRIGHT	THARSIS	E2
275	M0401720	-16.932782	-27.088471	54.0	87.00	125.00	155.00	BRIGHT	ARABIA	D4
276	M0401720	-16.948125	-26.767058	57.0	50.00	180.00	320.00	BRIGHT	ARABIA	D4
277	M0402037	126.390186	4.303855	29.0	30.00	55.00	78.00	BIMODAL	AMAZ.-ELYS.	E4
278	M0402037	126.389001	4.316196	26.0	32.00	54.00	68.00	BIMODAL	AMAZ.-ELYS.	E4
279	M0402037	126.382927	4.296011	30.0	26.00	42.00	61.00	BIMODAL	AMAZ.-ELYS.	E4
280	M0402408	-58.028080	8.380913	202.0	200.00	250.00	380.00	DARK	THARSIS	E4
281	M0402926	48.626958	8.875877	28.0	40.00	60.00	94.00	NEUTRAL	ARABIA	E3
282	M0403322	141.965417	-15.317642	243.0	750.00	910.00	1300.00	DARK	AMAZ.-ELYS.	D4
283	M0403322	142.012832	-15.632170	46.0	44.00	60.00	108.00	BIMODAL	AMAZ.-ELYS.	D3
284	M0403322	142.025394	-15.925154	241.0	300.00	450.00	710.00	DARK	AMAZ.-ELYS.	D4
285	M0403835	57.595070	6.545399	40.0	58.00	81.00	114.00	BRIGHT	ARABIA	E3
286	M0403835	57.612060	6.410227	19.0	19.00	28.00	45.00	BRIGHT	ARABIA	E4
287	M0702178	148.310848	-17.072348	142.0	171.00	275.00	375.00	DARK	AMAZ.-ELYS.	D3
288	M0702178	148.359663	-17.280263	89.0	74.00	92.00	210.00	DARK	AMAZ.-ELYS.	D3
289	M0801434	9.355818	5.927983	127.0	365.00	410.00	705.00	BIMODAL	ARABIA	D3
290	M0801434	9.406889	5.739044	65.0	80.00	135.00	185.00	BIMODAL	ARABIA	D2
291	M0801867	67.990634	27.543434	44.0	35.00	78.00	150.00	DARK	ARABIA	D4
292	M0801879	43.932682	-6.433152	79.0	62.00	104.00	155.00	DARK	ARABIA	E2
293	M0801879	43.943663	-6.440324	38.0	32.00	45.00	62.00	DARK	ARABIA	D4
294	M0801879	43.972161	-6.510628	36.0	33.00	41.00	60.00	DARK	ARABIA	E4
295	M0801879	43.936600	-6.527666	36.0	45.00	52.00	100.00	BIMODAL	ARABIA	E3
296	M0801879	43.981602	-6.613508	298.0	231.00	320.00	800.00	BRIGHT	ARABIA	E4
297	M0801879	43.954066	-6.640677	33.0	52.00	70.00	110.00	BIMODAL	ARABIA	E3
298	M0801879	43.969996	-6.665569	25.0	25.00	42.00	65.00	BIMODAL	ARABIA	E4
299	M0801879	43.965748	-6.690374	27.0	44.00	82.00	116.00	BIMODAL	ARABIA	E3
300	M0801879	43.988867	-6.706016	45.0	47.00	60.00	100.00	DARK	ARABIA	E3
301	M0801879	43.985198	-6.770085	41.0	42.00	74.00	125.00	DARK	ARABIA	E3
302	M0801879	43.973832	-6.824180	32.0	47.00	59.00	97.00	DARK	ARABIA	E4
303	M0801879	43.975124	-6.821482	28.0	19.00	34.00	52.00	DARK	ARABIA	E4
304	M0801879	44.002821	-6.829949	33.0	29.00	35.00	68.00	DARK	ARABIA	E4

SRC Id	Image Name	Longitude	Latitude	Crater	Min. Ejecta	Max Ejecta	Max Ray	Ejecta Tone	Study Region	Retention
				Diameter (m)	Blanket Radius (m)	Blanket Radius (m)	Length (m)			Sequence Stage
305	M0801879	43.998674	-6.834028	26.0	27.00	34.00	70.00	DARK	ARABIA	E4
306	M0801879	43.973993	-6.840173	47.0	35.00	50.00	106.00	DARK	ARABIA	E4
307	M0801879	44.001427	-6.879775	114.0	135.00	390.00	590.00	DARK	ARABIA	D2
308	M0801879	44.007653	-6.912526	45.0	38.00	52.00	122.00	DARK	ARABIA	E4
309	M0801879	43.987472	-6.917306	40.0	52.00	85.00	265.00	DARK	ARABIA	D3
310	M0801879	44.002423	-6.972398	52.0	76.00	97.00	194.00	BRIGHT	ARABIA	D4
311	M0801879	44.020859	-6.987851	44.0	95.00	100.00	145.00	BIMODAL	ARABIA	D4
312	M0801879	44.009573	-7.005988	54.0	53.00	63.00	84.00	DARK	ARABIA	E4
313	M0801879	44.032057	-7.075006	32.0	27.00	56.00	136.00	DARK	ARABIA	E3
314	M0801879	44.042729	-7.083266	67.0	70.00	95.00	270.00	DARK	ARABIA	D4
315	M0801879	44.006629	-7.092404	27.0	19.00	32.00	98.00	DARK	ARABIA	E4
316	M0801879	44.010452	-7.090373	28.0	24.00	34.00	93.00	DARK	ARABIA	D4
317	M0801879	44.039435	-7.105351	32.0	70.00	144.00	220.00	BIMODAL	ARABIA	D4
318	M0801879	44.037055	-7.113152	28.0	80.00	112.00	230.00	DARK	ARABIA	D4
319	M0801879	44.012731	-7.118760	31.0	36.00	47.00	115.00	DARK	ARABIA	D4
320	M0801879	44.029626	-7.122429	30.0	50.00	75.00	270.00	BIMODAL	ARABIA	D4
321	M0801879	44.037619	-7.204561	41.0	82.00	125.00	285.00	DARK	ARABIA	D3
322	M0801879	44.055298	-7.251211	47.0	75.00	90.00	215.00	BIMODAL	ARABIA	D3
323	M0801879	44.064089	-7.252595	33.0	53.00	72.00	115.00	DARK	ARABIA	D3
324	M0801879	44.049310	-7.264731	30.0	28.00	63.00	250.00	DARK	ARABIA	D4
325	M0803180	157.684454	6.314100	53.0	50.00	120.00	270.00	DARK	AMAZ.-ELYS.	D3
326	M0806206	8.381698	1.699329	27.0	35.00	55.00	150.00	DARK	ARABIA	D3
327	M0806984	59.821252	-13.387005	76.0	120.00	270.00	500.00	BRIGHT	ARABIA	D4
328	M0807846	-75.798487	-35.561204	87.0	180.00	250.00	395.00	BIMODAL	THARSIS	D4
329	M0807846	-75.828909	-35.413242	45.0	60.00	90.00	165.00	BRIGHT	THARSIS	D4
330	M0807846	-75.827439	-35.422747	30.0	37.00	70.00	105.00	BRIGHT	THARSIS	D4
331	M0900197	7.909293	12.630712	37.0	63.00	81.00	147.00	BRIGHT	ARABIA	D4
332	M0903755	51.886019	3.013952	62.0	52.00	95.00	350.00	DARK	ARABIA	D3
333	M0904954	33.500150	-8.677010	86.0	80.00	135.00	205.00	BRIGHT	ARABIA	D4
334	M0906476	-66.259910	-62.301694	349.0	350.00	540.00	860.00	BRIGHT	AUSTRALIS	E4
335	M1001474	-175.724871	-11.965767	47.0	32.00	93.00	114.00	BRIGHT	AMAZ.-ELYS.	E3
336	M1001474	-175.717906	-12.007681	29.0	40.00	60.00	85.00	BIMODAL	AMAZ.-ELYS.	E3
337	M1101159	9.139357	11.305463	592.0	675.00	825.00	1500.00	BRIGHT	ARABIA	D4
338	M1102194	13.274109	-12.453660	48.0	67.00	82.00	175.00	BRIGHT	ARABIA	D3
339	M1102194	13.293294	-12.565019	30.0	55.00	82.00	250.00	BIMODAL	ARABIA	D4
340	M1102194	13.314439	-12.867937	29.0	58.00	95.00	164.00	BIMODAL	ARABIA	D4
341	M1102844	-149.723170	-12.199188	37.0	32.00	40.00	163.00	NEUTRAL	AMAZ.-ELYS.	EE
342	M1102844	-149.681441	-12.593868	30.0	40.00	88.00	250.00	NEUTRAL	AMAZ.-ELYS.	EE
343	M1102844	-149.660375	-12.770994	34.0	55.00	88.00	140.00	NEUTRAL	AMAZ.-ELYS.	EE
344	M1102844	-149.642140	-12.806801	169.0	290.00	330.00	480.00	NEUTRAL	AMAZ.-ELYS.	EE
345	M1104273	174.656310	-9.642735	47.0	40.00	90.00	178.00	NEUTRAL	AMAZ.-ELYS.	EE
346	M1104273	174.668897	-9.710854	53.0	100.00	140.00	350.00	NEUTRAL	AMAZ.-ELYS.	EE
347	M1104273	174.730305	-10.349217	50.0	50.00	91.00	215.00	BRIGHT	AMAZ.-ELYS.	EE
348	M1104273	174.767254	-10.453372	63.0	90.00	190.00	310.00	BRIGHT	AMAZ.-ELYS.	EE

SRC Id	Image Name	Longitude	Latitude	Crater Diameter (m)	Min. Ejecta Blanket Radius (m)	Max Ejecta Blanket Radius (m)	Max Ray Length (m)	Ejecta Tone	Study Region	Retention Sequence Stage
349	M1104273	174.741817	-10.501613	99.0	125.00	265.00	290.00	BRIGHT	AMAZ.-ELYS.	E3
350	M1104273	174.768630	-10.519597	67.0	67.00	101.00	355.00	BRIGHT	AMAZ.-ELYS.	E2
351	M1104273	174.766238	-10.615242	57.0	71.00	95.00	315.00	BIMODAL	AMAZ.-ELYS.	E2
352	M1201040	164.594274	16.853001	39.0	45.00	115.00	215.00	BIMODAL	AMAZ.-ELYS.	D4
353	M1201040	164.588713	16.820016	48.0	60.00	110.00	300.00	BIMODAL	AMAZ.-ELYS.	D4
354	M1201040	164.558668	17.052051	49.0	59.00	125.00	300.00	BIMODAL	AMAZ.-ELYS.	D4
355	M1201230	168.850097	17.945558	25.0	24.00	36.00	44.00	BIMODAL	AMAZ.-ELYS.	E4
356	M1201230	168.851405	17.960855	23.0	23.00	35.00	46.00	BIMODAL	AMAZ.-ELYS.	E4
357	M1201871	151.056573	34.710472	84.0	230.00	375.00	620.00	BRIGHT	AMAZ.-ELYS.	D4
358	M1201884	69.095387	6.548359	34.0	37.00	48.00	91.00	BIMODAL	ARABIA	D3
359	M1300313	-70.581793	-2.495434	68.0	60.00	152.00	360.00	DARK	THARSIS	D3
360	M1300313	-70.586626	-2.587113	137.0	140.00	233.00	590.00	DARK	THARSIS	D3
361	M1302039	-42.991461	-27.270329	75.0	90.00	400.00	825.00	DARK	THARSIS	E1
362	M1302257	2.902868	0.186698	160.0	170.00	260.00	530.00	BIMODAL	ARABIA	E2
363	M1302257	2.870048	0.549611	49.0	108.00	175.00	600.00	DARK	ARABIA	E2
364	M1302257	2.838940	0.675146	36.0	48.00	94.00	135.00	DARK	ARABIA	E3
365	M1302257	2.823030	1.005149	42.0	53.00	99.00	125.00	DARK	ARABIA	E3
366	M1302257	2.794606	1.198160	30.0	33.00	55.00	82.00	DARK	ARABIA	E4
367	M1302257	2.802716	1.086168	46.0	48.00	85.00	125.00	DARK	ARABIA	E3
368	M1302257	2.813014	1.084036	91.0	134.00	178.00	255.00	DARK	ARABIA	E3
369	M1400820	-156.113281	-21.057921	32.0	32.00	43.00	83.00	BRIGHT	AMAZ.-ELYS.	E3
370	M1400820	-156.114939	-21.076713	43.0	56.00	75.00	110.00	BRIGHT	AMAZ.-ELYS.	E3
371	M1400820	-156.157311	-21.003259	33.0	25.00	63.00	133.00	BRIGHT	AMAZ.-ELYS.	E3
372	M1400820	-156.145439	-20.986789	29.0	25.00	37.00	90.00	BRIGHT	AMAZ.-ELYS.	E3
373	M1400820	-156.146197	-21.036101	42.0	34.00	80.00	158.00	BIMODAL	AMAZ.-ELYS.	E3
374	M1400820	-156.127121	-20.937528	30.0	29.00	39.00	91.00	BRIGHT	AMAZ.-ELYS.	E3
375	M1401570	6.921100	-5.168472	43.0	55.00	85.00	232.00	BRIGHT	ARABIA	E3
376	M1401918	44.245772	-4.131974	27.0	35.00	40.00	75.00	DARK	ARABIA	E3
377	M1700203	-136.414008	-32.785107	343.0	250.00	400.00	800.00	DARK	AUSTRALIS	D4
378	M1801615	146.235629	-3.795895	54.0	127.00	194.00	340.00	BIMODAL	AMAZ.-ELYS.	D2
379	M1901226	134.534118	6.749750	40.0	49.00	72.00	100.00	BIMODAL	AMAZ.-ELYS.	E3
380	M1901926	125.610006	18.319784	63.0	118.00	162.00	329.00	DARK	BOREALIS	D3
381	M2100328	-66.205785	-0.515583	107.0	185.00	210.00	415.00	BRIGHT	THARSIS	D2
382	M2100328	-66.172592	-0.550565	46.0	88.00	118.00	250.00	BRIGHT	THARSIS	D2
383	M2100328	-66.181732	-0.583143	99.0	104.00	158.00	385.00	BRIGHT	THARSIS	D2
384	M2100328	-66.189584	-0.616471	106.0	260.00	338.00	1035.00	BRIGHT	THARSIS	D2
385	M2100328	-66.176795	-0.812923	261.0	345.00	397.00	905.00	BRIGHT	THARSIS	D4
386	M2200043	-57.127968	-2.557423	54.0	60.00	167.00	232.00	DARK	THARSIS	D4
387	M2200043	-57.130714	-2.682204	53.0	74.00	99.00	130.00	DARK	THARSIS	D4
388	M2200772	-117.782686	-36.515386	24.0	22.00	32.00	58.00	BRIGHT	THARSIS	D4
389	M2201555	140.776937	-14.358013	120.0	95.00	165.00	770.00	DARK	AMAZ.-ELYS.	D3
390	M2201555	140.782609	-14.380284	30.0	30.00	124.00	144.00	BIMODAL	AMAZ.-ELYS.	E3
391	M2300435	72.025377	8.575007	35.0	32.00	105.00	222.00	DARK	ARABIA	D4
392	M2301790	141.383202	3.465399	94.0	115.00	280.00	450.00	BRIGHT	AMAZ.-ELYS.	D2

SRC Id	Image Name	Longitude	Latitude	Crater Diameter (m)	Min. Ejecta Blanket Radius (m)	Max Ejecta Blanket Radius (m)	Max Ray Length (m)	Ejecta Tone	Study Region	Retention Sequence Stage
393	M2301995	19.585265	-5.147534	44.0	36.00	85.00	148.00	BRIGHT	ARABIA	D2
394	M2301995	19.594463	-5.248963	28.0	34.00	50.00	94.00	NEUTRAL	ARABIA	D2
395	R0101230	159.917635	12.397353	79.0	106.00	267.00	670.00	BRIGHT	AMAZ.-ELYS.	E2
396	R0101230	159.952395	12.263866	48.0	50.00	71.00	170.00	BRIGHT	AMAZ.-ELYS.	E2
397	R0101230	159.947572	12.000441	73.0	84.00	215.00	406.00	BRIGHT	AMAZ.-ELYS.	E2
398	R0200542	163.371041	15.450697	48.0	68.00	125.00	265.00	BIMODAL	AMAZ.-ELYS.	E2
399	R0200542	163.372618	15.426448	34.0	57.00	106.00	150.00	BRIGHT	AMAZ.-ELYS.	E2
400	R0200542	163.367786	15.218478	38.0	38.00	64.00	168.00	BIMODAL	AMAZ.-ELYS.	E3
401	R0300454	159.235319	13.141726	59.0	95.00	152.00	285.00	BIMODAL	AMAZ.-ELYS.	E3
402	R0300454	159.268076	13.024648	43.0	61.00	97.00	160.00	BIMODAL	AMAZ.-ELYS.	E3
403	R0300454	159.290160	12.990492	80.0	86.00	154.00	204.00	BIMODAL	AMAZ.-ELYS.	E3
404	R0401249	-102.907785	-17.564084	76.0	145.00	215.00	380.00	BRIGHT	THARSIS	D4
405	R0401249	-102.808862	-18.057132	65.0	52.00	245.00	917.00	BIMODAL	THARSIS	D4
406	R0401684	118.305306	11.107248	47.0	70.00	86.00	180.00	BIMODAL	AMAZ.-ELYS.	E3
407	R0401684	118.289153	11.106468	32.0	43.00	48.00	70.00	BIMODAL	AMAZ.-ELYS.	E3
408	R0500274	44.571115	-19.085765	126.0	142.00	225.00	843.00	DARK	ARABIA	D2
409	R0501863	177.281985	27.980525	530.0	570.00	980.00	2085.00	DARK	BOREALIS	D3
410	R0501863	177.267794	27.859911	564.0	519.00	1018.00	1750.00	DARK	BOREALIS	D4
411	R0502103	-34.776103	48.298124	702.0	988.00	1592.00	2324.00	BRIGHT	BOREALIS	D3
412	R0600346	-148.749353	-16.142901	51.0	45.00	70.00	170.00	DARK	AMAZ.-ELYS.	D4
413	R0600346	-148.771231	-16.187048	202.0	135.00	275.00	405.00	DARK	AMAZ.-ELYS.	D4
414	R0600346	-148.738222	-16.410421	107.0	85.00	215.00	300.00	DARK	AMAZ.-ELYS.	D4
415	R0600346	-148.733749	-16.468478	130.0	100.00	168.00	253.00	DARK	AMAZ.-ELYS.	D4
416	R0600346	-148.663707	-16.741371	60.0	157.00	253.00	490.00	NEUTRAL	AMAZ.-ELYS.	EE
417	R0601460	-56.586408	2.333632	52.0	58.00	100.00	136.00	DARK	THARSIS	D4
418	R0601460	-56.585649	2.309617	44.0	37.00	50.00	76.00	DARK	THARSIS	D4
419	R0601460	-56.572278	2.294762	43.0	31.00	41.00	68.00	DARK	THARSIS	D4
420	R0601460	-56.580850	2.290472	53.0	35.00	85.00	114.00	DARK	THARSIS	D4
421	R0601460	-56.575207	2.266229	44.0	25.00	49.00	74.00	DARK	THARSIS	D4
422	R0601460	-56.574020	2.215537	54.0	63.00	78.00	130.00	DARK	THARSIS	D4
423	R0601460	-56.548645	2.138579	54.0	51.00	67.00	125.00	DARK	THARSIS	D4
424	R0800322	166.838934	13.363313	141.0	210.00	325.00	875.00	BIMODAL	AMAZ.-ELYS.	E2
425	R0800322	166.771740	13.767744	59.0	60.00	95.00	215.00	BIMODAL	AMAZ.-ELYS.	E2
426	R0800322	166.780993	13.720074	58.0	58.00	104.00	193.00	BIMODAL	AMAZ.-ELYS.	E2
427	R0800322	166.786270	13.623252	38.0	40.00	87.00	218.00	BIMODAL	AMAZ.-ELYS.	E2
428	R0800322	166.814559	13.560714	72.0	88.00	178.00	405.00	BIMODAL	AMAZ.-ELYS.	E2
429	R0800322	166.843950	13.523947	53.0	42.00	66.00	190.00	DARK	AMAZ.-ELYS.	E4
430	R0800322	166.859685	13.288798	53.0	50.00	144.00	475.00	DARK	AMAZ.-ELYS.	E2
431	R0800322	166.846284	13.274173	37.0	33.00	64.00	154.00	BIMODAL	AMAZ.-ELYS.	E2
432	R0801431	67.581555	-9.370768	191.0	248.00	292.00	380.00	BRIGHT	ARABIA	E2
433	R0801929	-57.616664	9.568444	156.0	178.00	548.00	1180.00	DARK	THARSIS	E3
434	R0802146	135.640518	8.403346	44.0	48.00	102.00	195.00	BIMODAL	AMAZ.-ELYS.	E3
435	R0802146	135.659337	8.362197	37.0	28.00	58.00	103.00	BIMODAL	AMAZ.-ELYS.	E3
436	R0802146	135.630192	8.349659	67.0	84.00	152.00	216.00	BIMODAL	AMAZ.-ELYS.	E3

SRC Id	Image Name	Longitude	Latitude	Crater	Min. Ejecta	Max Ejecta	Max Ray	Ejecta Tone	Study Region	Retention
				Diameter (m)	Blanket Radius (m)	Blanket Radius (m)	Length (m)			Sequence Stage
437	R0802146	135.647052	8.296473	39.0	30.00	53.00	111.00	BIMODAL	AMAZ.-ELYS.	E3
438	R0802146	135.648227	8.288916	46.0	30.00	81.00	257.00	BIMODAL	AMAZ.-ELYS.	E3
439	R0802146	135.647933	8.286930	46.0	32.00	102.00	167.00	BIMODAL	AMAZ.-ELYS.	E3
440	R0802146	135.649581	8.176924	38.0	32.00	57.00	108.00	BIMODAL	AMAZ.-ELYS.	E3
441	R0802146	135.663852	8.059539	50.0	36.00	102.00	294.00	BIMODAL	AMAZ.-ELYS.	E3
442	R0802146	135.665987	8.008788	42.0	48.00	71.00	156.00	BIMODAL	AMAZ.-ELYS.	E3
443	R0802196	-90.934507	-10.631537	63.0	80.00	115.00	250.00	DARK	THARSIS	D4
444	R0802196	-90.960078	-10.563612	37.0	46.00	56.00	93.00	BRIGHT	THARSIS	D4
445	R0802196	-90.978430	-10.245993	330.0	556.00	1280.00	2100.00	BIMODAL	THARSIS	D4
446	R0802196	-91.014508	-10.206860	224.0	517.00	810.00	1300.00	BRIGHT	THARSIS	D4
447	R0900362	45.673575	5.344070	77.0	89.00	102.00	240.00	NEUTRAL	ARABIA	EE
448	R0900362	45.691835	5.220942	25.0	22.00	45.00	75.00	BRIGHT	ARABIA	EE
449	R0900362	45.725536	5.053234	32.0	22.00	43.00	99.00	NEUTRAL	ARABIA	EE
450	R0900362	45.709372	5.036006	36.0	36.00	58.00	85.00	NEUTRAL	ARABIA	EE
451	R0901204	6.053039	-3.401430	148.0	381.00	487.00	1145.00	BIMODAL	ARABIA	D4
452	R0901204	6.105020	-4.025789	41.0	52.00	88.00	157.00	BIMODAL	ARABIA	E3
453	R0901565	12.192812	-18.634230	164.0	150.00	241.00	600.00	BRIGHT	ARABIA	E3
454	R0902905	37.147858	10.240328	47.0	100.00	133.00	210.00	NEUTRAL	ARABIA	D4
455	R0902905	37.155658	10.332411	36.0	77.00	141.00	190.00	NEUTRAL	ARABIA	D4
456	R0902905	37.171844	9.977232	18.0	140.00	500.00	600.00	BRIGHT	ARABIA	D1
457	R0902935	-20.208708	10.849444	182.0	508.00	791.00	1440.00	DARK	ARABIA	D2
458	R0903613	-6.525496	-29.461956	68.0	75.00	167.00	705.00	BRIGHT	ARABIA	E2
459	R0903613	-6.520532	-29.456520	43.0	24.00	107.00	294.00	BRIGHT	ARABIA	E2
460	R0903613	-6.541268	-29.512542	48.0	48.00	67.00	125.00	DARK	ARABIA	E3
461	R0903613	-6.514676	-29.531296	42.0	49.00	66.00	165.00	DARK	ARABIA	E3
462	R0903701	121.613683	-9.375825	55.0	98.00	155.00	510.00	DARK	AMAZ.-ELYS.	D2
463	R0903701	121.588355	-9.365776	42.0	66.00	83.00	195.00	BIMODAL	AMAZ.-ELYS.	E3
464	R0903707	118.597536	13.154619	63.0	89.00	112.00	176.00	BRIGHT	AMAZ.-ELYS.	E3
465	R0903707	118.640452	13.091246	57.0	105.00	132.00	203.00	BRIGHT	AMAZ.-ELYS.	E3
466	R0903869	163.698993	12.788591	23.0	37.00	88.00	168.00	BIMODAL	AMAZ.-ELYS.	E2
467	R0903869	163.709359	12.777558	45.0	49.00	97.00	210.00	BRIGHT	AMAZ.-ELYS.	E2
468	R0903869	163.744830	12.782152	37.0	24.00	57.00	91.00	DARK	AMAZ.-ELYS.	E4
469	R0903869	163.743439	12.784119	27.0	35.00	68.00	124.00	BIMODAL	AMAZ.-ELYS.	E2
470	R0903869	163.741828	12.765438	34.0	48.00	66.00	99.00	BIMODAL	AMAZ.-ELYS.	E2
471	R0903869	163.721478	12.747137	39.0	60.00	69.00	123.00	BIMODAL	AMAZ.-ELYS.	E2
472	R0903869	163.728683	12.728795	84.0	110.00	209.00	344.00	BIMODAL	AMAZ.-ELYS.	E3
473	R0903869	163.737496	12.719808	37.0	43.00	126.00	392.00	BIMODAL	AMAZ.-ELYS.	E2
474	R0903869	163.747727	12.731193	46.0	40.00	106.00	192.00	BIMODAL	AMAZ.-ELYS.	E3
475	R0903869	163.730247	12.718719	70.0	60.00	98.00	212.00	BIMODAL	AMAZ.-ELYS.	E3
476	R0903869	163.735276	12.708494	41.0	57.00	82.00	136.00	BIMODAL	AMAZ.-ELYS.	E3
477	R0903869	163.759548	12.711643	35.0	71.00	104.00	168.00	BIMODAL	AMAZ.-ELYS.	E2
478	R1000095	-87.537197	-4.854940	87.0	200.00	285.00	421.00	DARK	THARSIS	D4
479	R1000095	-87.512898	-4.989229	31.0	46.00	85.00	112.00	BIMODAL	THARSIS	D4
480	R1000095	-87.509430	-4.847677	87.0	139.00	178.00	247.00	BIMODAL	THARSIS	D4

SRC Id	Image Name	Longitude	Latitude	Crater	Min. Ejecta	Max. Ejecta	Max. Ray	Ejecta Tone	Study Region	Retention
				Diameter (m)	Blanket Radius (m)	Blanket Radius (m)	Length (m)			Sequence Stage
481	R1000224	-124.050321	-35.553957	135.0	108.00	178.00	473.00	DARK	THARSIS	D4
482	R1000224	-124.069584	-35.413246	41.0	36.00	87.00	142.00	DARK	THARSIS	D4
483	R1001318	140.685947	-2.243849	52.0	103.00	140.00	386.00	BIMODAL	AMAZ.-ELYS.	D2
484	R1001318	140.746632	-2.597759	54.0	82.00	130.00	324.00	DARK	AMAZ.-ELYS.	D4
485	R1001395	-85.640960	-23.377071	113.0	80.00	149.00	195.00	DARK	THARSIS	E4
486	R1002009	65.549466	-25.502442	95.0	99.00	110.00	220.00	DARK	AUSTRALIS	E4
487	R1002070	-107.840084	-14.604635	59.0	64.00	114.00	335.00	DARK	THARSIS	D2
488	R1002393	-132.036963	-19.411388	47.0	73.00	115.00	445.00	BRIGHT	THARSIS	D3
489	R1002393	-132.010042	-19.487154	25.0	42.00	48.00	70.00	BRIGHT	THARSIS	E3
490	R1003601	115.267875	47.058658	82.0	72.00	118.00	717.00	DARK	BOREALIS	D1
491	R1003791	137.391322	7.900293	58.0	87.00	112.00	168.00	BIMODAL	AMAZ.-ELYS.	E3
492	R1003791	137.431523	7.703292	45.0	50.00	83.00	216.00	BIMODAL	AMAZ.-ELYS.	E2
493	R1004287	-60.659071	18.095204	66.0	69.00	80.00	105.00	DARK	THARSIS	E4
494	R1004287	-60.643498	18.058300	74.0	61.00	99.00	137.00	DARK	THARSIS	E4
495	R1004287	-60.579083	17.463583	61.0	56.00	87.00	108.00	DARK	THARSIS	E4
496	R1100170	44.754921	-13.279128	26.0	36.00	54.00	63.00	BIMODAL	ARABIA	E3
497	R1100170	44.764381	-13.367174	63.0	50.00	140.00	278.00	BRIGHT	ARABIA	D2
498	R1100170	44.764753	-13.425040	30.0	27.00	41.00	77.00	BRIGHT	ARABIA	E4
499	R1100170	44.768364	-13.448808	25.0	30.00	44.00	64.00	DARK	ARABIA	E4
500	R1100170	44.748727	-13.502325	24.0	23.00	35.00	89.00	DARK	ARABIA	E4
501	R1100170	44.767437	-13.610003	40.0	33.00	96.00	195.00	BRIGHT	ARABIA	E2
502	R1100170	44.795400	-13.696765	30.0	53.00	70.00	99.00	BRIGHT	ARABIA	E3
503	R1100170	44.819243	-13.805236	92.0	220.00	300.00	610.00	BRIGHT	ARABIA	E2
504	R1102785	175.465975	-26.473741	104.0	145.00	200.00	594.00	BIMODAL	AUSTRALIS	D2
505	R1102785	175.529222	-27.183477	48.0	85.00	103.00	210.00	BIMODAL	AUSTRALIS	D3
506	R1103743	-58.276886	0.463529	34.0	35.00	45.00	71.00	DARK	THARSIS	E4
507	R1103743	-58.256461	0.374601	42.0	148.00	156.00	204.00	DARK	THARSIS	D3
508	R1103743	-58.256667	0.269211	41.0	31.00	59.00	270.00	DARK	THARSIS	D3
509	R1104144	-63.131050	-3.899836	44.0	53.00	74.00	105.00	DARK	THARSIS	E4
510	R1104144	-63.060834	-4.275735	130.0	86.00	167.00	330.00	DARK	THARSIS	E3
511	R1201219	-169.551684	-9.749947	63.0	70.00	157.00	400.00	DARK	AMAZ.-ELYS.	E2
512	R1201393	-152.344748	-16.880663	40.0	46.00	65.00	170.00	DARK	AMAZ.-ELYS.	D3
513	R1201393	-152.348159	-16.882835	61.0	146.00	162.00	370.00	BIMODAL	AMAZ.-ELYS.	D2
514	R1203893	-160.151818	-34.662482	43.0	53.00	76.00	127.00	BRIGHT	AUSTRALIS	E3
515	R1203893	-160.174352	-34.703704	36.0	41.00	63.00	105.00	BRIGHT	AUSTRALIS	E3
516	R1203893	-160.150498	-34.767829	64.0	90.00	138.00	428.00	BRIGHT	AUSTRALIS	E2
517	R1300987	13.595599	-28.867294	29.0	37.00	46.00	111.00	BRIGHT	ARABIA	E2
518	R1300987	13.634145	-29.177424	137.0	376.00	560.00	1200.00	BRIGHT	ARABIA	E1
519	R1300987	13.683176	-29.284003	120.0	255.00	346.00	549.00	BRIGHT	ARABIA	D4
520	R1300987	13.688418	-29.331330	42.0	51.00	63.00	109.00	BRIGHT	ARABIA	D3
521	R1300987	13.678134	-29.339010	54.0	75.00	97.00	152.00	BRIGHT	ARABIA	D4
522	R1302095	21.804277	-7.659674	46.0	102.00	210.00	370.00	BIMODAL	ARABIA	E1
523	R1303243	48.422891	-2.299773	40.0	38.00	71.00	117.00	DARK	ARABIA	D3
524	R1303243	48.403965	-2.188114	46.0	55.00	66.00	135.00	DARK	ARABIA	D3

SRC Id	Image Name	Longitude	Latitude	Crater	Min. Ejecta	Max. Ejecta	Max. Ray	Ejecta Tone	Study Region	Retention
				Diameter (m)	Blanket Radius (m)	Blanket Radius (m)	Length (m)			Sequence Stage
525	R1303243	48.437335	-2.429437	93.0	80.00	151.00	363.00	DARK	ARABIA	D4
526	R1303877	53.759038	13.272396	57.0	34.00	54.00	154.00	DARK	ARABIA	E3
527	R1303887	28.887720	-15.261776	60.0	88.00	123.00	267.00	DARK	ARABIA	D4
528	R1303887	28.917755	-15.454853	34.0	33.00	41.00	65.00	BRIGHT	ARABIA	E4
529	R1303887	28.933373	-15.603073	60.0	82.00	129.00	208.00	BRIGHT	ARABIA	E2
530	R1400327	1.233284	-4.899583	40.0	46.00	59.00	107.00	DARK	ARABIA	E4
531	R1400327	1.174262	-4.723669	30.0	28.00	43.00	64.00	DARK	ARABIA	E4
532	R1400479	-12.506956	4.891332	132.0	140.00	187.00	560.00	DARK	ARABIA	D2
533	R1400749	51.129813	-15.289063	37.0	57.00	88.00	165.00	BRIGHT	ARABIA	E2
534	R1400749	51.168781	-15.380454	41.0	64.00	79.00	108.00	BRIGHT	ARABIA	E3
535	R1400749	51.167114	-15.548805	49.0	104.00	120.00	272.00	BRIGHT	ARABIA	E1
536	R1400970	-9.012801	33.165922	357.0	325.00	830.00	1560.00	DARK	ARABIA	D2
537	R1402648	155.465152	4.109249	61.0	43.00	85.00	200.00	DARK	AMAZ.-ELYS.	E4
538	R1402648	155.469822	4.111014	52.0	46.00	92.00	206.00	DARK	AMAZ.-ELYS.	E4
539	R1402648	155.508839	4.029946	62.0	49.00	103.00	130.00	DARK	AMAZ.-ELYS.	E4
540	R1402648	155.509005	3.934217	85.0	43.00	111.00	288.00	DARK	AMAZ.-ELYS.	E4
541	R1500367	-31.127861	11.534885	45.0	44.00	67.00	139.00	DARK	ARABIA	E4
542	R1501007	58.001767	-21.910873	49.0	56.00	95.00	124.00	BRIGHT	ARABIA	E3
543	R1502671	117.432496	-1.749126	47.0	64.00	76.00	135.00	BIMODAL	AMAZ.-ELYS.	E3
544	R1502671	117.436069	-1.708134	56.0	95.00	138.00	302.00	BIMODAL	AMAZ.-ELYS.	E2
545	R1502671	117.436274	-1.698095	36.0	56.00	86.00	124.00	BIMODAL	AMAZ.-ELYS.	E3
546	R1502671	117.435741	-1.695551	38.0	83.00	98.00	106.00	BIMODAL	AMAZ.-ELYS.	E3
547	R1502671	117.438151	-1.667992	26.0	30.00	49.00	118.00	BIMODAL	AMAZ.-ELYS.	E3
548	R1502671	117.430041	-1.618645	33.0	44.00	68.00	99.00	BIMODAL	AMAZ.-ELYS.	E3
549	R1502671	117.424068	-1.523904	39.0	49.00	62.00	102.00	BRIGHT	AMAZ.-ELYS.	E3
550	R1601572	-144.352184	-28.189781	95.0	130.00	177.00	905.00	BRIGHT	AMAZ.-ELYS.	D1
551	R1602507	176.360420	-24.134622	72.0	60.00	95.00	209.00	BRIGHT	AUSTRALIS	E4
552	R1700163	119.566163	0.117837	37.0	49.00	72.00	114.00	BRIGHT	AMAZ.-ELYS.	E3
553	R1700163	119.541065	0.100888	26.0	30.00	52.00	79.00	BRIGHT	AMAZ.-ELYS.	E3
554	R1700163	119.549805	0.021202	27.0	30.00	55.00	69.00	BRIGHT	AMAZ.-ELYS.	E3
555	R1700163	119.572403	0.027634	30.0	29.00	35.00	64.00	BRIGHT	AMAZ.-ELYS.	E3
556	R1700163	119.568647	0.020191	26.0	35.00	43.00	81.00	BRIGHT	AMAZ.-ELYS.	E4
557	R1701945	130.092215	-14.241074	45.0	53.00	96.00	162.00	DARK	AMAZ.-ELYS.	E4
558	R1702074	-54.870662	-9.606529	53.0	70.00	108.00	337.00	DARK	THARSIS	D3
559	R1702074	-54.862450	-9.602519	57.0	74.00	134.00	220.00	DARK	THARSIS	D3
560	R1702074	-54.836808	-9.887380	77.0	155.00	197.00	545.00	DARK	THARSIS	D4
561	R1702074	-54.812837	-9.903878	32.0	35.00	42.00	80.00	DARK	THARSIS	E4
562	R1702201	143.789802	31.959252	314.0	608.00	966.00	1342.00	BRIGHT	AMAZ.-ELYS.	D1
563	R1801047	-176.802105	-12.507246	31.0	42.00	55.00	80.00	NEUTRAL	AMAZ.-ELYS.	EE
564	R1801047	-176.807210	-12.533231	50.0	53.00	74.00	145.00	NEUTRAL	AMAZ.-ELYS.	EE
565	R1801047	-176.818950	-12.539247	106.0	150.00	165.00	180.00	BRIGHT	AMAZ.-ELYS.	E4
566	R1801047	-176.817628	-12.537080	81.0	78.00	107.00	189.00	BRIGHT	AMAZ.-ELYS.	E4
567	R1801047	-176.816609	-12.578744	28.0	19.00	37.00	86.00	NEUTRAL	AMAZ.-ELYS.	EE
568	R1801047	-176.764469	-12.778297	53.0	34.00	114.00	216.00	NEUTRAL	AMAZ.-ELYS.	EE

SRC Id	Image Name	Longitude	Latitude	Crater Diameter (m)	Min. Ejecta Blanket Radius (m)	Max. Ejecta Blanket Radius (m)	Max. Ray Length (m)	Ejecta Tone	Study Region	Retention Sequence Stage
569	R1801047	-176.796642	-12.811874	43.0	120.00	157.00	245.00	BIMODAL	AMAZ.-ELYS.	D2
570	R1801726	169.387039	-12.730703	45.0	55.00	64.00	120.00	BRIGHT	AMAZ.-ELYS.	EE
571	R1801726	169.408281	-12.855733	37.0	40.00	60.00	108.00	DARK	AMAZ.-ELYS.	D4
572	R1801726	169.395573	-12.907114	43.0	33.00	51.00	86.00	NEUTRAL	AMAZ.-ELYS.	EE
573	R1802351	142.051900	-4.683546	66.0	80.00	135.00	183.00	BRIGHT	AMAZ.-ELYS.	D1
574	R1802351	142.078834	-4.803668	29.0	39.00	43.00	74.00	BRIGHT	AMAZ.-ELYS.	E3
575	R1900536	-123.351222	-62.172185	823.0	900.00	1300.00	1870.00	NEUTRAL	AUSTRALIS	D4
576	R2000372	169.183846	-16.131229	32.0	41.00	55.00	76.00	BIMODAL	AMAZ.-ELYS.	E3
577	R2000372	169.176362	-16.111910	40.0	34.00	36.00	60.00	NEUTRAL	AMAZ.-ELYS.	EE
578	R2000372	169.173774	-16.210813	34.0	34.00	52.00	87.00	BIMODAL	AMAZ.-ELYS.	E3
579	R2000372	169.188254	-16.213206	44.0	50.00	60.00	122.00	BRIGHT	AMAZ.-ELYS.	E3
580	R2200558	-179.735642	-0.630432	60.0	75.00	110.00	241.00	NEUTRAL	AMAZ.-ELYS.	E4
581	R2200558	-179.746213	-0.672802	60.0	45.00	125.00	330.00	NEUTRAL	AMAZ.-ELYS.	EE
582	R2200558	-179.721606	-0.678972	83.0	90.00	163.00	468.00	NEUTRAL	AMAZ.-ELYS.	EE
583	R2200558	-179.741069	-0.658066	49.0	36.00	126.00	223.00	NEUTRAL	AMAZ.-ELYS.	EE
584	R2200558	-179.715717	-0.711316	43.0	26.00	90.00	286.00	NEUTRAL	AMAZ.-ELYS.	EE
585	S0300112	59.805465	15.588164	55.0	69.00	132.00	233.00	BIMODAL	ARABIA	D2
586	S0300112	59.843462	15.583271	30.0	30.00	48.00	92.00	DARK	ARABIA	D3
587	S0300112	59.873582	15.230206	23.0	19.00	40.00	124.00	DARK	ARABIA	D3
588	S0300112	59.888117	15.203469	98.0	153.00	211.00	345.00	BRIGHT	ARABIA	D2
589	S0300112	59.885554	15.164478	30.0	33.00	50.00	111.00	DARK	ARABIA	D3
590	S0300112	59.892311	15.197652	27.0	26.00	67.00	132.00	DARK	ARABIA	D3
591	S0300823	-33.299015	22.925215	177.0	139.00	381.00	1043.00	DARK	BOREALIS	D2
592	S0400538	-15.306134	9.995443	58.0	77.00	162.00	238.00	DARK	ARABIA	D3
593	S0400538	-15.270647	9.999463	30.0	35.00	39.00	58.00	DARK	ARABIA	D4
594	S0400538	-15.268208	9.985651	28.0	27.00	35.00	46.00	DARK	ARABIA	D4
595	S0400538	-15.266527	9.983675	30.0	28.00	43.00	55.00	DARK	ARABIA	D4
596	S0400538	-15.262325	9.979307	42.0	47.00	111.00	170.00	DARK	ARABIA	D4
597	S0400538	-15.263461	9.948675	33.0	32.00	39.00	60.00	DARK	ARABIA	D4
598	S0400538	-15.281934	9.935643	41.0	53.00	60.00	95.00	DARK	ARABIA	D4
599	S0400538	-15.258505	9.937504	39.0	47.00	53.00	134.00	DARK	ARABIA	D4
600	S0400538	-15.257151	9.923433	29.0	41.00	51.00	64.00	DARK	ARABIA	D4
601	S0501033	11.837010	3.944866	93.0	165.00	430.00	836.00	BRIGHT	ARABIA	E2
602	S0501033	11.834912	3.808208	115.0	295.00	390.00	620.00	BIMODAL	ARABIA	E2
603	S0501033	11.890253	3.699023	33.0	32.00	41.00	90.00	BRIGHT	ARABIA	E3
604	S0501033	11.891508	3.668451	36.0	35.00	63.00	130.00	BRIGHT	ARABIA	E3
605	S0501033	11.863755	3.543988	71.0	78.00	216.00	530.00	BIMODAL	ARABIA	E2
606	S0501244	2.998495	4.753701	150.0	338.00	417.00	1612.00	DARK	ARABIA	E2
607	S0600035	-23.405275	28.006791	84.0	168.00	294.00	457.00	DARK	BOREALIS	D3
608	S0601332	-40.283521	-6.325733	449.0	549.00	555.00	1062.00	DARK	THARSIS	D4
609	S0601579	7.333064	1.576552	31.0	26.00	53.00	121.00	DARK	ARABIA	E3
610	S0601579	7.334724	1.502149	73.0	96.00	157.00	452.00	DARK	ARABIA	E3
611	S0602214	-179.389318	-18.374125	73.0	62.00	101.00	158.00	DARK	AUSTRALIS	E3
612	S0602214	-179.343489	-18.504209	40.0	41.00	67.00	87.00	BRIGHT	AUSTRALIS	E3

SRC Id	Image Name	Longitude	Latitude	Crater	Min. Ejecta	Max. Ejecta	Max Ray	Ejecta Tone	Study Region	Retention
				Diameter (m)	Blanket Radius (m)	Blanket Radius (m)	Length (m)			Sequence Stage
613	S0602214	-179.384342	-18.498128	38.0	49.00	57.00	100.00	BRIGHT	AUSTRALIS	E3
614	S0602214	-179.321823	-18.609981	49.0	65.00	83.00	129.00	BIMODAL	AUSTRALIS	E3
615	S0602214	-179.319726	-18.774337	41.0	37.00	65.00	151.00	DARK	AUSTRALIS	E4
616	S0602214	-179.327271	-18.630377	41.0	66.00	82.00	104.00	BIMODAL	AUSTRALIS	E3
617	S0602241	63.536750	1.012608	68.0	59.00	110.00	421.00	DARK	ARABIA	E2
618	S0602241	63.525301	1.018295	28.0	53.00	76.00	101.00	BIMODAL	ARABIA	E3
619	S0602241	63.482432	1.300167	39.0	66.00	94.00	107.00	DARK	ARABIA	E3
620	S0700595	54.913308	19.798571	57.0	42.00	59.00	192.00	DARK	ARABIA	D3
621	S0700595	54.903970	19.754587	33.0	39.00	52.00	124.00	DARK	ARABIA	D4
622	S0700789	-156.793377	9.982602	73.0	44.00	137.00	270.00	NEUTRAL	AMAZ.-ELYS.	EE
623	S0800367	38.212785	-16.219914	27.0	50.00	76.00	103.00	BIMODAL	ARABIA	E3
624	S0800367	38.199192	-16.279417	32.0	58.00	105.00	214.00	DARK	ARABIA	D3
625	S0800367	38.198277	-16.300589	26.0	38.00	53.00	135.00	DARK	ARABIA	D4
626	S0800367	38.189267	-16.289605	58.0	87.00	112.00	195.00	DARK	ARABIA	D4
627	S0800729	-59.193466	4.847221	45.0	38.00	56.00	122.00	DARK	THARSIS	E4
628	S0800729	-59.201859	4.889562	102.0	82.00	154.00	207.00	DARK	THARSIS	E4
629	S0803051	-9.368918	35.148505	49.0	52.00	71.00	105.00	DARK	ARABIA	E4
630	S1000940	-117.500048	18.763605	39.0	48.00	83.00	160.00	NEUTRAL	THARSIS	EE
631	S1001006	-11.305911	-11.872025	25.0	28.00	33.00	145.00	DARK	ARABIA	D3